frontiers | Research Topics

Highlights from Marie Skłodowska-Curie actions fellows 2021

Edited by
Gwilherm Evano, Luís D. Carlos, Nicole J. Jaffrezic-Renault, Valeria Conte, Nicola Maria Pugno, Diego Cazorla-Amoros, Valeria Cannillo and John L. Provis

Published in
Frontiers in Chemistry
Frontiers in Nanotechnology

ISSN 1664-8714
ISBN 978-2-8325-4203-3
DOI 10.3389/978-2-8325-4203-3

About Frontiers

Frontiers is more than just an open access publisher of scholarly articles: it is a pioneering approach to the world of academia, radically improving the way scholarly research is managed. The grand vision of Frontiers is a world where all people have an equal opportunity to seek, share and generate knowledge. Frontiers provides immediate and permanent online open access to all its publications, but this alone is not enough to realize our grand goals.

Frontiers journal series

The Frontiers journal series is a multi-tier and interdisciplinary set of open-access, online journals, promising a paradigm shift from the current review, selection and dissemination processes in academic publishing. All Frontiers journals are driven by researchers for researchers; therefore, they constitute a service to the scholarly community. At the same time, the *Frontiers journal series* operates on a revolutionary invention, the tiered publishing system, initially addressing specific communities of scholars, and gradually climbing up to broader public understanding, thus serving the interests of the lay society, too.

Dedication to quality

Each Frontiers article is a landmark of the highest quality, thanks to genuinely collaborative interactions between authors and review editors, who include some of the world's best academicians. Research must be certified by peers before entering a stream of knowledge that may eventually reach the public - and shape society; therefore, Frontiers only applies the most rigorous and unbiased reviews. Frontiers revolutionizes research publishing by freely delivering the most outstanding research, evaluated with no bias from both the academic and social point of view. By applying the most advanced information technologies, Frontiers is catapulting scholarly publishing into a new generation.

What are Frontiers Research Topics?

Frontiers Research Topics are very popular trademarks of the *Frontiers journals series*: they are collections of at least ten articles, all centered on a particular subject. With their unique mix of varied contributions from Original Research to Review Articles, Frontiers Research Topics unify the most influential researchers, the latest key findings and historical advances in a hot research area.

Find out more on how to host your own Frontiers Research Topic or contribute to one as an author by contacting the Frontiers editorial office: frontiersin.org/about/contact

2021 Highlights from Marie Skłodowska-Curie actions fellows

Topic editors

Gwilherm Evano — Université libre de Bruxelles, Belgium
Luís D. Carlos — University of Aveiro, Portugal
Nicole J. Jaffrezic-Renault — Université Claude Bernard Lyon 1, France
Valeria Conte — University of Rome Tor Vergata, Italy
Nicola Maria Pugno — University of Trento, Italy
Diego Cazorla-Amoros — University of Alicante, Spain
Valeria Cannillo — University of Modena and Reggio Emilia, Italy
John L. Provis — Paul Scherrer Institut (PSI), Switzerland

Citation

Evano, G., Carlos, L. D., Jaffrezic-Renault, N. J., Conte, V., Pugno, N. M., Cazorla-Amoros, D., Cannillo, V., Provis, J. L., eds. (2024). *2021 Highlights from Marie Skłodowska-Curie actions fellows*. Lausanne: Frontiers Media SA.
doi: 10.3389/978-2-8325-4203-3

Table of contents

frontiers in Nanotechnology

MINI REVIEW
published: 14 October 2021
doi: 10.3389/fnano.2021.770281

Surfactant-Free Precious Metal Colloidal Nanoparticles for Catalysis

Jonathan Quinson *

Department of Chemistry, University of Copenhagen, Copenhagen, Denmark

Colloidal syntheses of nanoparticles (NPs) are one of the preferred approaches to prepare precious metal catalysts. Unfortunately, most colloidal syntheses developed require stabilizing agents to avoid NP agglomeration and/or control NP size and morphology. While these *surfactants* can bring positive features, they typically block catalytically active sites on the NP surface. As a consequence, these additives often need to be removed by energy and/or time consuming steps, at the risk of complicating the synthesis, introducing irreproducibility and negatively altering the structure and properties of the prepared catalysts. Fortunately, several surfactant-free colloidal syntheses have been reported and are being developed. This Mini Review addresses the challenges in defining a surfactant-free colloidal synthesis of NPs and survey established and emerging strategies to obtain surfactant-free colloidal precious metal NPs. A focus is given to approaches that show promising features to bridge the gap between fundamental and applied research towards industrial applications.

Keywords: nanoparticles, precious metals, colloids, surfactant-free, catalysis, polyols, mono-alcohols, synthesis

OPEN ACCESS

Edited by:
Diego Cazorla-Amoros,
University of Alicante, Spain

Reviewed by:
Ángel Berenguer-Murcia,
University of Alicante, Spain
Wei Zhou,
Tianjin University, China

***Correspondence:**
Jonathan Quinson
jonathan.quinson@chem.ku.dk

Specialty section:
This article was submitted to Nanocatalysis, a section of the journal Frontiers in Nanotechnology

Received: *03 September 2021*
Accepted: *04 October 2021*
Published: *14 October 2021*

Citation:
Quinson J (2021) Surfactant-Free Precious Metal Colloidal Nanoparticles for Catalysis. Front. Nanotechnol. 3:770281. doi: 10.3389/fnano.2021.770281

INTRODUCTION

Nanoparticles (NPs) have found applications in a vast number of fields, ranging from medicine, imaging, sensing, water/air remediation, energy conversion or catalysis. While the benefits of NPs to address various challenges does not need to be demonstrated anymore, there is still a gap between fundamental research and the development of a nanotechnology (Stavis et al., 2018). Part of this gap comes from the production method of the NPs. Wet-chemical methods are commonly used to obtain NPs since a wide library of nanomaterials can be produced. In this bottom-up approach, a precursor molecule containing an atom of the desired element, e.g., H_2PtCl_6 for Pt (Quinson and Jensen 2020), is reduced in a solvent, often in presence of reducing agents and stabilizers. Some chemicals can play several roles during the synthesis, e.g., sodium citrate is both a reducing agent and stabilizer in the popular Turkevich synthesis of gold NPs (Wuithschick et al., 2015). It is very often claimed that *surfactants*/*stabilizers*/*ligands* or *capping agents* are needed to stabilize the NPs (Heuer-Jungemann et al., 2019). Examples of such stabilizers are polymers or long carbon chain molecules such as polyvinylpyrrolidone (PVP) or cetrimonium bromide (CTAB), plant extracts or DNA (Koczkur et al., 2015). The role of these *additives* - in the sense that these chemicals are not needed to reduce metal complexes and to form nano- or micro-materials in solution from molecules containing only one or few atoms of a transition metal element - is to avoid the undesirable agglomeration and overgrowth of the NPs in order to obtain stable colloids. The actual role of these additives *during* the formation of the NPs is complex to elucidate since they typically have multiple roles. For instance PVP is a dual protecting *and* reducing agent. This complexity prevents a detailed understanding of NP formation.

While additives allow controlling the stability but also the structure of the nanomaterials produced, they bring several challenges. 1) The additives are often toxic and their use raise

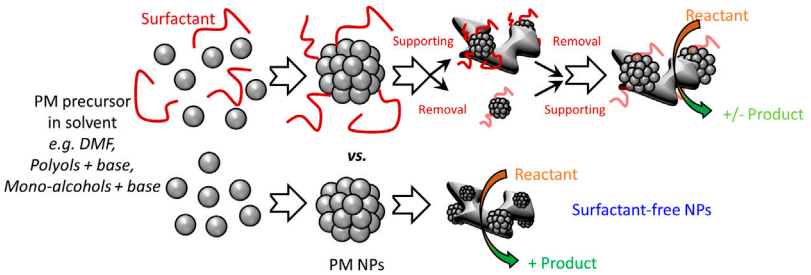

FIGURE 1 | Schematic representation of some colloidal syntheses of PM NPs and illustration of the benefits of surfactant-free approaches to develop supported catalysts with controlled NP size and loading.

safety concerns, especially at large scale (Johnson et al., 2021). 2) The additives typically derive from fossil fuels, which is not in the long term a sustainable approach to produce NPs. 3) Using additives add to the cost of a synthesis. 4) Using additives may bring impurities that reduce reproducibility, thus may impair the scalability of the NP synthesis (El Amri and Roger 2020). 5) For a range of applications like catalysis, the additives need to be removed (Cargnello et al., 2015). This is typically achieved by washing and/or heat treatments that add steps to the catalyst preparation and may impair reproducibility by potentially altering the structure of the prepared NPs, see **Figure 1**. The presence of residual surfactants on the NP surface might also impair further functionalization when the latter is desired, e.g., for medical applications or catalysis. 6) To advance our understanding of NP properties, the surfactant removal implies a full characterization of the *as-prepared* catalyst but also the *cleaned* catalyst, which is time and resource consuming (Losch et al., 2019).

Colloidal syntheses have been a key tool to advance the field of catalysis (Guntern et al., 2021; Losch et al., 2019) and strategies to overcome the above drawbacks have been reported. For heterogeneous catalytic applications and electrocatalysis, the NPs are typically supported on another material. A typical approach to overcome the use of surfactants is therefore to performed so-called one-pot syntheses where the NPs are obtained directly on the support. Unfortunately, this approach is support-dependent and requires the optimization of various syntheses parameters for every new support in order to obtain NPs with the same size or composition and reach the desired loading of NPs on the support. Furthermore, the NPs might form in parts of the support like pores not accessible during catalytic reactions (Park et al., 2016). This is a severe drawback for precious metal (PM) NPs, made of non-renewable and expensive materials, which are yet among the best-known materials for a range of chemical reactions and well-established industrial catalysts. To advance further the design of NP catalysts, *surfactant-free* colloidal syntheses are highly desirable, 1) to simplify the synthesis of NPs and make is safer, 2) to simplify the (large scale) use and processing of the NPs, 3) to develop catalysts readily active without the need for washing and/or activation steps. This ultimately reduce production cost and makes it more straightforward to transfer the knowledge gained in fundamental research to industrial applications: With a surfactant-free synthesis, the same production method of the catalyst would be suitable for both the fundamental and applied research involved in a catalyst development (Quinson et al., 2018).

While it is a popular belief, there is actually no need to use *surfactants* for a number of colloidal synthetic approaches to be successful. The last comprehensive review, not technique specific, on the topic of *surfactant-free* synthesis is probably from 2013 by Prof Kawasaki (Kawasaki 2013). The present Mini-Review therefore focuses on work published after this date and new strategies that emerged since. The pros and cons of commonly used syntheses are highlighted. A focus is given to applications for catalysis. In particular, electro-catalytic reactions performed at room temperature benefit from surfactant-free NPs. Since in catalysis the size of the NPs strongly influence the resulting properties, the opportunities to achieve size control without using surfactants are stressed.

OVERVIEW OF SURFACTANT-FREE COLLOIDAL SYNTHESES

A *surfactant-free* synthesis is challenging to define (Kawasaki 2013; Niu and Li 2014). From thermodynamics arguments, a NP *will* be stabilized in solutions by small molecules, solvent and/or electrostatic interactions. "Unprotected" NPs (Schrader et al., 2015) obtained by *surfactant-free* approaches here refer to syntheses where no chemicals with a molar mass greater than 100 g mol^{-1} is added during the synthesis. While they are commonly referred to as surfactant-free, this definition therefore excludes the majority of syntheses using benzyl-alcohol, methyl isobutyl ketone, amino-acids, plants extracts or biogenic syntheses using for instance micro-organisms.

Laser Synthesis and Processing of Colloids

The most established method to develop surfactant-free NPs is probably the laser synthesis and processing of colloids (Zhang et al., 2017). In a nutshell, in this top-down approach, a piece of metal plays the role of target for a laser beam, from which NPs form by a cavitation phenomenon. Alternatively, NPs properties can be modulated by fragmentation and melting still using a laser. The method has been extensively reviewed, especially by Prof Barcikowski and co-workers (Reichenberger et al., 2019; Zhang

et al., 2017). It requires relatively simple equipment, is scalable and suitable to obtain numerous PM NPs of various compositions, e.g., by controlling the composition of the target material. Examples of NPs obtained include Au, Ag, Pt, Pd based NPs and even multi-metallic (Reichenberger et al., 2019). Since it easily leads to *bare* NPs mainly stabilized by electrostatic interaction, it has been used to study the effect of chemical functionalization in toxicology, medicine or catalysis.

The main drawback of this approach is the size distribution obtained for as-produced NPs, in the range of few nm up to micrometers, typically showing a bimodal distribution, that requires post-treatment like centrifugation to isolate NPs of a given size range (Kohsakowski et al., 2020). Furthermore, the synthesis require the optimization of a vast range of experimental parameters such as laser fluence, pulse duration, repetition rate or laser wavelength, and therefore a certain degree of expertise.

Plasma Synthesis

In this relatively less common approach, an electrode is used to generate a plasma and surfactant-free colloidal NPs stabilized by electrostatic interaction are obtained from inorganic complexes. The opportunities offered by this approach have been reviewed by Prof Kim and co-workers (Mun et al., 2017). The main drawback of this approach is maybe to require somewhat specific equipment. Metal NPs like Au, Ag, Pt in the size range 2–30 nm were obtained.

N,N-Dimethylformamide Synthesis

Wet chemical syntheses remain relatively easier to perform since only simple reflux setups or autoclaves are needed. The use of N,N-Dimethylformamide (DMF) as solvent, reducing and stabilizing agent has proved to lead to small NPs. In many cases, a stabilizer like PVP is added to the synthesis but it is actually not needed. In particular, Prof Obora and co-workers demonstrated the benefits of this approach for various catalytic reactions (Nagata and Obora 2020). A wide range of NPs such as Au, Ag, Pd, Pt, Ir, Rh were obtained as well as PtNi nanomaterials (Cui et al., 2012) showing high activity for the oxygen reduction reaction (ORR). A unique feature of this approach is to lead to small NPs less than 10 nm in size or even to nanoclusters made of few atoms. The main drawbacks is the use of a relatively toxic solvent, the use of relatively high temperature and the possible need to partially remove the stabilizing DMF, e.g., by heat treatment.

Polyol Synthesis

The polyols synthesis first reported and recently reviewed by Fiévet and co-workers (Fiévet et al., 2018) is an extremely popular synthesis method since it is performed in alkaline ethylene glycol, a relatively safe solvent, with a relatively high boiling point temperature, allowing to produce a very wide range of nanomaterials. In many cases, additives are added. However, since the pioneer work by Wang and co-workers with Prof Tang (Wang et al., 2000), it is well-established that no surfactants are required to obtain a range of colloidal PM NPs with a size controlled in the range 2–10 nm, including bi-metallic. The resulting "unprotected" NPs, in the sense that they are stabilized typically by CO groups and OH/OH^- moieties (Schrader et al., 2015), are readily active for a range of catalytic reactions. Size control is typically achieved by adding water or controlling the Base/metal ratio. Due to its simplicity, it has also been a suitable model to study the formation mechanism of NPs. A positive feature of this approach is to lead to NPs that can be stored as unsupported powders and re-dispersed in a desired solvent (Neumann et al., 2017).

The "unprotected" NPs are ideal building blocks to study and develop a range of catalysts (Quinson et al., 2021) and Pt, Ir, Ru, Rh or Os NPs and various bi-metallic have been reported. Since several types of NPs can be obtained, the method is also suitable to investigate the effect of alloys or nanocomposites made of a mixture of NPs (Du et al., 2021). This approach is however more challenging to control to obtain small size Au, Ag and Pd NPs since the latter tend to overgrow. To date, Au NPs are best obtained using glycerol as reducing agent in mixture with water (Parveen et al., 2019). Due to the high redox potential of Au, the synthesis proceeds at room temperature. However the high viscosity of glycerol prevents the simple use of the colloidal NPs for catalysis and one-pot syntheses are preferred.

Another drawback of the polyol method is the need for washing steps or phase extraction to flocculate the NPs and/or separate them from the highly viscous polyol before the NPs can be used further, e.g., before being supported (Quinson et al., 2021). These steps are typically performed in concentrated acid and their influence on the properties of the NPs is not well established.

Mono-Alcohol Synthesis

While mono-alcohols like methanol and ethanol have long been used a solvents and reducing agents for NP synthesis, the need for surfactants was almost systematically stressed, until recently. We reported an alternative to the polyol-synthesis where alkaline methanol and ethanol and their mixtures with water were shown to be suitable solvents and reducing agents to develop surfactant-free PM NPs like Pt, Ir, Ru or Os (Quinson et al., 2018) and multi-mettalic. This so called Co4Cat^{TM} technology (Colloids for Catalysts) approach combines the benefits of the polyols synthesis but differs in that the synthesis can be performed at relatively low temperature (<100°C) and no flocculation steps is needed: Due to the low boiling point solvents used, the small NPs (<10 nm) can be readily supported by simple solvent evaporation. The solvent can be recovered and re-used to obtain NPs. Pt NPs prepared by this approach show higher activity than commercial catalyst benchmark for butanone hydrogenation since small size and well-dispersed NPs are obtained on a support. Ir NPs show up to ten times more activity compared to the state-of-the-art for the oxygen evolution reaction (OER) due to the small size (ca. 1.6 nm) of the surfactant-free NPs.

DISCUSSION

Avoiding surfactants to develop colloidal NPs for catalysis is 1) well documented, 2) allowing size control, 3) simpler than

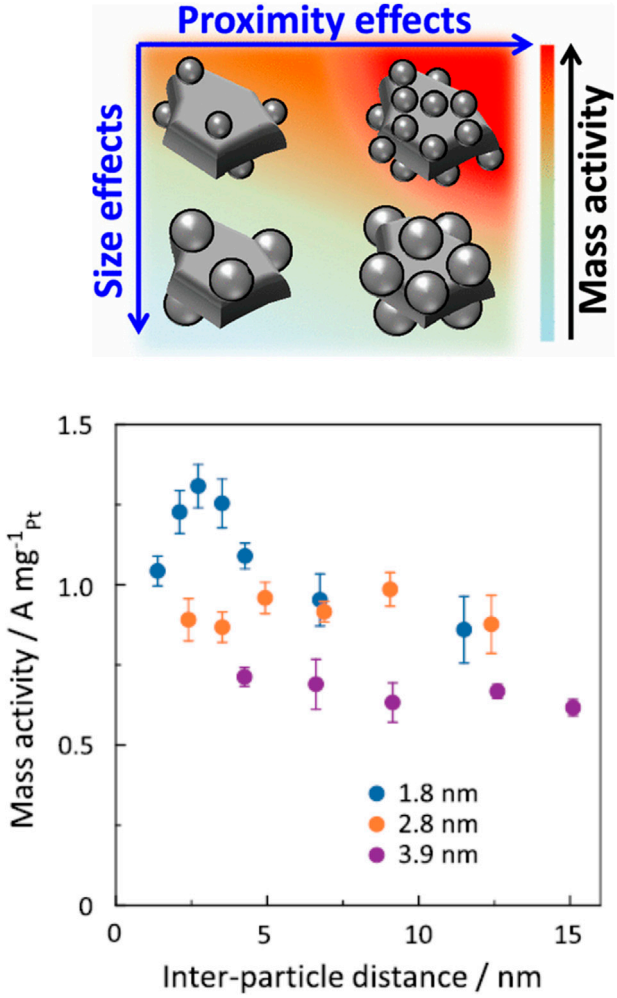

FIGURE 2 | ORR mass activity at 0.9 V *versus* the relative hydrogen electrode for Pt NPs supported on carbon with various Pt sizes and loadings and so different inter-particle distances. Reproduced with permission from (Inaba et al., 2021) Copyright 2021 American Chemical Society.

using surfactants, 4) beneficial to develop improved catalysts, 5) more likely to result in approaches with the potential to develop profitable businesses. In lights of the benefits of surfactant-free syntheses, they are relatively less implemented that the counterpart syntheses-with-additives. This can be inferred to two main factors. (1) It is a popular belief that surfactants are *absolutely* needed to obtain colloids. This belief might have prevented researchers to explore strategies without additives. (2) Control over shape and crystallographic structure has been shown to possibly bring positive features for catalysis. It is true that morphology control remains relatively more complex and challenging without additives. Nevertheless, it must be noted that if shape control is achieved with surfactants, the integrity of the as-produced structure might not be maintained with attempts to remove the surfactants in order to optimize the number of active sites on the NP surface, or may not even be maintained under catalytic operation.

With regard to shape control, it must be pointed out that if surfactant-free syntheses are *easier* they are not necessarily *simpler* and might be sensitive to parameters screened in approaches using surfactants. For example, it was shown that the nature of the cation present in the base used in alkaline methanol synthesis influences the stability of the surfactant-free Pt NPs obtained (Quinson et al., 2019). This observation suggests that some degree of shape control might be possible with simple inorganic salts. In the glycerol based synthesis of Au NPs, a mixture of rods and NPs were obtained (Nalawade et al., 2013). It is anticipated that the wide range of polyols and mono-alcohols available are likely to lead under the right experimental conditions to a certain degree of shape control without adding extra shape-directing agents.

Beyond active site design, i.e., beyond the optimization of catalyst structure, a range of parametric studies can be performed using surfactant-free NPs, for instance to optimize the nature of support and loading for a given catalytic reaction. It has been shown recently using the polyol synthesis in ethylene glycol that supported small size NPs close to each other without agglomeration could lead to a significant increase in mass activity (Inaba et al., 2021). This inter-particle proximity effect, that origins in an overlap in the electric double layer structure at the catalyst-electrolyte interface, was successfully exploited to develop improved catalysts for the ORR, see **Figure 2**. The preparation of the catalyst to observe this effect was greatly facilitated by the use of surfactant-free NPs. It was also shown using surfactant-free NPs that the key optimization of inks for electrochemical purposes was strongly dependent on the synthesis protocol of the NPs (Inaba et al., 2017). The influence of solvents used for the synthesis in mono-alcohols and the solvent used for re-dispersion and supporting steps was also studied to develop OER catalysts. It was shown that beyond developing the right Ir NPs in the right solvent, the properties of the solvent used to disperse the support material strongly influence the final catalytic activity (Bizzotto et al., 2021). As a consequence of the high activity of surfactant-free Ir NPs, benchmarking protocols for testing Ir NP activity for the OER could be developed (Bizzotto et al., 2019). Last, "unprotected" NPs are valuable tools and control materials to evaluate the effects of ligands on NP catalytic properties, to further understand how to best functionalize NPs for catalysis for instance by ligand design (Schrader et al., 2015).

For lab-scale experiments, relatively small quantities of materials are needed. To this extent, *how* the NPs are obtained is not a bottleneck. However, transferring a colloidal synthesis to larger scale, though it is possible, will gain from an approach using safe, cheap and few chemicals and compatibility with flow chemistry (Sui et al., 2020), as it is the case for the laser synthesis and processing of colloids approach. For PM NPs, the expensive price of the raw materials is not a variable easily controllable. As a consequence, any minor improvement in the synthesis of the PM NPs can have significant economic and ecological impact. Lower energy requirements, e.g., *via* lower temperature or even room temperature processes, would be ideal and the solvent used for the synthesis should be easily recycled to reduce even more the related costs of production. In this respect, the use of ethanol

as solvent is a promising alternative (Quinson et al., 2018). Although this point has not been investigated further, the fact that a base like NaOH is needed in the mono-alcohol syntheses suggest that the dry crystal could be recovered during the supporting step of the NPs when solvent evaporation is performed. This could ultimately allow developing a synthesis with the relatively safe chemicals that are ethanol and NaOH, and the latter being recycled few times for several syntheses. Importantly, preferring surfactant-free syntheses for fundamental research makes the findings more directly transferrable to larger scale in order to bridge the gap between academia and industry.

CONCLUSION

Surfactant-free colloidal syntheses of PM NPs are promising and probably overlooked approaches to develop NPs directly relevant for catalytic applications. Several surfactant-free colloidal synthetic strategies have been developed over the years, showing that it is indeed possible to develop stable colloids without surfactants. With the pioneer works reviewed here in mind, it is anticipated that exploring further surfactant-free colloidal syntheses of PM NPs will bring further benefits to fundamental as well as applied research and development in general but especially in the field of catalysis.

AUTHOR CONTRIBUTIONS

JQ: conceptualization, writing, review, editing.

FUNDING

JQ acknowledges the European Union's Horizon 2020 research and innovation programme under the Marie Skłodowska-Curie grant agreement No 840523 (CoSolCat).

REFERENCES

Amri, N. E., and Roger, K. (2020). Polyvinylpyrrolidone (PVP) Impurities Drastically Impact the Outcome of Nanoparticle Syntheses. *J. Colloid Interf. Sci.* 576, 435–443. doi:10.1016/j.jcis.2020.04.113

Bizzotto, F., Quinson, J., Schröder, J., Zana, A., and Arenz, M. (2021). Surfactant-free Colloidal Strategies for Highly Dispersed and Active Supported IrO_2 Catalysts: Synthesis and Performance Evaluation for the Oxygen Evolution Reaction. *J. Catal.* 401, 54–62. doi:10.1016/j.jcat.2021.07.004

Bizzotto, F., Quinson, J., Zana, A., Kirkensgaard, J. J. K., Dworzak, A., Oezaslan, M., et al. (2019). Ir Nanoparticles with Ultrahigh Dispersion as Oxygen Evolution Reaction (OER) Catalysts: Synthesis and Activity Benchmarking. *Catal. Sci. Technol.* 9, 6345–6356. doi:10.1039/c9cy01728c

Cargnello, M., Chen, C., Diroll, B. T., Doan-Nguyen, V. V. T., Gorte, R. J., and Murray, C. B. (2015). Efficient Removal of Organic Ligands from Supported Nanocrystals by Fast thermal Annealing Enables Catalytic Studies on Well-Defined Active Phases. *J. Am. Chem. Soc.* 137, 6906–6911. doi:10.1021/jacs.5b03333

Cui, C., Gan, L., Li, H.-H., Yu, S.-H., Heggen, M., and Strasser, P. (2012). Octahedral PtNi Nanoparticle Catalysts: Exceptional Oxygen Reduction Activity by Tuning the alloy Particle Surface Composition. *Nano Lett.* 12, 5885–5889. doi:10.1021/nl3032795

Du, J., Quinson, J., Zana, A., and Arenz, M. (2021). Elucidating Pt-Based Nanocomposite Catalysts for the Oxygen Reduction Reaction in Rotating Disk Electrode and Gas Diffusion Electrode Measurements. *ACS Catal.* 11, 7584–7594. doi:10.1021/acscatal.1c01496

Fiévet, F., Ammar-Merah, S., Brayner, R., Chau, F., Giraud, M., Mammeri, F., et al. (2018). The Polyol Process: a Unique Method for Easy Access to Metal Nanoparticles with Tailored Sizes, Shapes and Compositions. *Chem. Soc. Rev.* 47, 5187–5233. doi:10.1039/c7cs00777a

Guntern, Y. T., Okatenko, V., Pankhurst, J., Varandili, S. B., Iyengar, P., Koolen, C., et al. (2021). Colloidal Nanocrystals as Electrocatalysts with Tunable Activity and Selectivity. *ACS Catal.* 11, 1248–1295. doi:10.1021/acscatal.0c04403

Heuer-Jungemann, A., Feliu, N., Bakaimi, I., Hamaly, M., Alkilany, A., Chakraborty, I., et al. (2019). The Role of Ligands in the Chemical Synthesis and Applications of Inorganic Nanoparticles. *Chem. Rev.* 119, 4819–4880. doi:10.1021/acs.chemrev.8b00733

Inaba, M., Quinson, J., and Arenz, M. (2017). pH Matters: The Influence of the Catalyst Ink on the Oxygen Reduction Activity Determined in Thin Film Rotating Disk Electrode Measurements. *J. Power Sourc.* 353, 19–27. doi:10.1016/j.jpowsour.2017.03.140

Inaba, M., Zana, A., Quinson, J., Bizzotto, F., Dosche, C., Dworzak, A., et al. (2021). The Oxygen Reduction Reaction on Pt: Why Particle Size and Interparticle Distance Matter. *ACS Catal.* 11, 7144–7153. doi:10.1021/acscatal.1c00652

Johnson, P., Trybala, A., Starov, V., and Pinfield, V. J. (2021). Effect of Synthetic Surfactants on the Environment and the Potential for Substitution by Biosurfactants. *Adv. Colloid Interf. Sci.* 288, 102340. doi:10.1016/j.cis.2020.102340

Kawasaki, H. (2013). Surfactant-free Solution-Based Synthesis of Metallic Nanoparticles toward Efficient Use of the Nanoparticles' Surfaces and Their Application in Catalysis and Chemo-/biosensing. *Nanotechnol. Rev.* 2, 5–25. doi:10.1515/ntrev-2012-0079

Koczkur, K. M., Mourdikoudis, S., Polavarapu, L., and Skrabalak, S. E. (2015). Polyvinylpyrrolidone (PVP) in Nanoparticle Synthesis. *Dalton Trans.* 44, 17883–17905. doi:10.1039/c5dt02964c

Kohsakowski, S., Seiser, F., Wiederrecht, J.-P., Reichenberger, S., Vinnay, T., Barcikowski, S., et al. (2020). Effective Size Separation of Laser-Generated, Surfactant-free Nanoparticles by Continuous Centrifugation. *Nanotechnology* 31, 095603. doi:10.1088/1361-6528/ab55bd

Losch, P., Huang, W., Goodman, E. D., Wrasman, C. J., Holm, A., Riscoe, A. R., et al. (2019). Colloidal Nanocrystals for Heterogeneous Catalysis. *Nano Today* 24, 15–47. doi:10.1016/j.nantod.2018.12.002

Mun, M. K., Lee, W. O., Park, J. W., Kim, D. S., Yeom, G. Y., and Kim, D. W. (2017). Nanoparticles Synthesis and Modification Using Solution Plasma Process. *Appl. Sci. Converg. Technol.* 26, 164–173. doi:10.5757/asct.2017.26.6.164

Nagata, T., and Obora, Y. (2020). N,N-dimethylformamide-protected Single-Sized Metal Nanoparticles and Their Use as Catalysts for Organic Transformations. *ACS Omega* 5, 98–103. doi:10.1021/acsomega.9b03828

Nalawade, P., Mukherjee, T., and Kapoor, S. (2013). Green Synthesis of Gold Nanoparticles Using Glycerol as a Reducing Agent. *Adv. Nanoparticles* 2, 76–86. doi:10.4236/anp.2013.22014

Neumann, S., Grotheer, S., Tielke, J., Schrader, I., Quinson, J., Zana, A., et al. (2017). Nanoparticles in a Box: a Concept to Isolate, Store and Re-use Colloidal Surfactant-free Precious Metal Nanoparticles. *J. Mater. Chem. A.* 5, 6140–6145. doi:10.1039/c7ta00628d

Niu, Z., and Li, Y. (2014). Removal and Utilization of Capping Agents in Nanocatalysis. *Chem. Mater.* 26, 72–83. doi:10.1021/cm4022479

Park, Y.-C., Tokiwa, H., Kakinuma, K., Watanabe, M., and Uchida, M. (2016). Effects of Carbon Supports on Pt Distribution, Ionomer Coverage and Cathode Performance for Polymer Electrolyte Fuel Cells. *J. Power Sourc.* 315, 179–191. doi:10.1016/j.jpowsour.2016.02.091

Parveen, R., Ullah, S., Sgarbi, R., and Tremiliosi-Filho, G. (2019). One-pot Ligand-free Synthesis of Gold Nanoparticles: The Role of Glycerol as Reducing-Cum-Stabilizing Agent. *Colloids Surf. A: Physicochemical Eng. Aspects* 565, 162–171. doi:10.1016/j.colsurfa.2019.01.005

Quinson, J., Bucher, J., Simonsen, S. B., Kuhn, L. T., Kunz, S., and Arenz, M. (2019). Monovalent Alkali Cations: Simple and Eco-Friendly Stabilizers for Surfactant-free Precious Metal Nanoparticle Colloids. *ACS Sustainable Chem. Eng.* 7, 13680–13686. doi:10.1021/acssuschemeng.9b00681

Quinson, J., and Jensen, K. M. Ø. (2020). From Platinum Atoms in Molecules to Colloidal Nanoparticles: A Review on Reduction, Nucleation and Growth Mechanisms. *Adv. Colloid Interf. Sci.* 286, 102300. doi:10.1016/j.cis.2020.102300

Quinson, J., Kunz, S., and Arenz, M. (2021). Beyond Active Site Design: A Surfactant-Free Toolbox Approach for Optimized Supported Nanoparticle Catalysts. *ChemCatChem* 13, 1692–1705. doi:10.1002/cctc.202001858

Quinson, J., Neumann, S., Wannmacher, T., Kacenauskaite, L., Inaba, M., Bucher, J., et al. (2018). Colloids for Catalysts: A Concept for the Preparation of superior Catalysts of Industrial Relevance. *Angew. Chem. Int. Ed.* 57, 12338–12341. doi:10.1002/anie.201807450

Reichenberger, S., Marzun, G., Muhler, M., and Barcikowski, S. (2019). Perspective of Surfactant-Free Colloidal Nanoparticles in Heterogeneous Catalysis. *ChemCatChem* 11, 4489–4518. doi:10.1002/cctc.201900666

Schrader, I., Warneke, J., Backenköhler, J., and Kunz, S. (2015). Functionalization of Platinum Nanoparticles with L-Proline: Simultaneous Enhancements of Catalytic Activity and Selectivity. *J. Am. Chem. Soc.* 137, 905–912. doi:10.1021/ja511349p

Schrader, I., Warneke, J., Neumann, S., Grotheer, S., Swane, A. A., Kirkensgaard, J. J. K., et al. (2015). Surface Chemistry of "unprotected" Nanoparticles: A Spectroscopic Investigation on Colloidal Particles. *J. Phys. Chem. C.* 119, 17655–17661. doi:10.1021/acs.jpcc.5b03863

Stavis, S. M., Fagan, J. A., Stopa, M., and Liddle, J. A. (2018). Nanoparticle Manufacturing - Heterogeneity through Processes to Products. *ACS Appl. Nano Mater.* 1, 4358–4385. doi:10.1021/acsanm.8b01239

Sui, J., Yan, J., Liu, D., Wang, K., and Luo, G. (2020). Continuous Synthesis of Nanocrystals *via* Flow Chemistry Technology. *Small* 16, 1902828. doi:10.1002/smll.201902828

Wang, Y., Ren, J., Deng, K., Gui, L., and Tang, Y. (2000). Preparation of Tractable Platinum, Rhodium, and Ruthenium Nanoclusters with Small Particle Size in Organic media. *Chem. Mater.* 12, 1622–1627. doi:10.1021/cm0000853

Wuithschick, M., Birnbaum, A., Witte, S., Sztucki, M., Vainio, U., Pinna, N., et al. (2015). Turkevich in New Robes: Key Questions Answered for the Most Common Gold Nanoparticle Synthesis. *ACS Nano* 9, 7052–7071. doi:10.1021/acsnano.5b01579

Zhang, D., Gökce, B., and Barcikowski, S. (2017). Laser Synthesis and Processing of Colloids: Fundamentals and Applications. *Chem. Rev.* 117, 3990–4103. doi:10.1021/acs.chemrev.6b00468

Conflict of Interest: The author declares that the research was conducted in the absence of any commercial or financial relationships that could be construed as a potential conflict of interest.

Publisher's Note: All claims expressed in this article are solely those of the authors and do not necessarily represent those of their affiliated organizations, or those of the publisher, the editors and the reviewers. Any product that may be evaluated in this article, or claim that may be made by its manufacturer, is not guaranteed or endorsed by the publisher.

frontiers in Chemistry

PERSPECTIVE
published: 03 January 2022
doi: 10.3389/fchem.2021.810781

Designing Structural Electrochemical Energy Storage Systems: A Perspective on the Role of Device Chemistry

Adriana M. Navarro-Suárez[1]* *and Milo S. P. Shaffer*[1,2]*

[1]*Department of Chemistry, Imperial College London, Molecular Sciences Research Hub, London, United Kingdom,* [2]*Department of Materials, Imperial College London, London, United Kingdom*

Structural energy storage devices (SESDs), designed to simultaneously store electrical energy and withstand mechanical loads, offer great potential to reduce the overall system weight in applications such as automotive, aircraft, spacecraft, marine and sports equipment. The greatest improvements will come from systems that implement true multifunctional materials as fully as possible. The realization of electrochemical SESDs therefore requires the identification and development of suitable multifunctional structural electrodes, separators, and electrolytes. Different strategies are available depending on the class of electrochemical energy storage device and the specific chemistries selected. Here, we review existing attempts to build SESDs around carbon fiber (CF) composite electrodes, including the use of both organic and inorganic compounds to increase electrochemical performance. We consider some of the key challenges and discuss the implications for the selection of device chemistries.

Keywords: structural energy storage, carbon fibers, structural batteries, structural supercapacitors, multifunctional materials, battery chemistry

OPEN ACCESS

Edited by:
Diego Cazorla-Amoros,
University of Alicante, Spain

Reviewed by:
Atif Javaid,
University of Engineering and Technology, Pakistan
Ramiro Ruiz Rosas,
University of Malaga, Spain

***Correspondence:**
Adriana M. Navarro-Suárez
anavarrosuarez@gmail.com
Milo S. P. Shaffer
m.shaffer@imperial.ac.uk

Specialty section:
This article was submitted to Electrochemistry, a section of the journal Frontiers in Chemistry

Received: *07 November 2021*
Accepted: *03 December 2021*
Published: *03 January 2022*

Citation:
Navarro-Suárez AM and Shaffer MSP (2022) Designing Structural Electrochemical Energy Storage Systems: A Perspective on the Role of Device Chemistry. Front. Chem. 9:810781. doi: 10.3389/fchem.2021.810781

INTRODUCTION

Structural energy storage devices (SESDs), or "Structural Power" systems store electrical energy while carrying mechanical loads and have the potential to reduce vehicle weight and ease future electrification across various transport modes (Asp et al., 2019). Two broad approaches have been studied: multifunctional structures and multifunctional materials. The first combines conventional materials by embedding thin-film batteries within composite laminates or sandwich panels. Whilst there can be some synergies and particularly space saving, the structural and energy storage functions generally remain decoupled; *i.e.* one material bears loads, another stores energy electrochemically (Pereira et al., 2009; Thomas et al., 2013). The second approach formulates multifunctional materials that simultaneously and synergistically provide structural and electrochemical energy storage functions (Asp and Greenhalgh, 2014; Danzi et al., 2021). Both approaches have their advantages and challenges, the former offers modest savings under low mechanical loads but suffers from issues such as delamination at the device/composite interface and limited scope for synergy. The latter can potentially offer significantly greater savings in system level mass and volume but the material design is more complicated since the mechanical and electrical demands are often in conflict (Asp et al., 2015).

As discussed further below, SESDs based on fibrous composites are particularly promising. Extensive efforts have been made to identify and address the scientific challenges associated with the

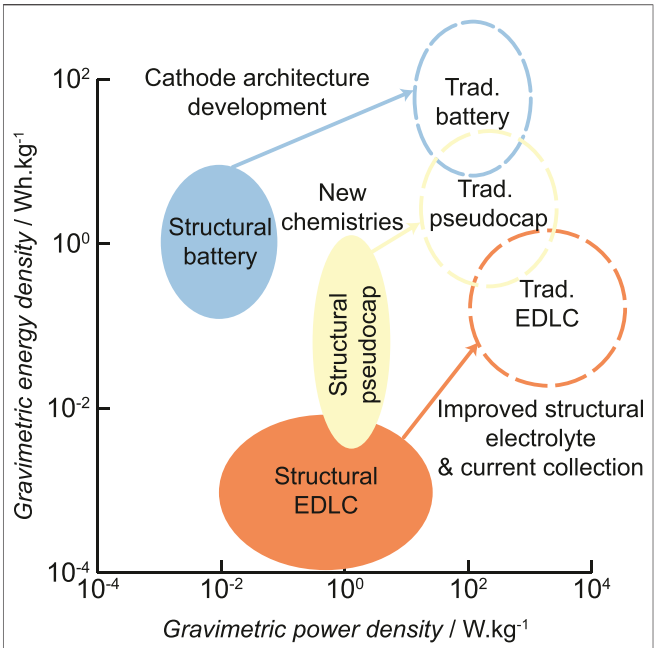

FIGURE 1 | Ragone plot of various SESDs with suggested developments to reach traditional electrochemical energy storage devices.

underlying multifunctional materials required, including structural electrodes (Liu et al., 2009; Kjell et al., 2011; Shirshova et al., 2013a), electrolytes (Snyder et al., 2007; Ihrner et al., 2017), and separators (Acauan et al., 2019; Patel et al., 2020a). Most of this research has targeted either electrical double-layer capacitors (EDLCs) or lithium-ion batteries (LIBs), leaving aside other chemistries. This focus has been driven by the cycle life/stability of EDLCs and the energy density of LIBs, but potentially misses important opportunities associated with other device chemistries and architectures, covering a wide range of energy and power densities. Novel energy storage concepts incorporating new materials and chemical processes may offer routes to circumvent some key obstacles to existing SESDs (**Figure 1**) and enable faster implementation in certain applications.

Wider reviews of SESDs are available, particularly describing manufacturing and engineering issues (Asp and Greenhalgh, 2014; Ferreira et al., 2016; Deka et al., 2017a; Danzi et al., 2021; Galos et al., 2021). This perspective examines the prospects for current and future device chemistries, as they may be implemented in SESDs based on fiber composites. The *Current Status Section* summarizes the requirements and current state-of-the-art in SESD chemistry, while the *Future Needs and Prospects Section* considers the selection and possible impact of alternative technologies on device performance.

CURRENT STATUS

Carbon-based materials, particularly CFs and carbon nanomaterials, are extensively used in SESDs for their electrochemical and structural performance, and low densities. Fiber composites are widely explored as the laminated architecture is common to both electrochemical and structural systems. CFs may be electrochemically active themselves, or act as framework and current collector for a multifunctional matrix packed around them. EDLCs are particularly attractive, since the energy storage process is entirely physical, depending only on the interface between electrode and electrolyte (**Figures 2A,B**) (Li et al., 2010; Qian et al., 2013a; Shirshova et al., 2013a; Qian et al., 2013b; Javaid et al., 2014; Shirshova et al., 2014; Westover et al., 2014; Greenhalgh et al., 2015; Javaid et al., 2016; Senokos et al., 2016; Kwon et al., 2017; Senokos et al., 2017; Shen and Zhou, 2017; Xu and Zhang, 2017; Li et al., 2018a; Chen et al., 2018; Javaid et al., 2018; Javaid and Irfan, 2018; Muralidharan et al., 2018; Senokos et al., 2018; Aderyani et al., 2019; Flouda et al., 2019a; Chen et al., 2019; Patel et al., 2019; Reece et al., 2019; Patel et al., 2020b; Rana et al., 2020; Reece et al., 2020; Sun et al., 2020; Sánchez-Romate et al., 2021; Subhani et al., 2021; Xu et al., 2021). The central advantage for SESDs, is that there is little or no change in volume, and no (re)dissolution of material, associated with the electrochemical process, minimizing stresses, and simplifying the structural design, whilst ensuring an excellent cycle life. These systems offer modest energy density, and are generally used for their power density in energy management applications, although the long lifetime, reliability, and safety means that they may be used in backup power contexts.

Energy density in EDLCs is broadly proportional to specific surface area, with the caveat that gas adsorption measurements may not reflect the electrochemically accessible regions. In general, the porosity, associated with the necessary high surface areas and electrolyte access, negatively affects mechanical properties, driving many of the efforts to exploit nanomaterials where the perfection of nanostructure may compensate for other performance losses. Whilst many promising systems have been developed, power density is also limited by the challenges of developing an effective structural electrolyte. Ionic conductivity of structural electrolyte "matrices" is usually inversely related to the mechanical properties needed to transfer load (Shirshova et al., 2013b; Ihrner et al., 2017; Schneider et al., 2019). This low ionic conductivity may dominate the equivalent series resistance of the whole device. In addition, whilst structural CFs have reasonable electrical conductivity, in larger devices/components, they may not be an adequate current collector without the addition of additional components. This constraint is more severe in EDLCs than in batteries, as the current densities are expected to be higher.

The balance of power density to energy density can be shifted by incorporating redox active constituents within the stable, high cycle life, porous framework developed for EDLCs. Many researchers have developed pseudocapacitors, by coating carbon electrodes with powders or films that can store charge through surface adsorption/desorption of ions, redox reactions with the electrolyte, or doping/undoping of the electrode materials. Modifications to improve pseudocapacitive behavior have included functional groups (Ganguly et al., 2020), conductive polymers (Benson et al., 2013; Liu et al., 2016; Shi

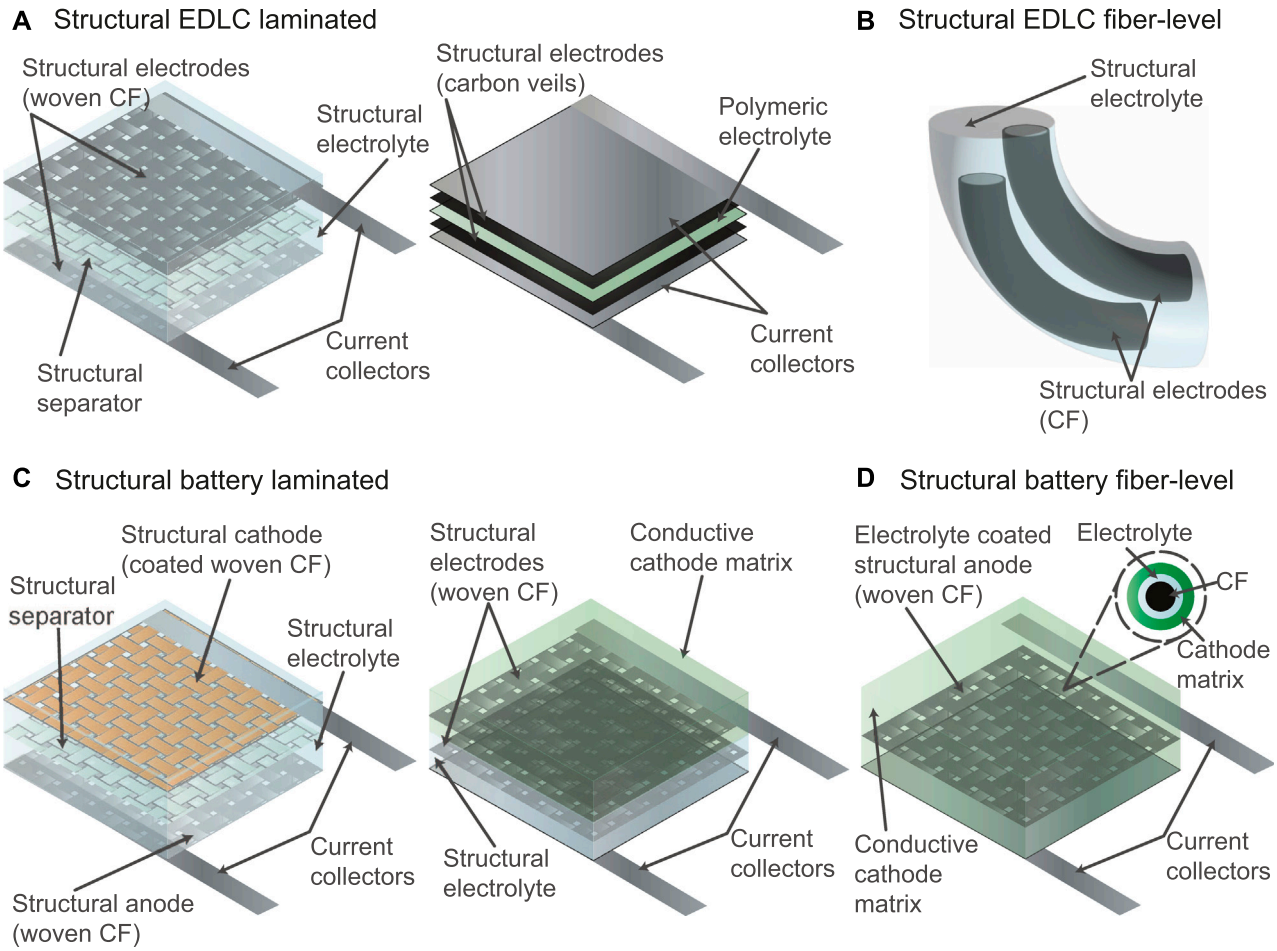

FIGURE 2 | Scheme of **(A)** structural EDLC laminates, **(B)** a structural EDLC fiber-level, **(C)** structural battery laminates, and **(D)** a structural battery fiber-level.

et al., 2016; Hudak et al., 2017; Flouda et al., 2019b; Javaid et al., 2021), metal particles (Mapleback et al., 2020), and metal oxides (Deka et al., 2016; Liu et al., 2016; Deka et al., 2017b; Choi et al., 2017; Deka et al., 2019; Sha et al., 2021).

LIBs exhibit relatively high energy density (~240 Wh kg^{-1} and 640 Wh L^{-1}), long cycle life, relatively high safety, and have a continuously decreasing cost (Armand et al., 2020). The general charge storage mechanism consists of Li ions being stored in, and released from a solid lattice, shuttling back and forth between the anode and cathode. Most of the SESD work in this area has focused on structural anodes, identifying polyacrylonitrile-based CFs with the optimal microstructure to promote good Li-ion intercalation (Wong et al., 2007; Ekstedt et al., 2010; Kjell et al., 2011; Jacques et al., 2012; Jacques et al., 2013; Kjell et al., 2013; Jacques et al., 2014; Hagberg et al., 2016; Feng et al., 2017; Yu et al., 2017; Fredi et al., 2018; Johannisson et al., 2018; Park et al., 2018; Xu et al., 2018; Moyer et al., 2020a; Thakur and Dong, 2020; Xu et al., 2020; Asp et al., 2021). The advantage is that the primary structural fibers act as the energy storage electrode, not simply a current collector; the volume changes may be small enough to be accommodated within the composite, with an appropriate structural electrolyte, and even open up opportunities for high performance actuation (Ferreira et al., 2016). To improve the energy density of the devices, surface modifications with SnO_2[81] and MoS_2-containing anodes have been tried, exhibiting high capacities and excellent cycling stability due to the conversion processes occurring in the SnO_2 and MoS_2 anodes.

To date only a limited number of studies on structural cathodes have been published, generally packing the cathode powder into the matrix either around each fiber (Hagberg et al., 2018) or within a separate structural cathode ply (**Figures 2C,D**) (Galos et al., 2020). The fiber architecture minimizes ionic resistances but increases the risk of shorts; the laminate architecture simplifies fabrication and current collection. Examples of structural LiB cathodes ($LiCoO_2$) (Pereira et al., 2007; Liu et al., 2009; Roberts and Aglietti, 2010; Javaid and Ali, 2018), lithium iron phosphate ($LiFePO_4$) (Snyder et al., 2006; Ekstedt et al., 2010; Carlson, 2013; Hagberg et al., 2018; Bouton et al., 2019; Moyer et al., 2020b), and lithium nickel manganese cobalt oxide (NMC) (Ladpli et al., 2019). $LiCoO_2$ electrodes are a popular choice for use with mobile devices such as smartphones, laptops, and digital cameras (Liu et al., 2015). However, using

cobalt raises issues with geo-politics and scarcity, particularly with the projection of at least a tenfold production increase of EVs in the next decade (Li et al., 2020). $LiFePO_4$ and NMC are two of the main cobalt-free and low-cobalt battery chemistries that are on the market. $LiFePO_4$ batteries benefit from flat voltage profile, low material cost, and abundant material supply, making them ideal for electric transportation. However, they have lower voltage and lower energy density than $LiCoO_2$ or NMC (Zhang, 2011). Moreover, they suffer from high electrical resistivity presenting a challenge to develop high cathodic mass fraction for mass efficiency in structural device configurations (Snyder et al., 2015). In NMC, nickel provides the cell with high-specific energy, thus the prevailing trend is to increase the nickel content. However, high-Ni cathode materials generally suffer from lattice and surface instabilities that diminish the longevity of the battery (Lee et al., 2021).

FUTURE NEEDS AND PROSPECTS

The choice of SESD type and chemistry must be related to the energy/power density required for the chosen application. Recent work has identified different targets with different balances of properties (Nguyen et al., 2021). Very often, in particular applications, the implementation of SESDs will be associated with other system savings, thus the required performance, and potential benefit, is very context dependent. More accessible gains can be accessed by developing secondary systems (*e.g.* aircraft cabin flooring) with more modest energy and power density demands. Here, the best outcomes may be achieved using alternative chemistries; for example, avoiding the fire risk and encapsulation challenges of LIBs, by using aqueous polymeric pseudocapacitors. More ambitious goals (*e.g.* full aircraft electrification) will require dramatic improvements in specific performance; SESDs may be one of the few approaches that can deliver the high effective energy densities required, because the structural functionality may allow much of the device mass to be discounted (Carlstedt and Asp, 2020).

The quest for high energy density structural EDLCs requires CFs to be modified to improve charge storage. Fiber etching to increase surface area typically reduces mechanical strength in fibers, although modest activation of fiber surfaces has been demonstrated without degradation (Shirshova et al., 2014; Snyder et al., 2015). The addition of carbon-based nanomaterials on the fiber or laminate surface can enhance electrochemical surface areas as well as interfacial properties (Anthony et al., 2018; Senokos et al., 2020). Adding nanostructured carbon throughout the multifunctional electrode matrix maximizes the utilization of the available volume (Qian et al., 2013b); however, it is important not to add excess material, as the effective structural fiber volume fraction is then reduced.

Most of the work on structural pseudocapacitors has coated the structural carbon with conductive polymers or metal oxides; usually resulting in a significant decrease in mechanical performance of the composites, although appropriate nanostructuring of the interface may resolve these issues. Transition metal chalcogenides (VS_2, CuS, CoE_2, NiS_2, $NiSe_2$), rare-earth metal sulfides (La_2S_3 and Sm_2S_3), and layer-structured chalcogenides (MoS_2 and SnSe) have been previously proposed as attractive electrode materials for flexible devices due their ability to host redox reactions and the tunable gap between the layers that can intercalate ions from the electrolyte (Palchoudhury et al., 2019). MXenes, 2D transition metal carbides and nitrides, have also shown promising results in flexible supercapacitors (Zhao et al., 2015; Yan et al., 2017; Zhang et al., 2017; Couly et al., 2018; Zheng et al., 2019), in both aqueous and ionic liquid electrolytes. Both transition metal (di) chalcogenides and MXenes could be extended to SESDs. To minimize the effect of modulating the primary fiber-matrix interfaces, and maximize the active volume, these species can be incorporated within a multifunctional matrix material, throughout the structural electrode; electrical conductivity can be supplemented by carbon nanomaterials or a continuous carbon aerogel network (Qian et al., 2013b), if required. In this case, the primary CFs may simply act as structural current collector. The contribution of the structural matrix will be limited by the available matrix volume fraction. Increasing the matrix volume fraction will not generally be attractive as the primary structural fiber volume fraction will fall, significantly degrading structural performance.

Most of the studies on structural LIBs used CFs as anodes, but many aspects, including dendrite formation and crack nucleation during the lithiation/delithiation cycles, have yet to be deeply addressed (Danzi et al., 2021). Interfacial adhesion between CFs and the structural electrolyte will be vital for the mechanical and electrochemical properties of SESDs; thus *operando* and modelling studies are needed to analyze the inherent behaviors, particularly over multiple cycles. The problem is even more complex where additional coatings of high-capacity materials are applied, although nanoscale texture can assist load transfer (Qian et al., 2008; Qian et al., 2010; Mikhalchan and Vilatela, 2019). The electrochemical performance of existing CFs has been enhanced by, for example, decorating them with different metal oxides (*e.g.* NiO, SnO_2, ZnO, $ZnCo_2O_4$) (Han et al., 2019; Han et al., 2020a; Han et al., 2020b; Han et al., 2020c). All these composites exhibited enhanced Li storage performance. However, no mechanical studies were performed; since the electrochemical testing was performed with a conventional, rather than multifunctional electrolyte, their suitability for SESDs is not yet clear. Computational studies have proposed Co_3O_4 as structural anode (Hu et al., 2021); experimental testing is yet to be performed. Most of high-capacity anode materials, including Co_3O_4 and silicon, exhibit low cycling stability, due to volume expansion during Li insertion/extraction. In general, the main challenge for these high energy density insertion anodes, whether designed at either fiber or laminate level, may remain how to accommodate volume changes during cycling within a structural composite material.

Due to its high theoretical capacity (3860 mAh g^{-1}), low density (0.59 g cm^{-3}) and negative electrochemical potential (−3.04 V *vs*. SHE), Li metal has many attractions as anode for batteries. However, Li-metal presents particular challenges with safety, due to potential dendrite formation and associated fire risk. In any case, in a SESD context, the pure metal will make little

mechanical contribution, both due to its intrinsic properties, and its structure as it dissolves and redeposits. Reactive anodes exploiting silicon, tin, or phosphorus, similarly may have limited value as the large volume changes may be hard to accommodate, and cycle life tends to be low. However, these additional components could be incorporated within a multifunctional matrix approach. Thermal runaway in case of damage by mechanical loads is a concern in all SESD but maybe be mitigated by the intrinsically distributed energy storage, large surface area for cooling, and opportunities for self-limiting delamination (Kalnaus et al., 2021). Nevertheless, where high volumetric and gravimetric energy densities are needed, primary aluminum–air and secondary zinc–air may offer better damage tolerance than Li systems (Hopkins et al., 2020). 3D printing has been proposed as an appropriate fabrication method for structural metal-oxygen batteries as the micro-structures and shapes of electrodes/electrolytes/current collectors/packaging materials can be controlled, improving mechanical and electrochemical performance (Zeng et al., 2020). However, the autophageous nature of pure metal batteries may limit their relevance as SESDs.

Conversion-type cathodes, such as sulfur, and oxygen, typically store 2-3 Li-ions per anion and therefore could potentially exhibit higher theoretical energy densities compared to the current LIBs (*e.g.* Li–O_2, 3505 Wh kg^{-1}; Li–S, 2600 Wh kg^{-1}) (Guo et al., 2017). Even so, they suffer from low conductivity (leading to low capacity utilization, poor kinetics, and poor reversibility of conversion reactions) and voltage hysteresis (typically linked to poor electronic resistance of the materials leading to low energy efficiency) (Wu and Yushin, 2017). Traditionally, conductive carbons, conducting polymers, metal organic frameworks and various metal oxides have been used to improve the conductivities of some conversion cathodes and reduce their dissolution during cycling (Guo and Fu, 2018). Conversion-type cathodes may be attractive in SESDs as CFs and CF-supported aerogels (Qian et al., 2013b; Nguyen et al., 2019) could potentially solve the low conductivity and voltage hysteresis issues. To date, there has only been one approach towards structural Li-S batteries (Huang et al., 2020); yet its electrolyte-to-sulfur weight ratio (~27) was extremely high for practical applications given that an excess of electrolyte (ratio >4) has an adverse impact on the energy density of the battery at the system level. Moreover, the energy density reported is calculated based on the sulfur contained in the electrode, ignoring the sulfur in the catholyte, thus, overestimating the energy density of the device in a practical sense.

Concerns about Li resource shortages have led to an interest in alternative chemistries in battery applications. CFs have been tested as anodes in potassium-ion (Harnden et al., 2021) and sodium-ion batteries (Harnden et al., 2018). Potassium-insertion gives a larger voltage-strain coupling than Na probably due to a slightly higher ionic diffusion coefficient; therefore, potassium-insertion appears more promising for creating actuation multifunctionality. Still, Li-insertion appears most promising for high-performance SESDs, where mass is the underlying driver.

As a more radical alternative to LIB or other high voltage systems, aqueous zinc batteries may be attractive due to the low cost of Zn, its low toxicity, low flammability, high stability and compatibility in aqueous electrolytes, as well as a high theoretical anode gravimetric and volumetric capacity (820 mAh g^{-1}, 5851 mAh cm^{-3}) (Jia et al., 2020). A CF Zn–MnO_2 structural composite battery was tested using a gel electrolyte exhibiting reasonably high stiffness and electrochemical performance (Chen et al., 2021). As the energy density was calculated per active material, instead of per device, it is difficult to assess the weight saving benefits of the SESDs, but an embodiment with a multifunctional matrix electrode could prove beneficial. The use of an aqueous electrolyte has obvious attractions for SESDs, reducing fire risk, toxicity, and minimizing encapsulation challenges.

The fabrication of batteries with inorganic cathodes is costly and environmentally damaging, from the extraction of the transition metals in ores with low metal content (Mauger et al., 2019), to the preparation of the active materials. Organic electroactive components can be used in both pseudocapacitors and organic batteries (small molecule or polymer) (Muench et al., 2016; Chen et al., 2020; John et al., 2020) and may offer environmental benefits both in production and recycling. In principle, these organic electrodes are composed of naturally abundant elements and they are less environmentally challenging compared to metal-based batteries. Both n- and p-type storage mechanisms can be implemented in organic electrodes, enabling various cell or electrode configurations (Poizot et al., 2018). The production of CFs themselves is relatively energy intensive; whilst over their lifetime, they may make a positive contribution to reducing emissions, though improved fuel efficiency in application, there is significant interest in developing "greener" CFs from renewable resources. Whilst absolute mechanical performance is relatively low, it is approaching the range needed for automotive applications and there may be opportunities for new types of multifunctional CFs (Mariano et al., 2014; Baker and Rials, 2013).

CONCLUDING REMARKS

Structural energy storage devices are a promising approach to reduce the weight of the battery pack, and hence increase range, in electric transportation. Many advances have been made in CF for structural EDLCs and LIB anodes, although the development of effective structural electrolytes remains challenging. The fiber-matrix interface also needs to be optimized to ensure both load transfer and electrochemical access, as well as accommodating intercalation-induced strains in structural batteries. Electrochemical performance can be enhanced by adding additional electroactive components, either coated at the fiber/lamina surface, or more beneficially incorporated throughout the multifunctional electrode matrix volume. There is significant scope to develop this concept, which is likely to be essential to developing structural cathodes to complement existing structural anodes.

Whilst high energy densities are a key driver, other factors may be more crucial; in some applications, more modest performance can offer significant benefits when the whole system is considered. In SESDs, longevity is particularly important, as the energy storage function is an inherent part of the whole product and cannot easily be replaced. In addition, the distribution of the electrochemical system over a large area, where fastenings and other connections are required, makes encapsulation and air-free fabrication challenging. SESDs may therefore particularly benefit from high cyclability systems, and aqueous, or at least water-tolerant, chemistries. Fire, smoke, and toxicity concerns will vary with application. The distributed character of the energy storage in SESDs tends to mitigate fire risk, and initial trials have indicated benign failures (Kalnaus et al., 2021); however, chemistries may be selected to further reduce risk. In addition, materials researchers are increasingly considering the sustainability and full life cycle analysis of new systems; there is significant scope to implement bio-derived materials, for both carbonaceous and organic redox-active constituents.

Fair performance comparisons in multifunctional applications can be difficult, but a variety of methodologies are emerging (Carlstedt and Asp, 2020; Johannisson et al., 2020; Nguyen et al., 2021). As well as the intrinsic electrochemical performance of different chemistries, it is important to consider device energy densities in existing embodiments and projected to future embodiments that might be compatible with the given storage system. Consideration must be given to the optimal architecture (fiber or laminate level), the need for current collection, and encapsulation, as well as the implications for mechanical integrity and load-carrying capacity. New modelling approaches are needed that combine the relevant thermomechanical-electrochemical processes. SESD composites represent an important and stimulating field of research, that requires interdisciplinary collaborations to accelerate progress towards real world deployment.

AUTHOR CONTRIBUTIONS

AN-S: Conceptualization, Writing—Original Draft, Funding acquisition. MS: Writing—Review and Editing, Funding acquisition. Both authors contributed to the article and approved the submitted version.

FUNDING

This project has received funding from the European Union's Horizon 2020 research and innovation programme under the Marie Sklodowska-Curie grant agreement No 838892.

REFERENCES

Acauan, L. H., Zhou, Y., Kalfon-Cohen, E., Fritz, N. K., and Wardle, B. L. (2019). Multifunctional Nanocomposite Structural Separators for Energy Storage. *Nanoscale* 11, 21964–21973. doi:10.1039/c9nr06954b

Aderyani, S., Flouda, P., Lutkenhaus, J. L., and Ardebili, H. (2019). The Effect of Nanoscale Architecture on Ionic Diffusion in rGo/aramid Nanofiber Structural Electrodes. *J. Appl. Phys.* 125 (18), 185106. doi:10.1063/1.5087280

Anthony, D. B., Sui, X., Kellersztein, I., De Luca, H. G., White, E. R., Wagner, H. D., et al. (2018). Continuous Carbon Nanotube Synthesis on Charged Carbon Fibers. *Composites A: Appl. Sci. Manufacturing* 112, 525–538. doi:10.1016/j.compositesa.2018.05.027

Armand, M., Axmann, P., Bresser, D., Copley, M., Edström, K., Ekberg, C., et al. (2020). Lithium-ion Batteries – Current State of the Art and Anticipated Developments. *J. Power Sourc.* 479, 228708. doi:10.1016/j.jpowsour.2020.228708

Asp, L. E., Bouton, K., Carlstedt, D., Duan, S., Harnden, R., Johannisson, W., et al. (2021). A Structural Battery and its Multifunctional Performance. *Adv. Energ. Sustain. Res.* 2 (3), 2000093. doi:10.1002/aesr.202000093

Asp, L. E., and Greenhalgh, E. S. (2014). Structural Power Composites. *Composites Sci. Tech.* 101, 41–61. doi:10.1016/j.compscitech.2014.06.020

Asp, L. E., Johansson, M., Lindbergh, G., Xu, J., and Zenkert, D. (2019). Structural Battery Composites: A Review. *Funct. Compos. Struct.* 1, 042001, 2019 . Available at: https://iopscience.iop.org/article/10.1088/2631-6331/ab5571. doi:10.1088/2631-6331/ab5571

Asp, L. E., Leijonmarck, S., Carlson, T., and Lindbergh, G. (2015). Realisation of Structural Battery Composite Materials in 20th International Conference on Composite Materials, ICCM20, Copenhagen, Denmark. doi:10.13140/RG.2.1.2029.1922

Baker, D. A., and Rials, T. G. (2013). Recent Advances in Low-Cost Carbon Fiber Manufacture from Lignin. *J. Appl. Polym. Sci.* 130, 713–728. doi:10.1002/app.39273

Benson, J., Kovalenko, I., Boukhalfa, S., Lashmore, D., Sanghadasa, M., and Yushin, G. (2013). Multifunctional CNT-Polymer Composites for Ultra-Tough Structural Supercapacitors and Desalination Devices. *Adv. Mater.* 25, 6625–6632. doi:10.1002/adma.201301317

Bouton, K., Chen, B., Zenkert, D., and Lindbergh, G. (2019). Structural Positive Electrodes for Multifunctional Composite Materials. *ICCM Int. Conf. Compos. Mater.*

Carlstedt, D., and Asp, L. E. (2020). Performance Analysis Framework for Structural Battery Composites in Electric Vehicles. *Composites B: Eng.* 186, 107822. doi:10.1016/j.compositesb.2020.107822

Chen, J., Zhou, Y., Islam, M. S., Cheng, X., Brown, S. A., Han, Z., et al. (2021). Carbon Fiber Reinforced Zn-MnO2 Structural Composite Batteries. *Composites Sci. Tech.* 209, 108787. doi:10.1016/j.compscitech.2021.108787

Chen, R., Bresser, D., Saraf, M., Gerlach, P., Balducci, A., Kunz, S., et al. (2020). A Comparative Review of Electrolytes for Organic-Material-Based Energy-Storage Devices Employing Solid Electrodes and Redox Fluids. *ChemSusChem* 13 (9), 2205–2219. doi:10.1002/cssc.201903382

Chen, Y., Amiri, A., Boyd, J. G., and Naraghi, M. (2019). Promising Trade-Offs Between Energy Storage and Load Bearing in Carbon Nanofibers as Structural Energy Storage Devices. *Adv. Funct. Mater.* 29(3), 1901425, 2019 . Available at: https://onlinelibrary.wiley.com/doi/abs/10.1002/adfm.201901425. doi:10.1002/adfm.201901425

Chen, Y., Cai, J., Boyd, J. G., Kennedy, W. J., and Naraghi, M. (2018). Mechanics of Emulsion Electrospun Porous Carbon Fibers as Building Blocks of Multifunctional Materials. *ACS Appl. Mater. Inter.* 10, 38310–38318. doi:10.1021/acsami.8b10499

Choi, C., Kim, J. H., Sim, H. J., Di, J., Baughman, R. H., and Kim, S. J. (2017). Supercapacitors: Microscopically Buckled and Macroscopically Coiled Fibers for Ultra-Stretchable Supercapacitors. *Adv. Energ. Mater.* 7 (6), 1602021. doi:10.1002/aenm.201770029

Couly, C., Alhabeb, M., Van Aken, K. L., Kurra, N., Gomes, L., Navarro-Suárez, A. M., et al. (2018). Asymmetric Flexible MXene-Reduced Graphene Oxide Micro-Supercapacitor. *Adv. Electron. Mater.* 4, 1700339. doi:10.1002/aelm.201700339

Danzi, F., Salgado, R. M., Oliveira, J. E., Arteiro, A., Camanho, P. P., and Braga, M. H. (2021). Structural Batteries: A Review. Molecules. *Molecules* 26, 2203. doi:10.3390/molecules26082203

Deka, B. K., Hazarika, A., Kim, J., Kim, N., Jeong, H. E., Park, Y.-B., et al. (2019). Bimetallic Copper Cobalt Selenide Nanowire-Anchored Woven Carbon Fiber-Based Structural Supercapacitors. *Chem. Eng. J.* 355, 551–559. doi:10.1016/j.cej.2018.08.172

Deka, B. K., Hazarika, A., Kim, J., Park, Y.-B., and Park, H. W. (2016). Multifunctional CuO Nanowire Embodied Structural Supercapacitor Based on Woven Carbon Fiber/ionic Liquid-Polyester Resin. *Composites Part A: Appl. Sci. Manufacturing* 87, 256–262. doi:10.1016/j.compositesa.2016.05.007

Deka, B. K., Hazarika, A., Kim, J., Park, Y.-B., and Park, H. W. (2017). Recent Development and Challenges of Multifunctional Structural Supercapacitors for Automotive Industries. *Int. J. Energ. Res.* 41, 1397–1411. Available at: http://doi.wiley.com/10.1002/er.3707. doi:10.1002/er.3707

Deka, B. K., Hazarika, A., Kwon, O., Kim, D., Park, Y.-B., and Park, H. W. (2017). Multifunctional Enhancement of Woven Carbon fiber/ZnO Nanotube-Based Structural Supercapacitor and Polyester Resin-Domain Solid-Polymer Electrolytes. *Chem. Eng. J.* 325, 672–680. doi:10.1016/j.cej.2017.05.093

Ekstedt, S., Wysocki, M., and Asp, L. E. (2010). Structural Batteries Made from Fibre Reinforced Composites. *Plastics, Rubber and Composites* 39, 148–150. doi:10.1179/174328910x12647080902259

Feng, M., Wang, S., Yu, Y., Feng, Q., Yang, J., and Zhang, B. (2017). Carboxyl Functionalized Carbon Fibers with Preserved Tensile Strength and Electrochemical Performance Used as Anodes of Structural Lithium-Ion Batteries. *Appl. Surf. Sci.* 392, 27–35. doi:10.1016/j.apsusc.2016.09.017

Ferreira, A. D. B. L., Nóvoa, P. R. O., and Marques, A. T. (2016). Multifunctional Material Systems: A State-Of-The-Art Review. *Compos. Structures* 151, 3–35. doi:10.1016/j.compstruct.2016.01.028

Flouda, P., Feng, X., Boyd, J. G., Thomas, E. L., Lagoudas, D. C., and Lutkenhaus, J. L. (2019). Interfacial Engineering of Reduced Graphene Oxide for Aramid Nanofiber-Enabled Structural Supercapacitors. *Batteries & Supercaps* 2, 464–472. doi:10.1002/batt.201800137

Flouda, P., Shah, S. A., Lagoudas, D. C., Green, M. J., and Lutkenhaus, J. L. (2019). Highly Multifunctional Dopamine-Functionalized Reduced Graphene Oxide Supercapacitors. *Matter* 1, 1532–1546. doi:10.1016/j.matt.2019.09.017

Fredi, G., Jeschke, S., Boulaoued, A., Wallenstein, J., Rashidi, M., Liu, F., et al. (2018). Graphitic Microstructure and Performance of Carbon Fibre Li-Ion Structural Battery Electrodes. *Multifunct. Mater.* 1, 015003. doi:10.1088/2399-7532/aab707

Galos, J., Best, A. S., and Mouritz, A. P. (2020). Multifunctional sandwich Composites Containing Embedded Lithium-Ion Polymer Batteries under Bending Loads. *Mater. Des.* 185, 108228. doi:10.1016/j.matdes.2019.108228

Galos, J., Pattarakunnan, K., Best, A. S., Kyratzis, I. L., Wang, C. H., and Mouritz, A. P. (2021). Energy Storage Structural Composites with Integrated Lithium-Ion Batteries: A Review. *Adv. Mater. Technol.* 6(8), 2001059. doi:10.1002/admt.202001059

Ganguly, A., Karakassides, A., Benson, J., Hussain, S., and Papakonstantinou, P. (2020). Multifunctional Structural Supercapacitor Based on Urea-Activated Graphene Nanoflakes Directly Grown on Carbon Fiber Electrodes. *ACS Appl. Energ. Mater.* 3, 4245–4254. Available at: https://pubs.acs.org/doi/10.1021/acsaem.9b02469. doi:10.1021/acsaem.9b02469

Greenhalgh, E., Ankersen, J., Asp, L., Bismarck, A., Fontana, Q., Houlle, M., et al. (2015). Mechanical, Electrical and Microstructural Characterisation of Multifunctional Structural Power Composites. *J. Compos. Mater.* 49, 1823–1834. doi:10.1177/0021998314554125

Guo, W., and Fu, Y. (2018). A Perspective on Energy Densities of Rechargeable Li-S Batteries and Alternative Sulfur-Based Cathode Materials. *Energy Environ. Mater.* 1, 20–27. doi:10.1002/eem2.12003

Guo, Y., Li, H., and Zhai, T. (2017). Reviving Lithium-Metal Anodes for Next-Generation High-Energy Batteries. *Adv. Mater.* 29, 1–25. doi:10.1002/adma.201700007

Hagberg, J., Leijonmarck, S., and Lindbergh, G. (2016). High Precision Coulometry of Commercial PAN-Based Carbon Fibers as Electrodes in Structural Batteries. *J. Electrochem. Soc.* 163, A1790–A1797. doi:10.1149/2.0041609jes

Hagberg, J., Maples, H. A., Alvim, K. S. P., Xu, J., Johannisson, W., Bismarck, A., et al. (2018). Lithium Iron Phosphate Coated Carbon Fiber Electrodes for Structural Lithium Ion Batteries. *Composites Sci. Tech.* 162, 235–243. doi:10.1016/j.compscitech.2018.04.041

Han, Q., Li, X., Wang, F., Han, Z., Geng, D., Zhang, W., et al. (2019). Carbon Fiber@ Pore-ZnO Composite as Anode Materials for Structural Lithium-Ion Batteries. *J. Electroanalytical Chem.* 833, 39–46. doi:10.1016/j.jelechem.2018.11.014

Han, Q., Shi, M., Han, Z., Zhang, W., Li, Y., Zhang, X., et al. (2020). Synthesis of One-Dimensional PAN-Based Carbon Fiber/NiO Composite as an Anode Material for Structural Lithium-Ion Batteries. *Ionics* 26 (12), 1–6. doi:10.1007/s11581-020-03762-8

Han, Q., Zhang, X., Zhang, W., Li, Y., and Sheng, Y. (2020). Preparation of Multifunctional P-CF@SnO2-MOF Composite Used as Structural Anode Materials. *J. Electroanalytical Chem.* 871, 114355. doi:10.1016/j.jelechem.2020.114355

Han, Q., Zhang, X., Zhang, W., Li, Y., and Zhang, Z. (2020). Preparation of Multifunctional Structural P-CF@ZnCo2O4 Composites Used as Structural Anode Materials. *J. Alloys Comp.* 842, 155743. doi:10.1016/j.jallcom.2020.155743

Harnden, R., Peuvot, K., Zenkert, D., and Lindbergh, G. (2018). Multifunctional Performance of Sodiated Carbon Fibers. *J. Electrochem. Soc.* 165, B616–B622. doi:10.1149/2.0971813jes

Harnden, R., Zenkert, D., and Lindbergh, G. (2021). Potassium-insertion in Polyacrylonitrile-Based Carbon Fibres for Multifunctional Energy Storage, Morphing, and Strain-Sensing. *Carbon* 171, 671–680. doi:10.1016/j.carbon.2020.09.042

Hopkins, B. J., Long, J. W., Rolison, D. R., and Parker, J. F. (2020). High-Performance Structural Batteries. *Joule* 4, 2240–2243. doi:10.1016/j.joule.2020.07.027

Hu, Z., Fu, Y., Hong, Z., Huang, Y., Guo, W., Yang, R., et al. (2021). Composite Structural Batteries With Co3O4/CNT Modified Carbon Fibers As Anode: Computational Insights On The Interfacial Behavior. *Compos. Sci. Technol.* 201, 108495. doi:10.1016/j.compscitech.2020.108495

Huang, W., Wang, P., Liao, X., Chen, Y., Borovilas, J., Jin, T., et al. (2020). Mechanically-Robust Structural Lithium-Sulfur Battery with High Energy Density. *Energ. Storage Mater.* 33, 416–422. doi:10.1016/j.ensm.2020.08.018

Hudak, N. S., Schlichting, A. D., and Eisenbeiser, K. (2017). Structural Supercapacitors with Enhanced Performance Using Carbon Nanotubes and Polyaniline. *J. Electrochem. Soc.* 164, A691–A700. doi:10.1149/2.0721704jes

Ihrner, N., Johannisson, W., Sieland, F., Zenkert, D., and Johansson, M. (2017). Structural Lithium Ion Battery Electrolytes *via* reaction Induced Phase-Separation. *J. Mater. Chem. A.* 5, 25652–25659. doi:10.1039/c7ta04684g

Jacques, E., Hellqvist Kjell, M., Zenkert, D., Lindbergh, G., and Behm, M. (2013). Expansion of Carbon Fibres Induced by Lithium Intercalation for Structural Electrode Applications. *Carbon* 59, 246–254. doi:10.1016/j.carbon.2013.03.015

Jacques, E., H. Kjell, M., Zenkert, D., and Lindbergh, G. (2014). The Effect of Lithium-Intercalation on the Mechanical Properties of Carbon Fibres. *Carbon* 68, 725–733. doi:10.1016/j.carbon.2013.11.056

Jacques, E., Kjell, M. H., Zenkert, D., Lindbergh, G., Behm, M., and Willgert, M. (2012). Impact of Electrochemical Cycling on the Tensile Properties of Carbon Fibres for Structural Lithium-Ion Composite Batteries. *Composites Sci. Tech.* 72, 792–798. doi:10.1016/j.compscitech.2012.02.006

Javaid, A., and Ali, M. Z. (2018). Multifunctional Structural Lithium Ion Batteries for Electrical Energy Storage Applications. *Mater. Res. Express* 5, 055701, 2018 . Available at: https://iopscience.iop.org/article/10.1088/2053-1591/aabeb1. doi:10.1088/2053-1591/aabeb1

Javaid, A., Ho, K., Bismarck, A., Shaffer, M., Steinke, J., and Greenhalgh, E. (2014). Multifunctional Structural Supercapacitors for Electrical Energy Storage Applications. *J. Compos. Mater.* 48, 1409–1416. doi:10.1177/0021998313487239

Javaid, A., Ho, K., Bismarck, A., Steinke, J., Shaffer, M., and Greenhalgh, E. (2016). Carbon Fibre-Reinforced Poly(ethylene Glycol) Diglycidylether Based Multifunctional Structural Supercapacitor Composites for Electrical Energy Storage Applications. *J. Compos. Mater.* 50, 2155–2163. doi:10.1177/0021998315602324

Javaid, A., Ho, K., Bismarck, A., Steinke, J., Shaffer, M., and Greenhalgh, E. (2018). Improving the Multifunctional Behaviour of Structural Supercapacitors by Incorporating Chemically Activated Carbon Fibres and Mesoporous Silica Particles as Reinforcement. *J. Compos. Mater.* 52, 3085–3097. doi:10.1177/0021998318761216

Javaid, A., and Irfan, M. (2018). Multifunctional Structural Supercapacitors Based on Graphene Nanoplatelets/carbon Aerogel Composite Coated Carbon Fiber Electrodes. *Mater. Res. Express* 6, 016310, 2018 . Available at: https://iopscience.iop.org/article/10.1088/2053-1591/aae862. doi:10.1088/2053-1591/aae862

Javaid, A., Khalid, O., Shakeel, A., and Noreen, S. (2021). Multifunctional Structural Supercapacitors Based on Polyaniline Deposited Carbon Fiber Reinforced Epoxy Composites. *J. Energ. Storage* 33, 102168. doi:10.1016/j.est.2020.102168

Jia, X., Liu, C., Neale, Z. G., Yang, J., and Cao, G. (2020). Active Materials for Aqueous Zinc Ion Batteries: Synthesis, Crystal Structure, Morphology, and Electrochemistry. *Chem. Rev.* 120 (15), 7795-7866. Available at: https://pubs.acs.org/doi/10.1021/acs.chemrev.9b00628. doi:10.1021/acs.chemrev.9b00628

Johannisson, W., Ihrner, N., Zenkert, D., Johansson, M., Carlstedt, D., Asp, L. E., et al. (2018). Multifunctional Performance of a Carbon Fiber UD Lamina Electrode for Structural Batteries. *Composites Sci. Tech.* 168, 81–87. doi:10.1016/j.compscitech.2018.08.044

Johannisson, W., Nguyen, S., Lindbergh, G., Zenkert, D., Greenhalgh, E., Shaffer, M., et al. (2020). A Residual Performance Methodology to Evaluate Multifunctional Systems. *Multifunct. Mater.* 3, 12, 2020 . Available at: https://iopscience.iop.org/article/10.1088/2399-7532/ab8e95. doi:10.1088/2399-7532/ab8e95

John, G., Miroshnikov, M., Mahankali, K., Thangavel, N. K., Satapathy, S., Arava, L. M. R., et al. (2020). Bioderived Molecular Electrodes for Next-Generation Energy-Storage Materials. *ChemSusChem* 13 (9), 2186–2204. doi:10.1002/cssc.201903589

Kalnaus, S., Asp, L. E., Li, J., Veith, G. M., Nanda, J., Daniel, C., et al. (2021). Multifunctional Approaches for Safe Structural Batteries. *J. Energ. Storage* 40, 102747. doi:10.1016/j.est.2021.102747

Kjell, M. H., Jacques, E., Zenkert, D., Behm, M., and Lindbergh, G. (2011). PAN-Based Carbon Fiber Negative Electrodes for Structural Lithium-Ion Batteries. *J. Electrochem. Soc.* 158, A1455. doi:10.1149/2.053112jes

Kjell, M. H., Zavalis, T. G., Behm, M., and Lindbergh, G. (2013). Electrochemical Characterization of Lithium Intercalation Processes of PAN-Based Carbon Fibers in a Microelectrode System. *J. Electrochem. Soc.* 160, A1473–A1481. doi:10.1149/2.054309jes

Kwon, S. R., Harris, J., Zhou, T., Loufakis, D., Boyd, J. G., and Lutkenhaus, J. L. (2017). Mechanically Strong Graphene/Aramid Nanofiber Composite Electrodes for Structural Energy and Power. *ACS Nano* 11, 6682–6690. doi:10.1021/acsnano.7b00790

Ladpli, P., Nardari, R., Kopsaftopoulos, F., and Chang, F.-K. (2019). Multifunctional Energy Storage Composite Structures with Embedded Lithium-Ion Batteries. *J. Power Sourc.* 414, 517–529. doi:10.1016/j.jpowsour.2018.12.051

Lee, S., Li, W., Dolocan, A., Celio, H., Park, H., Warner, J. H., et al. (2021). In-Depth Analysis of the Degradation Mechanisms of High-Nickel, Low/No-Cobalt Layered Oxide Cathodes for Lithium-Ion Batteries. *Adv. Energ. Mater.* 11, 2100858. doi:10.1002/aenm.202100858

Li, H., Wang, S., Feng, M., Yang, J., and Zhang, B. (2018). Self-assembly and Performances of Wrinkled rGO@carbon Fiber with Embedded SnO2 Nanoparticles as Anode Materials for Structural Lithium-Ion Battery. *J. Mater. Sci.* 53, 11607–11619. doi:10.1007/s10853-018-2401-6

Li, Q., Zhu, Y. Q., and Eichhorn, S. J. (2018). Structural Supercapacitors Using a Solid Resin Electrolyte with Carbonized Electrospun Cellulose/carbon Nanotube Electrodes. *J. Mater. Sci.* 53, 14598–14607. doi:10.1007/s10853-018-2665-x

Li, W., Lee, S., and Manthiram, A. (2020). High-Nickel NMA: A Cobalt-Free Alternative to NMC and NCA Cathodes for Lithium-Ion Batteries. *Adv. Mater.* 32, 1–6. doi:10.1002/adma.202002718

Li, X., Rong, J., and Wei, B. (2010). Electrochemical Behavior of Single-Walled Carbon Nanotube Supercapacitors under Compressive Stress. *ACS Nano* 4, 6039–6049. doi:10.1021/nn101595y

Liu, P., Sherman, E., and Jacobsen, A. (2009). Design and Fabrication of Multifunctional Structural Batteries. *J. Power Sourc.* 189, 646–650. doi:10.1016/j.jpowsour.2008.09.082

Liu, W., Oh, P., Liu, X., Lee, M.-J., Cho, W., Chae, S., et al. (2015). Nickel-Rich Layered Lithium Transition-Metal Oxide for High-Energy Lithium-Ion Batteries. *Angew. Chem. Int. Ed.* 54, 4440–4457. doi:10.1002/anie.201409262

Liu, X., Jervis, R., Maher, R. C., Villar-Garcia, I. J., Naylor-Marlow, M., Shearing, P. R., et al. (2016). 3D Printing: 3D-Printed Structural Pseudocapacitors (Adv. Mater. Technol. 9/2016). *Adv. Mater. Technol.* 1, 1–7. doi:10.1002/admt.201670043

Mapleback, B. J., Simons, T. J., Shekibi, Y., Ghorbani, K., and Rider, A. N. (2020). Structural Composite Supercapacitor Using Carbon Nanotube Mat Electrodes with Interspersed Metallic Iron Nanoparticles. *Electrochimica Acta* 331, 135233. doi:10.1016/j.electacta.2019.135233

Mariano, M., Kissi, N. E., and Dufresne, A. (2014). Cellulose Nanocrystals and Related Nanocomposites: Review of some Properties and Challenges. *J. Polym. Sci. B Polym. Phys.* 52 (12). doi:10.1002/polb.23490

Mauger, A., Julien, C., Paolella, A., Armand, M., and Zaghib, K. (2019). Building Better Batteries in the Solid State: A Review.Materials. *Materials (Basel)* 12, 1–57. doi:10.3390/ma12233892

Mikhalchan, A., and Vilatela, J. J. (2019). A Perspective on High-Performance CNT Fibres for Structural Composites. *Carbon* 150, 191–215. Available at: https://linkinghub.elsevier.com/retrieve/pii/S0008622319304567. doi:10.1016/j.carbon.2019.04.113

Moyer, K., Boucherbil, N. A., Zohair, M., Eaves-Rathert, J., and Pint, C. L. (2020). Polymer Reinforced Carbon Fiber Interfaces for High Energy Density Structural Lithium-Ion Batteries. *Sust. Energ. Fuels* 4, 2661–2668. Available at: http://xlink.rsc.org/?DOI=D0SE00263A. doi:10.1039/d0se00263a

Moyer, K., Meng, C., Marshall, B., Assal, O., Eaves, J., Perez, D., et al. (2020). Carbon Fiber Reinforced Structural Lithium-Ion Battery Composite: Multifunctional Power Integration for CubeSats. *Energ. Storage Mater.* 24, 676–681. doi:10.1016/j.ensm.2019.08.003

Muench, S., Wild, A., Friebe, C., Häupler, B., Janoschka, T., and Schubert, U. S. (2016). Polymer-Based Organic Batteries. *Chem. Rev.* 116, 9438–9484. Available at: http://pubs.acs.org/doi/abs/10.1021/acs.chemrev.6b00070. doi:10.1021/acs.chemrev.6b00070

Muralidharan, N., Teblum, E., Westover, A. S., Schauben, D., Itzhak, A., Muallem, M., et al. (2018). Carbon Nanotube Reinforced Structural Composite Supercapacitor. *Sci. Rep.* 8, 1–9. doi:10.1038/s41598-018-34963-x

Nguyen, S., Anthony, D. B., Qian, H., Yue, C., Singh, A., Bismarck, A., et al. (2019). Mechanical and Physical Performance of Carbon Aerogel Reinforced Carbon Fibre Hierarchical Composites. *Composites Sci. Tech.* 182, 107720. doi:10.1016/j.compscitech.2019.107720

Nguyen, S. N., Millereux, A., Pouyat, A., Greenhalgh, E. S., Shaffer, M. S. P., Kucernak, A. R. J., et al. (2021). Conceptual Multifunctional Design, Feasibility and Requirements for Structural Power in Aircraft Cabins. *J. Aircraft* 58, 677–687. doi:10.2514/1.c036205

Palchoudhury, S., Ramasamy, K., Gupta, R. K., and Gupta, A. (2019). Flexible Supercapacitors: A Materials Perspective. *Front. Mater.* 5, 1–9. doi:10.3389/fmats.2018.00083

Park, M. Y., Kim, J.-H., Kim, D. K., and Kim, C. G. (2018). Perspective on Carbon Fiber Woven Fabric Electrodes for Structural Batteries. *Fibers Polym.* 19, 599–606. doi:10.1007/s12221-018-7937-1

Patel, A., Johnson, L., Arroyave, R., and Lutkenhaus, J. (2019). Design of Multifunctional Supercapacitor Electrodes Using an Informatics Approach. *Mol. Syst. Des. Eng.* 4 (3), 654-663. Available at: http://pubs.rsc.org/en/Content/ArticleLanding/2019/ME/C8ME00060C. doi:10.1039/C8ME00060C

Patel, A., Loufakis, D., Flouda, P., George, I., Shelton, C., Harris, J., et al. (2020). Carbon Nanotube/Reduced Graphene Oxide/Aramid Nanofiber Structural Supercapacitors. *ACS Appl. Energ. Mater.* 3, 11763–11771. doi:10.1021/acsaem.0c01926

Patel, A., Wilcox, K., Li, Z., George, I., Juneja, R., Lollar, C., et al. (2020). High Modulus, Thermally Stable, and Self-Extinguishing Aramid Nanofiber Separators. *ACS Appl. Mater. Inter.* 12, 25756–25766. doi:10.1021/acsami.0c03671

Pereira, T., Guo, Z., Nieh, S., Arias, J., and Hahn, H. T. (2007). Embedding Thin-Film Lithium Energy Cells In Structural Composites. *Compos. Sci. Technol.* 68 (7–8), 1935–1941. doi:10.1016/j.compscitech.2008.02.019

Pereira, T., Guo, Z., Nieh, S., Arias, J., and Hahn, H. T. (2009). Energy Storage Structural Composites: a Review. *J. Compos. Mater.* 43, 549–560. doi:10.1177/0021998308097682

Poizot, P., Dolhem, F., and Gaubicher, J. (2018). Progress in All-Organic Rechargeable Batteries Using Cationic and Anionic Configurations: Toward Low-Cost and Greener Storage Solutions? *Curr. Opin. Electrochemistry* 9, 70–80. doi:10.1016/j.coelec.2018.04.003

Qian, H., Bismarck, A., Greenhalgh, E. S., Kalinka, G., and Shaffer, M. S. P. (2008). Hierarchical Composites Reinforced with Carbon Nanotube Grafted Fibers:

The Potential Assessed at the Single Fiber Level. *Chem. Mater.* 20, 1862–1869. doi:10.1021/cm702782j

Qian, H., Diao, H., Shirshova, N., Greenhalgh, E. S., Steinke, J. G. H., Shaffer, M. S. P., et al. (2013). Activation of Structural Carbon Fibres for Potential Applications in Multifunctional Structural Supercapacitors. *J. Colloid Interf. Sci.* 395, 241–248. doi:10.1016/j.jcis.2012.12.015

Qian, H., Greenhalgh, E. S., Shaffer, M. S. P., and Bismarck, A. (2010). Carbon Nanotube-Based Hierarchical Composites: A Review. *J. Mater. Chem.* 20, 4751–4762. doi:10.1039/c000041h

Qian, H., Kucernak, A. R., Greenhalgh, E. S., Bismarck, A., and Shaffer, M. S. P. (2013). Multifunctional Structural Supercapacitor Composites Based on Carbon Aerogel Modified High Performance Carbon Fiber Fabric. *ACS Appl. Mater. Inter.* 5, 6113–6122. doi:10.1021/am400947j

Rana, M., Boaretto, N., Mikhalchan, A., Vila Santos, M., Marcilla, R., and Vilatela, J. J. (2021). Composite Fabrics of Conformal MoS2 Grown on CNT Fibers: Tough Battery Anodes without Metals or Binders. *ACS Appl. Energ. Mater.* 4, 5668–5676. doi:10.1021/acsaem.1c00482

Rana, M., Ou, Y., Meng, C., Sket, F., González, C., and Vilatela, J. J. (2020). Damage-Tolerant, Laminated Structural Supercapacitor Composites Enabled by Integration of Carbon Nanotube Fibres. *Multifunct. Mater.* 3, 015001. doi:10.1088/2399-7532/ab686d

Reece, R., Lekakou, C., and Smith, P. A. (2020). A High-Performance Structural Supercapacitor. *ACS Appl. Mater. Inter.* 12, 25683–25692. Available at: https://pubs.acs.org/doi/10.1021/acsami.9b23427. doi:10.1021/acsami.9b23427

Reece, R., Lekakou, C., and Smith, P. A. (2019). A Structural Supercapacitor Based on Activated Carbon Fabric and a Solid Electrolyte. *Mater. Sci. Tech.* 35, 368–375. doi:10.1080/02670836.2018.1560536

Roberts, S. C., and Aglietti, G. S. (2010). Structural Performance of a Multifunctional Spacecraft Structure Based on Plastic Lithium-Ion Batteries. *Acta Astronautica* 67, 424–439. doi:10.1016/j.actaastro.2010.03.004

Sánchez-Romate, X. F., Bosque, A. D., Artigas-Arnaudas, J., Muñoz, B. K., Sánchez, M., and Ureña, A. (2021). A Proof of Concept of a Structural Supercapacitor Made of Graphene Coated Woven Carbon Fibers: EIS Study and Mechanical Performance. *Electrochimica Acta* 370, 137746. doi:10.1016/j.electacta.2021.137746

Schneider, L. M., Ihrner, N., Zenkert, D., and Johansson, M. (2019). Bicontinuous Electrolytes via Thermally Initiated Polymerization for Structural Lithium Ion Batteries. *ACS Appl. Energ. Mater.* 2 (6), 4362–4369. Available at: http://pubs.acs.org/doi/10.1021/acsaem.9b00563. doi:10.1021/acsaem.9b00563

Senokos, E., Ou, Y., Torres, J. J., Sket, F., González, C., Marcilla, R., et al. (2018). Energy Storage in Structural Composites by Introducing CNT Fiber/polymer Electrolyte Interleaves. *Sci. Rep.* 8, 1–10. doi:10.1038/s41598-018-21829-5

Senokos, E., Rana, M., Vila, M., Fernandez-Cestau, J., Costa, R. D., Marcilla, R., et al. (2020). Transparent and Flexible High-Power Supercapacitors Based on Carbon Nanotube Fibre Aerogels. *Nanoscale* 12, 16980–16986. doi:10.1039/d0nr04646a

Senokos, E., Reguero, V., Cabana, L., Palma, J., Marcilla, R., and Vilatela, J. J. (2017). Large-Area, All-Solid, and Flexible Electric Double Layer Capacitors Based on CNT Fiber Electrodes and Polymer Electrolytes. *Adv. Mater. Technol.* 2 (7), 1600290. doi:10.1002/admt.201600290

Senokos, E., Reguero, V., Palma, J., Vilatela, J. J., and Marcilla, R. (2016). Macroscopic Fibres of CNTs as Electrodes for Multifunctional Electric Double Layer Capacitors: from Quantum Capacitance to Device Performance. *Nanoscale* 8, 3620–3628. doi:10.1039/c5nr07697h

Sha, Z., Huang, F., Zhou, Y., Zhang, J., Wu, S., Chen, J., et al. (2021). Synergies of Vertical Graphene and Manganese Dioxide in Enhancing the Energy Density of Carbon Fibre-Based Structural Supercapacitors. *Composites Sci. Tech.* 201, 108568. doi:10.1016/j.compscitech.2020.108568

Shen, Z., and Zhou, H. (2017). Mechanical and Electrical Behavior of Carbon Fiber Structural Capacitors: Effects of Delamination and Interlaminar Damage. *Compos. Structures* 166, 38–48. doi:10.1016/j.compstruct.2016.12.062

Shi, K., Yang, X., Cranston, E. D., and Zhitomirsky, I. (2016). Efficient Lightweight Supercapacitor with Compression Stability. *Adv. Funct. Mater.* 26, 6437–6445. doi:10.1002/adfm.201602103

Shirshova, N., Bismarck, A., Carreyette, S., Fontana, Q. P. V., Greenhalgh, E. S., Jacobsson, P., et al. (2013). Structural Supercapacitor Electrolytes Based on Bicontinuous Ionic Liquid-Epoxy Resin Systems. *J. Mater. Chem. A.* 1, 15300, 2013 . Available at: http://xlink.rsc.org/?DOI=c3ta13163g. doi:10.1039/c3ta13163g

Shirshova, N., Qian, H., Houllé, M., Steinke, J. H. G., Kucernak, A. R. J., Fontana, Q. P. V., et al. (2014). Multifunctional Structural Energy Storage Composite Supercapacitors. *Faraday Discuss.* 172, 81–103. doi:10.1039/c4fd00055b

Shirshova, N., Qian, H., Shaffer, M. S. P., Steinke, J. H. G., Greenhalgh, E. S., Curtis, P. T., et al. (2013). Structural Composite Supercapacitors. *Composites Part A: Appl. Sci. Manufacturing* 46, 96–107. doi:10.1016/j.compositesa.2012.10.007

Snyder, J. F., Carter, R. H., Wong, E. L., Nguyen, P. A., Ngo, E. H., and Wetzel, E. D. (2006). "Multifunctional Structural Composite Batteries" in Proceedings From SAMPE 06 Fall Technical Conference, Dallas, TX.

Snyder, J. F., Carter, R. H., Wong, E. L., Nguyen, P. A., Xu, K., Ngo, E. H., et al. (2006). *Int. SAMPE Tech. Conf.*, 1–13.

Snyder, J. F., O'Brien, D. J., and Wetzel, E. D. (2015). "Structural Batteries, Capacitors and Supercapacitors," in *Handbook of Solid State Batteries*. Editors N. J. Dudney, W. C. West, and J. Nanda (Singapore: World Scientific), 657–699. Available at: http://www.worldscientific.com/doi/abs/10.1142/9789814651905_0019. doi:10.1142/9789814651905_0019

Subhani, K., Jin, X., Mahon, P. J., Kin Tak Lau, A., and Salim, N. V. (2021). Graphene Aerogel Modified Carbon Fiber Reinforced Composite Structural Supercapacitors. *Composites Commun.* 24, 100663. doi:10.1016/j.coco.2021.100663

Sun, J., Gargitter, V., Pei, S., Wang, T., Yan, Y., Advani, S. G., et al. (2020). Mechanical and Electrochemical Performance of Hybrid Laminated Structural Composites with Carbon Fiber/Solid Electrolyte Supercapacitor Interleaves. *Composites Sci. Tech.* 196, 108234. doi:10.1016/j.compscitech.2020.108234

Carlson, T. (2013). Multifunctional Composite Materials: Design, Manufacture And Experimental Characterisation. Thesis: Doctoral dissertation Lulea University of Technology.

Thakur, A., and Dong, X. (2020). Additive Manufacturing of 3D Structural Battery Composites with Coextrusion Deposition of Continuous Carbon Fibers. *Manufacturing Lett.* 26, 42–47. doi:10.1016/j.mfglet.2020.09.007

Thomas, J., Qidwai, S., Pogue, W., and Pham, G. (2013). Multifunctional Structure-Battery Composites for marine Systems. *J. Compos. Mater.* 47, 5–26. doi:10.1177/0021998312460262

Westover, A. S., Tian, J. W., Bernath, S., Oakes, L., Edwards, R., Shabab, F. N., et al. (2014). A Multifunctional Load-Bearing Solid-State Supercapacitor. *Nano Lett.* 14, 3197–3202. doi:10.1021/nl500531r

Wong, E. L., Baechle, D. M., Xu, K., Carter, R. H., Snyder, J. F., and Wetzel, E. D. (2007). Design and Processing of Structural Composite Batteries.

Wu, F., and Yushin, G. (2017). Conversion Cathodes for Rechargeable Lithium and Lithium-Ion Batteries. *Energy Environ. Sci.* 10, 435–459. doi:10.1039/c6ee02326f

Xu, J., Johannisson, W., Johansen, M., Liu, F., Zenkert, D., Lindbergh, G., et al. (2020). Characterization of the Adhesive Properties between Structural Battery Electrolytes and Carbon Fibers. *Composites Sci. Tech.* 188, 107962, 2020 . Available at: https://linkinghub.elsevier.com/retrieve/pii/S0266353819326879. doi:10.1016/j.compscitech.2019.107962

Xu, J., Lindbergh, G., and Varna, J. (2018). Carbon Fiber Composites with Battery Function: Stresses and Dimensional Changes Due to Li-Ion Diffusion. *J. Compos. Mater.* 52, 2729–2742. doi:10.1177/0021998317752825

Xu, J., and Zhang, D. (2017). Multifunctional Structural Supercapacitor Based on Graphene and Geopolymer. *Electrochimica Acta* 224, 105–112. doi:10.1016/j.electacta.2016.12.045

Xu, Y., Pei, S., Yan, Y., Wang, L., Xu, G., Yarlagadda, S., et al. (2021). High-Performance Structural Supercapacitors Based on Aligned Discontinuous Carbon Fiber Electrodes and Solid Polymer Electrolytes. *ACS Appl. Mater. Inter.* 13, 11774–11782. doi:10.1021/acsami.0c19550

Yan, J., Ren, C. E., Maleski, K., Hatter, C. B., Anasori, B., Urbankowski, P., et al. (2017). Flexible MXene/Graphene Films for Ultrafast Supercapacitors with Outstanding Volumetric Capacitance. *Adv. Funct. Mater.* 27, 1701264, 2017 . Available at: http://doi.wiley.com/10.1002/adfm.201701264. doi:10.1002/adfm.201701264

Yu, Y., Zhang, B., Feng, M., Qi, G., Tian, F., Feng, Q., et al. (2017). Multifunctional Structural Lithium Ion Batteries Based on Carbon Fiber Reinforced Plastic Composites. *Composites Sci. Tech.* 147, 62–70. doi:10.1016/j.compscitech.2017.04.031

Zeng, L., Li, P., Yao, Y., Niu, B., Niu, S., and Xu, B. (2020). Recent Progresses of 3D Printing Technologies for Structural Energy Storage Devices. *Mater. Today Nano* 12, 100094. doi:10.1016/j.mtnano.2020.100094

Zhang, C. J., Anasori, B., Seral-Ascaso, A., Park, S.-H., McEvoy, N., Shmeliov, A., et al. (2017). Transparent, Flexible, and Conductive 2D Titanium Carbide (MXene) Films with High Volumetric Capacitance. *Adv. Mater.* 29, 1702678, 2017 . Available at: http://doi.wiley.com/10.1002/adma.201702678. doi:10.1002/adma.201702678

Zhang, W.-J. (2011). Structure and Performance of LiFePO4 Cathode Materials: A Review. *J. Power Sourc.* 196, 2962–2970. doi:10.1016/j.jpowsour.2010.11.113

Zhao, M.-Q., Ren, C. E., Ling, Z., Lukatskaya, M. R., Zhang, C., Van Aken, K. L., et al. (2015). Flexible MXene/Carbon Nanotube Composite Paper with High Volumetric Capacitance. *Adv. Mater.* 27, 339–345. Available at: http://doi.wiley.com/10.1002/adma.201404140. doi:10.1002/adma.201404140

Zheng, S., Zhang, C., Zhou, F., Dong, Y., Shi, X., Nicolosi, V., et al. (2019). Ionic Liquid Pre-intercalated MXene Films for Ionogel-Based Flexible Micro-supercapacitors with High Volumetric Energy Density. *J. Mater. Chem. A.* 7, 9478–9485. doi:10.1039/c9ta02190f

Conflict of Interest: The authors declare that the research was conducted in the absence of any commercial or financial relationships that could be construed as a potential conflict of interest.

frontiers in Chemistry

ORIGINAL RESEARCH
published: 03 January 2022
doi: 10.3389/fchem.2021.794247

Effect of Trastuzumab–HER2 Complex Formation on Stress-Induced Modifications in the CDRs of Trastuzumab

Baubek Spanov[1], *Victoria Aboagye*[1], *Oladapo Olaleye*[1], *Natalia Govorukhina*[1], *Nico C. van de Merbel*[1,2] *and Rainer Bischoff*[1]*

[1]Department of Analytical Biochemistry, Groningen Research Institute of Pharmacy, University of Groningen, Groningen, Netherlands, [2]Bioanalytical Laboratory, ICON, Assen, Netherlands

Asparagine deamidation and aspartic acid isomerization in the complementarity determining regions (CDRs) of monoclonal antibodies may alter their affinity to the target antigen. Trastuzumab has two hot spots for deamidation and one position for isomerization in the CDRs. Little is known how complex formation with its target antigen HER2 affects these modifications. Modifications in the CDRs of trastuzumab were thus compared between the free antibody and the trastuzumab–HER2 complex when stressed under physiological conditions at 37°C. Complex formation and stability of the complex upon stressing were assessed by size-exclusion chromatography. Deamidation of light-chain Asn-30 (Lc-Asn-30) was extensive when trastuzumab was stressed free but reduced about 10-fold when the antibody was stressed in complex with HER2. Almost no deamidation of heavy-chain (Hc-Asn-55) was detected in the trastuzumab–HER2 complex, while deamidation was observed when the antibody was stressed alone. Hc-Asp-102 isomerization, a modification that critically affects biological activity, was observed to a moderate degree when the free antibody was stressed but was not detected at all in the trastuzumab–HER2 complex. This shows that complex formation has a major influence on critical modifications in the CDRs of trastuzumab.

Keywords: trastuzumab, HER2, deamidation, trastuzumab–HER2 complex, cation-exchange chromatography, size-exclusion chromatography, peptide mapping

OPEN ACCESS

Edited by:
Nicole J. Jaffrezic-Renault, Université Claude Bernard Lyon 1, France

Reviewed by:
Piliang Hao, ShanghaiTech University, China
Xavier Gallart-Palau, Institut d'Investigació Sanitària Pere Virgili (IISPV), Spain

***Correspondence:**
Rainer Bischoff
r.p.h.bischoff@rug.nl

Specialty section:
This article was submitted to Analytical Chemistry, a section of the journal Frontiers in Chemistry

Received: *13 October 2021*
Accepted: *30 November 2021*
Published: *03 January 2022*

Citation:
Spanov B, Aboagye V, Olaleye O, Govorukhina N, van de Merbel NC and Bischoff R (2022) Effect of Trastuzumab–HER2 Complex Formation on Stress-Induced Modifications in the CDRs of Trastuzumab. Front. Chem. 9:794247. doi: 10.3389/fchem.2021.794247

INTRODUCTION

Monoclonal antibodies (mAbs) are an important class of biopharmaceuticals for the treatment of a variety of severe diseases due to their high specificity and long half-life (Chames et al., 2009). The high specificity is defined by the antigen-binding fragment (Fab) of mAbs. The Fab consists of heavy and light chains of an antibody connected by an inter-chain disulfide bond. Each chain has three complementarity determining regions (CDRs), hypervariable loops that consist of several amino acid residues forming the antigen-binding sites. Formation of the antigen–antibody complex is governed by electrostatic and hydrophobic interactions between amino acid residues of the CDRs and epitope(s) of the target antigen (Davies et al., 1990). Chemical change of CDR amino acids both *in vitro* and *in vivo* due to susceptibility to modifications, such as asparagine deamidation or aspartic acid isomerization, may have a negative effect on antigen binding or diminish potency in cell-based assays (Cacia et al., 1996; Vlasak et al., 2009). It is hard to predict the impact of CDR modifications on

antigen binding because each particular antibody represents a unique case. For example, deamidation in the heavy chain CDR2 resulted in 14 times reduction in binding affinity of a proprietary mAb (Huang et al., 2005). However, for another mAb, deamidation in the heavy chain CDR2 had no effect on potency in a cell-based assay (Lyubarskaya et al., 2006). Besides CDRs, amino acid residues of the framework regions (FR) may play an important role in the generation of high-affinity antibodies. Firstly, FR amino acids can be in contact with the antigen when the antibody–antigen complex is formed. Secondly, FR amino acids can contribute to antigen binding by affecting the conformation of a particular CDR. Humanization studies of trastuzumab showed that replacement of FR amino acids at particular positions resulted in higher affinity variants (Carter et al., 1992).

Trastuzumab is a recombinant humanized mAb that targets sub-domain IV of the extracellular domain of human epidermal growth factor receptor 2 (HER2). After Food and Drug Administration (FDA) approval in 1998, trastuzumab is presently one of the main drugs used for the treatment of HER2-positive breast cancer at different stages. Harris et al. were the first to show charge heterogeneity of trastuzumab by separating charge variants by cation-exchange chromatography (Harris et al., 2001). The source of heterogeneity was due to asparagine deamidation and aspartic acid isomerization in the CDRs of trastuzumab. Later, several other studies presented a similar charge heterogeneity profile of trastuzumab confirming that cation-exchange chromatography is a reliable approach for charge variant separation (Lingg et al., 2013; Schmid et al., 2018; Spanov et al., 2021). Some studies reported that acidic variants of trastuzumab caused by asparagine deamidation have a lower affinity to HER2 compared to the unmodified antibody isolated by cation-exchange chromatography (Dakshinamurthy et al., 2017; Schmid et al., 2018). Harris et al. reported that the basic variant, which was due to Hc-Asp-102 isomerization to isoaspartic acid in one of the heavy chains, has significantly reduced potency (Harris et al., 2001). Interestingly, the degree of both asparagine deamidation and aspartic acid isomerization in trastuzumab increases when incubated under physiological conditions (Schmid et al., 2018; Spanov et al., 2021). Earlier studies have shown that modifications in the CDRs of trastuzumab lead to a decrease in the affinity for the target receptor (Schmid et al., 2018; Dakshinamurthy et al., 2017). Here we wanted to investigate whether the formation of the complex influences the level of modifications or whether the modifications occur independently of the complex formation.

In the present study, the level of CDR modifications was assessed when trastuzumab was stressed under physiological conditions [phosphate-buffered saline (PBS), pH 7.4, and 37°C] free or in complex with HER2. Cation-exchange chromatography was used to isolate unmodified trastuzumab and size-exclusion chromatography (SEC) served to study trastuzumab–HER2 complex formation and stability. Peptide mapping by liquid chromatography-mass spectrometry (LC-MS) was used to localize modifications in the CDRs and to compare the relative level of modifications.

MATERIALS AND METHODS

Materials and Chemicals

Trastuzumab (Herceptin®, Lot N3024H10) was obtained from Roche (Grenzach-Wyhlen, Germany). Human HER2/ErbB2 Protein (His Tag protein, extracellular domain Thr23–Thr652; cat # HE2-H5225) was purchased from Acrobiosystems (Delaware, United States). 2-(N-morpholino)ethanesulfonic acid, 4-morpholineethanesulfonic acid monohydrate (MES monohydrate, cat # 69892), 4-(2-hydroxyethyl)piperazine-1-ethanesulfonic acid (HEPES, cat # H4034), N,N-bis(2-hydroxyethyl)glycine (bicine, cat # B3876), 3-(cyclohexylamino)-2-hydroxy-1-propanesulfonic acid (CAPSO, cat # C2278), 3-(cyclohexylamino)-1-propanesulfonic acid (CAPS, cat # C6070), sodium chloride (cat # 746398), DL-dithiothreitol (DTT, cat # D0632), iodoacetamide (IAA, cat # 16125), and sodium deoxycholate (SDC, cat # 30970) were obtained from Sigma-Aldrich (St. Louis, Missouri, United States). PBS 10× (cat # 14200-067) was purchased from Thermo Fisher Scientific (Waltham, MA, United States). Trypsin/Lys-C mix, Mass Spec Grade (cat # V5073), was obtained from Promega (Madison, WI, United States). Difluoroacetic acid (DFA, cat # 162120025) was acquired from Acros Organics (Fair Lawn, NJ, United States).

Cation-Exchange Chromatography

Cation-exchange chromatography was performed by pH-gradient separation on a MabPac SCX-10 (4 × 250 mm, 5 µm, Thermo Fisher Scientific, cat # 078655) column using an Agilent 1200 HPLC system as previously described (Spanov et al., 2021). pH gradient buffers were prepared according to Lingg et al. (2013), where buffer A (HEPES, Bicine, CAPSO, CAPS) had a pH of 8.0, and buffer B (Bicine, CAPSO, CAPS) had a pH of 10.5, respectively. A gradient change from 0% to 60% B over 10 column volumes (62.8 min) at a 0.5 ml/min flow rate was used for the separation of charge variants at room temperature. UV absorbance was measured at 280 nm with Agilent G4212B Diode Array Detector. The main peak (main fraction) from the cation-exchange chromatography was fractionated from non-stressed trastuzumab in several consecutive runs to obtain unmodified trastuzumab. The main fraction was collected into a Protein LoBind 96-well plate (cat # 0030504208; Eppendorf, Hamburg, Germany) filled with 100 µl of 300 mM MES buffer (pH 6) for pH neutralization to prevent deamidation. The main fraction was concentrated and buffer exchanged to 10 mM MES pH 6 with Amicon Ultra-2 Centrifugal Filter Units (cut-off 50 kDa, UFC205024, Merck Millipore, Darmstadt, Germany). Protein concentration of the main fraction was measured on a NanoPhotometer® N120 (Implen GmbH, Munich, Germany) at 280 nm (extinction coefficient was 1.36 L/g•cm).

Trastuzumab–HER2 Complex Formation at Different Trastuzumab to HER2 Ratios

Trastuzumab–HER2 complexes at molar ratios of 1:1, 1:2, and 2:1 were made by mixing corresponding amounts of 0.5 µg/µl HER2

and 0.5 μg/μl of trastuzumab main fraction followed by incubation at room temperature for 2 h at 500 rpm. The molecular weight of the HER2 extracellular domain (ECD) 115 kDa, determined by sodium dodecyl sulfate polyacrylamide gel electrophoresis (SDS-PAGE) (**Supplementary Figure S1**), was used to make complexes with different molar ratios. Samples were analyzed by SEC.

Size-Exclusion Chromatography

An Agilent 1200 HPLC system coupled with a TSKgel SuperSW mAb HR (7.8 mm × 300 mm, 4 μm, Tosoh Bioscience, United States) column was used to study formation and stability of the trastuzumab–HER2 complex. The mobile phase was 50 mM phosphate buffer pH 6.5 containing 450 mM NaCl. Isocratic elution at a flow rate of 1 ml/min at room temperature was performed, and eluting proteins were detected by UV absorbance at 280 nm.

Stressing Free Trastuzumab and the Trastuzumab–HER2 Complex

About 5.65 μg of unmodified trastuzumab (main fraction) in 20 μl PBS was stressed free and in complex with 8.7 μg of HER2 (trastuzumab to HER2 ratio 1:2) at 37°C for up to 4 weeks. Samples containing trastuzumab and HER2 were first left at room temperature for 2 h for complex formation and then incubated at 37°C for the indicated time periods. 5 μl of the stressed sample was injected into the size-exclusion column.

LC-MS/MS Peptide Mapping

Stressed samples were denatured and reduced in the presence of 0.5% SDC in 50 mM HEPES buffer pH 7 and 5 mM DTT at 60°C for 30 min. Alkylation was performed by adding IAA to a final concentration of 15 mM at room temperature for 20 min in the dark. Subsequently, a trypsin/Lys-C mix was added to the samples at a ratio of 25:1 (protein to enzyme), and proteins were digested for 6 h at 37°C. SDC was removed by precipitation prior to LC-MS analysis by adding 0.2% final concentration of DFA and centrifugation at 10,000 rpm for 10 min.

Digested samples were loaded on an Acclaim® PepMap® RSLC column (0.3 × 150 mm, 2 μm, 100 Å, Thermo Fisher Scientific) for chromatographic separation using a gradient from 2% to 35% B in 65 min, where mobile phase A consisted of 0.1% formic acid in water and mobile phase B of 0.1% formic acid in acetonitrile. The flow rate was 5 μl/min, and the column temperature was set to 40°C. LC-MS/MS peptide mapping analysis was conducted using an Eksigent NanoLC 425 system with a microflow pump (1–10 μl) coupled to a SCIEX TT6600 quadrupole-time-of-flight (QTOF) mass spectrometer with an OptiFlow® source (SCIEX, Toronto, Canada). The following source settings were applied: ion source gas 1 (GS1) 10 psi, ion source gas 2 (GS2) 20 psi, curtain gas (CUR) 25 psi, temperature (TEM) 100°C, IonSpray Voltage Floating (ISVF) 4.5 kV, and declustering potential (DP) 90 V. Measurements were performed in the data-dependent acquisition mode where one MS scan was followed by MS/MS of the top five most intense precursor ions. The MS scan range was 350–2m000 m/z. The threshold for precursor ion selection was set at 500 counts per second, and the charge states for the MS/MS fragmentation of precursor ions were set to +2 to +5 with an exclusion window of 4 s after two occurrences.

BPV Flex 2.1 and PeakView (SCIEX, Toronto, Canada) were employed for data analysis. Precursor mass tolerance was set to 20 ppm, and fragment mass tolerance was set to 0.03 Da. Carbamidomethylation was defined as fixed modification, while methionine oxidation and asparagine deamidation were defined as variable modifications.

RESULTS AND DISCUSSION

Isolation of Main Fraction of Trastuzumab by Cation-Exchange Chromatography

Trastuzumab is known to be heterogeneous in terms of charge. In our previous study (Spanov et al., 2021) we have shown that cation-exchange chromatography is an appropriate tool to study the stability of trastuzumab under stress conditions. Stressing trastuzumab for up to 3 weeks under physiological conditions (PBS buffer pH 7.4 and 37°C) resulted in complex chromatographic profiles. The source of charge heterogeneity was due to Lc-Asn-30, Hc-Asn-55, and Hc-Asn-387 deamidation, Hc-Asp-102 isomerization, and N-terminal pyroglutamate formation at the heavy chain. To initiate our study with unmodified trastuzumab, we decided to work with the main fraction after isolation by cation-exchange chromatography to discriminate modifications that occurred during stressing from those that were already present in clinical grade trastuzumab.

Size-Exclusion Chromatography to Study Formation of the Trastuzumab–HER2 Complex

To study trastuzumab–HER2 complex formation at different molar ratios, samples were subjected to size exclusion chromatography. Trastuzumab and HER2 were also analyzed separately as controls. An overlay of the chromatograms of trastuzumab and HER2 are shown in **Figure 1A**. Interestingly, HER2 ECD eluted slightly earlier than trastuzumab which has a molecular weight of around 149 kDa. The calculated molecular weight of HER2 ECD based on the amino acid sequence was 70.2 kDa. The molecular weight of HER2 ECD determined by SDS-PAGE was around 115 kDa (**Supplementary Figure S1**), and this molecular weight was used to prepare complexes at different ratios (as mentioned in the *Materials and Methods* section). However, additional molecular weight measurements by mass photometry (Refeyn Ltd., Oxford, England) and matrix-assisted laser desorption/ionization time-of-flight mass spectrometry (MALDI-TOF MS) (Bruker Daltonics, Bremen, Germany) showed the value lower than determined by SDS-PAGE, in the range of 80–90 kDa showing high heterogeneity of the protein, probably due to glycosylation (**Supplementary Figures S2, S3**). Despite the discrepancies in molecular weight values determined by different techniques, none of the values were higher than 149 kDa. Since HER2 ECD eluted earlier than

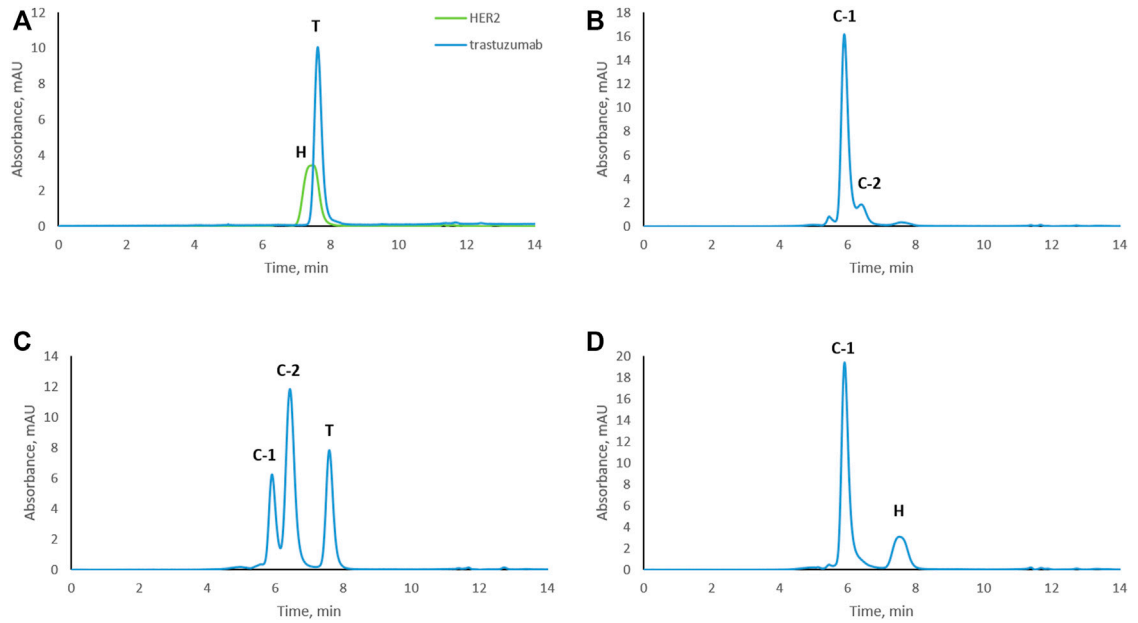

FIGURE 1 | Size-exclusion chromatograms of trastuzumab–HER2 complexes formed at different molar ratios. **(A)** Overlay chromatograms of trastuzumab and HER2. **(B)** Complex formed at 1:1 molar ratio. **(C)** Complex formed at 2:1 molar ratio (excess of trastuzumab). **(D)** Complex formed at 1:2 molar ratio (excess of HER2). C-1, complex-1 at 5.9 min; C-2, complex-2 at 6.4 min; T, trastuzumab at 7.7 min; H, HER2 at 7.5 min. UV absorbance was measured at 280 nm.

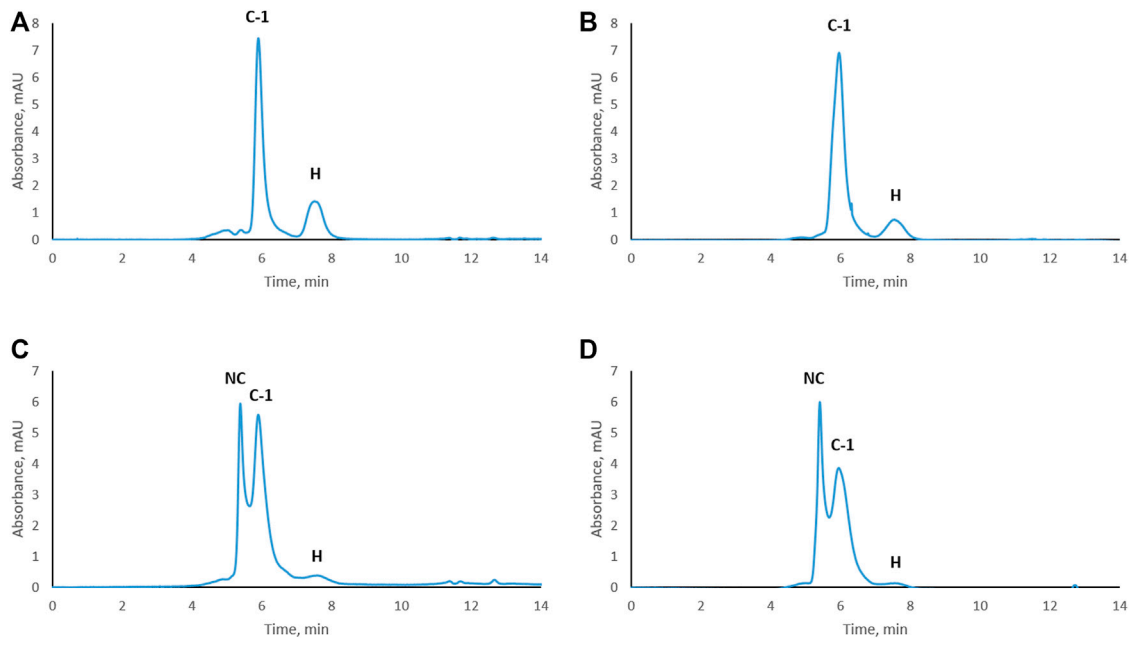

FIGURE 2 | Size-exclusion chromatograms of the trastuzumab–HER2 complex stressed under physiological conditions. Complex stressed for 1 week **(A)**, 2 weeks **(B)**, 3 weeks **(C)**, and 4 weeks **(D)**. NC, new complex; C-1, complex-1; H, HER2. UV absorbance was measured at 280 nm.

trastuzumab in SEC, we assume that HER2 ECD might be in dimer form in solution. A sample in which the complex was formed at a 1:1 molar ratio resulted in one main peak [complex-1 (C-1) at 5.9 min] and a shoulder peak (C-2) at 6.4 min (**Figure 1B**) next to a very minor, earlier eluting peak. Complex formation at a trastuzumab to HER2 ratio of 2:1 showed free trastuzumab, complex C-2 as the major peak, and complex C-1 (**Figure 1C**) indicating that C-2 represents a 1:1

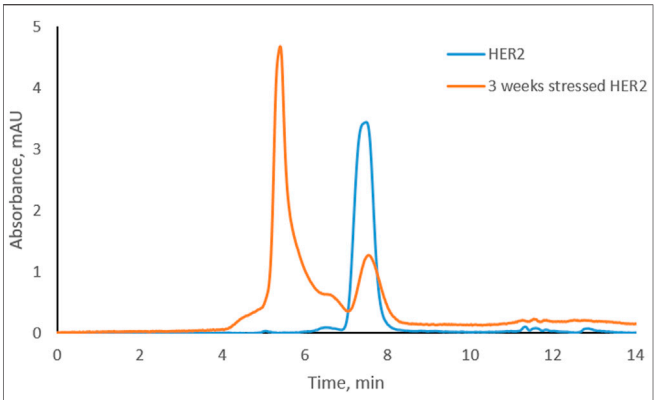

FIGURE 3 | Overlay of size-exclusion chromatograms of free HER2 at the beginning and after 3 weeks under physiological conditions.

complex while C-1 contains two molecules of HER2 for each molecule of trastuzumab. Complex formation in the presence of an excess of HER2 (trastuzumab: HER2 1:2) resulted in complex C-1 and a peak for free HER2 (**Figure 1D**) but no remaining free trastuzumab. Conditions under which there was no remaining free trastuzumab (1:2 trastuzumab: HER2 molar ratio) were chosen for the subsequent stress tests to assure that modifications occurred while trastuzumab was in complex with HER2.

Stressing the Trastuzumab–HER2 Complex

Trastuzumab was stressed free and in complex with HER2 (trastuzumab: HER2 molar ratio 1:2, complex C-1; see **Figure 1D**) under physiological conditions. Aliquots were taken every week to study the level of CDR modifications. Size exclusion chromatography was used to assure that the complex did not dissociate under these conditions and that there was no free trastuzumab in the solution. **Figure 2** shows the chromatographic profiles after 1, 2, 3, and 4 weeks of stressing. There was no change from the initial profile (see **Figure 1D**) after 1 or 2 weeks (**Figures 2A, B**) with complex C-1 remaining the main peak and free HER2 being still present. It must be noted though that the peak for the C-1 complex broadened slightly after 2 weeks and the peak for free HER2 diminished. A major change was observed after 3 weeks when a new, earlier eluting complex appeared (NC, retention time of 5.4 min) and the excess of free HER2 had almost disappeared. (**Figures 2C, D**). The broadening of peak C-1 after 2 weeks may have been due to the formation of a minor amount of NC, which was not separated from the excess of C-1. We assume that the new complex is due to oligomerization of HER2. To check whether this is the case, free HER2 was stressed for 3 weeks under the same conditions showing that HER2 oligomerizes to a form eluting at about 5.4 min in the absence of trastuzumab (**Figure 3**). This indicates that the newly observed complex after 3 weeks is due to HER2–HER2 interactions.

Based on SEC results, we assume that C-1 is a complex between a HER2 dimer and trastuzumab. HER2 is known to form homo- and heterodimers through sub-domain II (Adams et al., 2006; Smith et al., 2012). However, trastuzumab binds to sub-domain IV, which should still be available for trastuzumab binding even if HER2 is present as a dimer. C-2 is likely a 1:1 complex between a HER2 monomer and trastuzumab, since it was the main complex formed when trastuzumab was in excess. The presence of free HER2-ECD in **Figure 1D** can be explained by the use of a molecular weight of 115 kDa as determined by SDS-PAGE for the preparation of complexes. Upon detection of free HER2-ECD, we reassessed the molecular weight by mass photometry and MALDI-TOF MS and found that it was approximately 85 kDa. Considering this molecular weight, the actual trastuzumab:HER2 ratio in **Figure 1D** is calculated to be approximately 1:2.7 rather than 1:2, which may explain the free excess of HER2-ECD. It is important to note that we had a stochiometric amount of HER2-ECD or an excess to assure that there was no free trastuzumab during the stress study. In addition, having free HER2 also allowed to observe formation of higher-order complexes after 3 and 4 weeks of stressing trastuzumab–HER2 complex (**Figures 2C, D**) and also to find out that HER2 can oligomerize in solution upon stressing (**Figure 3**).

Peptide Mapping of Trastuzumab Stressed Free and in Complex With HER2

In order to assess whether complex formation with HER2 affects critical modifications in the CDRs of trastuzumab, we analyzed trastuzumab after stressing for up to 4 weeks by LC-MS-based peptide mapping. Native and deamidated peptides were distinguished by being chromatographically separated and due to differences in their MS/MS spectra (**Supplementary Figures S4–S9**). Asp isomerization resulted in the formation of isobaric peptides which could not be distinguished based on their MS or MS/MS spectra. However, chromatographic separation between the Asp and isoAsp forms was achieved. Deamidation of Lc-Asn-30 located in CDR1 was reported previously as a position that is highly susceptible to deamidation (Harris et al., 2001; Schmid et al., 2018; Spanov et al., 2021). Our peptide mapping results of free trastuzumab agree with these observations showing up to 85% deamidation after 4 weeks of stressing (**Figure 4**). However, when trastuzumab was stressed for 4 weeks in complex with HER2, Lc-Asn-30 deamidation was decreased to about 8%. Hc-Asp-102 isomerization, a modification that critically affects activity, increased to 32% after 4 weeks when trastuzumab was stressed in its free form. Strikingly, isomerization was not detected at all when trastuzumab was stressed in complex with HER2. Hc-Asn-55 is another position that is known to deamidate albeit at a slower rate compared to Lc-Asn-30. While 20% deamidation of Hc-Asn-55 was detected when free trastuzumab was stressed for 4 weeks, this level decreased to about 3% in the trastuzumab–HER2 complex.

Deamidation is known to be sequence dependent, and usually motifs such as NG and NS may have higher deamidation rate. However, this is not always the case as it depends also on conformational flexibility and solvent exposure of the particular position (Lu et al., 2018). In the case of

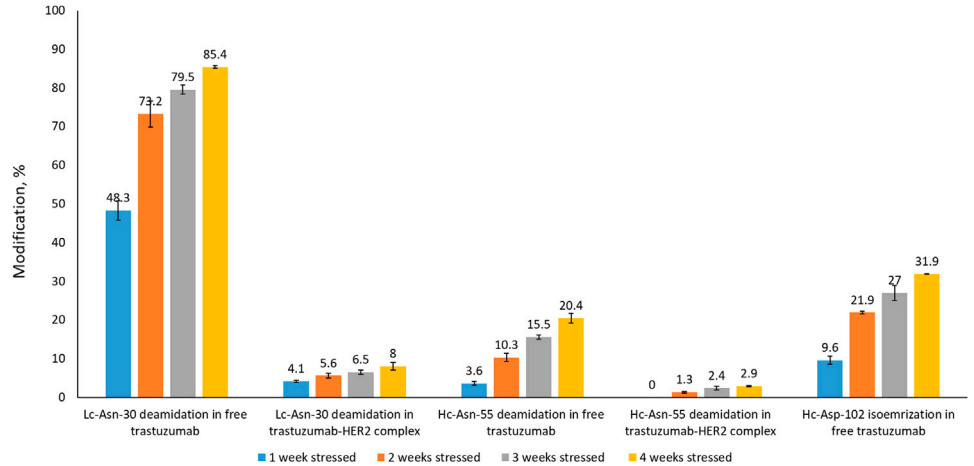

FIGURE 4 | Peptide mapping results of trastuzumab stressed free and in complex with HER2 for 1, 2, 3, or 4 weeks. Isomerization of Hc-Asp-102 was not detected in the trastuzumab–HER2 complex. Numbers given here are an average of two measurements.

trastuzumab, deamidation of N30 in the light chain, which is followed by threonine (T), is faster compared to the deamidation of N55 in the heavy chain, which is followed by glycine (G). These differences in deamidation of N residues in trastuzumab have been reported in the literature, and our results are in agreement with previously published results (Harris et al., 2001; Schmid et al., 2018; Spanov et al., 2021).

Peptide mapping is a widely used approach for the characterization of mAbs in terms of confirming their primary amino acid sequence as well as to localize potential modifications. The results presented here are based on label-free analyses, where the level of modification is calculated based on the ratio of the chromatographic peak area of the modified peptide to the sum of the peak areas of the modified and unmodified peptides. As this approach does not take differences in ionization efficiency between non-modified and modified peptides into account, it must be considered semi-quantitative. However, considering the large differences in deamidation or isomerization of trastuzumab free in solution and in complex with HER2, it is safe to assume that complex formation reduces the level of modification of these amino acid residues to a very significant extent.

Early studies on trastuzumab humanization showed that both Lc-Asn-30 and Hc-Asp-102 are important for antigen binding (Kelley and O'Connell, 1993; Gerstner et al., 2002). The fact that Lc-Asn-30 and Hc-Asn-55 were able to deamidate when trastuzumab was stressed in complex with HER2 indicates that there is still some conformational flexibility around these residues in the complex, while isomerization of Hc-Asp-102 was not detected at all when trastuzumab was stressed when bound to HER2. Isomerization of an aspartic acid residue introduces a major conformational change in the peptide backbone through the introduction of an extra methylene group (Du et al., 2012; Liu et al., 2014). Our results indicate that there is no flexibility around Hc-Asp-102 to accommodate such a conformational change when trastuzumab is in a complex with HER2. This may be due to the tight binding of CDR3 to HER2, as indicated by the previously reported importance of heavy chain CDR3 for antigen binding (Xu and Davis, 2000; D'Angelo et al., 2018). In fact, Shang et al. were able to prepare an alternative affinity binder for HER2 by mimicry of CDR3 (Shang et al., 2012). Moon et al. showed that substitution of a few amino acid residues in CDR3 of trastuzumab, including Hc-Asp-102, for other residues may increase the binding affinity of trastuzumab to HER2 (Moon et al., 2016). In their original study, Harris et al. reported that isomerization of Hc-Asp-102 reduces the potency of trastuzumab to block proliferation of a breast cancer cell line significantly (Harris et al., 2001). The absence of isomerization of Hc-Asp-102 in CDR3 when trastuzumab was stressed in complex with HER2 may be taken as indirect indication of the tight interaction between CDR3 of trastuzumab and HER2.

CONCLUSION

This study investigated the effect of complex formation on modifications in three different positions of CDRs in the therapeutic mAb trastuzumab when stressed under physiological conditions. Formation of the trastuzumab–HER2 complex and its stability under stress conditions was followed by SEC. Analysis by size exclusion chromatography indicated further that there are complexes with different stoichiometries, the 1:2 complex (trastuzumab: HER2) being the most abundant for up to 2–3 weeks of incubation, after which HER dimerization leads to formation of a larger, earlier eluting complex. Complex formation has a major effect on the deamidation of Lc-Asn-30 and Hc-Asn-55 but did not prevent it altogether. However, complex formation prevented isomerization of Hc-Asp-102, which was undetectable.

Further structural studies are needed to elucidate the underlying reasons for our observations. *In vivo* complex formation may explain some of the puzzling observations of different levels of deamidation of Hc-Asn-55 in breast cancer

patients treated with trastuzumab (Bults et al., 2016). Since the rate of the deamidation reaction is not known to be affected by enzymatic activities or other biochemical factors other than pH and temperature, it is fair to hypothesize that the different levels in patients may be due to different amounts of trastuzumab being complexed with HER2. This hypothesis is intriguing but must await further testing before any conclusions can be drawn.

DATA AVAILABILITY STATEMENT

The raw data supporting the conclusion of this article will be made available by the authors, without undue reservation.

AUTHOR CONTRIBUTIONS

BS performed experiments and wrote the manuscript. VA performed experiments and commented on the manuscript. OO contributed to writing the manuscript. NG contributed to writing the manuscript and to designing the study. NM contributed to writing the manuscript and to designing the study. RB contributed to writing the manuscript and to designing the study.

FUNDING

BS and OO are funded by a grant of the European Commission (H2020 MSCA-ITN 2017 "Analytics for Biologics," grant agreement ID 765502).

ACKNOWLEDGMENTS

We would like to thank Dennis Nanninga from Laboratory of Macromolecules and Interactomes for helping with Mass Photometry analysis and Dr. Hjalmar Permentier from Interfaculty Mass Spectrometry Center for helping with MALDI-TOF MS analysis. Mass photometry experiments presented in this research were made possible by co-financing from the Netherlands Ministry of Economic Affairs and Climate Policy by means of an allowance made available to the Laboratory of Macromolecules and Interactomes by the Top Sector Life Sciences and Health to stimulate public-private partnerships.

SUPPLEMENTARY MATERIAL

The Supplementary Material for this article can be found online at: https://www.frontiersin.org/articles/10.3389/fchem.2021.794247/full#supplementary-material

REFERENCES

Adams, C. W., Allison, D. E., Flagella, K., Presta, L., Clarke, J., Dybdal, N., et al. (2006). Humanization of a Recombinant Monoclonal Antibody to Produce a Therapeutic HER Dimerization Inhibitor, Pertuzumab. *Cancer Immunol. Immunother.* 55, 717–727. doi:10.1007/s00262-005-0058-x

Bults, P., Bischoff, R., Bakker, H., Gietema, J. A., and van de Merbel, N. C. (2016). LC-MS/MS-Based Monitoring of *In Vivo* Protein Biotransformation: Quantitative Determination of Trastuzumab and its Deamidation Products in Human Plasma. *Anal. Chem.* 88, 1871–1877. doi:10.1021/acs.analchem.5b04276

Cacia, J., Keck, R., Presta, L. G., and Frenz, J. (1996). Isomerization of an Aspartic Acid Residue in the Complementarity-Determining Regions of a Recombinant Antibody to Human IgE: Identification and Effect on Binding Affinity. *Biochemistry* 35, 1897–1903. doi:10.1021/bi951526c

Carter, P., Presta, L., Gorman, C. M., Ridgway, J. B., Henner, D., Wong, W. L., et al. (1992). Humanization of an Anti-p185HER2 Antibody for Human Cancer Therapy. *Proc. Natl. Acad. Sci.* 89, 4285–4289. doi:10.1073/pnas.89.10.4285

Chames, P., Van Regenmortel, M., Weiss, E., and Baty, D. (2009). Therapeutic Antibodies: Successes, Limitations and Hopes for the Future. *Br. J. Pharmacol.* 157, 220–233. doi:10.1111/j.1476-5381.2009.00190.x

Dakshinamurthy, P., Mukunda, P., Prasad Kodaganti, B., Shenoy, B. R., Natarajan, B., Maliwalave, A., et al. (2017). Charge Variant Analysis of Proposed Biosimilar to Trastuzumab. *Biologicals* 46, 46–56. doi:10.1016/j.biologicals.2016.12.006

D'Angelo, S., Ferrara, F., Naranjo, L., Erasmus, M. F., Hraber, P., and Bradbury, A. R. M. (2018). Many Routes to an Antibody Heavy-Chain CDR3: Necessary, yet Insufficient, for Specific Binding. *Front. Immunol.* 9, 1–13. doi:10.3389/fimmu.2018.00395

Davies, D. R., Padlan, E. A., and Sheriff, S. (1990). Antibody-Antigen Complexes 1. Available at: www.annualreviews.org (Accessed June 15, 2021).

Du, Y., Walsh, A., Ehrick, R., Xu, W., May, K., and Liu, H. (2012). Chromatographic Analysis of the Acidic and Basic Species of Recombinant Monoclonal Antibodies. *MAbs* 4, 578–585. doi:10.4161/mabs.21328

Gerstner, R. B., Carter, P., and Lowman, H. B. (2002). Sequence Plasticity in the Antigen-Binding Site of a Therapeutic Anti-Her2 Antibody. *J. Mol. Biol.* 321, 851–862. doi:10.1016/S0022-2836(02)00677-0

Harris, R. J., Kabakoff, B., Macchi, F. D., Shen, F. J., Kwong, M., Andya, J. D., et al. (2001). Identification of Multiple Sources of Charge Heterogeneity in a Recombinant Antibody. *J. Chromatogr. B: Biomed. Sci. Appl.* 752, 233–245. doi:10.1016/S0378-4347(00)00548-X

Huang, L., Lu, J., Wroblewski, V. J., Beals, J. M., and Riggin, R. M. (2005). *In Vivo* deamidation Characterization of Monoclonal Antibody by LC/MS/MS. *Anal. Chem.* 77, 1432–1439. doi:10.1021/ac0494174

Kelley, R. F., and O'Connell, M. P. (1993). Thermodynamic Analysis of an Antibody Functional Epitope. *Biochemistry* 32, 6828–6835. doi:10.1021/bi00078a005

Lingg, N., Tan, E., Hintersteiner, B., Bardor, M., and Jungbauer, A. (2013). Highly Linear pH Gradients for Analyzing Monoclonal Antibody Charge Heterogeneity in the Alkaline Range. *J. Chromatogr. A* 1319, 65–71. doi:10.1016/j.chroma.2013.10.028

Liu, H., Ponniah, G., Zhang, H.-M., Nowak, C., Neill, A., Gonzalez-Lopez, N., et al. (2014). *In Vitro* and *In Vivo* Modifications of Recombinant and Human IgG Antibodies. *MAbs* 6, 1145–1154. doi:10.4161/mabs.29883

Lu, X., Nobrega, R. P., Lynaugh, H., Jain, T., Barlow, K., Boland, T., et al. (2018). Deamidation and Isomerization Liability Analysis of 131 Clinical-Stage Antibodies. *MAbs* 11, 45–57. doi:10.1080/19420862.2018.1548233

Lyubarskaya, Y., Houde, D., Woodard, J., Murphy, D., and Mhatre, R. (2006). Analysis of Recombinant Monoclonal Antibody Isoforms by Electrospray Ionization Mass Spectrometry as a Strategy for Streamlining Characterization of Recombinant Monoclonal Antibody Charge Heterogeneity. *Anal. Biochem.* 348, 24–39. doi:10.1016/j.ab.2005.10.003

Moon, S. K., Park, S. R., Park, A., Oh, H. M., Shin, H. J., Jeon, E. J., et al. (2016). Substitution of Heavy Complementarity Determining Region 3 (CDR-H3) Residues Can Synergistically Enhance Functional Activity of Antibody and its Binding Affinity to HER2 Antigen. *Mol. Cell* 39, 217–228. doi:10.14348/molcells.2016.2235

Schmid, I., Bonnington, L., Gerl, M., Bomans, K., Thaller, A. L., Wagner, K., et al. (2018). Assessment of Susceptible Chemical Modification Sites of Trastuzumab and Endogenous Human Immunoglobulins at Physiological Conditions. *Commun. Biol.* 1, 28. doi:10.1038/s42003-018-0032-8

Shang, Y., Mernaugh, R., and Zeng, X. (2012). Characterization of the Native and Denatured Herceptin by Enzyme Linked Immunosorbent Assay and Quartz crystal Microbalance Using a High-Affinity Single Chain Fragment Variable Recombinant Antibody. *Anal. Chem.* 84, 8164–8170. doi:10.1021/ac301235a

Smith, M. B., Reardon, J., and Olson, E. M. (2012). Pertuzumab for the Treatment of Patients with Previously Untreated HER2-Positive Metastatic Breast Cancer. *Drugs Today* 48, 713–722. doi:10.1358/dot.2012.48.11.1885879

Spanov, B., Olaleye, O., Lingg, N., Bentlage, A. E. H., Govorukhina, N., Hermans, J., et al. (2021). Change of Charge Variant Composition of Trastuzumab upon Stressing at Physiological Conditions. *J. Chromatogr. A* 1655, 462506. doi:10.1016/j.chroma.2021.462506

Vlasak, J., Bussat, M. C., Wang, S., Wagner-Rousset, E., Schaefer, M., Klinguer-Hamour, C., et al. (2009). Identification and Characterization of Asparagine Deamidation in the Light Chain CDR1 of a Humanized IgG1 Antibody. *Anal. Biochem.* 392, 145–154. doi:10.1016/j.ab.2009.05.043

Xu, J. L., and Davis, M. M. (2000). Diversity in the CDR3 Region of VH Is Sufficient for Most Antibody Specificities. *Immunity* 13, 37–45. doi:10.1016/s1074-7613(00)00006-6

Conflict of Interest: Author NM was employed by company ICON.

The remaining authors declare that the research was conducted in the absence of any commercial or financial relationships that could be construed as a potential conflict of interest.

frontiers in Chemistry

ORIGINAL RESEARCH
published: 05 January 2022
doi: 10.3389/fchem.2021.780608

Dendriplex-Impregnated Hydrogels With Programmed Release Rate

Evgeny Apartsin[1,2,3,4]*, *Alya Venyaminova*[3], *Jean-Pierre Majoral*[1,2] and *Anne-Marie Caminade*[1,2]*

[1]Laboratoire de Chimie de Coordination, CNRS, Toulouse, France, [2]LCC-CNRS, Université de Toulouse, CNRS, Toulouse, France, [3]Institute of Chemical Biology and Fundamental Medicine SB RAS, Novosibirsk, Russia, [4]Novosibirsk State University, Novosibirsk, Russia

Hydrogels are biocompatible matrices for local delivery of nucleic acids; however, functional dopants are required to provide efficient delivery into cells. In particular, dendrimers, known as robust nucleic acid carriers, can be used as dopants. Herein, we report the first example of impregnating neutral hydrogels with siRNA–dendrimer complexes. The surface chemistry of dendrimers allows adjusting the release rate of siRNA-containing complexes. This methodology can bring new materials for biomedical applications.

Keywords: dendrimers, oligonucleotides, hydrogel, polyelectrolyte complexes, controlled release

OPEN ACCESS

Edited by:
Pavel Anzenbacher, Bowling Green State University, United States

Reviewed by:
Jorge Morgado, Universidade de Lisboa, Portugal
Jean-Louis Reymond, University of Bern, Switzerland
Victoria Leiro, Universidade do Porto, Portugal

***Correspondence:**
Evgeny Apartsin
evgeny.apartsin@lcc-toulouse.fr
Anne-Marie Caminade
anne-marie.caminade@lcc-toulouse.fr

Specialty section:
This article was submitted to Supramolecular Chemistry, a section of the journal Frontiers in Chemistry

Received: *21 September 2021*
Accepted: *13 December 2021*
Published: *05 January 2022*

Citation:
Apartsin E, Venyaminova A, Majoral J-P and Caminade A-M (2022) Dendriplex-Impregnated Hydrogels With Programmed Release Rate. Front. Chem. 9:780608. doi: 10.3389/fchem.2021.780608

INTRODUCTION

Local delivery of therapeutic nucleic acids, alone (Sarett et al., 2015) or in combination with other drugs (Larsson et al., 2017), is an emerging topic in nanomedicine. To date, various approaches have been developed to deliver nucleic acid constructions locally, either into the skin (Rogers et al., 2013; Vij et al., 2017) or internal organs (Kwekkeboom et al., 2015; Xie et al., 2020). Depending on the application, a long-term treatment may be required. Therefore, materials are needed to provide a sustained drug release into tissues in contact. For instance, hydrogels are convenient matrices for local drug delivery, in particular for the delivery of therapeutic nucleic acids (Fliervoet et al., 2018). They are also frequently combined with hard or soft nanoparticles complexing nucleic acids and acting as carriers at the cellular or tissue level (Fattal et al., 2004; Wang and Burdick, 2017; Saleh et al., 2019). The choice of a carrier system is crucial as it can define the therapeutic performance of a material as well as modulate its physicochemical properties. Dendritic molecules, that is, dendrimers and dendrons, can be well suited for this purpose (Caminade, 2016; Caminade, 2017; Apartsin and Caminade, 2021).

Dendritic molecules are hyperbranched macromolecules of precisely defined molecular structure exposing numerous functional groups on the periphery. Due to the richness of the surface chemistry, dendrimers and dendrons can be functionalized with biomimetic moieties and therefore used as biocompatible carriers for both low-molecular drugs (such as anticancer chemodrugs) and macromolecular therapeutic substances (DNA, mRNA, proteins) (Hsu et al., 2017; Knauer et al., 2019; Mignani et al., 2020). Decorating the surface with cationic moieties promotes the interaction of dendrimer-based complexes (dendriplexes) or supramolecular assemblies with the cell surface inducing endocytosis. Inherent dendrimer multivalency, together with precise structure, is their advantage over other classes of macromolecular carriers. Having been applied to the nucleic acid delivery, dendrimers have shown considerable binding capacity and high efficiency for the internalization into target cells, inducing programmed therapeutic effects *in vitro* and *in vivo* (Palmerston Mendes et al., 2017; Dzmitruk et al., 2018). In particular, topical delivery of therapeutic nucleic acids into skin tissue can be achieved. Recent findings show that dendrimer-assisted topical

delivery can be accomplished even for thousand-base-long self-amplifying RNA (Saviano et al., 2020), opening new opportunities for dendrimers in nanomedicine.

Due to the presence of multiple functional groups on the surface, dendrimers can be used as cross-linking moieties to develop dense hydrogel networks (Nummelin et al., 2015; Hodgson et al., 2017; Wang et al., 2017). Dendrimer-containing hydrogels can be loaded with bioactive compounds and show good therapeutic activity upon topical application (Conde et al., 2016; Wang et al., 2016; Xu et al., 2017). These hydrogels have been shown to possess functional performance similar to commercially available hydrogel species (Villa-Camacho et al., 2015).

The synergistic combination of two methodologies, namely, dendrimer-mediated nucleic acid delivery and hydrogel-based local drug delivery, can yield highly biocompatible materials for the long-term local delivery of therapeutic nucleic acids into target tissues. Conceptually, the hydrogel scaffold is to bring biocompatibility or bioresorption and to regulate the rate of drug release, whereas the dendrimer is to provide highly efficient and specific delivery of nucleic acid therapeutics into cells that are in contact with a biomaterial. However, no such system has been reported yet.

Herein, we report a proof-of-concept study in preparing neutral hydrogel scaffolds impregnated with nanoscale polyelectrolyte complexes of therapeutic nucleic acids and polycationic dendrimers. We hypothesized that the entrapment of complexes into a hydrogel network will result in their long-term release. That would be highly useful for the design of biomaterials for local drug delivery.

MATERIALS AND METHODS

Polycationic phosphorus dendrimers were synthesized according to previously published procedures (Ihnatsyeu-Kachan et al., 2017; Apartsin et al., 2018). Mcl-1 siRNA (sense strand: 5′-GGACUUUUAUACCUGUUAUtt-3′-FAM; antisense strand: 5′-AUAACAGGUAUAAAAGUCCtg; lowercase letters denote deoxyribonucleotides) was synthesized and annealed as described in Krasheninina et al. (2019).

Dendriplexes Formation

Dendriplexes were formed by siRNA and dendrimers in an RNase-free PBS buffer (10 mM phosphate buffer, pH 7.4, 137 mM NaCl, 2.7 mM KCl), followed by incubation for 10 min at 25°C. The dendrimer-to-siRNA charge ratio (i.e., the excess of cations over anions) was calculated as follows:

$$CR = \frac{N_+ C_D}{N_- C_{siRNA}},$$

where CR is the charge ratio; $N_+ = 48$ is the number of cations per dendrimer molecule; $N_- = 40$ is the number of anions per siRNA molecule; C_D is the dendrimer concentration; and C_{siRNA} is the siRNA concentration in a sample.

Gel Retardation Assay

The ability of the cationic dendrimers to form complexes with siRNAs was studied by gel electrophoresis in 1% agarose gel. Dendriplexes were prepared by mixing siRNA (40 pmol per sample), ethidium bromide (EB) (0.4 μM, ~1 EB molecule per 2 bp of siRNA), and dendrimers (at increasing concentrations depending on the charge ratios) and dissolved in PBS. After 15-min incubation at 25°C, electrophoresis was carried out in 1% agarose gel at 80 V (Mini-Sub® Cell GT, Bio-Rad, United States) in TBE buffer (89 mM Tris–borate, pH 8.4, 10 mM Na_2EDTA), and the bands were visualized under a UV using gel documentation system (Helicon, Russia).

Fluorescence Polarization

Mcl-1 siRNA (1 μM) in PBS (30 μL) was placed in wells of a black Costar 96 half-area microplate (Costar, United States). A solution of dendrimer AG3, TG3, or PG3 was added gradually to achieve the desired charge ratio from 0.25 to 5. In a control experiment, water was added, instead of dendrimer solution. After each addition, solutions were mixed by pipetting and incubated for 5 min; then fluorescence polarization values were read using a microplate reader (BMG Labtech, Germany). The experiments were performed in triplicate, and results were presented as mean ± S.D.

Atomic Force Microscopy

An aliquot of dendriplex solution was dropped on a mica slide for 1–2 min. The slide was then washed 3 times with deionized water and air-dried. Scanning was performed in the tapping mode using a Multimode 8 atomic force microscope (Bruker) with NSG10_DLC cantilevers with a tip curvature radius of 1–3 nm (NT-MDT, Russia) at a scanning rate of 3 Hz. Images were processed using Gwyddion 2.36 software.

Hydrogel Impregnation and Dendriplex Release

Dendriplexes were formed by mixing Mcl-1 siRNA (100 μM) and dendrimers (AG3, TG3, PG3 or mixtures AG3/TG3, AG3/PG3) at dendrimer-to-siRNA charge ratio of 5 in 15 μL PBS, followed by incubation for 15 min at 25°C. Then, 10 μL of a dendriplex solution was added to 40 μL of hot 2% agarose solution in PBS. When the solution cooled down to room temperature and hydrogel was formed, 100 μL of PBS was added, and the gel was gently shaken at 25°C. 5 μL aliquots were taken at 0, 10, 20, 30 min, 1, 2, 3, 16, and 24 h of incubation; diluted in 30 μL of PBS; and transferred into wells of a black Costar 96 half-area microplate (Costar, United States); fluorescence intensity and fluorescence polarization values were read using a microplate reader (BMG Labtech, Germany). The remaining 5 μL dendriplex solution was treated in the same way and used as a control. The experiments were performed in triplicate, and the results were represented as mean ± S.D. To fit release values in kinetic profiles, the exponential model was used. Fitting was considered satisfactory if $r^2 > 0.95$.

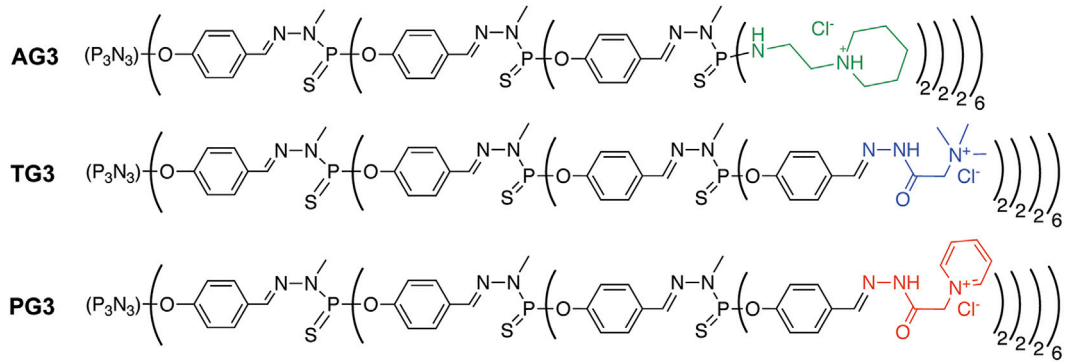

FIGURE 1 | Structures of polycationic phosphorus dendrimers used for preparing dendriplexes.

RESULTS AND DISCUSSION

Choosing a matrix for a hydrogel network, we were looking for a neutral compound, either biomimetic or of biological origin, able to form hydrogels with pores of 100–200 nm diameter (comparable to sizes of polyelectrolyte complexes). For instance, agarose is a good candidate, for it is a cheap mass produced biocompatible polymer forming soft bioresorbable physical hydrogels (Zarrintaj et al., 2018). The mean pore diameter in agarose hydrogels can be simply controlled by the agarose percentage (Pluen et al., 1999; Narayanan et al., 2006).

As a bioactive cargo, we have chosen small interfering RNA (siRNA) Mcl-1 possessing anticancer activity. This siRNA activates programmed cell death by suppressing the expression of one of the antiapoptotic proteins of the Bcl-2 family regulating the mitochondrial apoptosis pathway (Chetoui et al., 2008; Guoan et al., 2010; Krasheninina et al., 2019).

As carriers, we have chosen phosphorus dendrimers bearing cationic groups on the periphery. Phosphorus dendrimers are widely used as nanodrugs *per se* (Hayder et al., 2011; Caminade et al., 2015) and as carriers for low-molecular and macromolecular bioactive compounds. For instance, polycationic phosphorus dendrimers of high generations are versatile carriers for intracellular delivery of nucleic acid constructions such as siRNA (Ferenc et al., 2013; Ionov et al., 2015; Dzmitruk et al., 2015; Bohr et al., 2017; Deriu et al., 2018; Ihnatsyeu-Kachan et al., 2017) or plasmid DNA (Loup et al., 1999; Padié et al., 2009). Herein, we have used three types of dendrimers of generation 3 bearing 48 surface groups each: piperidinium chloride (AG3), trimethylammonium chloride acetohydrazone (Girard reagent T; TG3), and pyridinium chloride acetohydrazone (Girard reagent P; PG3). The structures of dendrimers are given in **Figure 1**. Dendrimers TG3 and PG3 can form hydrogels through multiple hydrogen bonds between branches, with biomimetic additives facilitating the gelation (Marmillon et al., 2001; Apartsin et al., 2018). Such dendrimer hydrogels were able to bind oligonucleotides reversibly. Dendrimer AG3, though unable to form hydrogels, has been shown to provide highly efficient delivery of anticancer siRNAs into tumor cells inducing apoptosis (Ihnatsyeu-Kachan et al., 2017).

As dendrimers bind siRNAs by means of electrostatic interactions, the dendrimer-to-siRNA charge ratio strongly matters. To find a ratio, where siRNA is mostly bound, we mixed it with three cationic dendrimers at different ratios and analyzed the complexes formed by means of agarose gel electrophoresis upon visualization with ethidium bromide (**Supplementary Figure S1**).We observed no band of free siRNA at the cation excess >3 for AG3, and at the cation excess >2 for PG3 and TG3. This difference can be explained by the presence of hydrophilic hydrazone moieties on the surface of PG3 and TG3 dendrimers, which makes peripheral cations more available to the complexation with oligonucleotides. To evaluate how strongly dendrimers bind siRNA, we measured the fluorescence polarization of 3′-fluorescein–labeled siRNA upon complexing with AG3, PG3, and TG3. Fluorescence polarization assay is sensitive to hindering of the fluorophore rotation in an oligonucleotide upon complexation and thus gives information about the strength of the siRNA complexation. The fluorescence polarization values grew upon the cation excess reaching a plateau at the ratio > 3 (**Supplementary Figure S2**) as it is supposed to (Szewczyk et al., 2012; Conti et al., 2014). However, in the case of AG3- and TG3-containing complexes, the siRNA binding leads to the ~2.8-fold increase in polarization, whereas in PG3-containing complexes, >6-fold increase was observed. The most likely reason for such a difference is the difference in the geometry of peripheral cations and their availability for the interaction with the sugar–phosphate backbone (Deriu et al., 2018). Furthermore, hydrophobic interactions between siRNA and dendrimers should be taken into account, for they are known to contribute to the complexation along with electrostatic interactions (Slita et al., 2007; Filippov et al., 2010). To work with dendriplexes, where siRNA is fully saturated with dendrimers, we have used the 5-fold cation excess for further experiments.

To estimate the size of dendriplexes, we did AFM of samples just after adsorption on a mica slide. This allowed us to visualize dendriplexes, though not in their native form as in solution, but not dehydrated either. Observed particles were round, and their mean size was 100 nm (**Figure 2**). The composition of dendriplexes did not significantly change their size, even when mixtures of dendrimers at different proportions were used to form dendriplexes (see below). Size values obtained by DLS measurements (**Supplementary Figure S3**) were in good agreement with the AFM data.

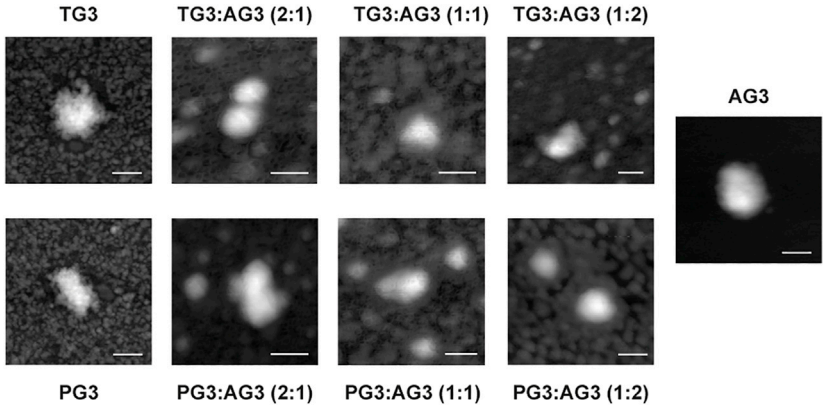

FIGURE 2 | Representative AFM images of dendriplexes. Charge ratio 5. Scale bar is 100 nm.

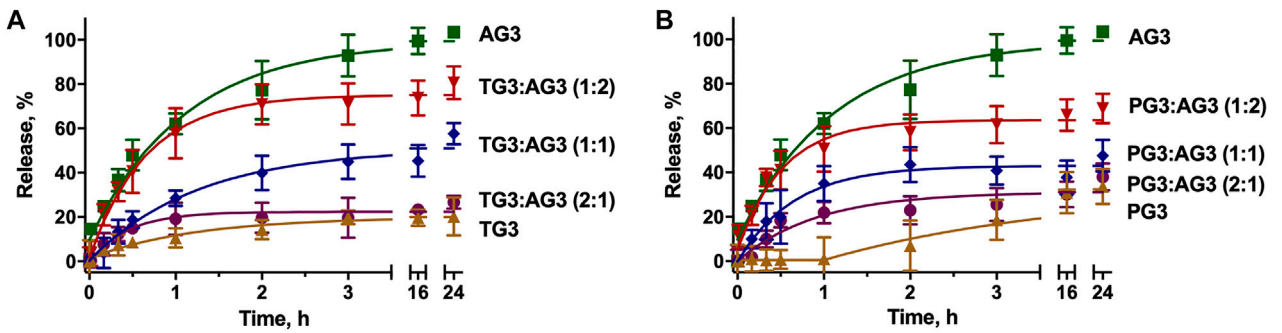

FIGURE 3 | Kinetic profiles of dendriplexes release from the agarose gel. Dendriplexes contain either AG3 and TG3 **(A)** or AG3 and PG3 **(B)** in different ratios. Charge ratio 5.

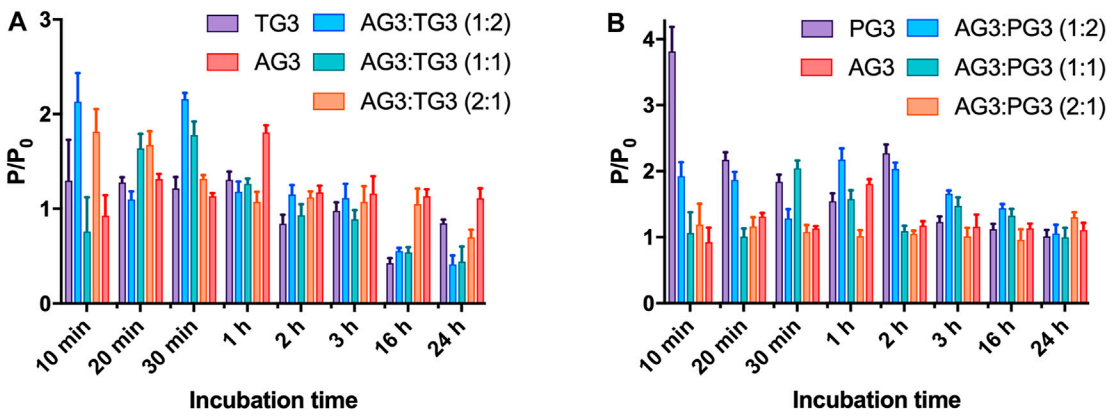

FIGURE 4 | Evolution of fluorescence polarization of siRNA upon release of dendriplexes from the agarose gel. Dendriplexes contain either AG3 and TG3 **(A)** or AG3 and PG3 **(B)**. The ratio P/P_0 represents the ratio of fluorescence polarization values in a sample (P) and that of free siRNA (P_0). Charge ratio 5.

To impregnate dendriplexes into a hydrogel network, we added them to hot 2% agarose solution prior to gelation. Cooling down, agarose forms a physical gel entrapping dendriplexes in its pores. We then incubated dendriplex-containing hydrogels in a buffer following the release of siRNA by measuring the fluorescence acquisition in eluates. We considered the size of dendriplexes to be smaller than the pore diameter in 1% agarose hydrogel network [100–350 nm (Viovy, 2000; Stellwagen, 2009)], so dendriplexes cannot be physically retained in a hydrogel. We therefore expected that the release rate would be defined mostly by the diffusion of

complexes from the hydrogel. Dendriplexes containing AG3 behaved exactly as we predicted: burst release was observed with >90% release being achieved in 3 h. However, surprisingly, dendriplexes containing TG3 and PG3 were released quite poorly; the 50% release was not achieved even after 24-h incubation (**Figure 3**). We hypothesized that such effects arise from the differences in the chemical structure of dendrimer periphery as apart from that, the dendriplexes were identical. Indeed, dendrimers TG3 and PG3 expose multiple hydrazone moieties on the periphery that can form hydrogen bonds with the hydrogel scaffold. This is a likely reason why these dendriplexes are retained in a hydrogel. With this in mind, we have impregnated hydrogels with dendriplexes containing mixtures AG3:TG3 and AG3:PG3 and studied the siRNA release (**Figure 3**). We have found that the ratio AG3/TG3 or AG3/PG3 in a dendriplex strongly affects both the rate and completeness of release. The increase in the hydrazone-terminated dendrimer content up to 1/3 does not affect the release rate within the first hour of incubation; however, the increase in the content up to 50% slows the release within the whole 24-h observation span. Interestingly, the profile of release of the PG3-containing dendriplex has a considerable delay in the first hour of incubation. Given that the TG3 dendriplex does not exhibit this delay, we suppose that this phenomenon originates rather from differences in the character of siRNA complexation between TG3 and PG3, as observed in the fluorescence polarization profiles (see above).Whereas fluorescence intensity in samples (**Figure 3**) represents the overall release of siRNA from the hydrogel, fluorescence polarization (**Figure 4**) shows the degree of siRNA complexation: the higher the polarization value, the stronger is the siRNA bound to dendriplexes. Basing on the evolution of the fluorescence polarization in samples over time, we suggest that siRNA is released from the hydrogel in the form of dendriplexes. The effects of PG3-containing dendriplexes are more pronounced in comparison with TG3 ones, which agrees with the strength of siRNA complexation by these dendrimers (**Supplementary Figure S2**). This finding is important as complexation with dendrimers is known to stimulate the cellular uptake of oligonucleotides. Given that endocytosis is quite a quick process, with multiple endocytosis events occurring in a cell in a few-minutes span (Liang et al., 2017), we can assume that released dendriplexes could be endocytosed shortly after release from a hydrogel, before they could decompose.

Thus, varying the content of dendrimers in complexes, we can modulate the speed of their elution from hydrogels. This feature can be used for the precise design of a material for a given biomedical task. For instance, agarose gels are considered prospective biomaterials for the regeneration of cartilage and brain implants (Lecomte et al., 2018; Choi et al., 2020; Salati et al., 2020). Being in contact with tissues, agarose hydrogels undergo bioresorption (Rousselle et al., 2019). This would lead to the degradation of the hydrogel network, driving the release of dendriplexes still retained in a gel network, as it has been shown for cationic silica nanoparticles (Wang et al., 2015). This option can be useful for the sustained release of small quantities of regulatory nucleic acids (siRNA or microRNA). For instance, this technique can be used to achieve long-term local tumor treatment (Han et al., 2011), to improve wound healing (Saleh et al., 2019; Berger et al., 2021), or to suppress local inflammatory reaction (Zhou et al., 2018), which can occur in the proximity of an implant.

CONCLUSION

In summary, we have reported the first example of a neutral biocompatible agarose hydrogel impregnated with polyelectrolyte complexes of siRNA with polycationic phosphorus dendrimers. The anchoring of complexes in a gel is due to the formation of numerous hydrogen bonds between cationic moieties on the periphery of dendrimers and the hydrogel scaffold. Changing the content of different dendrimer species in complexes, we have found an easy way to control the rate of release of complexes from a hydrogel. We believe this methodology can be useful for the development of functional hydrogels as local drug delivery systems and tissue engineering tools.

DATA AVAILABILITY STATEMENT

The raw data supporting the conclusions of this article will be made available by the authors, without undue reservation.

AUTHOR CONTRIBUTIONS

EA, AV, J-PM, and A-MC contributed to the conception and design of the study. EA performed the experiments. EA and A-MC interpreted the data. EA wrote the first draft of the manuscript. AV, J-PM, and A-MC revised the manuscript. All authors contributed to manuscript revision, read, and approved the submitted version.

FUNDING

The project has received funding from the European Union's Horizon 2020 research and innovation program under the Marie Sklodowska-Curie grant agreement No 844217. This article is based on work from COST Action CA 17140 "Cancer Nanomedicine from the Bench to the Bedside" supported by the COST (European Cooperation in Science and Technology). The financial support from the CNRS is also appreciated.

ACKNOWLEDGMENTS

The authors thank Mariya Meschaninova (ICBFM) for the synthesis of oligoribonucleotides.

SUPPLEMENTARY MATERIAL

The Supplementary Material for this article can be found online at: https://www.frontiersin.org/articles/10.3389/fchem.2021.780608/full#supplementary-material

REFERENCES

Apartsin, E., and Caminade, A. M. (2021). *Supramolecular Self-Associations of Amphiphilic Dendrons and Their Properties*. Chemistry European Journal. doi:10.1002/chem.202102589

Apartsin, E. K., Grigoryeva, A. E., Malrin-Fournol, A., Ryabchikova, E. I., Venyaminova, A. G., Mignani, S., et al. (2018). Hydrogels of Polycationic Acetohydrazone-Modified Phosphorus Dendrimers for Biomedical Applications: Gelation Studies and Nucleic Acid Loading. *Pharmaceutics* 10, 120. doi:10.3390/pharmaceutics10030120

Berger, A. G., Chou, J. J., and Hammond, P. T. (2021). Approaches to Modulate the Chronic Wound Environment Using Localized Nucleic Acid Delivery. *Adv. Wound Care* 10, 503–528. doi:10.1089/wound.2020.1167

Bohr, A., Tsapis, N., Andreana, I., Chamarat, A., Foged, C., Delomenie, C., et al. (2017). Anti-Inflammatory Effect of Anti-TNF-α SiRNA Cationic Phosphorus Dendrimer Nanocomplexes Administered Intranasally in a Murine Acute Lung Injury Model. *Biomacromolecules* 18, 2379–2388. doi:10.1021/acs.biomac.7b00572

Caminade, A.-M., Fruchon, S., Turrin, C.-O., Poupot, M., Ouali, A., Maraval, A., et al. (2015). The Key Role of the Scaffold on the Efficiency of Dendrimer Nanodrugs. *Nat. Commun.* 6, 7722. doi:10.1038/ncomms8722

Caminade, A.-M. (2016). Inorganic Dendrimers: Recent Advances for Catalysis, Nanomaterials, and Nanomedicine. *Chem. Soc. Rev.* 45, 5174–5186. doi:10.1039/C6CS00074F

Caminade, A.-M. (2017). Phosphorus Dendrimers for Nanomedicine. *Chem. Commun.* 53, 9830–9838. doi:10.1039/C7CC04949H

Chetoui, N., Sylla, K., Gagnon-Houde, J.-V., Alcaide-Loridan, C., Charron, D., Al-Daccak, R., et al. (2008). Down-Regulation of Mcl-1 by Small Interfering RNA Sensitizes Resistant Melanoma Cells to Fas-Mediated Apoptosis. *Mol. Cancer Res.* 6, 42–52. doi:10.1158/1541-7786.MCR-07-0080

Choi, J. H., Kim, J. S., Kim, W. K., Lee, W., Kim, N., Song, C. U., et al. (2020). Evaluation of Hyaluronic Acid/Agarose Hydrogel for Cartilage Tissue Engineering Biomaterial. *Macromol. Res.* 28, 979–985. doi:10.1007/s13233-020-8137-6

Conde, J., Oliva, N., Atilano, M., Song, H. S., and Artzi, N. (2016). Self-assembled RNA-Triple-helix Hydrogel Scaffold for microRNA Modulation in the Tumour Microenvironment. *Nat. Mater* 15, 353–363. doi:10.1038/nmat4497

Conti, D. S., Brewer, D., Grashik, J., Avasarala, S., and Da Rocha, S. R. P. (2014). Poly(amidoamine) Dendrimer Nanocarriers and Their Aerosol Formulations for siRNA Delivery to the Lung Epithelium. *Mol. Pharmaceutics* 11, 1808–1822. doi:10.1021/mp4006358

Deriu, M. A., Tsapis, N., Noiray, M., Grasso, G., El Brahmi, N., Mignani, S., et al. (2018). Elucidating the Role of Surface Chemistry on Cationic Phosphorus Dendrimer-siRNA Complexation. *Nanoscale* 10, 10952–10962. doi:10.1039/C8NR01928B

Dzmitruk, V., Apartsin, E., Ihnatsyeu-Kachan, A., Abashkin, V., Shcharbin, D., and Bryszewska, M. (2018). Dendrimers Show Promise for siRNA and microRNA Therapeutics. *Pharmaceutics* 10, 126. doi:10.3390/pharmaceutics10030126

Dzmitruk, V., Szulc, A., Shcharbin, D., Janaszewska, A., Shcharbina, N., Lazniewska, J., et al. (2015). Anticancer siRNA Cocktails as a Novel Tool to Treat Cancer Cells. Part (B). Efficiency of Pharmacological Action. *Int. J. Pharmaceutics* 485, 288–294. doi:10.1016/j.ijpharm.2015.03.034

Fattal, E., De Rosa, G., and Bochot, A. (2004). Gel and Solid Matrix Systems for the Controlled Delivery of Drug Carrier-Associated Nucleic Acids. *Int. J. Pharmaceutics* 277, 25–30. doi:10.1016/j.ijpharm.2003.01.002

Ferenc, M., Pedziwiatr-Werbicka, E., Nowak, K., Klajnert, B., Majoral, J.-P., and Bryszewska, M. (2013). Phosphorus Dendrimers as Carriers of siRNA-Characterisation of Dendriplexes. *Molecules* 18, 4451–4466. doi:10.3390/molecules18044451

Filippov, S. K., Koňák, Č., Kopečková, P., Starovoytova, L., Špírková, M., and Štěpánek, P. (2010). Effect of Hydrophobic Interactions on Properties and Stability of DNA−Polyelectrolyte Complexes. *Langmuir* 26, 4999–5006. doi:10.1021/la9036716

Fliervoet, L. A. L., Engbersen, J. F. J., Schiffelers, R. M., Hennink, W. E., and Vermonden, T. (2018). Polymers and Hydrogels for Local Nucleic Acid Delivery. *J. Mater. Chem. B* 6, 5651–5670. doi:10.1039/C8TB01795F

Guoan, X., Hanning, W., Kaiyun, C., and Hao, L. (2010). Adenovirus-mediated siRNA Targeting Mcl-1 Gene Increases Radiosensitivity of Pancreatic Carcinoma Cells *In Vitro* and *In Vivo*. *Surgery* 147, 553–561. doi:10.1016/j.surg.2009.10.033

Han, H. D., Mora, E. M., Roh, J. W., Nishimura, M., Lee, S. J., Stone, R. L., et al. (2011). Chitosan Hydrogel for Localized Gene Silencing. *Cancer Biol. Ther.* 11, 839–845. doi:10.4161/cbt.11.9.15185

Hayder, M., Poupot, M., Baron, M., Nigon, D., Turrin, C.-O., Caminade, A.-M., et al. (2011). A Phosphorus-Based Dendrimer Targets Inflammation and Osteoclastogenesis in Experimental Arthritis. *Sci. Transl. Med.* 3, 81ra35. doi:10.1126/scitranslmed.3002212

Hodgson, S. M., McNelles, S. A., Abdullahu, L., Marozas, I. A., Anseth, K. S., and Adronov, A. (2017). Reproducible Dendronized PEG Hydrogels via SPAAC Cross-Linking. *Biomacromolecules* 18, 4054–4059. doi:10.1021/acs.biomac.7b01115

Hsu, H. J., Bugno, J., Lee, S. r., and Hong, S. (2017). Dendrimer-based Nanocarriers: a Versatile Platform for Drug Delivery. *WIREs Nanomed Nanobiotechnol* 9, e1409. doi:10.1002/wnan.1409

Ihnatsyeu-Kachan, A., Dzmitruk, V., Apartsin, E., Krasheninina, O., Ionov, M., Loznikova, S., et al. (2017). Multi-Target Inhibition of Cancer Cell Growth by SiRNA Cocktails and 5-Fluorouracil Using Effective Piperidine-Terminated Phosphorus Dendrimers. *Colloids Inter.* 1, 6. doi:10.3390/colloids1010006

Ionov, M., Lazniewska, J., Dzmitruk, V., Halets, I., Loznikova, S., Novopashina, D., et al. (2015). Anticancer siRNA Cocktails as a Novel Tool to Treat Cancer Cells. Part (A). Mechanisms of Interaction. *Int. J. Pharmaceutics* 485, 261–269. doi:10.1016/j.ijpharm.2015.03.024

Knauer, N., Pashkina, E., and Apartsin, E. (2019). Topological Aspects of the Design of Nanocarriers for Therapeutic Peptides and Proteins. *Pharmaceutics* 11, 91. doi:10.3390/pharmaceutics11020091

Krasheninina, O., Apartsin, E., Fuentes, E., Szulc, A., Ionov, M., Venyaminova, A., et al. (2019). Complexes of Pro-apoptotic siRNAs and Carbosilane Dendrimers: Formation and Effect on Cancer Cells. *Pharmaceutics* 11, 25. doi:10.3390/pharmaceutics11010025

Kwekkeboom, R. F. J., Lei, Z., Bogaards, S. J. P., Aiazian, E., Kamp, O., Paulus, W. J., et al. (2015). Ultrasound and Microbubble-Induced Local Delivery of MicroRNA-Based Therapeutics. *Ultrasound Med. Biol.* 41, 163–176. doi:10.1016/j.ultrasmedbio.2014.08.012

Larsson, M., Huang, W.-T., Liu, D.-M., and Losic, D. (2017). Local Co-administration of Gene-Silencing RNA and Drugs in Cancer Therapy: State-Of-The Art and Therapeutic Potential. *Cancer Treat. Rev.* 55, 128–135. doi:10.1016/j.ctrv.2017.03.004

Lecomte, A., Descamps, E., and Bergaud, C. (2018). A Review on Mechanical Considerations for Chronically-Implanted Neural Probes. *J. Neural Eng.* 15, 031001. doi:10.1088/1741-2552/aa8b4f

Liang, K., Wei, L., and Chen, L. (2017). Exocytosis, Endocytosis, and Their Coupling in Excitable Cells. *Front. Mol. Neurosci.* 10, 109. doi:10.3389/fnmol.2017.00109

Loup, C., Zanta, M.-A., Caminade, A.-M., Majoral, J.-P., and Meunier, B. (1999). Preparation of Water-Soluble Cationic Phosphorus-Containing Dendrimers as DNA Transfecting Agents. *Chem. Eur. J.* 5, 3644–3650. doi:10.1002/(SICI)1521-3765(19991203)5:12<3644:AID-CHEM3644>3.0

Marmillon, C., Gauffre, F., Gulik-Krzywicki, T., Loup, C., Caminade, A.-M., Majoral, J.-P., et al. (2001). Organophosphorus Dendrimers as New Gelators for Hydrogels. *Angew. Chem. Int. Ed.* 40, 2626–2629. doi:10.1002/1521-3773(20010716)40:14<2626:AID-ANIE2626>3.0

Mignani, S., Shi, X., Ceña, V., and Majoral, J.-P. (2020). Dendrimer- and Polymeric Nanoparticle-Aptamer Bioconjugates as Nonviral Delivery Systems: a New Approach in Medicine. *Drug Discov. Today* 25, 1065–1073. doi:10.1016/j.drudis.2020.03.009

Narayanan, J., Xiong, J.-Y., and Liu, X.-Y. (2006). Determination of Agarose Gel Pore Size: Absorbance Measurements Vis a Vis Other Techniques. *J. Phys. Conf. Ser.* 28, 83–86. doi:10.1088/1742-6596/28/1/017

Nummelin, S., Liljeström, V., Saarikoski, E., Ropponen, J., Nykänen, A., Linko, V., et al. (2015). Self-Assembly of Amphiphilic Janus Dendrimers into Mechanically Robust Supramolecular Hydrogels for Sustained Drug Release. *Chem. Eur. J.* 21, 14433–14439. doi:10.1002/chem.201501812

Padié, C., Maszewska, M., Majchrzak, K., Nawrot, B., Caminade, A.-M., and Majoral, J.-P. (2009). Polycationic Phosphorus Dendrimers: Synthesis,

Characterization, Study of Cytotoxicity, Complexation of DNA, and Transfection Experiments. *New J. Chem.* 33, 318–326. doi:10.1039/B815259D

Palmerston Mendes, L., Pan, J., and Torchilin, V. (2017). Dendrimers as Nanocarriers for Nucleic Acid and Drug Delivery in Cancer Therapy. *Molecules* 22, 1401. doi:10.3390/molecules22091401

Pluen, A., Netti, P. A., Jain, R. K., and Berk, D. A. (1999). Diffusion of Macromolecules in Agarose Gels: Comparison of Linear and Globular Configurations. *Biophysical J.* 77, 542–552. doi:10.1016/S0006-3495(99)76911-0

Rogers, F. A., Hu, R.-H., and Milstone, L. M. (2013). Local Delivery of Gene-Modifying Triplex-Forming Molecules to the Epidermis. *J. Invest. Dermatol.* 133, 685–691. doi:10.1038/jid.2012.351

Rousselle, S. D., Ramot, Y., Nyska, A., and Jackson, N. D. (2019). Pathology of Bioabsorbable Implants in Preclinical Studies. *Toxicol. Pathol.* 47, 358–378. doi:10.1177/0192623318816681

Salati, M. A., Khazai, J., Tahmuri, A. M., Samadi, A., Taghizadeh, A., Taghizadeh, M., et al. (2020). Agarose-Based Biomaterials: Opportunities and Challenges in Cartilage Tissue Engineering. *Polymers* 12, 1150. doi:10.3390/polym12051150

Saleh, B., Dhaliwal, H. K., Portillo-Lara, R., Shirzaei Sani, E., Abdi, R., Amiji, M. M., et al. (2019). Local Immunomodulation Using an Adhesive Hydrogel Loaded with miRNA-Laden Nanoparticles Promotes Wound Healing. *Small* 15, 1902232. doi:10.1002/smll.201902232

Sarett, S. M., Nelson, C. E., and Duvall, C. L. (2015). Technologies for Controlled, Local Delivery of siRNA. *J. Controlled Release* 218, 94–113. doi:10.1016/j.jconrel.2015.09.066

Saviano, F., Lovato, T., Russo, A., Russo, G., Bouton, C. R., Shattock, R. J., et al. (2020). Ornithine-derived Oligomers and Dendrimers for *In Vitro* Delivery of DNA and *Ex Vivo* Transfection of Skin Cells via saRNA. *J. Mater. Chem. B* 8, 4940–4949. doi:10.1039/D0TB00942C

Slita, A. V., Kasyanenko, N. A., Nazarova, O. V., Gavrilova, I. I., Eropkina, E. M., Sirotkin, A. K., et al. (2007). DNA-polycation Complexes Effect of Polycation Structure on Physico-Chemical and Biological Properties. *J. Biotechnol.* 127, 679–693. doi:10.1016/j.jbiotec.2006.07.016

Stellwagen, N. C. (2009). Electrophoresis of DNA in Agarose Gels, Polyacrylamide Gels and in Free Solution. *Electrophoresis* 30 (Suppl. 1), S188–S195. doi:10.1002/elps.200900052

Szewczyk, M., Drzewinska, J., Dzmitruk, V., Shcharbin, D., Klajnert, B., Appelhans, D., et al. (2012). Stability of Dendriplexes Formed by Anti-HIV Genetic Material and Poly(propylene Imine) Dendrimers in the Presence of Glucosaminoglycans. *J. Phys. Chem. B* 116, 14525–14532. doi:10.1021/jp304449v

Vij, M., Alam, S., Gupta, N., Gotherwal, V., Gautam, H., Ansari, K. M., et al. (2017). Non-invasive Oil-Based Method to Increase Topical Delivery of Nucleic Acids to Skin. *Mol. Ther.* 25, 1342–1352. doi:10.1016/j.ymthe.2017.03.009

Villa-Camacho, J. C., Ghobril, C., Anez-Bustillos, L., Grinstaff, M. W., Rodríguez, E. K., and Nazarian, A. (2015). The Efficacy of a Lysine-Based Dendritic Hydrogel Does Not Differ from Those of Commercially Available Tissue Sealants and Adhesives: an *Ex Vivo* Study. *BMC Musculoskelet. Disord.* 16, 116. doi:10.1186/s12891-015-0573-7

Viovy, J.-L. (2000). Electrophoresis of DNA and Other Polyelectrolytes: Physical Mechanisms. *Rev. Mod. Phys.* 72, 813–872. doi:10.1103/RevModPhys.72.813

Wang, C., Wang, X., Dong, K., Luo, J., Zhang, Q., and Cheng, Y. (2016). Injectable and Responsively Degradable Hydrogel for Personalized Photothermal Therapy. *Biomaterials* 104, 129–137. doi:10.1016/j.biomaterials.2016.07.013

Wang, J., He, H., Cooper, R. C., and Yang, H. (2017). In Situ-Forming Polyamidoamine Dendrimer Hydrogels with Tunable Properties Prepared via Aza-Michael Addition Reaction. *ACS Appl. Mater. Inter.* 9, 10494–10503. doi:10.1021/acsami.7b00221

Wang, L. L., and Burdick, J. A. (2017). Engineered Hydrogels for Local and Sustained Delivery of RNA-Interference Therapies. *Adv. Healthc. Mater.* 6, 1601041. doi:10.1002/adhm.201601041

Wang, X., Hélary, C., and Coradin, T. (2015). Local and Sustained Gene Delivery in Silica-Collagen Nanocomposites. *ACS Appl. Mater. Inter.* 7, 2503–2511. doi:10.1021/am507389q

Xie, Y., Hang, Y., Wang, Y., Sleightholm, R., Prajapati, D. R., Bader, J., et al. (2020). Stromal Modulation and Treatment of Metastatic Pancreatic Cancer with Local Intraperitoneal Triple miRNA/siRNA Nanotherapy. *ACS Nano* 14, 255–271. doi:10.1021/acsnano.9b03978

Xu, L., Cooper, R. C., Wang, J., Yeudall, W. A., and Yang, H. (2017). Synthesis and Application of Injectable Bioorthogonal Dendrimer Hydrogels for Local Drug Delivery. *ACS Biomater. Sci. Eng.* 3, 1641–1653. doi:10.1021/acsbiomaterials.7b00166

Zarrintaj, P., Manouchehri, S., Ahmadi, Z., Saeb, M. R., Urbanska, A. M., Kaplan, D. L., et al. (2018). Agarose-based Biomaterials for Tissue Engineering. *Carbohydr. Polym.* 187, 66–84. doi:10.1016/j.carbpol.2018.01.060

Zhou, Y. L., Yang, Q. Q., Yan, Y. Y., Zhu, C., Zhang, L., and Tang, J. B. (2018). Localized Delivery of miRNAs Targets Cyclooxygenases and Reduces Flexor Tendon Adhesions. *Acta Biomater.* 70, 237–248. doi:10.1016/j.actbio.2018.01.047

Conflict of Interest: The authors declare that the research was conducted in the absence of any commercial or financial relationships that could be construed as a potential conflict of interest.

Publisher's Note: All claims expressed in this article are solely those of the authors and do not necessarily represent those of their affiliated organizations, or those of the publisher, the editors, and the reviewers. Any product that may be evaluated in this article, or claim that may be made by its manufacturer, is not guaranteed or endorsed by the publisher.

frontiers in Chemistry

MINI REVIEW
published: 10 January 2022
doi: 10.3389/fchem.2021.810029

Perfluorocarbon Emulsion Contrast Agents: A Mini Review

Ryan Holman[1], Orane Lorton[1], Pauline C. Guillemin[1], Stéphane Desgranges[2], Christiane Contino-Pépin[2] and Rares Salomir[1,3]*

[1]Image Guided Interventions Laboratory (GR-949), Faculty of Medicine, University of Geneva, Geneva, Switzerland, [2]University of Avignon, CBSA-IBMM, (UMR5247), Avignon, France, [3]Radiology Department, University Hospitals of Geneva, Geneva, Switzerland

Perfluorocarbon emulsions offer a variety of applications in medical imaging. The substances can be useful for most radiological imaging modalities; including, magnetic resonance imaging, ultrasonography, computed tomography, and positron emission tomography. Recently, the substance has gained much interest for theranostics, with both imaging and therapeutic potential. As MRI sequences improve and more widespread access to ^{19}F-MRI coils become available, perfluorocarbon emulsions have great potential for new commercial imaging agents, due to high fluorine content and previous regulatory approval as antihypoxants and blood substitutes. This mini review aims to discuss the chemistry and physics of these contrast agents, in addition to highlighting some of the past, recent, and potential applications.

Keywords: contrast agents, emulsions, perfluorocarbons, fluorine chemistry, radiology

OPEN ACCESS

Edited by:
Nicole J. Jaffrezic-Renault, Université Claude Bernard Lyon 1, France

Reviewed by:
Yohann Corvis, Université de Paris, France

****Correspondence:***
Ryan Holman
Ryan.Holman@unige.edu

Specialty section:
This article was submitted to Medicinal and Pharmaceutical Chemistry, a section of the journal Frontiers in Chemistry

Received: *05 November 2021*
Accepted: *09 December 2021*
Published: *10 January 2022*

Citation:
Holman R, Lorton O, Guillemin PC, Desgranges S, Contino-Pépin C and Salomir R (2022) Perfluorocarbon Emulsion Contrast Agents: A Mini Review. Front. Chem. 9:810029. doi: 10.3389/fchem.2021.810029

INTRODUCTION

Typical radiological contrast agents are generally iodinated substances for computed tomography (CT) and are gadolinium-based substances for magnetic resonance imaging (MRI). Liquid perfluorocarbon emulsions have been well studied as a diagnostic contrast agent, but has not received regulatory approval for routine clinical use as an intravenous contrast agent by the United States Food and Drug Administration (FDA) or the European Medicines Agency (EMA).

Liquid and gaseous perfluorocarbons have been used in commercial imaging agents. The phase of the perfluorocarbon at physiological conditions is generally dependent on the boiling point, which varies with the molecular weight of the substance; though some substances, like perfluorooctylbromide (PFOB), do not completely adhere to this trend due to intermolecular interactions (Cosco et al., 2015). The optimal perfluorocarbon formula varies with the application. For instance, ultrasonography implements gaseous perfluorocarbon in microbubbles as contrast agents; while, ^{19}F-MRI uses unemulsified gases and high density perfluorocarbon emulsions to increase fluorine signal (Cosco et al., 2015).

Due to the high oxygen solubility, perfluorocarbons were heavily studied as antihypoxants and blood substitutes. Later generations benefited from a reduced side-effect profile, longer storage life, ability to be frozen, ability to be sterilized by autoclave, a more uniform size distribution, and shorter accumulation times in tissue (Vorob'ev, 2009). Many alternative formulas and experimental applications, like radiological contrast agents, have developed alongside. Methods like X-ray CT and MRI allow quantitative concentration measurements and improved tissue contrast (Mattrey et al., 1990; Riess, 2001). Many recent preclinical studies of potential liquid perfluorocarbon emulsions are aimed at theranostic (*i.e.,* therapy and diagnostic) capabilities and alternative applications. The clinical and preclinical studies include drug delivery (Al Rifai et al., 2020),

adjuvants for blood-brain barrier opening (Peng et al., 2018), anti-ischemics and antihypoxants (Leese et al., 2000; Noveck et al., 2000; Hill et al., 2002; Kachalina et al., 2007; Kligunenko et al., 2007; Moroz et al., 2007; Yermolenko et al., 2007; Culp et al., 2019; Huang et al., 2020), liquid ventilation therapy (EU/3/20/2383, 2021; EU/3/20/2361, 2021), radiological contrast agents (Mattrey et al., 1987a; Mattrey et al., 1987b; Bruneton et al., 1988; Mattrey et al., 1988; Mattrey, 1989), and thermal enhancement for focused ultrasound ablation (Zhang et al., 2011; Desgranges et al., 2019; Lorton et al., 2020).

SYNTHESIS AND PHYSIOCHEMICAL PROPERTIES OF PERFLUOROCARBON CONTRAST AGENTS

Perfluorocarbons can be generated from hydrocarbons by fluorination to substitute the hydrogen atoms with fluorine, with PFOB being of great interest for imaging agents (Riess, 2001). Of primary commercial benefit to the use of PFOB is the capability for large-scale production. The molecule can be derived in a high yield, by a one-step telomerization process through direct bromination of the F-alkyl iodides used in the production of *Teflon* (Riess, 2001). As perfluorocarbons are immiscible in aqueous solution, these require emulsification for stability (Corvis et al., 2018). The emulsifiers are often phospholipids, poloxamers, or fluorosurfactants. Phospholipids are based on egg lecithin isolated from egg yolk through solvent extraction, and composed largely of phosphatidylcholine (Gobley, 1846; Hensing, 2004). Poloxamer surfactants include *Pluronic-F68* used as an emulsifier in *Fluosol* emulsions and *Proxanol-268* used as an emulsifier in *Perftoran* (Riess, 2001). Poloxamers are made with high polydispersity for other industrial applications, and can be purified for medical grade applications (Riess, 2001). Amphiphilic fluorosurfactants are composed of a fluorinated tail group and a hydrophilic head group, and allow very low interfacial tension (Riess, 2001). The lethal doses (LD_{50}) of some selected poloxamers and fluorosurfactants are *Proxanol-268* at 20 g. kg^{-1}, *Pluronic-F68* at 9.4 g. kg^{-1}, and F-TAC at 4.5 g. kg^{-1} in rodents (Vorob'ev, 2009; Maurizis et al., 1994).

The industrial process of large-scale emulsions manufacturing is well developed in pharmaceutics and has long been implemented in the production of parenteral nutrition (Riess, 2001). The emulsion solutions have generally been produced through sonochemical ultrasonic processes which are linked with cavitation, where cavitation nuclei originate from small air bubbles or dust particles in solution, imploding upon excitation to promote further emulsification (Canselier et al., 2002). Cavitation events form when the fluid hydrodynamic pressure becomes lessened to the vapour pressure (Bondy and Söllner, 1935). The vapour pressure of perfluorocarbons in emulsion contrast agents (about 1–3 kPa) are comparable, but slightly lower than water (6.3 kPa) and blood plasma (6.4 kPa) at physiological temperature (Vorob'ev, 2009; Grollman, 1928). These effects will alter the emulsification process, including the droplet diameter and size distribution. Short sonication times tend to generate larger droplets while longer sonication times result in smaller droplet size (Canselier et al., 2002). Cavitation effects can be enhanced with lower ultrasound frequency, lower acoustic pressure, lower medium viscosity, lower medium surface tension, higher energy density, and higher acoustic intensity (Lorimer and Mason, 1987; Canselier et al., 2002). Cavitation implosion effects are also reduced in solvents with higher vapour pressures or at increased temperatures that raise vapour pressure in the fluid-vapour mixture in cavitation sites (Canselier et al., 2002).

Early investigations noted that the incorporation of chlorine or bromine atoms into the perfluorocarbons resulted in faster excretion rates, not predicted based on molecular weights alone (Kabalnov et al., 1992; Riess, 2001). This halogen gives the molecule lipophilic character and enhances clearance rates by allowing the molecule to bind to circulating lipids *en route* to pulmonary excretion (Long et al., 1972a; Long et al., 1982a; Kabalnov et al., 1992; Weers, 1993; Riess, 2001). Although perfluorocarbons have low hydrocarbon affinity, halogen bonding is observed in some systems, to generate self-assembly of supramolecular and crystalline structures (Fox et al., 2004). In these systems, there is a non-covalent interaction between a halogen atom in a perfluorocarbon molecule that acts as an Lewis acid electron acceptor and an atom that acts as a Lewis base electron donor. Similar to hydrogen bonding effects, the halogen atoms are prone to accept electron density from the free electron pairs in neighboring molecules, as the fluorine atoms have a strong electron withdrawing effect (Fox et al., 2004).

The high gas solubility in the liquid perfluorocarbons can be explained by the nonpolar nature of both molecular species. The perfluorocarbons show low polarity and low polarizability, allowing the molecules to readily dissolve molecular gases like noble gases, oxygen, nitrogen, and carbon dioxide (Riess, 2001; Dias et al., 2004). The low polarizability generates a lipophobic character while the overall nonpolar character leads to hydrophobicity (Riess, 2001; Israelachvili, 2015). Some physical and chemical properties of PFOB are given in **Table 1**.

COMPUTED TOMOGRAPHY PERFLUOROCARBON EMULSION CONTRAST AGENTS

In computed tomography, an X-ray beam is rotated circumferentially around the patient while measuring the X-ray transmission at each interval (Hasebroock and Serkova, 2009). Iodinated contrast media are common for computed tomography, particularly for angiography, but also for identifying lesions (Hasebroock and Serkova, 2009). These are often substances like *Lipiodol®* which is derived from poppy seed oil. This medium can be taken up by tumours for cases like hepatocellular carcinoma, where the oil remains longer than in healthy tissue, allowing contrast enhancement on CT images (Rasmussen, 2008). Much initial success for perfluorocarbon contrast enhancement came during studies involving radiopaque brominated perfluorocarbon for radiography, namely PFOB (Long et al., 1982a; Wolf et al., 1994; Hirschl

TABLE 1 | PFOB Physical Properties

Molecular formula Riess, (2001)	$C_8F_{17}Br$
Molecular weight, ($g.mol^{-1}$) Astafyeva et al. (2015)	500.0
Molar Volume, ($Å^3$) Riess, (2001)	432.0
Boiling point, (°C) Astafyeva et al. (2015)	143.0
Melting point, (°C) Riess, (2001)	5.0
Critical solution temperature (n-hexane, °C)	-20.0
Solubility in water, ($mol.m^{-3}$) Riess (2001); Astafyeva et al. (2015)	5.0E-6
Ostwald coefficient for O_2 in PFOB, 308 K Deschamps et al. (2007)	0.5
Ostwald coefficient for CO_2 in PFOB, 308 K Deschamps et al. (2007)	2.2
Henry's constant for O_2 in PFOB, (MPa at 308 K) Deschamps et al. (2007)	21.6
Diffusion coefficient, $m.s^{(-1)}$ Astafyeva et al. (2015)	5.2E-10
Density, ($kg.m^{-3}$) Astafyeva et al. (2015)	1920.0
Sound velocity, ($m.s^{-1}$) Astafyeva et al. (2015)	631.8
Refractive index (at 298 K) Riess, (2001)	1.3
Adiabatic compressibility, ($m.kg^{-3}.Pa^{-1}$) Astafyeva et al. (2015)	6.9E-13
Surface tension, ($mN.m^{-1}$) Riess, (2001)	18.0
Interfacial tension with water, ($mN.m^{-1}$) Astafyeva et al. (2015)	48.7
Spreading coefficient, ($mN.m^{-1}$) Riess, (2001)	2.7
Vapour pressure, (kPa at 37 °C); Dimitrov et al. (2016)	1.3
Heat of vaporization, ($kJ.mol^{-1}$) Riess, (2001)	4.8
LD_{50} in rodents, ($g.kg^{-1}$) Kim et al. (2021)	14.7
Toxic hazard classification by Cramer Dimitrov et al. (2016)	High (Class III)
DNA binding by OASIS Dimitrov et al. (2016)	AN2
Genetic toxicity Dimitrov et al. (2016)	Negative

§Ostwald coefficient for O_2 in Water at 308 K and 1 atm is about 0.028 (Rettich et al., 2000).

et al., 1996; Riess, 2001; Riess, 2005; Tak and Barraclough, 2018). Perfluorohexylbromide (PFHB) and PFOB, have long been studied as CT contrast agents for viewing areas like the bronchia, gastrointestinal tract, and tumours (Patronas et al., 1983).

As the bromine halogen provides radiopacity, intravenous PFOB emulsified with lecithin at doses between 1 and 3 g. kg^{-1} were previously tested in human studies as a CT contrast agent to image the blood vessels, liver, and spleen (Bruneton et al., 1989). The substance was effective at identifying small metastatic lesions and distinguishing blood vessels from small lesions, compared to non-contrast CT. Tumour lesion enhancement of small metastatic lesions on MRI, CT, and ultrasonography, has been observed after intravenous injection of PFOB emulsions; thought to be attributed to the enhanced permeability and retention effect or macrophage phagocytosis (Mattrey, 1989). Perfluorocarbons have shown utility in diagnostic X-ray radiography for bronchography and alveolography in humans (Long et al., 1982b; Voynikov et al., 1990). CT contrast agent perfluorocarbon emulsions have shown attenuation increases in dogs and pigs of 117 Hounsfield units (HU), 77 HU, and 54 HU in the vasculature (~13–50 HU normal), spleen (~45 HU normal), and liver (~60 HU normal), respectively (Mattrey et al., 1984). These values are very similar to attenuation increases reported with commercial iodinated contrast agents (Amato et al., 2013). It has also been shown as a macrophage-specific CT contrast agent of liver tumours (Voynikov et al., 1990). *Ftoran-RK* has also been reported as an effective contrast agent for X-ray CT attenuation, composed of PFOB and perfluoromethycyclohexylpiperidine (PFMCP), emulsified with poloxamer *Proxanol-268*, with 50–80 nm diameter, and a circulatory half-life around 24 h (Vorob'ev, 2009; Vorob'ev et al., 1993). Additionally, perflubron injection was used as a contrast agent for lymph node CT imaging in human volunteers with only site injection discomfort as a reported side-effect (Hanna et al., 1994).

MAGNETIC RESONANCE IMAGING PERFLUOROCARBON EMULSION CONTRAST AGENTS

MRI uses radiofrequency (RF) to excite protons and measure the RF emissions as the protons relax to equilibrium. Inside the bore, the protons align in the direction of the scanner's main, longitudinal, magnetic field. The protons do not align completely, but precess at a resonant frequency around the direction of the net magnetic field (Katti et al., 2011). Then, a RF pulse, with the same frequency as the precessing protons, is absorbed and displaces the spins into the transverse plane. The proton net magnetization vector relaxes towards the main magnetic field, emitting a free induction decay signal that is detected in the RF receiver coil. The amplitude and phase over a range of emitted RF signals is then correlated to the intensity and location to generate the contrast seen in the MRI image (Westbrook, 2016). The signal has a T_1 component in the direction of the main magnetic field and T_2 component transverse to the main magnetic field direction, with the phase lag generating the image contrast. Magnetic resonance contrast agents generally work by reducing the T_1 or T_2 relaxation rates of the tissue in the image, with diseased tissue like tumours having a varying amount of contrast agent than other tissue (Geraldes and

Laurent, 2009). Positive contrast agents result in a reduction in T_1 relaxation rate to create signal hyperintensity, while negative contrast agents alter the T_2 relaxation rate and generate signal hypointensity (Laurent et al., 2009). Perfluorocarbon contrast agents operate through a different mechanism, reducing the local proton density signal to act as a negative contrast agent.

Molecular imaging is a technique to image biomarkers indicative of a disease, by using ligand-mediated agents to target specific cell receptors; for instance to target molecules highly or exclusively expressed in atherosclerotic plaques, ischemic tissues, and tumours (Krafft and Riess, 2021). The liquid perfluorocarbon emulsions have also been studied as a molecular imaging probe. The emulsions can be conjugated with molecular markers specific to certain cell types, including antibodies, peptides, and oligosaccharides; and the accumulation can be visualized with ^{19}F-MRI (Krafft and Riess, 2021). Other contrast agents like gadolinium chelates, iron oxides, hyperpolarized ions, or fluorodeoxyglucose (^{18}F-FDG), can be incorporated into the emulsions to allow contrast enhancement with, ^{19}F-MRI, ^{1}H-MRI, or PET (Wolber et al., 1999; Fabiilli et al., 2013; Amir et al., 2017; Krafft and Riess, 2021). The colloids can also be loaded with drugs and act as theranostics, to both treat the disease and monitor biodistribution (Krafft and Riess, 2021). ^{19}F-MRI cell tracking with intravenous perfluorocarbon emulsions has been used in humans in a phase I clinical trial for tracking dendritic cell vaccine immunotherapy during treatment of late-stage colorectal cancer (Ahrens et al., 2014), benefiting from being implemented in previous clinical studies for oxygenation after brain trauma and stroke (Darçot et al., 2020).

Imagent GI was a previously FDA-approved unemulsified PFOB oral negative contrast agent for ^{1}H-MRI that has since been discontinued (Brown et al., 1991; Bisset et al., 1996; Geraldes and Laurent, 2009). PFOB molecules contain no hydrogen atoms and create a proton density weighted image, effectively darkening the bowel loop, allowing better delineation of blood vessels and abdominal organs like the spleen, liver, kidneys, and pancreas (Mattrey et al., 1988; Mattrey, 1989; André et al., 1990; Mattrey et al., 1991). Also, the use of ^{19}F-MRI with gaseous unemulsified perfluorocarbon as a contrast agent for respiratory disease has completed many early phase clinical trials (Couch et al., 2013; Halaweish et al., 2013; Goralski et al., 2020; Krafft, 2021). Perfluoropropane (PFP) and ^{19}F-MRI has shown in human trials the ability to distinguish healthy and diseased lungs from patients with COPD, cystic fibrosis, asthma, and emphysema. (Halaweish et al., 2013; Couch et al., 2019; Gutberlet et al., 2018) ^{19}F-MRI of the lungs can provide functional imaging and generally uses a mixture of about 21% oxygen and 79% PFP or sulfur hexafluoride (SF_6) (Couch et al., 2013). Healthy volunteers show a homogenous distribution of PFP throughout the lungs, while patients with diseased lungs show incomplete heterogeneous gas distribution. The technique has also shown useful to assess proper lung function from patients that received a lung transplant (Halaweish et al., 2013). The modality would surely be useful in understanding the effects of coronavirus disease 2019 (COVID-19) on lung structure and function, though a specialized MRI receiver coil is required, and to date no studies have reported results; though at least one trial has been initiated (NCT04872309).

OTHER APPLICATIONS

Though, radiological studies have indicated the efficacy, many preclinical formulas have yet to undergo costly toxicological safety studies needed for an investigative new drug application, to permit clinical studies on humans. Much of the literature describing toxicological safety studies of perfluorocarbon emulsions has been for blood oxygenation (Spahn, 1999; Leese et al., 2000; Noveck et al., 2000; Hill et al., 2002; Spiess, 2009; Hill, 2019). *Perftoran*, also known as Perfluorane, is a perfluorocarbon emulsion composed of 10% w:v perfluorodecalin and perfluoromethycyclohexylpiperidine, currently approved as an anti-ischemic and antihypoxant drug in the Russian Federation, Uzbekistan, and Mexico, and was previously approved in many former Soviet states (Khan et al., 2020; Maevsky et al., 2020). *Perftoran* has been shown to induce vasodilation in patients with vascular disease; including patients with limb ischemia, atherosclerosis, diabetes mellitus, oedema after trauma, and oedema post-surgery (Moroz et al., 2007). These emulsions have also shown to improve preterm birth outcomes during gestosis and preeclampsia, which can exhibit acute damage to the peripheral vasculature, platelet damage, vessel constriction, and organ hypoperfusion; in severe cases, leading to acidosis and organ failure. When used in combination with cytoflavin, improved outcomes have been shown in the treatment of moderate preeclampsia, by increasing vascular perfusion and reducing hypoxia, to prolong pregnancy (Kachalina et al., 2007). Moreover, human studies have shown decreased mortality during severe sepsis by oxygenation and improved microcirculation (Yermolenko et al., 2007). *Perftoran* has shown improved outcomes when administered intra-operatively during lobectomy of lung cancer patients with severe respiratory disorders (Kligunenko et al., 2007). The developers have indicated the need and utility for re-establishing large-scale industrial production for the treatment of COVID-19 (Maevsky et al., 2020).

Liquid perfluorocarbons are also used extensively in ophthalmological surgery for applications including: giant retinal tears, vitreoretinopathy, and retinal detachment repairs (Kramer et al., 1995; Mikhail et al., 2017). Also, the perfluorocarbon emulsions are under study as potential focused ultrasound adjuvants due to their enhanced absorption of ultrasonic energy and resulting increasing heat generation (Schad and Hynynen, 2010; Zhang et al., 2011; Kopechek et al., 2013; Phillips et al., 2013; Moyer et al., 2015; Desgranges et al., 2019; Lorton et al., 2020). *Echogen* was a previously FDA approved ultrasonography perfluorocarbon phase-shift emulsion, causing a change from a liquid to gas state when imaged with ultrasonography; composed of C_5F_{12} and an albumin surfactant (Lin and Pitt, 2013). *Perftoran* is effective as an ultrasonography contrast agent in identifying fluid foci liver lesions and for echocardiography (Vakulenko et al., 2021). *Fluosol* emulsions have been used in early phase clinical

trials as an adjuvant to radiotherapy for high-grade gliomas, and late-stage squamous cell carcinomas in the neck and head (Lustig et al., 1989; Evans et al., 1990).

CLEARANCE, TOXICITY, AND SIDE-EFFECTS

PFOB has been well-studied as an emulsion contrast agent in humans, particularly due to its fast excretion rate (Burgan et al., 1987; Mattrey, 1989); approximately 3 days at 2.7 g. kg^{-1} (Riess, 2001). Intravenous injection of 1 g. kg^{-1} 0.1–0.2 μm lecithin-PFOB emulsions in 60 patients gave no detectable toxicity (Mattrey, 1989). Oral administration of unemulsified gastrointestinal PFOB contrast agent at 2–12 ml. kg^{-1} doses resulted in no toxic symptoms within 3 days in 60 human subjects, with almost all PFOB eliminated within 24 h (Long et al., 1972b). The contrast agent pharmacokinetics can be quantified with MRI, CT, positron emission tomography, gamma counting, high-performance liquid chromatography, and elemental analysis (Pierre and Allen, 2017). Lecithin-PFOB pharmacokinetic studies indicated that intravenous emulsions are opsonized to a large extent by Kupffer cells and splenocytes, resulting in large deposits of PFOB in the liver and spleen within a few minutes of injection (Riess, 2001; Blanco et al., 2015). Here, the emulsions are degraded, then unmetabolized PFOB re-enters the blood stream, binds to plasma lipids, accumulates in the lungs, before being expelled by respiration (Spahn, 1999).

Intravenous lecithin-PFOB at doses between 1 and 3 g. kg^{-1} were previously tested in humans as a CT contrast agent to image the blood vessels, liver, and spleen (Bruneton et al., 1989). The toxicity was assessed with laboratory tests 2 days before and 7 days following using blood samples, electrolytes, liver function, renal function, proteins, and endocrine factors. The side-effects were mainly asymptomatic and included splenomegaly, and abnormal gamma glutamyl transferase, alkaline phosphatase, and blood platelet levels. Slight lower back pain was observed in some patients thought perhaps to result from venous constriction. These symptoms and influenza-like symptoms are typical of perfluorocarbon emulsions, also seen in liposomal parenteral nutrition formulas, and generally all substances with adsorbent surfaces (Vorob'ev, 2009). The side-effects have also been linked with a size-dependence, as smaller emulsions are less detectable by the macrophage phagocytosis system (MPS) (Spahn, 1999). A concentration dependence of side-effects has also been linked to the increased release of cytokines that can result in flushing and fever (Flaim, 1994). Early emulsion formulas incorporated *Proxonol-F68* emulsifier, later replaced by phospholipids or *Proxonol-268*, which were designed to avoid the immune system and resulted in improved circulatory half-lives, reduced cytokine response, and reduced side-effects (Vorob'ev, 2009). Though, not reported to have caused adverse health effects, some long-term accumulation has been suspected from CT imaging of patients whom were administered PFOB for liquid ventilation therapy during severe respiratory distress syndrome (Hagerty et al., 2008; Servaes and Epelman, 2009; Tak and Barraclough, 2018).

The primary constituent in perfluorocarbon contrast agents are a class of chemicals known as perfluoroalkyl substances (PFAS). The adverse reports are generally associated with prolonged environmental exposures. Certain PFAS molecules have very long half-lives of 3.5–8 years and have been indicated in many potential adverse health effects (Olsen et al., 2007; Cardenas et al., 2018). The prolonged exposure to PFAS typically occur through contaminated water and food (Cardenas et al., 2018; Fraser et al., 2012; D'eon and Mabury, 2011). There have been clinical trials and cohort studies of adverse health associated with elevated levels of perfluorooctane sulfonate (PFOS) and perfluorooctanoic acid (PFOA) in blood serum, particularly in pregnant women (Granum et al., 2013; Cardenas et al., 2018; Wikström et al., 2019).

PATH TO CLINICAL TRANSLATION

For FDA investigational new drug applications (iNDA), products must show efficacy and safety through a series of *in vitro* and *in vivo* tests. A comprehensive overview of the toxicological testing needed prior to iNDA are given by Andrade et al. (2016) Toxicity studies for contrast agents are generally performed after sufficient image enhancement has been verified, pharmacokinetics are known, and elimination routes have been observed (Pierre and Allen, 2017). The studies are aimed at determining the toxic effects on animals so that the effects can be monitored in human studies and also to determine a limit for no observable adverse effects at higher limits than the desired dose, to create a factor of safety in human studies (Pierre and Allen, 2017). Toxicity studies for MRI contrast agents include local site toxicity, allergies and immunogenicity, genotoxicity, and blood compatibility (Pierre and Allen, 2017).

In vitro test kits offer an affordable alternative to some animal testing and include assays for fetal-embryonic development (EMA/CHMP/ICH/544278/1998, 2020), gene toxicology assessment, macrophage and neutrophil function assays (CHMP/167235/2004, 2006), among others. *In vitro* enzymatic screening, like liver microsomal preparations, are used in most pharmaceuticals to assess metabolism of the substance based on the clearance route (Pierre and Allen, 2017). Perfluorocarbon emulsion contrast agents have been shown to accumulate in the liver and spleen, before being cleared through the lungs. Illustrating safety to these organs would certainly be necessary for translation. Cytochrome P450 enzymes metabolize the majority of drugs in the liver and assay testing the drug reaction can limit adverse effects in patients and establish half-maximal inhibitory concentration (IC_{50}) values (Lynch and Price, 2007). Other *in vitro* test kits include human colon adenocarcinoma cells (Caco-2) for intestinal permeability, plasma protein binding with ultrafiltration, the Ames test for mutations, micronucleus assay for chromosome damage, and high-throughput screening of hERG channel inhibition for cardiovascular safety effects (Andrade et al., 2016).

Clinical trials for pharmaceutical development generally consist of early phase clinical studies on a small patient cohort

to determine pharmacokinetics, dose, efficacy and assess side-effects (Lipsky and Sharp, 2001). Subsequent late-phase clinical trials are randomized controlled trials on larger groups to further test efficacy, adverse reactions, and long-term safety effects; including post-market trials for rare adverse events (Lipsky and Sharp, 2001). The quickest route for clinical translation of a new perfluorocarbon emulsion contrast agent formula might be using previously approved perfluorocarbon and emulsifier components in the formula, or using an off-label commercial perfluorocarbon emulsion formula. During the COVID-19 pandemic, many medical products have received streamlined clinical testing for the treatment, prevention, and diagnosis of COVID-19 (Avdeev et al., 2019). *Remdesivir*, for instance, was repurposed from an Ebola virus therapeutic to treat coronavirus disease after being streamlined in the United States, in only 4 months, from new drug application (NDA) submission to emergency use authorization (EUA) (Avdeev et al., 2019). Gaseous perfluorocarbons with ^{19}F-MRI have previously been tested in early phase clinical trials for respiratory complications (Couch et al., 2013; Halaweish et al., 2013; Goralski et al., 2020; Krafft, 2021) and has great potential for assessing effects of coronavirus disease on pulmonary structure and function; recently being initiated in early phase clinical trials for assessing effects on lungs, vasculature, and the heart from patients with COVID-19 (NCT04872309). Additionally, potential exists with perfluorocarbon antihypoxants and blood substitutes as an off-label COVID-19 therapeutic, having previous approval for alternative therapies from the Russian Ministry of Health and FDA. The reports from studies with antihypoxant perfluorocarbon emulsions (Yermolenko et al., 2007; Moroz et al., 2007; Kligunenko et al., 2007; Kachalina et al., 2007; EU/3/20/2383, 2021; EU/3/20/2361, 2021) suggest significant benefit for treating complications associated with severe COVID-19 (Avdeev et al., 2019; Maevsky et al., 2020).

CONCLUSION

In this mini review, the physiochemical properties, radiological imaging applications, and previous clinical studies with perfluorocarbon emulsion contrast agents have been discussed. Perfluorocarbons provide useful contrast on CT and MRI and current research with theranostics, molecular imaging, and ^{19}F-MRI have great potential for future commercial medical products. Many alternative therapies, including blood substitutes and antihypoxants, have been developed using similar formulas to perfluorocarbon emulsion contrast agents. Studies with these alternative therapies have established large amounts of preclinical and clinical data pertaining to biodistribution, clearance, and safety studies, applicable to these imaging agents. Utilizing results from these previous clinical studies and implementing an off-label approach could reduce the complexity to initiate clinical testing. Beyond radiological contrast agents, antihypoxant perfluorocarbon emulsions and diagnostic pulmonary ^{19}F-MRI have potential for streamlined clinical translation for the treatment and diagnosis of COVID-19.

AUTHOR CONTRIBUTIONS

All authors listed have made a substantial, direct, and intellectual contribution to the work and approved it for publication.

FUNDING

This project has received funding from the European Union's Horizon 2020 research and innovation programme under the Skłodowska-Curie grant agreement No 813766.

REFERENCES

Ahrens, E. T., Helfer, B. M., O'Hanlon, C. F., and Schirda, C. (2014). Clinical Cell Therapy Imaging Using a Perfluorocarbon Tracer and Fluorine-19 MRI. *Magn. Reson. Med.* 72 (6), 1696–1701. doi:10.1002/mrm.25454

Al Rifai, N., Desgranges, S., Le Guillou-Buffello, D., Giron, A., Urbach, W., Nassereddine, M., et al. (2020). Ultrasound-triggered Delivery of Paclitaxel Encapsulated in an Emulsion at Low Acoustic Pressures. *J. Mater. Chem. B* 8 (8), 1640–1648. doi:10.1039/c9tb02493j

Amato, E., Salamone, I., Naso, S., Bottari, A., Gaeta, M., and Blandino, A. (2013). Can Contrast Media Increase Organ Doses in CT Examinations? A Clinical Study. *Am. J. Roentgenology* 200 (6), 1288–1293. doi:10.2214/ajr.12.8958

Amir, N., Green, D., Kent, J., Xiang, Y., Gorelikov, I., Seo, M., et al. (2017). 18F-Labeled Perfluorocarbon Droplets for Positron Emission Tomography Imaging. *Nucl. Med. Biol.* 54, 27–33. doi:10.1016/j.nucmedbio.2017.07.001

Andrade, E. L., Bento, A. F., Cavalli, J., Oliveira, S. K., Schwanke, R. C., Siqueira, J. M., et al. (2016). Non-clinical Studies in the Process of New Drug Development - Part II: Good Laboratory Practice, Metabolism, Pharmacokinetics, Safety and Dose Translation to Clinical Studies. *Braz. J. Med. Biol. Res.* 49 (12), e5646. doi:10.1590/1414-431X20165646

André, M., Nelson, T., and Mattrey, R. (1990). Physical and Acoustical Properties of Perfluorooctylbromide, an Ultrasound Contrast Agent. *Invest. Radiol.* 25 (9), 983–987. doi:10.1097/00004424-199009000-00004

Astafyeva, K., Somaglino, L., Desgranges, S., Berti, R., Patinote, C., Langevin, D., et al. (2015). Perfluorocarbon Nanodroplets Stabilized by Fluorinated Surfactants: Characterization and Potentiality as Theranostic Agents. *J. Mater. Chem. B* 3 (14), 2892–2907. doi:10.1039/c4tb01578a

Avdeev, S. N., Adamyan, L. V., Baranov, A. A., Natal'ya, N. B., Briko, N. I., Vasil'Eva, I. A., et al. (2019). The Prevention, Diagnosis and Treatment of the New Coronavirus Infection 2019-nCoV: Temporary Guidelines Ministry of Health of the Russian Federation. *Pulmonologiya* 29 (6).

Barnett, B. P., Ruiz-Cabello, J., Hota, P., Liddell, R., Walczak, P., Howland, V., et al. (2011). Fluorocapsules for Improved Function, Immunoprotection, and Visualization of Cellular Therapeutics with MR, US, and CT Imaging. *Radiology* 258 (1), 182–191. doi:10.1148/radiol.10092339

Bisset, G. S., Emery, K. H., Meza, M. P., Rollins, N. K., Don, S., and Shorr, J. S. (1996). Perflubron as a Gastrointestinal MR Imaging Contrast Agent in the Pediatric Population. *Pediatr. Radiol.* 26 (6), 409–415. doi:10.1007/bf01387316

Blanco, E., Shen, H., and Ferrari, M. (2015). Principles of Nanoparticle Design for Overcoming Biological Barriers to Drug Delivery. *Nat. Biotechnol.* 33 (9), 941–951. doi:10.1038/nbt.3330

Bondy, C., and Söllner, K. (1935). On the Mechanism of Emulsification by Ultrasonic Waves. *Trans. Faraday Soc.* 31, 835–843. doi:10.1039/tf9353100835

Brown, J. J., Duncan, J. R., Heiken, J. P., Balfe, D. M., Corr, A. P., Mirowitz, S. A., et al. (1991). Perfluoroctylbromide as a Gastrointestinal Contrast Agent for MR Imaging: Use with and without Glucagon. *Radiology* 181 (2), 455–460. doi:10.1148/radiology.181.2.1924788

Bruneton, J. N., Falewee, M. N., Balu-Maestro, C., Normand, F., and Mattrey, R. F. (1988). Perfluoroctylbromide and Hepatosplenic Computed Tomography Preliminary Clinical Study. *Invest. Radiol.* 23, S306–S307. doi:10.1097/00004424-198809001-00068

Bruneton, J. N., Falewée, M. N., François, E., Cambon, P., Philip, C., Riess, J. G., et al. (1989). Liver, Spleen, and Vessels: Preliminary Clinical Results of CT with Perfluorooctylbromide. *Radiology* 170 (1), 179–183. doi:10.1148/radiology.170.1.2909093

Burgan, A. R., Long, D. M., and Mattrey, R. F. (1987). Results of Pharmacokinetic and Toxicologic Studies with PFOB Emulsions. *Biomater. Artif. Cells Artif. Organs* 15 (2), 403.

Canselier, J., Delmas, H., Wilhelm, A., and Abismail, B. (2002). Ultrasound Emulsification—An Overview. *J. Dispersion Sci. Technol.* 23 (1-3), 333–349. doi:10.1080/01932690208984209

Cardenas, A., Hauser, R., Gold, D. R., Kleinman, K. P., Hivert, M.-F., Fleisch, A. F., et al. (2018). Association of Perfluoroalkyl and Polyfluoroalkyl Substances with Adiposity. *JAMA Netw. Open* 1 (4), e181493. doi:10.1001/jamanetworkopen.2018.1493

CHMP/167235/2004 (2006). *ICH S8 Immunotoxicity Studies for Human Pharmaceuticals*. European Medicines Agency.

ClinicalTrials.gov (2021). Identifier NCT04872309, MUlti-Nuclear MR Imaging Investigation of Respiratory Disease-Associated CHanges in Lung Physiology (MURDOCH). Internet. Bethesda (MD): National Library of Medicine US. May 4. Available at: https://clinicaltrials.gov/ct2/show/NCT04872309.

Corvis, Y., Manta, S., Thebault, C., Couture, O., Dhotel, H., Michel, J.-P., et al. (2018). Novel Perfluorinated Triblock Amphiphilic Copolymers for Lipid-Shelled Microbubble Stabilization. *Langmuir* 34 (33), 9744–9753. doi:10.1021/acs.langmuir.8b01668

Cosco, D., Fattal, E., Fresta, M., and Tsapis, N. (2015). Perfluorocarbon-loaded Micro and Nanosystems for Medical Imaging: a State of the Art. *J. Fluorine Chem.* 171, 18–26. doi:10.1016/j.jfluchem.2014.10.013

Couch, M. J., Ball, I. K., Li, T., Fox, M. S., Biman, B., and Albert, M. S. (2019). 19F MRI of the Lungs Using Inert Fluorinated Gases: Challenges and New Developments. *J. Magn. Reson. Imaging* 49 (2), 343–354. doi:10.1002/jmri.26292

Couch, M. J., Ball, I. K., Li, T., Fox, M. S., Littlefield, S. L., Biman, B., et al. (2013). Pulmonary Ultrashort Echo Time 19F MR Imaging with Inhaled Fluorinated Gas Mixtures in Healthy Volunteers: Feasibility. *Radiology* 269 (3), 903–909. doi:10.1148/radiol.13130609

Culp, W. C., Onteddu, S. S., Brown, A., Nalleballe, K., Sharma, R., Skinner, R. D., et al. (2019). Dodecafluoropentane Emulsion in Acute Ischemic Stroke: A Phase Ib/II Randomized and Controlled Dose-Escalation Trial. *J. Vasc. Interv. Radiol.* 30 (8), 1244–1250. doi:10.1016/j.jvir.2019.04.020

Darçot, E., Colotti, R., Brennan, D., Deuchar, G. A., Santosh, C., and van Heeswijk, R. B. (2020). A Characterization of ABL-101 as a Potential Tracer for Clinical Fluorine-19 MRI. *NMR Biomed.* 33 (1), e4212. doi:10.1002/nbm.4212

D'eon, J. C., and Mabury, S. A. (2011). Is Indirect Exposure a Significant Contributor to the Burden of Perfluorinated Acids Observed in Humans. *Environ. Sci. Technol.* 45 (19), 7974–7984.

Deschamps, J., Menz, D.-H., Padua, A. A. H., and Costa Gomes, M. F. (2007). Low Pressure Solubility and Thermodynamics of Solvation of Oxygen, Carbon Dioxide, and Carbon Monoxide in Fluorinated Liquids. *The J. Chem. Thermodynamics* 39 (6), 847–854. doi:10.1016/j.jct.2006.11.012

Desgranges, S., Lorton, O., Gui-Levy, L., Guillemin, P., Celicanin, Z., Hyacinthe, J.-N., et al. (2019). Micron-sized PFOB Liquid Core Droplets Stabilized with Tailored-Made Perfluorinated Surfactants as a New Class of Endovascular Sono-Sensitizers for Focused Ultrasound Thermotherapy. *J. Mater. Chem. B* 7 (6), 927–939. doi:10.1039/c8tb01491d

Dias, A. M. A., Freire, M., Coutinho, J. A. P., and Marrucho, I. M. (2004). Solubility of Oxygen in Liquid Perfluorocarbons. *Fluid Phase Equilibria* 222-223, 325–330. doi:10.1016/j.fluid.2004.06.037

Dimitrov, S. D., Diderich, R., Sobanski, T., Pavlov, T. S., Chankov, G. V., Chapkanov, A. S., et al. (2016). QSAR Toolbox - Workflow and Major Functionalities. *SAR QSAR Environ. Res.* 27 (3), 203–219. doi:10.1080/1062936x.2015.1136680

EU/3/20/2361 (2021). Perflubron for the Treatment of Congenital Pulmonary Hypoplasia. June. Available at: https://www.ema.europa.eu/en/documents/orphan-designation/eu/3/20/2361-public-summary-opinion-orphan-designation-perflubron-treatment-congenital-pulmonary-hypoplasia_en.pdf.

EU/3/20/2383 (2021). Perflubron for the Treatment of Respiratory Distress Syndrome. June. Available at: https://www.ema.europa.eu/en/documents/orphan-designation/eu/3/20/2383-public-summary-opinion-orphan-designation-perflubron-treatment-respiratory-distress-syndrome_en.pdf.

Evans, R. G., Kimler, B. F., Morantz, R. A., Vats, T. S., Gemer, L. S., Liston, V., et al. (1990). A Phase I/II Study of the Use of Fluosol as an Adjuvant to Radiation Therapy in the Treatment of Primary High-Grade Brain Tumors. *Int. J. Radiat. Oncol. Biol. Phys.* 19 (2), 415–420. doi:10.1016/0360-3016(90)90551-t

Fabiilli, M. L., Piert, M. R., Koeppe, R. A., Sherman, P. S., Quesada, C. A., and Kripfgans, O. D. (2013). Assessment of the Biodistribution of an [18F]FDG-Loaded Perfluorocarbon Double Emulsion Using Dynamic Micro-PET in Rats. *Contrast Media Mol. Imaging* 8 (4), 366–374. doi:10.1002/cmmi.1532

Flaim, S. F. (1994). Pharmacokinetics and Side Effects of Perfluorocarbon-Based Blood Substitutes. *Artif. Cell Blood Substitutes, Biotechnol.* 22 (4), 1043–1054. doi:10.3109/10731199409138801

Fox, D. B., Liantonio, R., Metrangolo, P., Pilati, T., and Resnati, G. (2004). Perfluorocarbon-hydrocarbons Self-Assembly: Halogen Bonding Mediated Intermolecular Recognition. *J. Fluorine Chem.* 125 (2), 271–281. doi:10.1016/j.jfluchem.2003.07.020

Fraser, A. J., Webster, T. F., Watkins, D. J., Nelson, J. W., Stapleton, H. M., Calafat, A. M., et al. (2012). Polyfluorinated Compounds in Serum Linked to Indoor Air in Office Environments. *Environ. Sci. Technol.* 46 (2), 1209–1215. doi:10.1021/es2038257

Geraldes, C. F. G. C., and Laurent, S. (2009). Classification and Basic Properties of Contrast Agents for Magnetic Resonance Imaging. *Contrast Media Mol. Imaging* 4 (1), 1–23. doi:10.1002/cmmi.265

Gobley, T. (1846). Chemical Researches on Egg Yolk. *J. Pharm. Chem.* 9, 81–91.

Goralski, J. L., Chung, S. H., Glass, T. M., Ceppe, A. S., Akinnagbe-Zusterzeel, E. O., Trimble, A. T., et al. (2020). Dynamic Perfluorinated Gas MRI Reveals Abnormal Ventilation Despite normal FEV1 in Cystic Fibrosis. *JCI Insight* 5 (2). doi:10.1172/jci.insight.133400

Granum, B., Haug, L. S., Namork, E., Stølevik, S. B., Thomsen, C., Aaberge, I. S., et al. (2013). Pre-natal Exposure to Perfluoroalkyl Substances May Be Associated with Altered Vaccine Antibody Levels and Immune-Related Health Outcomes in Early Childhood. *J. Immunotoxicology* 10 (4), 373–379. doi:10.3109/1547691x.2012.755580

Grollman, A. (1928). The Vapor Pressure of Dog's Blood at Body Temperature. *J. Gen. Physiol.* 11 (5), 495–506. doi:10.1085/jgp.11.5.495

Gutberlet, M., Kaireit, T. F., Voskrebenzev, A., Lasch, F., Freise, J., Welte, T., et al. (2018). Free-breathing Dynamic 19F Gas MR Imaging for Mapping of Regional Lung Ventilation in Patients with COPD. *Radiology* 286 (3), 1040–1051. doi:10.1148/radiol.2017170591

Hagerty, R. D., Phelan, M. P., Morrison, S. C., and Hatem, S. F. (2008). Radiographic Detection of Perflubron Fluoromediastinum and Fluororetroperitoneum 9 Years after Partial Liquid Ventilation. *Emerg. Radiol.* 15 (1), 71–75. doi:10.1007/s10140-007-0673-2

Halaweish, A. F., Moon, R. E., Foster, W. M., Soher, B. J., McAdams, H. P., MacFall, J. R., et al. (2013). Perfluoropropane Gas as a Magnetic Resonance Lung Imaging Contrast Agent in Humans. *Chest* 144 (4), 1300–1310. doi:10.1378/chest.12-2597

Hanna, G., Hopkins, R., Flam, K., Leese, P., Schmid-schönbein, G., and Wolf, G. L. (1994). Indirect Lymphography with Perflubron Emulsion Preclinical and Clinical Results. *Invest. Radiol.* 29, S33–S35. doi:10.1097/00004424-199406001-00012

Hasebroock, K. M., and Serkova, N. J. (2009). Toxicity of MRI and CT Contrast Agents. *Expert Opin. Drug Metab. Toxicol.* 5 (4), 403–416. doi:10.1517/17425250902873796

Hensing, J. T. (2004). The Discovery of Lecithin, the First Phospholipid. *Bull. Hist. Chem.* 29 (1), 9.

Hill, S. E., Leone, B. J., Faithfull, N. S., Flaim, K. E., Keipert, P. E., and Newman, M. F. (2002). Perflubron Emulsion (AF0144) Augments Harvesting of Autologous Blood: A Phase II Study in Cardiac Surgery. *J. Cardiothorac. Vasc. Anesth.* 16 (5), 555–560. doi:10.1053/jcan.2002.126947

Hill, S. E. (2019). Perfluorocarbons: Knowledge Gained from Clinical Trials. *Shock* 52 (1S), 60–64. doi:10.1097/shk.0000000000001045

Hirschl, R. B., Pranikoff, T., Wise, C., Overbeck, M. C., Gauger, P., Schreiner, R. J., et al. (1996). Initial Experience with Partial Liquid Ventilation in Adult Patients

with the Acute Respiratory Distress Syndrome. *JAMA* 275 (5), 383–389. doi:10.1001/jama.275.5.383

Huang, B., Chen, S., Pei, W., Xu, Y., Jiang, Z., Niu, C., et al. (2020). Oxygen-Sufficient Nanoplatform for Chemo-Sonodynamic Therapy of Hypoxic Tumors. *Front. Chem.* 8 (358), 1–13. doi:10.3389/fchem.2020.00358

EMA/CHMP/ICH/544278/1998 (2020). - *ICH S5 (R3) Guideline on Reproductive Toxicology: Detection of Toxicity to Reproduction for Human Pharmaceuticals*. European Medicines Agency.

Israelachvili, J. N. (2015). *Intermolecular and Surface Forces*. 3 ed. Academic Press.

Kabalnov, A. S., Makarov, K. N., and Shchukin, E. D. (1992). Stability of Perfluoroalkyl Halide Emulsions. *Colloids Surf.* 62 (1-2), 101–104. doi:10.1016/0166-6622(92)80040-9

Kachalina, T. S., Lebedeva, N. V., and Ilyina, L. N. (2007). New Approaches to Treating Gestosis with Perfluorane and Cytoflavin. *Gen. Resusc* III, 63–66.

Katti, G., Ara, S. A., and Shireen, A. (2011). Magnetic Resonance Imaging (MRI)–A Review. *Int. J. Dent Clin.* 3 (1), 65–70.

Khan, F., Singh, K., Singh, K., and Friedman, M. T. (2020). Artificial Blood: The History and Current Perspectives of Blood Substitutes. *Discoveries (Craiova)* 8 (1), e104. doi:10.15190/d.2020.1

Kim, S., Chen, J., Cheng, T., Gindulyte, A., He, J., He, S., et al. (2021). PubChem in 2021: New Data Content and Improved Web Interfaces. *Nucleic Acids Res.* 49 (D1), D1388–D1395. doi:10.1093/nar/gkaa971

Kligunenko, Y. N., Ryabchenko, Y. V., Novikov, S., and Kirillova, Y. A. (2007). The Central Hemodynamics in Oncothoracic Patients with Varying Baseline Ventilatory Failure after Intraoperative Administration of Perftoran and Perfluorane. *Gen. Resusc* III, 43–48.

Kopechek, J., Park, E., Mei, C.-S., McDannold, N., and Porter, T. (2013). Accumulation of Phase-Shift Nanoemulsions to Enhance MR-Guided Ultrasound-Mediated Tumor Ablation *In Vivo*. *J. Healthc. Eng.* 4 (1), 109–126. doi:10.1260/2040-2295.4.1.109

Krafft, M. P. (2021). "Perfluorocarbons and Perfluorocarbon Emulsions for Pulmonary Indications," in *The Curious World of Fluorinated Molecules* (Elsevier), 219–239. doi:10.1016/b978-0-12-819874-2.00009-6

Krafft, M. P., and Riess, J. G. (2021). Therapeutic Oxygen Delivery by Perfluorocarbon-Based Colloids. *Adv. Colloid Interf. Sci.* 294, 102407. doi:10.1016/j.cis.2021.102407

Kramer, S. G., Hwang, D., Peyman, G. A., Schulman, J. A., and Sullivan, B. (1995). Perfluorocarbon Liquids in Ophthalmology. *Surv. Ophthalmol.* 39 (5), 375–395. doi:10.1016/s0039-6257(05)80093-1

Laurent, S., Vander Elst, L., and Muller, R. N. (2009). Contrast Agents for MRI: Recent Advances. *In Vivo* 2, 3. doi:10.1002/9780470034590.emrstm1049

Leese, P. T., Noveck, R. J., Shorr, J. S., Woods, C. M., Flaim, K. E., and Keipert, P. E. (2000). Randomized Safety Studies of Intravenous Perflubron Emulsion. I. Effects on Coagulation Function in Healthy Volunteers. *Anesth. Analgesia* 91 (4), 804–811. doi:10.1097/00000539-200010000-00008

Lin, C. Y., and Pitt, W. G. (2013). Acoustic Droplet Vaporization in Biology and Medicine. *Biomed. Res. Int.* 2013, 404361. doi:10.1155/2013/404361

Lipsky, M. S., and Sharp, L. K. (2001). From Idea to Market: the Drug Approval Process. *J. Am. Board Fam. Pract.* 14 (5), 362–367.

Long, D., Higgins, C., Mattrey, R., Mitten, R., and Multer, F. (1982). *Is There a Time and Place for Radiopaque Fluorocarbons. Preparation, Properties and Industrial Applications of Organofluorine Compounds*. New York: Ellis Horwood Limited, 139–156.

Long, D. M., Liu, M. S., Szanto, P. S., and Alrenga, P. (1972). Initial Observations with a New X-Ray Contrast Agent--Radiopaque Perfluorocarbon. *Rev. Surg.* 29 (1), 71–76.

Long, D. M., Higgins, C. B., Mattrey, R. F., Mitten, R., and Multer, F. K. (1982). in *Preparation, Properties, and Industrial Applications of Organofluorine Compounds*. Editor R. E. Banks (New York: Ellis Horwood Limited).

Long, D. M., Liu, M.-s., Szanto, P. S., Alrenga, D. P., Patel, M. M., Rios, M. V., et al. (1972). Efficacy and Toxicity Studies with Radiopaque Perfluorocarbon. *Radiology* 105 (2), 323–332. doi:10.1148/105.2.323

Lorimer, J. P., and Mason, T. J. (1987). Sonochemistry. Part 1-The Physical Aspects. *Chem. Soc. Rev.* 16, 239–274. doi:10.1039/cs9871600239

Lorton, O., Guillemin, P. C., Holman, R., Desgranges, S., Gui, L., Crowe, L. A., et al. (2020). Enhancement of HIFU thermal Therapy in Perfused Tissue Models Using Micron-Sized FTAC-Stabilized PFOB-Core Endovascular Sonosensitizers. *Int. J. Hyperthermia* 37 (1), 1116–1130. doi:10.1080/02656736.2020.1817575

Lustig, R., McIntosh-Lowe, N., Rose, C., Haas, J., Krasnow, S., Spaulding, M., et al. (1989). Phase I/II Study of Fluosol-DA and 100% Oxygen as an Adjuvant to Radiation in the Treatment of Advanced Squamous Cell Tumors of the Head and Neck. *Int. J. Radiat. Oncol. Biol. Phys.* 16 (6), 1587–1593. doi:10.1016/0360-3016(89)90967-x

Lynch, T., and Price, A. (2007). The Effect of Cytochrome P450 Metabolism on Drug Response, Interactions, and Adverse Effects. *Am. Fam. Physician* 76 (3), 391–396.

Maevsky, E. I., Golovnenkova, A. E., Alekseev, S. V., Kaptsov, A. V., and Bogdanova, L. A. (2020). Perftoran. The Untapped Potential of Medicine against Covid-19. *Biomed. J. MEDLINE.RU, Pharm* 21.

Mattrey, R. F., Hilpert, P. L., Levine, D., and Long, D. C. (1988). PFOB as a Negative Oral MR Contrast Agent Identifies Bowel Clinical Results. *Invest. Radiol.* 23 (9), S3. doi:10.1097/00004424-198809000-00068

Mattrey, R. F., Long, D. M., Peck, W. W., Slutsky, R. A., and Higgins, C. B. (1984). Perfluoroctylbromide as a Blood Pool Contrast Agent for Liver, Spleen, and Vascular Imaging in Computed Tomography. *J. Comp. Assist. Tomography* 8 (4), 739–744. doi:10.1097/00004728-198408000-00028

Mattrey, R. F., Nemcek, A. A., Jr, Shelton, R., Andr, M. P., Mitten, R. M., and Peterson, T. (1990). *In Vivo* Estimation of Perfluorooctylbromide Concentration in Tissues. *Invest. Radiol.* 25 (8), 915–921. doi:10.1097/00004424-199008000-00008

Mattrey, R. F., Strich, G., Shelton, R. E., Gosink, B. B., Leopold, G. R., Lee, T., et al. (1987). Perfluorochemicals as US Contrast Agents for Tumor Imaging and Hepatosplenography: Preliminary Clinical Results. *Radiology* 163 (2), 339–343. doi:10.1148/radiology.163.2.3550878

Mattrey, R. F., Trambert, M. A., Brown, J. J., Bruneton, J. N., Young, S. W., and Schooley, G. L. (1991). Results of the Phase III Trials with Imagent GI as an Oral Magnetic Resonance Contrast Agent. *Invest. Radiol.* 26, S65–S66. doi:10.1097/00004424-199111001-00021

Mattrey, R., Hajek, P., Gylys-Morin, V., Baker, L., Martin, J., Long, D., et al. (1987). Perfluorochemicals as Gastrointestinal Contrast Agents for MR Imaging: Preliminary Studies in Rats and Humans. *Am. J. Roentgenology* 148 (6), 1259–1263. doi:10.2214/ajr.148.6.1259

Mattrey, R. (1989). Perfluorooctylbromide: a New Contrast Agent for CT, Sonography, and MR Imaging. *Am. J. Roentgenology* 152 (2), 247–252. doi:10.2214/ajr.152.2.247

Maurizis, J. C., Azim, M., Rapp, M., Pucci, B., Pavia, A., Madelmont, J. C., et al. (1994). Disposition in Rat of a New Fluorinated, Biocompatible, Non-ionic Telomeric Carrier. *Xenobiotica* 24 (6), 535–541. doi:10.3109/00498259409043256

Mikhail, M. A., Mangioris, G., Best, R. M., McGimpsey, S., and Chan, W. C. (2017). Management of Giant Retinal Tears with Vitrectomy and Perfluorocarbon Liquid Postoperatively as a Short-Term Tamponade. *Eye* 31 (9), 1290–1295. doi:10.1038/eye.2017.157

Moroz, V. V., Maevsky, E. I., Ivanitsky, G. R., Carmen, N. B., Bogdanova, L. A., Lezhneva, I. E., et al. (2007). Emulsion of Perfluoroorganic Compounds as a Means for the Treatment of Disorders of Regional Blood Flow. *Gen. Resusc* III, 49–53.

Moyer, L. C., Timbie, K. F., Sheeran, P. S., Price, R. J., Miller, G. W., and Dayton, P. A. (2015). High-intensity Focused Ultrasound Ablation Enhancement *In Vivo* via Phase-Shift Nanodroplets Compared to Microbubbles. *J. Ther. Ultrasound* 3, 7. doi:10.1186/s40349-015-0029-4

Noveck, R. J., Shannon, E. J., Leese, P. T., Shorr, J. S., Flaim, K. E., Keipert, P. E., et al. (2000). Randomized Safety Studies of Intravenous Perflubron Emulsion. II. Effects on Immune Function in Healthy Volunteers. *Anesth. Analgesia* 91 (4), 812–822. doi:10.1097/00000539-200010000-00009

Olsen, G. W., Burris, J. M., Ehresman, D. J., Froehlich, J. W., Seacat, A. M., Butenhoff, J. L., et al. (2007). Half-Life of Serum Elimination of Perfluorooctanesulfonate, Perfluorohexanesulfonate, and Perfluorooctanoate in Retired Fluorochemical Production Workers. *Environ. Health Perspect.* 115 (9), 1298–1305. doi:10.1289/ehp.10009

Patronas, N. J., Hekmatpanah, J., and Doi, K. (1983). Brain-tumor Imaging Using Radiopaque Perfluorocarbon. *J. Neurosurg.* 58 (5), 650–653. doi:10.3171/jns.1983.58.5.0650

Peng, C., Sun, T., Vykhodtseva, N., Zhang, Y., Power, C., McDannold, N., et al. (2018). Phase Shift Nanoemulsions Facilitated Focused Ultrasound

Nonthermal Ablation in Mice Brain. *The J. Acoust. Soc. America* 144 (3), 1889 doi:10.1121/1.5068283

Phillips, L. C., Puett, C., Sheeran, P. S., Dayton, P. A., Wilson Miller, G., and Matsunaga, T. O. (2013). Phase-shift Perfluorocarbon Agents Enhance High Intensity Focused Ultrasound Thermal Delivery with Reduced Near-Field Heating. *J. Acoust. Soc. America* 134 (2), 1473–1482. doi:10.1121/1.4812866

Pierre, V. C., and Allen, M. J. (2017). *Contrast Agents for MRI: Experimental Methods*. London, UK: Royal Society of Chemistry.

Rasmussen, F. (2008). "Contrast Media, Iodinated, Oily," in *Encyclopedia of Diagnostic Imaging*. Editor A. L. Baert (Berlin, Heidelberg: Springer Berlin Heidelberg), 501–503.

Rettich, T. R., Battino, R., and Wilhelm, E. (2000). Solubility of Gases in Liquids. 22. High-Precision Determination of Henry's Law Constants of Oxygen in Liquid Water fromT=274 K toT=328 K. *J. Chem. Thermodynamics* 32 (9), 1145–1156. doi:10.1006/jcht.1999.0581

Riess, J. G. (2001). Oxygen Carriers ("Blood Substitutes") Raison d'Etre, Chemistry, and Some Physiology Blut ist ein ganz besondrer Saft. *Chem. Rev.* 101 (9), 2797–2920. doi:10.1021/cr970143c

Riess, J. G. (2005). Understanding the Fundamentals of Perfluorocarbons and Perfluorocarbon Emulsions Relevant to In Vivo Oxygen Delivery. *Artif. Cell Blood Substitutes, Biotechnol.* 33 (1), 47–63. doi:10.1081/bio-200046659

Schad, K. C., and Hynynen, K. (2010). In Vitro characterization of Perfluorocarbon Droplets for Focused Ultrasound Therapy. *Phys. Med. Biol.* 55 (17), 4933–4947. doi:10.1088/0031-9155/55/17/004

Servaes, S., and Epelman, M. (2009). Perflubron Residua: 12 Years Following Therapy. *Pediatr. Radiol.* 39 (4), 393–395. doi:10.1007/s00247-008-1139-8

Spahn, D. R. (1999). Blood Substitutes Artificial Oxygen Carriers: Perfluorocarbon Emulsions. *Crit. Care* 3 (5), R93. doi:10.1186/cc364

Spiess, B. D. (2009). Perfluorocarbon Emulsions as a Promising Technology: a Review of Tissue and Vascular Gas Dynamics. *J. Appl. Physiol.* 106 (4), 1444–1452. doi:10.1152/japplphysiol.90995.2008

Tak, S., and Barraclough, M. (2018). Case Report: 'Pseudo-Calcifications': Detection of Perfluorocarbon Residue on a Computed Tomography Scan 15 Years after Liquid Ventilation Therapy at 3 Months of Age. *BMJ Case Rep.* 2018, bcr2017223958. doi:10.1136/bcr-2017-223958

Vakulenko, I. P., Khatsko, V. V., Kuzmenko, O. Y., Voytyuk, V. N., Fominov, V. M., Polulyach-Chornovol, I. F., et al. (2021). Radial Diagnostics of Liquid Focal Liver Formations with Their Identification of a Communications with the Intrahepatic Biliary Ducts. *Khark. Surg. Sch.* 2021 (1), 40–45. doi:10.37699/2308-7005.1.2021.08

Vorob'ev, S. I. (2009). First- and Second-Generation Perfluorocarbon Emulsions. *Pharm. Chem. J.* 43 (4), 209–218.

Vorob'ev, S., Ivanitskii, G., and Makarov, K. (1993). *Perfluorocarbon Emulsions*. Pushchino: Department of Scientific and Technical Information, Russ Acad Sci.

Voynikov, T., Nikolova, I., Suzuki, A., Higashino, H., Petkova, M., and Mega, N. (1990). A Review on the Properties and Applications of Perfluorocarbon Emulsions. *Acta Med. Kinki Univ.* 15 (1), 1–20.

Weers, J. G. (1993). A Physicochemical Evaluation of Perfluorochemicals for Oxygen Transport Applications. *J. Fluorine Chem.* 64 (1-2), 73–93. doi:10.1016/s0022-1139(00)80064-0

Westbrook, C. (2016). "MRI at a Glance," in *At a Glance*. 3rd ed. (Wiley-Blackwell).

Wikström, S., Lindh, C. H., Shu, H., and Bornehag, C. G. (2019). Early Pregnancy Serum Levels of Perfluoroalkyl Substances and Risk of Preeclampsia in Swedish Women. *Sci. Rep.* 9 (1), 9179. doi:10.1038/s41598-019-45483-7

Wolber, J., Rowland, I. J., Leach, M. O., and Bifone, A. (1999). Perfluorocarbon Emulsions as Intravenous Delivery Media for Hyperpolarized Xenon. *Magn. Reson. Med.* 41 (3), 442–449. doi:10.1002/(sici)1522-2594(199903)41:3<442:aid-mrm3>3.0.co;2-7

Wolf, G., Rogowska, J., Gazelle, G., and Halpern, E. (1994). Methods for Quantitative CT Lymphography. *Lymphology* 27, 261–264.

Yermolenko, S. V., Shapovalova, N. V., and Lavrentyev, A. A. (2007). Experience in Using Perfluorane for Severe Sepsis. *Gen. Resusc* III, 67–70.

Zhang, M., Fabiilli, M. L., Haworth, K. J., Padilla, F., Swanson, S. D., Kripfgans, O. D., et al. (2011). Acoustic Droplet Vaporization for Enhancement of Thermal Ablation by High Intensity Focused Ultrasound. *Acad. Radiol.* 18 (9), 1123–1132. doi:10.1016/j.acra.2011.04.012

Conflict of Interest: The authors declare that the research was conducted in the absence of any commercial or financial relationships that could be construed as a potential conflict of interest.

Publisher's Note: All claims expressed in this article are solely those of the authors and do not necessarily represent those of their affiliated organizations, or those of the publisher, the editors and the reviewers. Any product that may be evaluated in this article, or claim that may be made by its manufacturer, is not guaranteed or endorsed by the publisher.

frontiers in Chemistry

REVIEW
published: 19 January 2022
doi: 10.3389/fchem.2021.809676

Nature-Derived and Synthetic Additives to poly(ε-Caprolactone) Nanofibrous Systems for Biomedicine; an Updated Overview

Shahin Homaeigohar[1]* *and Aldo R. Boccaccini*[2]*

[1]School of Science and Engineering, University of Dundee, Dundee, United Kingdom, [2]Institute of Biomaterials, Department of Materials Science and Engineering, University of Erlangen-Nuremberg, Erlangen, Germany

As a low cost, biocompatible, and bioresorbable synthetic polymer, poly (ε-caprolactone) (PCL) is widely used for different biomedical applications including drug delivery, wound dressing, and tissue engineering. An extensive range of *in vitro* and *in vivo* tests has proven the favourable applicability of PCL in biomedicine, bringing about the FDA approval for a plethora of PCL made medical or drug delivery systems. This popular polymer, widely researched since the 1970s, can be readily processed through various techniques such as 3D printing and electrospinning to create biomimetic and customized medical products. However, low mechanical strength, insufficient number of cellular recognition sites, poor bioactivity, and hydrophobicity are main shortcomings of PCL limiting its broader use for biomedical applications. To maintain and benefit from the high potential of PCL, yet addressing its physicochemical and biological challenges, blending with nature-derived (bio)polymers and incorporation of nanofillers have been extensively investigated. Here, we discuss novel additives that have been meant for enhancement of PCL nanofiber properties and thus for further extension of the PCL nanofiber application domain. The most recent researches (since 2017) have been covered and an updated overview about hybrid PCL nanofibers is presented with focus on those including nature-derived additives, e.g., polysaccharides and proteins, and synthetic additives, e.g., inorganic and carbon nanomaterials.

Keywords: polycaprolactone, additive, nanocomposite, blend, core-shell, wound dressing, tissue engineering

OPEN ACCESS

Edited by:
Nicola Maria Pugno,
University of Trento, Italy

Reviewed by:
Ahmed El-Fiqi,
Dankook University, South Korea
Masami Okamoto,
Toyota Technological Institute, Japan

***Correspondence:**
Shahin Homaeigohar
Shomaeigohar001@dundee.ac.uk
Aldo R. Boccaccini
aldo.boccaccini@fau.de

Specialty section:
This article was submitted to Nanoscience, a section of the journal Frontiers in Chemistry

Received: *05 November 2021*
Accepted: *16 December 2021*
Published: *19 January 2022*

Citation:
Homaeigohar S and Boccaccini AR (2022) Nature-Derived and Synthetic Additives to poly(ε-Caprolactone) Nanofibrous Systems for Biomedicine; an Updated Overview. Front. Chem. 9:809676. doi: 10.3389/fchem.2021.809676

INTRODUCTION

Thanks to its promising biocompatibility and low biodegradation rate, poly (ε-caprolactone) (PCL) is among the most widely applied synthetic polymers in biomedicine (Mochane et al., 2019). PCL was developed for the first time in the 1930s by the Carothers group (Natta et al., 1934). Its commercialization was aimed very soon due to the need of biodegradable synthetic polymers, i.e., those that could be degraded *in vivo* by cells and microorganisms (Woodruff and Hutmacher, 2010). Despite early popularity of PCL, it was rapidly outstripped by biodegradable polymers like polylactic acid (PLA) and polyglycolic acid (PGA), due to an emerging need to obtain degradable drug delivery systems able to release cargo in a few days or a few weeks with the carriers totally bioresorbed in 2–4 months after application (Woodruff and Hutmacher, 2010). On the other hand, the medical device market was looking for replacement of metal implants (e.g., nails, screws, plates,

among others) by their biodegradable versions. In this regard, PCL could not be applicable due to its insufficient mechanical properties for such high load bearing applications. Most importantly, it was proven that the polymers with a high resorption rate are less problematic in terms of biological responses compared to those with a lengthy degradation process (e.g., PCL with a 3–4 year degradation cycle). As a result, PCL was ignored for around 2 decades (Woodruff and Hutmacher, 2010). Afterwards, during the 1990s and 2000s, coinciding with a revolution in regenerative medicine with tissue engineering, interest in PCL as a biomedical material resurged. Such renewed interest in PCL originated from its appropriate viscoelastic and rheological properties compared to other biodegradable polymers, rendering its manufacturing simple and its integration into a variety of scaffolds feasible (Lee et al., 2003; Huang et al., 2007; Luciani et al., 2008; Marrazzo et al., 2008).

PCL can be synthesized via ring-opening polymerization (ROP) of ε-caprolactone involving a diverse range of cationic, anionic, and co-ordination catalysts. Additionally, it can be prepared through the free radical ROP of 2-methylene-1-3-dioxepane (Pitt, 1990). In order to catalyze the ROP, non-toxic, efficient catalysts, e.g., stannous (II) 2-ethylhexanoate and to govern PCL's molecular weight, low molecular weight alcohols are typically employed (Woodruff and Hutmacher, 2010). Other than ROP, PCL can be also synthesized through polycondensation of 6-hydroxycaproic (6-hydroxyhexanoic) acid. ROP is advantageous over the polycondensation technique in terms of production of a less polydisperse polymer with a higher molecular weight (Labet and Thielemans, 2009; Siddiqui et al., 2018).

PCL is a hydrophobic and semi-crystalline polymer (depending on its molecular weight, crystallinity varies). PCL is dissolved in a variety of solvents and is readily melted at low to moderate temperatures (59–64°C). Moreover, it can be properly blended with many polymers and biopolymers, thereby being proposed for diverse biomedical applications (Chandra and Rustgi, 1998; Okada, 2002; Nair and Laurencin, 2007). Such features of PCL and its derivatives (blends, composites, and copolymers) led to their wide implementation in drug delivery systems, during the 1970s and 1980s (Woodruff and Hutmacher, 2010). Compared to other available biodegradable polymers, PCL could offer distinct advantages, thereby surpassing other candidates for biomedical applications. For instance, customizable degradation rate and mechanical properties, simple shaping and production that could allow for creation of pore sizes suitable for tissue ingrowth, and the possibility of drug delivery in a controlled manner are important merits of PCL based systems (Woodruff and Hutmacher, 2010). Additionally, PCL could be functionalized by inclusion of various functional groups, rendering it adhesive, hydrophilic, and biocompatible with proper cell-matter interactions. Taking into account the slower degradation rate of PCL compared to its counterparts such as PGA and poly D,L-lactide acid (PDLA), it could be employed in drug delivery systems with a life span of over 1 year and in commercial suture materials (Maxon™) (Woodruff and Hutmacher, 2010). The caprolactone polymers including PCL are mainly degraded via hydrolysis. The first step of hydrolysis involves diffusion of water molecules into the polymer. Subsequently, the polymer undergoes arbitrary fragmentation and eventually major hydrolysis that is intensified by metabolism and phagocytosis. In general, hydrolysis is governed by the size (molecular weight), crystallinity, and hydrophilicity of the polymer, and hydrolysis rate is modulated by temperature and pH of the nearby environment (Lacoulonche et al., 1999; Kim et al., 2012). The hydrolysis (degradation) of PCL solely produces caproic acid, that is a non-toxic metabolite, either removed from the body through urinary secretion or metabolized via the citric acid cycle (Kweon et al., 2003). The bioresorption time of PCL spans from several months to more than 1 year, and can be controlled through copolymerization and hybridization with additives and blending materials (Cohn and Hotovely Salomon, 2005). PCL has also been shown to undergo enzymatic degradation by lipase-type enzymes such as *pseudomonas* lipase (PS) within a short time of 4 days (Gan et al., 1997). Such degradation process is notably faster than hydrolytic degradation that could take up to several years (Li and Vert, 1999). Among the lipase-based enzymes, Aspergillus sp. lipases, which are in fact a type of fungal lipases, have been appealing in recent years due to their industrial application (Contesini et al., 2010; Wang H. et al., 2017). As a result, the degradation behaviour of PCL mediated by Aspergillus sp. Lipases under various environmental conditions (pH, temperature, etc.) has been precisely studied (Hermanová et al., 2012; Hermanová et al., 2013). In this regard, PCL hydrophobicity has been proven to be a hindering factor against rapid enzymatic degradation (Wang H. et al., 2017). Thus, surface treatment of PCL via aminolysis, hydrolysis, laser ablation, etc., and blending or copolymerization of PCL with hydrophilic polymers, e.g., PEG can be considered as solutions to expedite the enzymatic degradation (Wang H. et al., 2017).

PCL can be processed in different physicochemical ways to produce biomedical systems at low cost compared to other aliphatic polyesters. Among all the production techniques, electrospinning is the most widely studied one for development of PCL nanofibrous materials for wound dressing and tissue engineering. The applicability of PCL nanofibers can be extended and their properties can be optimized by employment of benign solvents that assure eco-friendly processing (Liverani et al., 2018; Homaeigohar et al., 2021a) and/or inclusion of additives that raise hydrophilicity, bioactivity, and mechanical stability. In this review, as schematically shown in **Figure 1**, we introduce newly (since 2017) proposed additives and blending materials for PCL electrospun nanofibers that have found application in biomedicine. It is worthy to note that in many studies a combination of various types of additives, e.g. nature derived compounds alongside a drug, has been employed. This feature makes distinct categorization of additives challenging and therefore the overlap of different classes is inevitable.

REINFORCING AND HYDROPHILIZING ADDITIVES

Given the direct impact of nanofiber physicochemical properties on the cell-material interactions, it is crucial to optimize surface

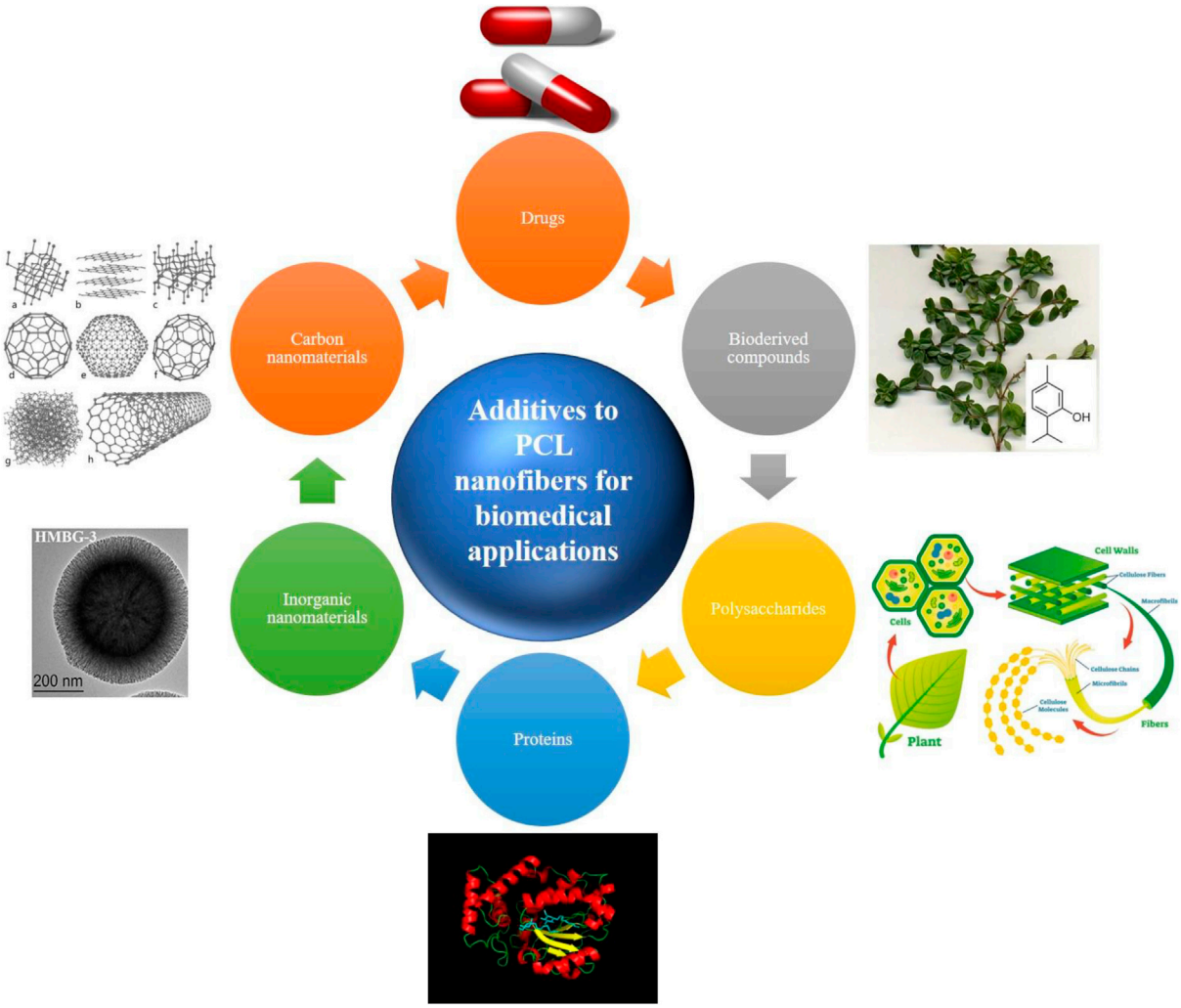

FIGURE 1 | Various classes of additives employed to reinforce biological and physicochemical properties of PCL nanofibers. The used images have been reproduced with permission (inorganic nanomaterials (Wang Y. et al., 2019); CC BY licence, proteins (upload.wikimedia.org/wikipedia/commons/9/95/Sec14p_Protein_Figure.png; CC BY-SA 4.0), polysaccharides (researchoutreach.org/articles/cellulose-nanodefects-key-biofuels-biomaterials-future; CC BY-NC-ND 4.0), bioderived compounds (commons.wikimedia.org/wiki/File:Thyme-thymol; CC BY-SA 4.0), drugs (freepngimg.com/png/26873-pills-photos; CC BY-NC 4.0), and carbon nanomaterials (upload.wikimedia.org/wikipedia/commons/f/f8/Eight_Allotropes_of_Carbon.png; CC BY-SA 3.0).

hydrophilicity and mechanical properties of the PCL nanofibrous biomaterials. The resilience and mechanical strength of nanofiber materials have been proven to affect *in vitro* cell behaviour including migration, proliferation, and differentiation, and also cell shape (Carnegie and Cabaca, 1993; Zhang et al., 2005). Generally, cells are optimally extended and spread on a resilient, flexible underlying material. They exert a tensile force on the substrate, particularly while they migrate. Cells sense the elasticity of the surface they are migrating on by using their integrins, that perform as mechanotransducers. In contrast to a pliable surface, cells have to apply an extremely large tension force to migrate on a notably stiff or rigid material, thus adopting a less extended shape (Gunn et al., 2005; Homaeigohar et al., 2019). Therefore, developing a mechanically compatible PCL nanofiber material, depending on the target tissue and biomedical purpose profoundly matters.

To achieve this goal, a variety of additives have been proposed that raise mechanical properties of PCL nanofibers, particularly in terms of tensile strain, flexural strain, elastic modulus, tensile stress, and thermomechanical strength (Gönen et al., 2016; Adeli-Sardou et al., 2019; Nazeer et al., 2019; Zanetti et al., 2019). In this regard, various fillers such as nanosilicates (Wang et al., 2018), graphene, cellulose nanocrystals, Ag nanoparticles (Leonés et al., 2020), among others, have been incorporated into PCL nanofibers to confer them with improved mechanical properties. Additionally, PCL has been blended with natural (Ren et al., 2017) or synthetic polymers (Nadim et al., 2017) to create mechanically robust blend PCL nanofibers for biomedical applications. **Table 1** tabulates several examples of PCL nanofiber materials that have been mechanically reinforced by inclusion of fillers and blending agents.

TABLE 1 | Mechanically stabilized PCL-based nanofibers for biomedical applications (studies reported after 2017).

Reinforcing additive	Nanofiber carrier material	Additive loading method	Optimized mechanical property	Target application	References
Nanosilicate	PCL	Blend electrospinning	Tensile strength (50.17 Vs. 4.53 MPa for PCL nanofibers)	Bone tissue engineering	Wang et al. (2018)
Gel	PCL	Blend electrospinning	Elastic modulus (105 Vs. 40 MPa for PCL nanofibers)	Bone tissue regeneration	Ren et al. (2017)
CNC	PCL	Blend electrospinning	Tensile strength (3 Vs. 1 MPa for PCL nanofibers)	---	Leonés et al. (2020)
PCL grafted GO	PCL	Blend electrospinning	Tensile strength (14.32 Vs. 5.4 MPa for PCL nanofibers)	---	Bagheri and Mahmoodzadeh (2020)
CNT	PCL	Blend electrospinning	Tensile strength (8.84 Vs. 3.13 MPa for PCL nanofibers)	---	Wang et al. (2017b)
Cartilage-derived ECM	PCL	Blend electrospinning	Tensile strength (3.38 Vs 2.15 MPa for PCL nanofibers)	Cartilage regeneration	Feng et al. (2020)
TPU	PCL	Blend electrospinning	Circumferential tensile strength (7.5 Vs. 6 MPa for PCL nanofibers)	Vascular grafts	Mi et al. (2018)
Nanofibrillated CS	PCL	Blend electrospinning	Tensile strength (6 Vs. 2.57 MPa for PCL nanofibers)	---	Fadaie et al. (2018)

CNC, cellulose nanocrystal; CNT, carbon nanotube; CS, chitosan; ECM, extracellular matrix; Gel, gelatine; GO, graphene oxide; TPU, thermoplastic polyurethane.

Surface hydrophilicity of nanofiber materials has been shown to be a decisive factor in cell-material interaction, particularly on cell adhesion. One important reason is the increased protein adsorption on the surfaces with moderate hydrophilicity (Lee et al., 1998). The improved adsorption of cell-adhesive serum proteins such as vitronectin and fibronectin can highly affect cell adhesion, growth, and morphology (van Wachem et al., 1987; Underwood and Bennett, 1989; Steele et al., 1995). PCL nanofibers are inherently hydrophobic and do not expose polar functional groups on the surface. To address this shortcoming and to improve wettability thus cell interactivity of PCL nanofibers, they have been either surface coated/blended with hydrophilic natural polymers, e.g., collagen (Col), gelatine (Gel), chitosan (CS), etc., or incorporated with polar inorganic nanofillers made of, e.g., Ag and TiO_2 and bio-derived compounds, e.g., *lawsone*, *Nigella Sativa,* etc. (Wang H. et al., 2017; Ghosal et al., 2017; Ren et al., 2017; Adeli-Sardou et al., 2019; Sharifi et al., 2020). In this regard, recently, Li et al. (2021) developed a Col/PCL nanofiber wound dressing with superior wettability and mechanical stability. Col, as a natural (biological) polymer and the main constituent of ECM, has been extensively employed for the repair of damaged skin tissues and wound healing, thanks to its outstanding biocompatibility and inferior antigenicity (Rho et al., 2006; Kubow et al., 2015). However, Col is mechanically unable to support large colonies of cells and is rapidly degraded by enzymes (Engelhardt et al., 2011). Such shortcomings discourage the researchers to benefit from Col in practical wound healing applications (Li et al., 2021). These limitations can be addressed by hybridizing Col with mechanically robust synthetic polymers such as PCL. On the other hand, inherent hydrophobicity issue of PCL, adversely impacting its biological properties including cell adhesion and proliferation, can be resolved (Li et al., 2021). As reported by Li et al. (Li et al., 2021), Col/PCL nanofibers show improved hydrophilicity, reflected in a reduced water contact angle to 40° from 88°, thus offering a high exudate uptake capacity over the course of the wound healing process. Additionally, the most optimum hydrophilicity seen for Col/PCL (1:1) nanofibers brings about raised cell adhesion.

Table 2 tabulates a variety of PCL nanofiber systems that have been hydrophilized by addition of fillers and blending agents.

THERAPEUTIC ADDITIVES

Drugs

Thanks to an enhanced therapeutic effect and a lower toxicity, localized drug delivery with a steady, controlled rate is preferred over systemic drug administration (Zeng et al., 2003). Therefore, development of efficient drug delivery systems has been extensively researched during the past decades. In this regard, the drug carrier material needs to be properly biodegradable, not only shielding the drug against aggressive biological environments, but also allowing the drug to be delivered in a tailored manner (Karuppuswamy et al., 2015).

Electrospun nanofibers have shown promising applicability for topical drug delivery, for example assuring a steadier drug release compared to cast films (Kenawy et al., 2002). This feature originates from the high surface area of nanofibers and interconnectivity of the nanofibrous mat, allowing high permeability of drug molecules and other therapeutic agents such as peptides, proteins, and antibodies, already incorporated into or loaded onto the nanofibers (Son et al., 2014). In this regard, various biodegradable polymers including PCL have been investigated to create nanofibrous drug delivery systems for wound healing and tissue engineering. It has been shown that tissue engineering scaffolds loaded with therapeutic agents, e.g. antibacterial, anti-inflammatory, and anti-cancer synthetic or natural drugs, offer a higher tissue regeneration efficiency (Jayakumar et al., 2011).

Tetracycline (TC) is an antibiotic that is placed within the World Health Organization (WHO)'s list of Essential Medicines,

TABLE 2 | Hydrophilized PCL-based nanofibers for biomedical applications (studies reported after 2017).

Hydrophilic additive	Nano/microfiber carrier material	Additive loading method	Reduced water contact angle (from–to)	Target application	References
Lawsone	PCL/Gel core-shell	Blend electrospinning	116°–111°	Skin tissue regeneration	Adeli-Sardou et al. (2019)
Gel	PCL	Blend electrospinning	127°–57°	Bone tissue regeneration	Ren et al. (2017)
NS	PCL	Blend electrospinning	107°–46°	Wound healing	Sharifi et al. (2020)
CS	CNT/PCL	Surface coating via immersion of the nanofibers in a CS solution	128.4°–14.7°	---	Wang et al. (2017b)
PEO	PCL	Blend electrospinning	115.35°–10.86°	Drug delivery	Eskitoros-Togay et al. (2019)
Col	PCL	Coating the nanofibers	88°–40°	Skin tissue engineering	Ghosal et al. (2017)
TiO_2	PCL	Blend electrospinning	88°–80°	Skin tissue engineering	Ghosal et al. (2017)
Nano hydroxyapatite	PCL	Blend electrospinning	104°–98°	Bone tissue regeneration	Perumal et al. (2020)

Col, collagen; NS, nigella sativa.

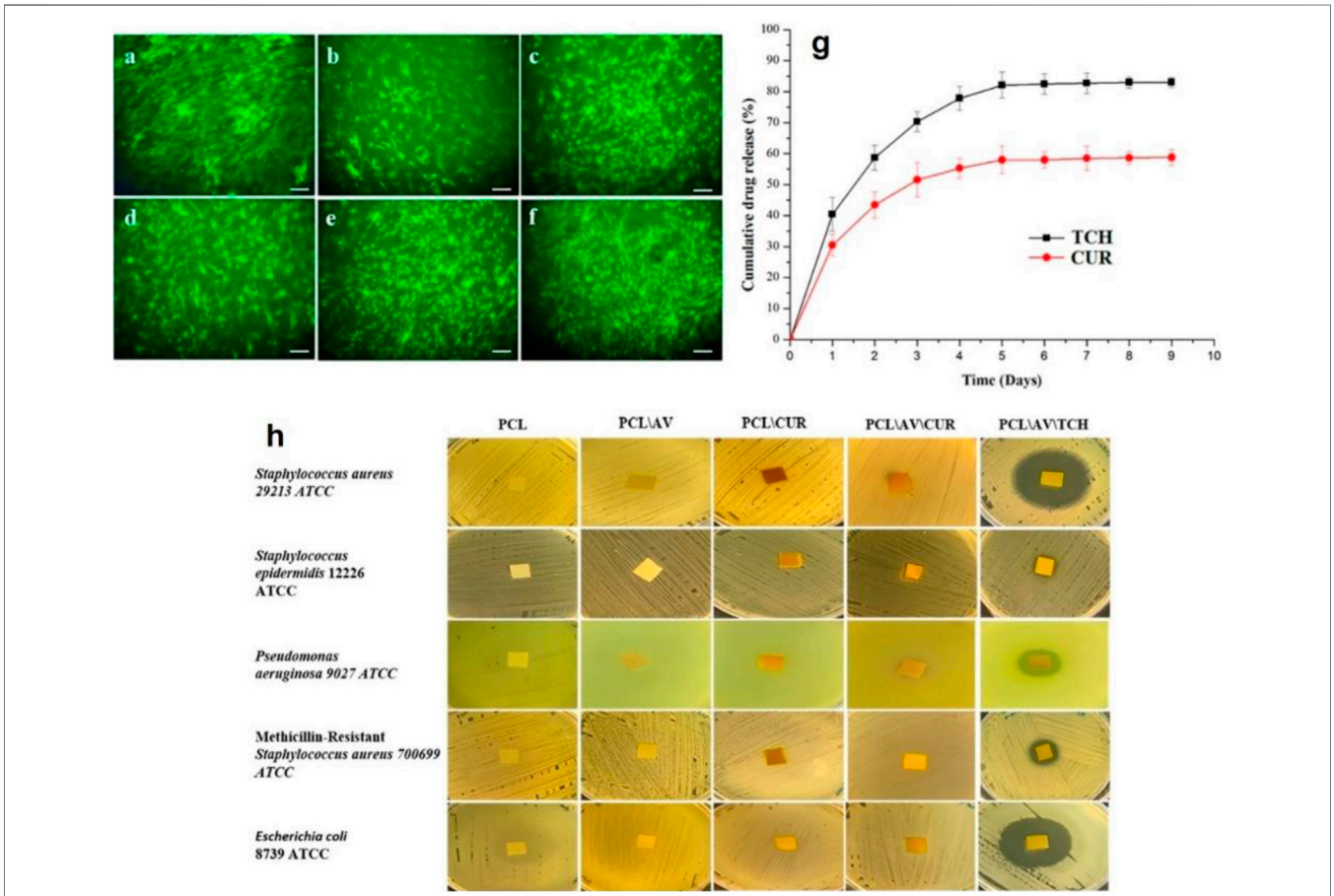

FIGURE 2 | Live fibroblast cells present on **(A)** control, **(B)** PCL nanofibers, **(C)** AV/PCL nanofibers, **(D)** CUR/PCL nanofibers, **(E)** AV/CUR/PCL nanofibers, and **(F)** AV/TCH/PCL nanofibers (scale bars represent 50 μm). **(G)** TCH and CUR release profiles of the AV/CUR/PCL and AV/TCH/PCL nanofibers over a 9-days time period. **(H)** Antibacterial activity of the drug loaded PCL nanofiber systems. The images were reproduced under CC BY licence (Ezhilarasu et al., 2019), Copyright 2019, MDPI.

which includes the vital medications necessary for any basic health system (Karuppuswamy et al., 2015). As a proven fact, steady release of TC facilitates the proliferation of fibroblasts and osteoblasts and properly limits infections, when used as bone and skin ointments (Karuppuswamy et al., 2015). PCL nanofibers have been employed as a TC hydrochloride (TCH) carrier for skin

tissue engineering. For example, synergistically, alongside aloe vera (AV) and curcumin (CUR), the TCH-AV-CUR/PCL nanofibers are able to induce a proper fibroblast cell viability, as shown in **Figures 2A–F** (Ezhilarasu et al., 2019). Compared to the composite PCL nanofibers, the neat ones induced an insignificant proliferation rate most likely due to lack of cell recognition moieties that could encourage cell-nanofiber interaction and cell adhesion. **Figure 2G** shows how steady CUR and TCH are released form the PCL nanofibers over a 9-days time period. However, surface residence of some part of the loaded drugs brings about an initial burst release of 30.1% (CUR) and 41.5% (TCH). Moreover, the appropriate release profile of TCH indicated a favourable antibacterial performance, as shown in **Figure 2H**, represented by formation of clear zones around the TCH-AV/PCL nanofiber mat.

Oxytetracycline hydrochloride (OTC) is a member of the TC antibiotics family that plays a bacteriostatic role via hampering the synthesis of bacterial protein. These antibiotics are lethal to an extensive range of both Gram-negative and Gram-positive bacteria (Chopra and Roberts, 2001). TC antibiotics are excreted in the gingival crevicular fluid (GCF) and firmly adsorb to the tooth surface. As a result, TC antibiotics are preserved in the oral cavity for a long time (Baker et al., 1983), and can be largely applied for periodontal disease treatment. PCL nanofibers have been considered as a carrier of OTC for the mentioned application (Dias et al., 2019). Alongside OTC, ZnO nanoparticles have also been employed to further support the system's antibacterial activity. ZnO's antibacterial effect is fulfilled through three main mechanisms: 1) generation of reactive oxygen species (ROS) on the ZnO surface (Lakshmi Prasanna and Vijayaraghavan, 2015; Sirelkhatim et al., 2015), 2) disintegration of cell (bacteria) membrane upon contact with the ZnO nanoparticles and subsequent interaction between the nanoparticles and the cell content (Joe et al., 2017), and 3) release of bactericidal Zn^{2+} ions from ZnO when subjected to the aqueous medium (Joe et al., 2017). In addition to an enhanced antibacterial activity, OTC/PCL nanofibers containing ZnO nanoparticles were shown to offer a steadier OTC release behaviour, most likely due to electrostatic interaction between the additives, i.e. the drug and the nanoparticles. Despite entrapment of OTC within PCL nanofibers, hydrolysis of the nanofibers eventually leads to the total release of the antibiotic into the periodontal pockets after 5 days. While an enhanced antibacterial effect for the system comprising both OTC and ZnO was expected, the challenging release of OTC led to a weaker antibacterial efficiency (97.5%) compared to the OTC/PCL nanofibrous system (98%). On the other hand, while ZnO is beneficial in terms of antibacterial activity, it might also induce cytotoxicity. According to a study by Cho et al. (Cho et al., 2013), among ZnO, CuO, SiO_2, and Co_3O_4 nanoparticles, ZnO and CuO showed the highest level of cytotoxicity *in vitro* and could impose acute lung inflammogenicity *in vivo*.

Table 3 tabulates the studies dealing with drug incorporated PCL and PCL blend nanofibers carried out after 2017.

Bioderived Therapeutic Compounds

In addition to drugs, natural substances or bio-derived agents are also considered as a potential therapeutic additive to the PCL nanofibers for biomedical applications. For instance, resveratrol (RSV) is a natural substance with therapeutic effects against periodontal disease. It shows anti-oxidative and anti-inflammatory effects that alleviate the adverse consequences of the periodontal disease such as lower generation of NO (Rizzo et al., 2012), excessive expression of vascular endothelial growth factor (VEGF) by human gingival fibroblasts, and reduced permeability of vessels (Núñez et al., 2010). Furthermore, RSV hampers the large production of chemokines, inflammatory cytokines, and the factors driving leucocyte differentiation (Fordham et al., 2014). Performing as a blocker for the aryl-hydrocarbon receptor, RSV positively influences periodontal tissue regeneration (Singh et al., 2000) and notably declines bone tissue loss (Casati et al., 2013). Despite the mentioned merits, RSV is unstable under *in vivo* conditions thanks to its undesired biopharmaceutical characteristics such as poor solubility, fast metabolism, and insufficient chemical resistance. Accordingly, there is a need to creation of a carrier system that tackles the biopharmaceutical challenges and thereby maximizes the prophylactic and therapeutic capacity of RSV (Amri et al., 2012). In this regard, nanofibers are employed to develop state of the art drug delivery systems that can hold RSV and similar bioderived agents and release them in a tailored manner through engineering of their composition and morphology (Zamani et al., 2010; Zupančič et al., 2015). Additionally, having an extensive surface-to-volume ratio, nanofibers tend to stick to the periodontal pocket tissue and due to their specific morphology allow for penetration of the gingival crevicular fluid (GCF) through them. This feature declines the possibility of removal of the delivery system from the periodontal pockets, in contrast to less porous chip or film shaped counterparts (Jain et al., 2008; Pelipenko et al., 2015). One of the most suitable materials for the synthesis of RSV carrier nanofibers is PCL. In this regard, Zupancic et al. (Zupančič et al., 2015) included RSV in the PCL nanofibers and validated its applicability for periodontal disease treatment. According to their study, RSV was released steadily from PCL nanofibers. However, at the lower RSV concentrations, release took place at a slower rate owing to hydrophobic interaction and hydrogen bonding between RSV and PCL.

Plant polyphenols include a variety of compounds with several phenolic functionalities and are synthesized by the majority of higher plants as secondary metabolites. Such compounds have been proven to show chemopreventive, cardioprotective, and neuroprotective properties (Havsteen, 2002; Williams et al., 2004). More importantly, plant polyphenols could block the formation pathway of malignant tumors, through inactivating carcinogen and provoking the carcinogen-detoxifying systems (Birt et al., 2001). As an example, Epigallocatechin-3-O-gallate (EGCG), a well-known polyphenolic compound commonly found in green tea, shows a preventive role against cancer (Kim et al., 2012). This compound hinders formation of tumor *in vivo* and offers anticancer effects *in vitro* (Moyers and Kumar, 2004), when altering the release (expression) of

TABLE 3 | Drug loaded PCL-based nanofibers for biomedical applications (studies reported after 2017).

Drug	Nano/microfiber carrier material	Drug loading method	Therapeutic function	Target application	References
TCH	PLA/Gel/PCL	Blend electrospinning	Antibacterial effect	Dental implant coating	Shahi et al. (2017)
TCH	GO/Gel/PCL	Blend electrospinning	Antibacterial effect	Neural tissue engineering	Heidari et al. (2019)
TNZ	Chitosan/PCL	Blend electrospinning	Antibacterial effect	Treatment of periodontitis	Khan et al. (2017)
BSA	PLA/PCL	Blend electrospinning	Drug model	---	Herrero-Herrero et al. (2018)
Ketoprofen	PCL/Gel	Blend electrospinning	Anti-inflammatory effect	Wound dressing	Basar et al. (2017)
Cefazolin	PCL	Blend, emulsion, and co-axial electrospinning	Antibacterial effect	---	Radisavljevic et al. (2018)
Phenytoin	PVA (core)/PCL (shell)	Core-shell electrospinning	Proliferative effect	Tissue regeneration and wound healing	Mohamady Hussein et al. (2021)
Doxorubicin	PAMAM-PCL/PCL	Blend electrospinning	Chemotherapeutic effect	A delivery system of anticancer drugs	Bala Balakrishnan et al. (2018)
Curcumin	PEDOT NP/PCL	Blend electrospinning	antibacterial, antiviral, antifungal, and anticancer	---	Puiggalí-Jou et al. (2018)
Ibuprofen	PCL	Blend electrospinning	Anti-inflammatory effect	---	Kamath et al. (2020)
Doxycycline	PEO/PCL	Blend electrospinning	Antibacterial effect	---	Eskitoros-Togay et al. (2019)
TC/β-cyclodextrin	PCL	Blend electrospinning	Antibacterial effect	Treatment of periodontitis	Monteiro et al. (2017)

BSA, bovine serum albumin; NP, nanoparticle; PLA, polylactide acid; PEDOT, poly (3,4-ethylenedioxythiophene); PEO, polyethylene oxide; PAMAM, poly (amido-amine); PVA, polyvinyl alcohol; TNZ, tinidazole.

the main molecules involved in transcription and cell cycle progression. It also triggers the mitogen-driven protein kinase cascade and eventually inhibits telomerase (Nam et al., 2001). Caffeic acid (CA), a plentiful hydroxycinnamic acid, is another plant polyphenol compound typically found in several plant-originated materials (Caccetta et al., 2000). Dietary CA can be easily absorbed through gut and enters into the blood plasma with a concentration at micromolar levels. CA induces various anticarcinogenic, antimutagenic, anti-inflammatory, and antioxidative effects (Chung et al., 2006). As reported by Chung et al. (Chung et al., 2004), CA can potentially drive apoptosis in the cancer cell lines and as a result it inhibits tumor growth *in vivo*. Benefitting from the anticancer properties of CA and EGCG, Kim et al. (Kim et al., 2012) developed CA and EGCG incorporated PCL nanofibers to assure a long term cancer treatment following surgery. No burst release of polyphenols was recorded after loading into the PCL nanofibers and the plant-based compounds were released in a controlled manner. As a result, H_2O_2 was generated that could optimally activate caspase-3 of gastric cancer cells and eventually induce cell apoptosis.

Table 4 tabulates the main bioderived compounds that have been investigated as an additive to PCL nanofibers for biomedicine.

BIOACTIVE ADDITIVES

Blending Bioagents (Polysaccharides)

Natural polymers, e.g., chitosan, alginate, and lignin, can play a structural/supportive role for PCL nanofibers raising their functionality. Lignin, that is commonly found in the vascular plants' cell walls, is ranked second among organic molecules in terms of abundancy (Wang D. et al., 2019). It comprises phenylpropanes and monolignols in different ratios depending on the type of the plant source and structurally is a randomly cross-linked polymer (Wang D. et al., 2019). Each year the pulp industry produces over 70 million tons of lignin by-products, thereof only 2% is commercialized as a constituent of adhesives, surfactants and dispersants for rubbers and plastics (Norgren and Edlund, 2014). Lignin is highly durable, thermally resistant, and biocompatible. Moreover, it shows desirable antibacterial activity and protects the cells against oxidative stresses. Therefore, it is potentially applicable for various healthcare purposes (e.g., as a drug carrier material for cancer treatment, antibacterial material, and free-radical scavenger) (Naseem et al., 2016). Nevertheless, lignin is quite brittle, possesses a largely intricate three-dimensional (3D) structure, and is incompatible with apolar polymers (Sen et al., 2015). Such shortcomings have motivated researchers to develop lignin biomaterials with proper elasticity and homogeneity. In this regard, one promising solution is blending of lignin with a polar polymer. The presence of phenolic hydroxyl group in lignin that can properly form hydrogen bonds with the polymer's electron accepting groups such as carbonyl and ether groups, enable creation of a homogenous lignin/polymer blend. PCL is considered a superior candidate for this objective, and lignin/PCL blends offer remarkable miscibility, thereby favourable mechanical and biological property, and also enhanced functionality (e.g., by exposure of hydroxyl groups) (Li et al., 2001; Salami et al., 2017). Wang et al. (Wang D. et al., 2019) developed a lignin/PCL blend nanofiber system that could benefit from the functionality of lignin to induce biomineralization and to form an integrated bioactive, osteoconductive bone-mimicking hydroxyapatite (HA) layer on the nanofibers, **Figure 3A**. Possessing a plethora of hydroxyl groups including aliphatic and phenolic hydroxyl

TABLE 4 | Bioderived compound loaded PCL nanofibers for biomedical applications (studies carried out since 2017).

Bioderived compound	Nano/microfiber carrier material	Loading method	Therapeutic function	Target application	References
Carvacrol	PCL	Blend electrospinning	Antimicrobial and anti-oxidative effects	---	Tampau et al. (2017)
Thymol	Mesoporous silicon dioxide NP/PCL	Physical blending and electrospinning	Antibacterial activity	Wound dressing	Gámez et al. (2020)
Spirulina	Alginate/PCL	Blend electrospinning	Anti-inflammatory and anti-oxidative effects	Wound dressing	Kim et al. (2018)
Calendula officinalis/ Gum Arabic/Zein	PCL	Suspension, and two nozzle electrospinning	Calendula officinalis: blood coagulation activity, antibacterial, antiseptic, antiviral, antifungal, anti-inflammatory, free radical inhibitors, antioxidant activity Gum Arabic: hemostatic, antibacterial and antioxidant activities Zein: antioxidative activity	Skin regeneration	Pedram Rad et al. (2019)
Nigella sativa	PCL	Blend electrospinning	Antibacterial activity	Wound healing	Sharifi et al. (2020)
Wattakaka volubilis	PCL	Blend electrospinning	Bone regeneration effect	Bone and cartilage tissue engineering	Venugopal et al. (2019)
Tridax procumbens	PCL	Surface deposition	Antibacterial activity	Wound healing	Suryamathi et al. (2019)
Peppermint essential oil	PCL	Blend electrospinning	Antibacterial activity	Wound healing	Unalan et al. (2019)
Inula graveolens	PCL	Blend electrospinning	Antimicrobial and anti-oxidative effects	Not reported	Al-Kaabi et al. (2021)

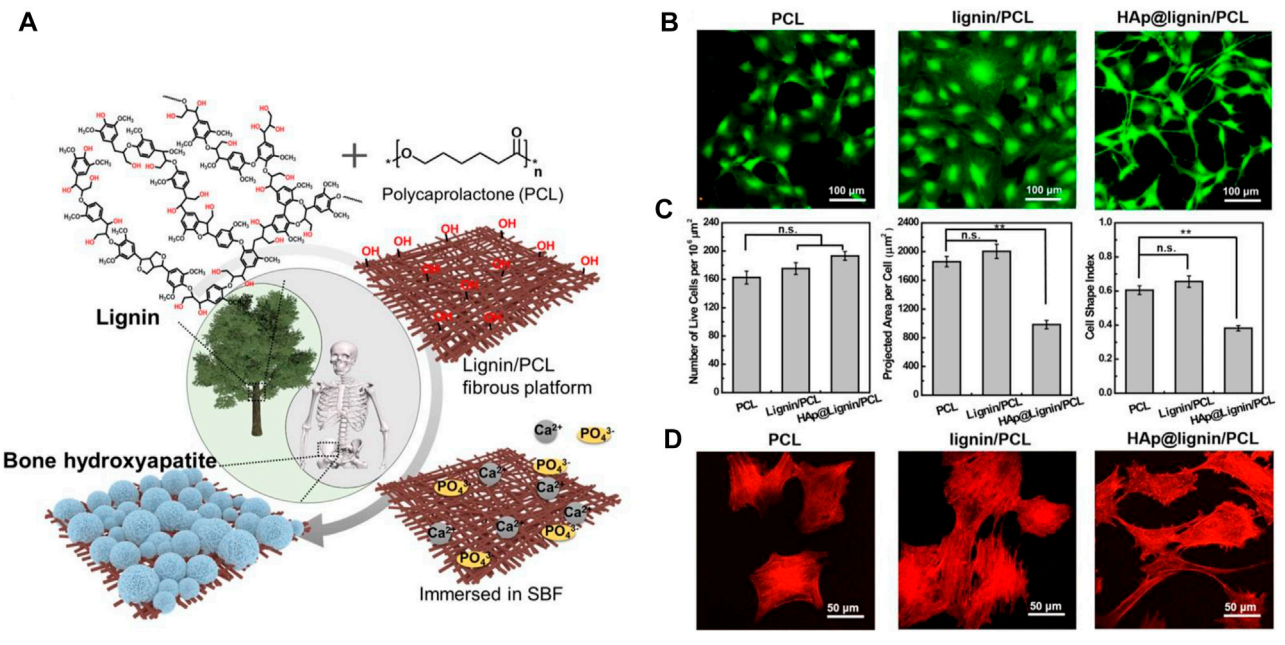

FIGURE 3 | (A) Schematic diagram illustrating the biomineralization process taking place on the surface of lignin/PCL nanofibers thanks to abundance of hydroxyl groups that facilitate nucleation and growth of the SBF's calcium and phosphate ions. *In vitro* biocompatibility test of the HA-lignin/PCL nanofibers, validated through **(B)** LIVE/DEAD assay on the MC3T3-E1 cells after 48 h incubation in the presence of the nanofibers, **(C)** live cell density/10^6 μm^2 (left), projected cell area (middle), Cell shape index (CSI) analysed based on the fluorescent images (right). The CSI indicates how circular a cell is. It ranges from 0 (linear) to 1 (circle) (**$p < 0.01$, n. s not significant). **(D)** Cytoskeleton configuration of the MC3T3-E1 cells present on the nanofibers. Reproduced with permission. (Wang D. et al., 2019), Copyright 2019, American Chemical Society.

groups, lignin can expose many reducing sites for metal ions, whereby enabling the biomineralization (nucleation and growth) of HA via co-deposition of Ca^{2+} and phosphate ions. The HA-lignin/PCL nanofibrous scaffold offers a bioactive platform that encourages the adhesion and proliferation of osteoblastic cells, **Figures 3B–D**.

Alginate is a well-known anionic polysaccharide that is derived from seaweed and contains guluronic acid and mannuronic acid units (Homaeigohar et al., 2019). By forming an ionic bond between the carboxylate group of alginate's backbone and a positively charged crosslinking agent, e.g., Ba^{2+}, Al^{3+}, Ca^{2+}, and Zn^{2+} a hydrogel is created (Shi et al., 2016). Offering desirable biocompatibility, enzymatic degradability, insignificant inflammatory reaction, and chemical flexibility and imitating the 3D structure of extracellular matrix (Kim and Kim, 2014), alginate hydrogels have been frequently applied for the development of tissue engineering scaffolds (Marrella et al., 2017; Reakasame and Boccaccini, 2017) and drug delivery systems (Guarino et al., 2018). Alginate can be coupled with PCL to form blend and core-shell nanofibers with drug delivery ability (Kim et al., 2018). Regarding the latter case, Kim et al. (Kim et al., 2018) devised a core-shell nanofibrous dressing made of PCL (shell) and alginate (core) that could steadily release *Spirulina* as a bioactive material, already incorporated in the core segment. The as-developed dressing material also showed high water uptake capacity.

As a polysaccharide biopolymer, chitosan (CS) is derived from incomplete deacetylation of chitin. It contains many functional amine and hydroxyl groups and thus shows an exclusive polycationic nature and chelating and film-forming properties. As a proven fact, N-acetyl D-glucosamine as a constituent of chitosan drives cell proliferation and hemostasis, thereby accelerating the wound healing process (Keong and Halim, 2009; Patrulea et al., 2015). Chitosan is optimally biocompatible and does not induce adverse reactions when exposed to human cells. Additionally, it is readily biodegraded by enzymes to non-harmful by-products (Chou et al., 2015). Causing prompt blood clotting, chitosan-based bandages and hemostatic products have been approved by the US FDA (Wedmore et al., 2006). Thanks to a non-desirable exceedingly high viscosity of chitosan solutions, their processing via electrospinning is challenging. Moreover, chitosan nanofibers typically show inferior mechanical properties and are unstable when exposed to aqueous media (Cr et al., 2018). As a result, they are commonly blended with biocompatible synthetic polymers such as PCL. For instance, curcumin (CUR)/chitosan (CS) has been blended with PCL as a nanofibrous wound dressing with antioxidant, antibacterial, and cell proliferative effect (Fahimirad et al., 2021). Such blend nanofibers were subsequently surface decorated with electrosprayed curcumin loaded chitosan nanoparticles. According to a variety of biological tests including antibacterial test, *in vitro* cell culture test, *in vivo* wound healing assay, and histological analysis, the hierarchical, blend nanofibers were successful in induction of a wound healing effect in the methicillin-resistant *Staphylococcus aureus* (MRSA) infected wounds. According to the *in vivo* tests, in the presence of PCL/CS/CUR nanofibers, wounds are re-epithelized faster, thereby accelerating the wound closure. In fact, such a consequence enables the wound to be further healed and the damaged skin tissue to be regenerated (Borena et al., 2015). Particularly, PCL/CS/CUR nanofibers that were electrosprayed with CUR/CS nanoparticles provoked the wound healing process, reflected in 96.25 and 98.5% wound healing percentage for the MRSA treated and untreated wounds, respectively.

Biomolecules (Proteins)

The poor bioactivity and insufficient number of cellular recognition sites (biochemical cues) are major shortcomings of PCL nanofiber mats that lead to lower cellular activities such as cell adhesion, proliferation, and migration, and thus hinder their extensive use in biomedicine (Homaeigohar et al., 2021a). On the other hand, the *in vivo* interaction of the PCL nanofibers is crucial to avoid foreign body reactions such as infection, inflammation, embolization, and thrombosis. To tackle the mentioned bottlenecks and to achieve the desired biological features, PCL has been blended with hydrophilic biomolecules (proteins), e.g., collagen (Lee et al., 2008), gelatine (Anjum et al., 2017; Jiang et al., 2017), bovine serum albumin (BSA) (Homaeigohar et al., 2021a), and silk fibroin (Nazeer et al., 2019) among others.

As a general strategy to improve bioactivity of synthetic biomaterials including PCL, natural polymers with cell recognition sequences are hybridized to modulate the cell-material interactions (Shakesheff et al., 1998; Langer, 2000; Entcheva et al., 2004). Many ECM proteins possess the RGD (arginine-glycine-aspartate) motif, where cells adhere to. The cell adhesion is governed by the interaction of integrins, i.e., cell surface (membrane) receptors to the ligands available in the ECM proteins (Jabbari, 2011). RGD coupled polymers typically show increased cell adhesion and proliferation, as previously validated for fibroblasts (Collier and Segura, 2011) and osteoblasts (Benoit and Anseth, 2005).

In a recent study (Homaeigohar et al., 2021a), we enhanced the bioactivity and cell-material interaction of PCL nanofibers by inclusion of BSA. The BSA protein is obtained from cow blood which is an abundant by-product in the cattle industry (Homaeigohar et al., 2020). Therefore, BSA can be used as a commercial, low cost biomolecule for the purpose of biofunctionalization of the PCL nanofibers at a large scale. The BSA/PCL nanofibers were proved to be bioactive as reflected in the formation of inorganic minerals (calcium carbonate) on the nanofiber surface when submerged in simulated body fluid (SBF). Additionally, the formation of hydrogen bonding between the functional groups of PCL and BSA led to a more profound mechanical stability of the BSA/PCL nanofiber mats, as validated through a tensile test as well as a hydrolysis test. As seen in **Figures 4A–F**, in contrast to the BSA/PCL nanofibers, neat PCL nanofibers were notably degraded after one and 3 months in phosphate buffered saline (PBS). Particularly, after 3 months, PCL nanofibers were crumpled and transformed to spheres and their dominant fraction disappears. The positive impact of BSA is not limited to improvement of structural properties of PCL nanofibers, but biological properties were also enhanced. According to the WST-8 cell viability results, fibroblast (NIH3T3) cells could adequately interact with the BSA/PCL nanofibers and properly proliferated when exposed to them, **Figures 4G–I** (Homaeigohar et al., 2021a). This finding is promising with respect to the wound healing process wherein fibroblasts play a major role.

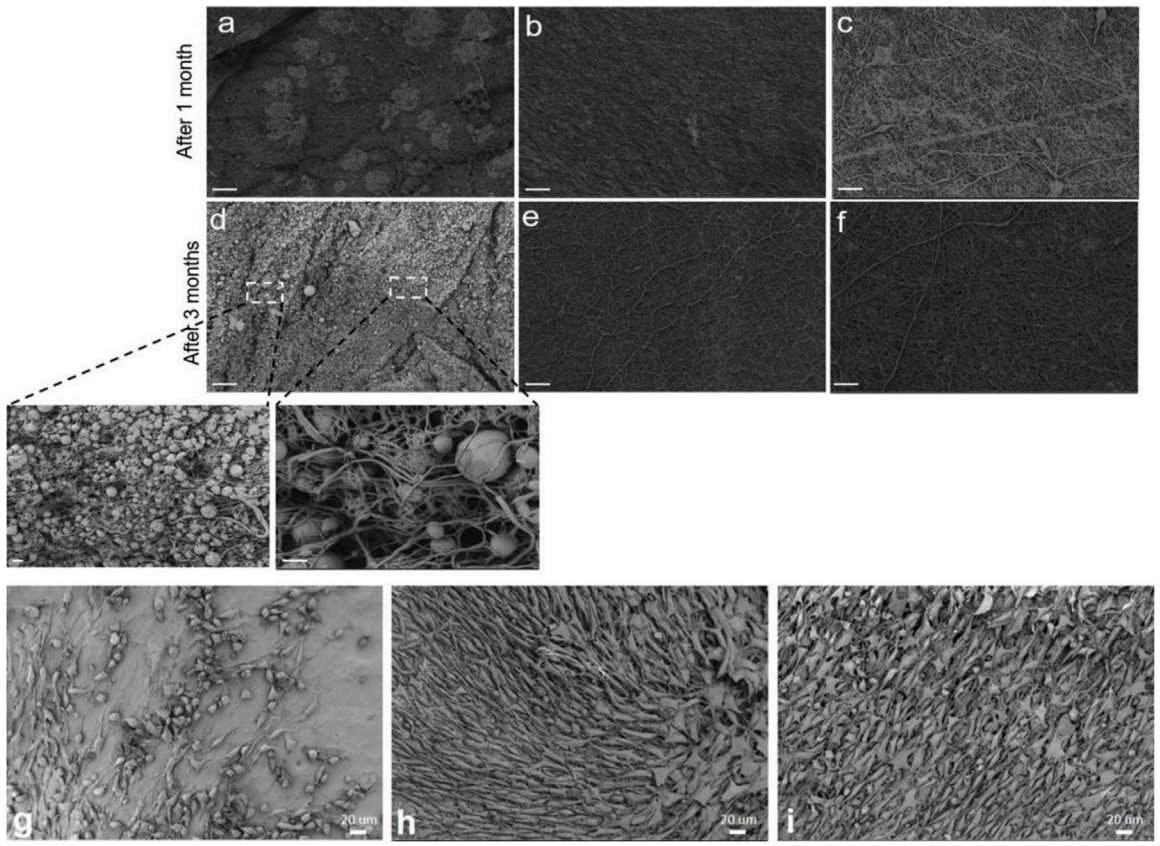

FIGURE 4 | Time dependent hydrolytic degradation process in PBS visualized by SEM images for: PCL nanofibers **(A,D)**, 1 wt% BSA/PCL nanofibers **(B,E)**, and 3 wt% BSA/PCL nanofibers **(C,F)** (scale bars **(A–F)** 20 μm and inset images of **(D)** 1 μm (right) and 3 μm (left)). SEM images represent the NIH 3T3 cell population cultured on: **(G)** PCL nanofibers, **(H)** 1 wt% BSA/PCL nanofibers, and **(I)** 3 wt% BSA/PCL nanofibers, after 4 days. Reproduced with permission. (Homaeigohar et al., 2021a), Copyright 2021, Elsevier.

Other than blending, surface treatment of PCL nanofibers and their decoration with biomolecules have been also investigated. For instance, the PCL nanofibers surface can be carboxylated through plasma treatment, allowing for adhesion of protein molecules based on a covalent bond between carboxyl and protein (platelet-rich plasma (PRP))'s amine groups (Miroshnichenko et al., 2019). This simple and technologically feasible strategy enables human fibroblasts to adhere, to spread, and to grow on the PRP/PCL nanofibers. Such a biofunctionalized PCL nanofiber system can be potentially employed for wound healing, given the proper, stable immobilization of PRP assuring its long-lasting biological activity, particularly within the harsh medium of wounds (Miroshnichenko et al., 2019).

As a natural protein, silk fibroin (SF)'s biocompatibility has justified its extensive applicability in biomedicine, e.g., pertaining to bone and skin tissue engineering (Koh et al., 2015; Ribeiro et al., 2017; Sang et al., 2018). *Bombyx mori* (*B. mori*) silk fibroin comprises two distinct chain polypeptides in terms of molecular weight (i.e., light and heavy chain with Mw~26 and 390 kDa, respectively) that are coupled via a disulfide bond (Zhou et al., 2000). The SF fibers are coated with sericin, i.e., a hydrophilic protein (20–310 kDa), that is removed via the degumming process (Inoue et al., 2000). As proven in literature (Nazeer et al., 2019), incorporation of SF in PCL nanofibers can optimize biomechanical properties as well as fibroblast cell proliferation. The latter feature originates from improved hydrophilicity of the PCL nanofibers after inclusion of SF that performs as a cell anchorage site and emanates polar amine and hydroxyl groups. As a proven fact, SF's RGD sequence positively affects the adhesion of mammalian cells (such as stem cells, fibroblasts, and osteoblasts) (Sofia et al., 2001; Chen et al., 2003).

Gelatine (Gel), as a conventional natural polymer, is synthesized via incomplete hydrolysis of collagen. In comparison with collagen, Gel possesses a lower molecular weight rendering its electrospinning easier. On the other hand, its integrin anchorage zones are abundant, allowing for better cell adhesion, cell migration, and cell differentiation (Nichol et al., 2010). By coupling Gel and PCL, their respective deficiencies are properly addressed (Gloria et al., 2010; Pok et al., 2013), and the Gel/PCL hybrid can be applicable with respect to reconstruction of skin (Chong et al., 2007), tooth (Yang et al., 2010), nerve (Ghasemi-Mobarakeh et al., 2008), and muscle tissues (Kim et al., 2010). The Gel/PCL nanofibers are properly bioresorbable. As

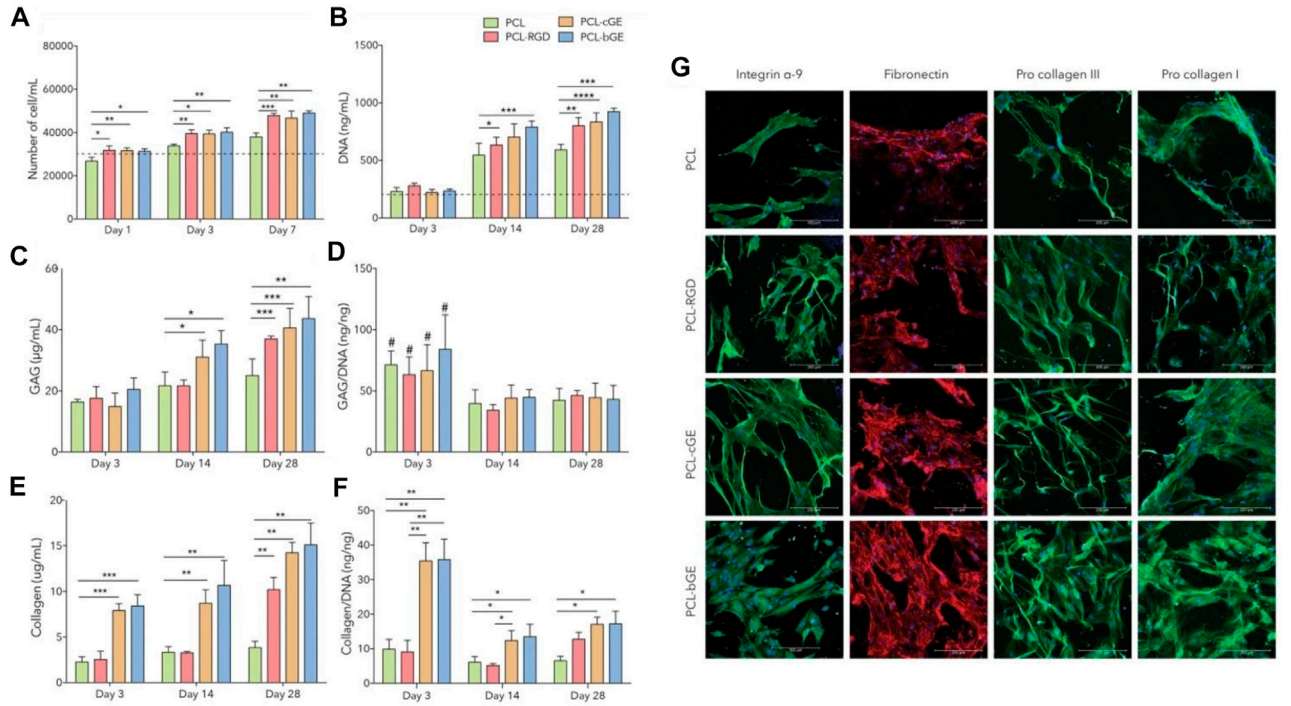

FIGURE 5 | Gel/PCL nanofibers provoke the generation of ECM components by hSKPs. **(A)** hSKPs cell proliferation, **(B)** DNA content of the cells rises over the course of co-culture of the cells and the blended nanofibers implying the impact of Gel and RGD on the cell proliferation. PCL-cGE and PCL-bGE represent Gel coated and Gel blended PCL nanofibers, respectively. In (a&b), the dotted line is representative of primary cell number and DNA content, respectively, **(C)** The amount of GAG secreted in adjacent to different classes of the nanofibers, **(D)** GAG/DNA ratio of the nanofibers (#, i.e., $p < 0.05$ implies a statistically significant difference between day 3 and day 14/day 28, **(E)** The total amount of secreted collagen, **(F)** Collagen/DNA ratio (****, ***, **, and * represent $p = 0.0001$, $p < 0.001$, $p < 0.01$ and $p < 0.05$, respectively). **(G)** Immunofluorescent images show the cellular activities of hSKPs on the Gel/PCL nanofibers, represented by expression of integrin α-9 (green), fibronectin (red), and procollagen I & III (green). Reproduced with permission. (Anjum et al., 2017), Copyright 2017, Nature.

mentioned earlier, PCL can be degraded through several mechanisms involving chemistry and enzymatic activities. On the other hand, Gel is degraded by stromelysin and gelatinases (Atkinson et al., 1992), that are released by epithelial cells, fibroblasts, etc., for instance over the course of the inflammatory phase of wound healing and affect cell migration in the proliferative phase (Clark et al., 2007).

As a skin regenerating material, Gel/PCL nanofibers could stimulate endogenous wound healing and allow for controlled delivery of dermal progenitors (adult human skin-derived precursor cells (hSKPs)). As Anjum et al. (2017) reported, when seeded with adult hSKPs, the composite nanofibers provoke the deposition of sulphated glycosaminoglycans (GAG) and extracellular matrix proteins (Col) (**Figures 5C,E**). Two distinct classes of Gel/PCL hybrid nanofibers were developed as Gel coated and Gel blended PCL nanofibers for the treatment of skin wounds. In their study, as a control group, PCL nanofiber surfaces were also coated with GRGDS, i.e., a cell binding protein originated from fibronectin, via aminolysis. As compared to the hSKP cells cultured with the neat PCL nanofibers, the total DNA content of those cultured with the PCL-RGD and Gel/PCL nanofibers was at a higher level, implying larger proliferation rate of the cells exposed to the modified and blend nanofibers (**Figures 5A,B,D,F**). Moreover, the hSKPs seeded on the nanofiber mats secreted fibronectin, i.e., a vital constituent of the ECM that plays a role in the growth of nerve fiber (**Figure 5G**) (Sakai et al., 2001). The hSKPs also secrete fiber forming Col I and III, that are structural ECM proteins involved in wound healing (**Figure 5G**). The *in vivo* study also confirmed that after 21 days, all classes of Gel/PCL nanofibers but the blended type could stimulate re-epithelialization and develop a fully epithelialized tissue. Additionally, by immunohistochemical staining of βIII tubulin, it was proved that PCL-RGD and the Gel/PCL blend nanofibers induce formation of nerve fibers that re-innervate a notably larger length of the wound area compared to the gauze control.

Gel/PCL blend nanofibers have also been studied for blood vessel tissue engineering, where inclusion of Gel leads to a more robust system with improved hydrophilicity, in contrast to the neat PCL nanofibers (Jiang et al., 2017). Despite optimum biocompatibility, and enhanced mechanical properties and hydrophilicity, the processing of PCL and Gel combination via electrospinning is challenging due to their phase separation that adversely impacts the nanofiber quality. One solution for this issue could be the use of acetic acid that potentially governs the miscibility of the components, i.e., PCL and Gel, thereby creating homogeneous nanofibers (Feng et al., 2012). Other than blending, VEGF loaded Gel nanoparticles have been also embedded in PCL

TABLE 5 | Bioblended PCL nanofibers for biomedical applications (studies carried out since 2017 have been taken into account).

Blending agent	Nanofiber material	Loading method	Biological effect	Target application	References
Silk fibroin	PCL	Blend electrospinning	Bioactivity	Meniscus regeneration	Li et al. (2020)
Recombinant spider silk protein	Gel/PCL	Blend electrospinning	Bioactivity	Vascular tissue engineering	Xiang et al. (2018)
m-RNA	PELCL/PCL-REDV	Emulsion electrospinning	Post-transcriptional gene regulators provoking tissue regeneration	Vascular tissue regeneration	Zhou et al. (2018)
Cartilage derived ECM	PCL	Blend electrospinning	Cartilage regeneration	Cartilage tissue engineering	Feng et al. (2020)
Kartogenin	PGS (core)/PCL (shell)	Coaxial electrospinning	Chondrogenic differentiation promoter and chondroprotective	Cartilage tissue engineering	Silva et al. (2020)
Gel	PCL	Blend electrospinning	Osteogenesis	Guided bone regeneration	Ren et al. (2017)
Synthetic polypeptide	PCL	Blend electrospinning	Antibacterial effect	vascular grafts or wound healing	Liu et al. (2018)
Starch	PCL	Co-axial electrospinning	Enhanced cell viability	Wound dressing	Komur et al. (2017)
Alginate	PCL	Blending and co-electrospinning	Providing a low cell-adhesive platform	*Cancer* stem cells enrichment	Hu W.-W. et al. (2019)
Nanofibrillated chitosan	PCL	Physical blending and electrospinning	Mechanical reinforcement and biocompatibility enhancement	---	Fadaie et al. (2018)
Collagen	PCL	Blend electrospinning	Bioactivity	Corneal endothelium tissue engineering	Hu Y. et al. (2019)
Chitosan	PCL	Blending and co-electrospinning	Improved biocompatibility and antibacterial activity	Skin tissue engineering	Guha Ray et al. (2018)

PELCL, poly (ethylene glycol)-b-poly (L-lactide-co-ε-caprolactone); PGS, poly (glycerol sebacate); REDV, peptide: Arg-Glu-Asp-Val.

nanofibers to raise the differentiation rate of mesenchymal stem cell (MSC) and to provoke angiogenesis of endothelial cells (Jiang et al., 2018). The encapsulation of VEGF in Gel particles shields the growth factor molecule against degradation in the harsh physical and biological media within the human body and assures their steady and tailored delivery. Additionally, the Gel nanoparticles endow the PCL nanofibers with larger biofunctional anchor points and thus encourage cell adhesion and proliferation, as reflected in the higher NANOG expression of the cells. In contrast, inclusion of VEGF in Gel nanoparticles downregulated such a factor (along with OCT3/4) in MSCs and upregulated CD31 and vWF quantities, implying its significant contribution to differentiation of MSCs to endothelial cells (EC). Such a system could be proposed as a growth factor delivery platform with potential applications in vascular tissue engineering.

Table 5 tabulates the main blending bioagents that have been investigated as additives to PCL nanofibers for biomedicine.

Inorganic Nanomaterials

For particular tissue engineering applications, inorganic bioactive nanomaterials have been added to the PCL nanofibers. For instance, regarding bone tissue engineering, PCL nanofibers alone or as blended with natural polymers, e.g., chitosan, Col, etc. have been reinforced by addition of bioceramics such as hydroxyapatite (HA), tri-calcium phosphates (TCP), bioactive glass, silica (Burton et al., 2019), among others to acquire improved mechanical properties, bioactivity, and even degradability.

The majority of bone tissue engineering scaffolds are based on composite or hybrid materials, developed either by inclusion of hydroxyapatite nanoparticles (nHA [Ca_{10} $(PO_4)_6(OH)_2$]) and bioactive glass nanoparticles into polymeric materials or via surface deposition (mineralization) of nHA on a polymeric substrate (Sadi et al., 2006; Araujo et al., 2008; Yari Sadi et al., 2008). Considering that nHA is the dominant inorganic phase in bone (hard) tissues, its application as an additive to PCL nanofibers specifically for bone tissue engineering has been frequently explored. nHA shows an exclusive affinity for a variety of adhesive proteins and directly contributes to differentiation of bone cells and also to the mineralization processes (Chen and Chang, 2011). Bone tissue comprises Col type I nanofilaments and hydroxyapatite nanocrystals. Imitating such a structure and composition, nanocomposite scaffolds encompassing bioactive inorganic nanoparticles have shown enhanced bone cell interactions. As validated through *in vitro* and *in vivo* tests, such organic/inorganic composite systems encourage adhesion, proliferation, and differentiation of osteoblasts or MSCs, thereby driving the bone regeneration process (Wang et al., 2007).

To fully mimic bone tissue both in terms of biofunctional composition and structure, it is crucial to develop nanostructured scaffolds with micro/nano-sized hierarchical architecture. By now, biomimicking the native nano-structured bone tissue, comprising Col fibers alongside nHA, has been a sophisticated target in tissue engineering. In this regard, electrospun nanofibers have been appealing due to their extraordinary characteristics such as extensive surface area and mimicry of ECM of native tissues (Yoshimoto et al., 2003; Gautam et al., 2021). PCL nanofibers have been shown to be a suitable platform for bone regeneration and can properly stimulate the differentiation of MSCs and their differentiation to osteoblastic cells (Li W. J. et al., 2005). As an example, very recently, Gautam et al. (Gautam et al., 2021) developed a HA surface deposited Gel/PCL blend

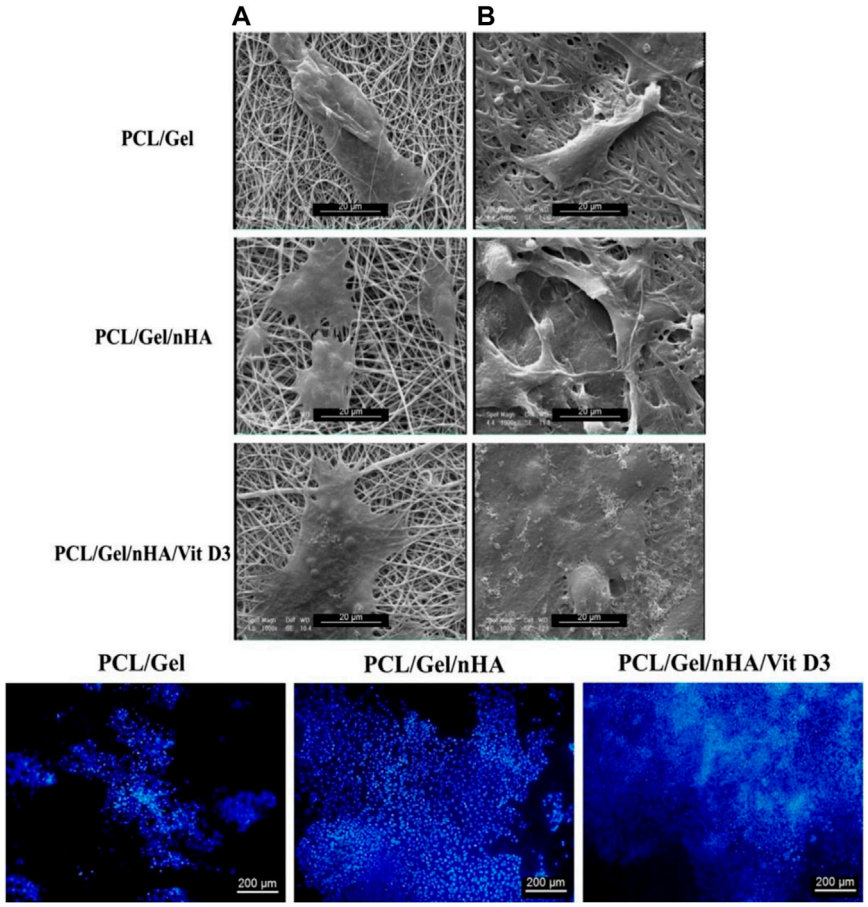

FIGURE 6 | Upper row: SEM images imply the adhesion of MG-63 cells onto PCL/Gel nanofibers with or without hydroxyapatite nanoparticles (nHA) and Vitamin D3 (Vit D3) after 1 **(A)** and 7 **(B)** days cell culture. Lower row: Fluorescence images of the DAPI stained MG-63 cells on the PCL/Gel nanofibers with or without hydroxyapatite nanoparticles (nHA) and Vitamin D3 (Vit D3) after 7 days cell culture. Reproduced with permission. (Sattary et al., 2018), Copyright 2017, Wiley.

nanofiber scaffold for bone tissue engineering. According to the cell viability (MTT) assay and the measured DNA quantities, human osteoblasts were viable and proliferated well on the nanocomposite scaffold. Additionally, the osteoblast cells attached efficiently onto the scaffolds and spread with their specific polygonal morphology. In a similar study, Gel/PCL nanofibers have been reinforced biologically and mechanically by inclusion of HA nanoparticles and Vitamin D3 (Sattary et al., 2018). As shown in **Figure 6**, SEM images indicate a proper adhesion mode (across a wider area) for the cells (MG63) on the Gel/PCL nanofibers containing HA and Vitamin D3. Additionally, as represented by Fluorescence microscopy images and after DAPI staining of the cells, a higher proliferation rate is observed for the blend nanofibers containing the mentioned additives. The presence of the HA nanoparticles raises the surface roughness of the nanofibers that would promote the cell adhesion.

ZnO is a FDA approved inorganic material with therapeutic effects. ZnO nanoparticles have been embedded in PCL nanofibers to realize a bone/cartilage regenerating composite system with Zn delivery in a controlled manner (He et al., 2021). PCL nanofibers containing ZnO alongside HA are notably effective in terms of angiogenesis and osteogenesis, and can inactivate bacteria and thus prevent infection. As verified via SR-μXRF, Zn is mainly concentrated in the fibrocartilage area of the bone-tendon interface (BTI), implying its likely involvement in the regeneration process of the BTI. Witnessed by Alizarin red staining and picrosirius red staining images, the extent of the putative osteogenic potential of the HA-ZnO/PCL nanofibers was clearly reflected in larger Col secretion and calcium deposition (He et al., 2021). The increased OPN expression, that is a recognized indicator of late osteogenesis, was also monitored to help the identification of early osteogenesis. The therapeutic role of Zn and its contribution to the repair of bone fractures and defects through modulation (upregulating) of TGFβ-SMAD signalling have been already reported (Yu et al., 2017; Rahmani et al., 2019; Shitole et al., 2019). As verified through the Alcian blue staining images, a higher amount of glycosaminoglycans (GAGs) is generated on the nanocomposite nanofibers (He et al., 2021). This finding was in harmony with the immunofluorescence imaging results that clearly verified the improved levels of Col II on the HA-ZnO/PCL

nanofibers. According to these results, Zn^{2+} release was reported to promote the release of the insulin-like growth factors (IGF-1), thereby providing better conditions for chondrogenesis (He et al., 2021). IGF-1 can raise chondrogenesis via enhancement of the proliferation of chondrocytes and the expression of their markers, regardless of TGF-β signalling (Longobardi et al., 2006). Additionally, Zn^{2+} declines the degeneration of Col via inactivation of matrix metalloproteinases (MMPs) (Toledano et al., 2012).

Silica (SiO_2) is another inorganic additive to PCL nanofibers that are meant to act as bone tissue engineering scaffolds, for example for nonunion injuries of bone (Burton et al., 2019). Silicon is an element that plays a crucial role in bone growth and mineralization (calcification) during the periosteal ossification processes (Jugdaohsingh, 2007). Lack of silicon has been shown to lead to skeletal deformities in chickens and rats (Carlisle, 1972; Schwarz and Milne, 1972). Burton et al. (Burton et al., 2019) developed $nSiO_2$-incorporated PCL nanofiber scaffolds and reported that adult human periosteal cells seeded on such materials find better conditions for proliferation and putative differentiation, eventually leading to the healing of nonunion injuries of bone. As a crucial source of osteoprogenitor and chondroprogenitor cells, periosteum plays a pivotal role in development, growth, and preservation of normal bone or augmentation and repair of injured bone (Colnot et al., 2012). The existence of a healthy periosteum covering the damaged bone segments, particularly in the case of complicated bone damages leading to bone nonunion, is a prerequisite for healing (Ueno et al., 1999). However, rarely the amount of periosteum suffices for bone healing and thus nonunion injuries impose notable clinical burdens (Panagiotis, 2005). To address this bottleneck, engineered nanofiber mats such as $nSiO_2$-incorporated PCL nanofiber scaffolds can potentially help the periosteal cells expand and the nonunion injury heal.

The other prominent inorganic additive to PCL nanofibers is bioactive glass (BG) that is meant to raise bioactivity of the composite made thereof. The era of inorganic bioactive materials started with the invention of 45S5 bioactive glass (45S5 Bioglass®) by Lary Hench in 1971 (El-Rashidy et al., 2017). This bioactive silicate glass is composed of 45 wt% silica (SiO_2), 24.5 wt% sodium oxide (Na_2O), 24.5 wt% calcium oxide (CaO), and 6 wt% phosphorous pentoxide (P_2O_5) and as the term "bioactive" implies, BG can form a robust interface with natural tissues as a consequence of a particular biological reaction taking place at the material surface (Hench, 1991). Thanks to the synthesis of a surface layer composed of profoundly reactive carbonated hydroxyapatite, a stable interface with bone (Hench, 1991; Jones, 2013) and even with soft tissues emerges (Miguez-Pacheco et al., 2015). As a crucial feature, BGs can be tailored in terms of chemical composition (Si, Ca, P and Na ions) and ion release capability, thereby stimulating the expression of bone cell genes and thus bone regeneration (Xynos et al., 2001). Inclusion of BG in PCL nanofibers has been diligently pursued by researchers to address the poor cell-matter interaction of PCL. For instance, Luginina et al. (Luginina et al., 2020) incorporated silicate and borosilicate BG nanoparticles in poly (glycerol-sabacate)(PGS)/PCL blend nanofibers to develop a wound healing material. Thanks to the release of pro-angiogenetic ions from the BG particles into body fluid (Day et al., 2004; Gorustovich et al., 2010; Balasubramanian et al., 2018), the as-developed composite nanofiber material can be potentially applied as a wound dressing system. Barrier membranes are conventionally employed for the purpose of guided tissue regeneration (GTR) therapy. One important shortcoming of such systems is their poor bioactivity and inability to induce bone regeneration. To address this challenge, inclusion of osteogenic BG particles in polymeric membranes, e.g. those made from PCL nanofibers, has proven to be an efficient strategy (Hidalgo Pitaluga et al., 2018). Doping of 45S5 BG with beneficial ions such as Sr, Mg, and Zn has been also adopted as a practical approach to provoke bone regeneration by a composite ion substituted BG/PCL nanofiber formulation (Sergi et al., 2020). For example, Sr has shown promising capacity to support osteoblast and osteogenic differentiation, fibroblast proliferation, angiogenesis, and thus to drive osteogenesis (Bonnelye et al., 2008; Gorustovich et al., 2010; Yang et al., 2011; Zhang et al., 2015; Yu et al., 2016; Mao et al., 2017; Weng et al., 2017). Mg also notably contributes to bone regeneration (Cacciotti, 2017), and provokes the proliferation and differentiation of stem cells and impacts on ALP secretion thereby it largely modulates bone metabolism (Dasgupta et al., 2010). Zn is an essential ion that plays a role in the proliferation and growth of cells and is involved in enzyme and growth factor expression, as well as DNA replication (Huang et al., 2017; Maret, 2017). Additionally, Zn ions are potentially able to inactivate pathogens and bacteria (Pasquet et al., 2014). Co-existence of such beneficial ions in the BG phase of BG/PCL nanofibers assures improved wound healing conditions thanks to the higher bioactivity of such nanocomposite nanofibers. Upon exposure to the nanofibers, cell viability (cell adhesion and proliferation) and thus wound-healing rate were reported to raise (Sergi et al., 2020).

Carbon Nanomaterials

The biomimicry of the ECM, not only in terms of composition but also morphology, is critical to assure the suitability of a scaffold for tissue engineering purposes. Despite having a similar morphology with the Col nanofibrils of the ECM, the electrospun nanofibers' surface is typically smooth, which does not replicate that of natural nanofibrils. To maximize the biomimicry, thereby influencing cell adhesion and proliferation, it is crucial to develop nanofibers with a periodic nanostructured surface topography as seen in ECM collagen nanofibrils (Fiedler et al., 2013; Wu et al., 2019). In this regard, inclusion of carbon nanotubes (CNTs) into a polymer matrix has been a successful strategy to form a unique structure, called collagen-like nanohybrid shish-kebab (NHSK), wherein fibrous CNTs and polymer lamellae simulate shish and kebab, respectively (Li C. Y. et al., 2005; Li et al., 2006). Wu et al. (2019) extended this idea to electrospun nanofibers composed of CNT and PCL whose shish-kebab structure, developed through a self-induced crystallization approach, could promote osteoblast cell-matter interactions beneficial for bone tissue engineering. The CNT concentration can modulate the mechanical properties of the composite nanofibers and more importantly the frequency,

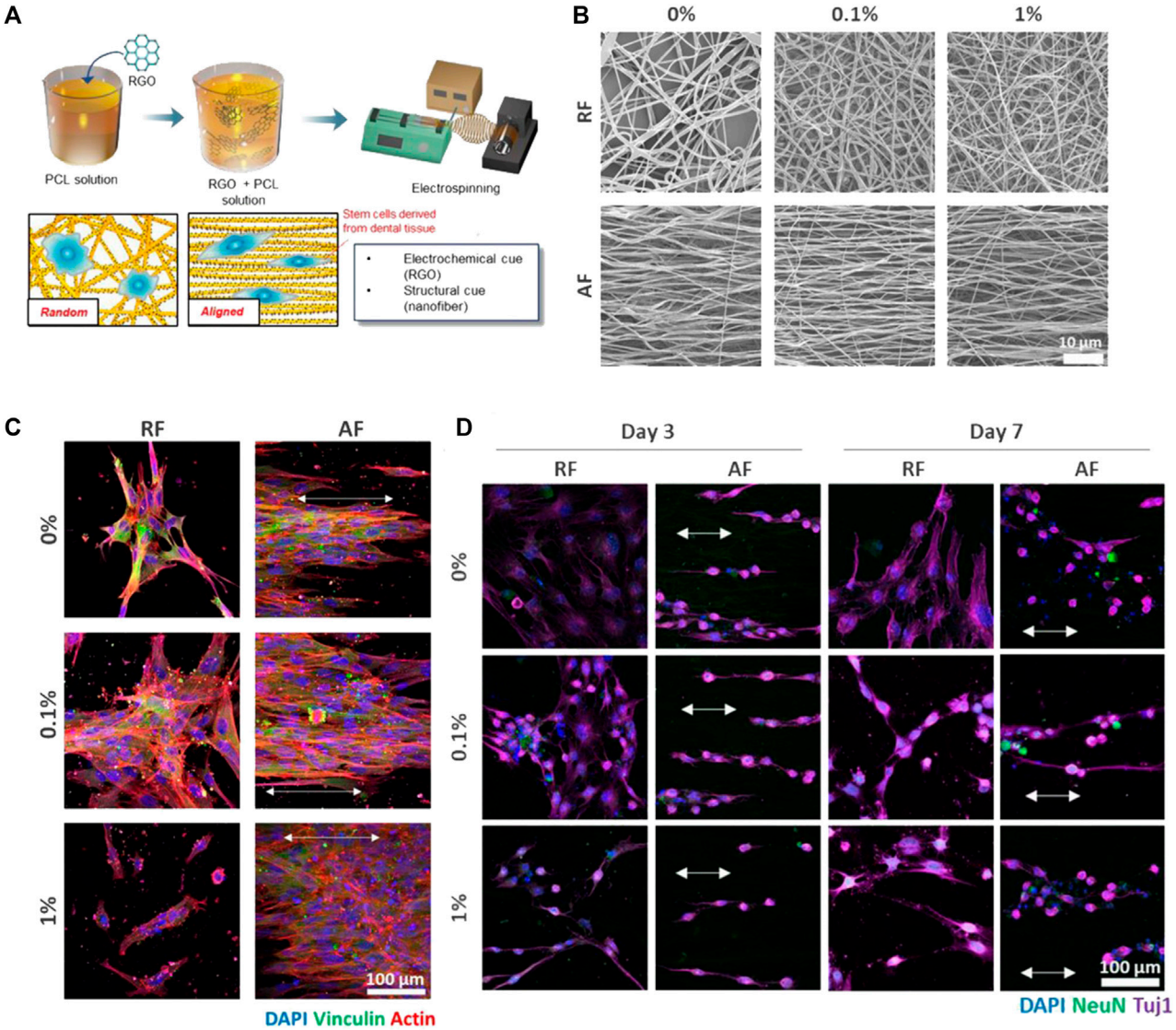

FIGURE 7 | (A) The preparation procedure of the rGO/PCL nanofibers and schematic of DPSCs-nanofiber interactions depending on the nanofibers' alignment mode. **(B)** SEM images show the morphology and alignment of the rGO/PCL nanofibers at different rGO concentrations. **(C)** The immunocytochemistry images taken after 48 h seeding of the cells alongside the rGO/PCL nanofibers imply the interplay between the nanofiber alignment and the cells' shape. Noteworthy, the cells present on the nanofibers containing the highest rGO filling factor (1%), were not stained with vinculin, which represents focal adhesion. This indicates poor cell adhesion probably due to the adverse effect of rGO at high amounts. **(D)** The immunocytochemistry images imply the neurogenic differentiation of DPSCs induced by the rGO/PCL nanofibers, that encourage morphological transformation in a shorter time and NeuN and Tuji-1 expression at an early stage. The arrows indicate the alignment of DPSCs on the AFs. Reproduced with permission. (Seonwoo et al., 2018), Copyright 2018, MDPI.

i.e., the repetitive number, of the shish-kebab structure that further impacts the cell behaviour (adhesion and proliferation). Other than the mentioned structural role, CNTs *per se* affect osteoblasts and their interaction leads to bone formation through an enhanced calcification, i.e., a necessary step of *de novo* bone formation (Shimizu et al., 2012). It has been shown that the genes related to osteoblast phenotype are more expressed when exposed to CNT-incorporated nanocomposite films compared to the pristine polymeric ones (Lee et al., 2015). Additionally, CNTs trigger the release of fibroblast growth factors, thereby stimulating the formation of new bone tissue (Hirata et al., 2013). An extra merit of CNTs is their electrical conductivity that enables electrical stimulation through electroactive CNT/polymer (e.g., PLA) nanofibers and thus bone regeneration (Shao et al., 2011). Although CNTs are indeed versatile additives in polymeric scaffolds (e.g., PCL nanofibrous scaffolds), their high cost and relatively notable unit cost restrict their extensive applications (Santhosh et al., 2016; Ghadimi et al., 2020). Furthermore, raw CNTs contain potentially toxic metal catalysts, while those chemically treated are reported to be non-toxic (Chen and Wang, 2006). Therefore, the use of CNTs as additive in polymeric scaffolds for broader

TABLE 6 | Inorganic and carbon nanofillers of PCL nanofibers for biomedical applications (the studies carried out since 2017 have been taken into account).

Nanofiller	Nanofiber material	Loading method	Biological effect	Target application	References
Ag NP	Collagen coated PLGA/PCL	Polydopamine based reduction of Ag NPs on polymer blend nanofibers	Antibacterial effect	Alveolar/craniofacial bone regeneration	Qian et al. (2019)
Ag NP	PVP/PCL	Physical blending and electrospinning	Antibacterial effect	---	Li et al. (2019)
GO	Gel/PCL	Physical blending and electrospinning	Cell Proliferation enhancement, mechanical reinforcement, and drug carrier	Neural tissue engineering	Heidari et al. (2019)
Graphene nanoplatelets	PLA-PCL copolymer	Physical blending and electrospinning	Mechanical reinforcement	---	Chiesa et al. (2020)
Bioactive glass NP	Chitosan/PCL	Physical blending and electrospinning	Osteogenesis, angiogenesis, and antibacterial activity	---	Liverani et al. (2018)
Bioactive glass NP	PGS/PCL	Physical blending and electrospinning	Pro-angiogenesis, wound healing effect	Soft tissue engineering	Luginina et al. (2020)
Silica NP	PCL	Physical blending and electrospinning	Mechanical reinforcement and osteoconductivity	Guided bone regeneration	Castro et al. (2018)
Hydroxyapatite NP	Gel/PCL	Physical blending and electrospinning	Mechanical reinforcement and bioactivity	Bone tissue engineering	Sattary et al. (2018)
Octacalcium phosphate	PLGA/PCL	Physical blending and electrospinning	Osteoinductive effect	Guided bone regeneration	Wang Z. et al. (2019)
magnesium phosphate nanoflakes	PCL	Physical blending and electrospinning	Osteoconductivity	Bone tissue engineering	Perumal et al. (2020)

PLGA, poly-lactic-co-glycolic acid; PVP, polyvinylpyrrolidone.

clinical translation is only relevant when economical synthesis techniques are available and their potential hazardous effects are minimized either chemically or by creation of less risky alternatives, e.g., carbon nanocrystals (Santhosh et al., 2016).

As a well-known state of the art additive to polymeric scaffolds/substrates, graphene and its derivatives including graphene oxide (GO) and reduced graphene oxide (rGO) have been appealing for potential applications ranging from biosensors, membranes, and superconductive materials to drug delivery and tissue engineering (Pinto et al., 2013; Lee et al., 2014; Homaeigohar and Elbahri, 2017; Homaeigohar et al., 2021b). In biomedicine, the outstanding potential of graphene stems from its aromatic groups (enabling π-π bonding), polar, reactive functional groups, robust C=C bonding, superior elasticity, and excellent electrical conductivity allowing for its promising interaction with biomolecules, cells (fibroblast, nerve, osteoblast, MSC, etc.), drugs, and tissues (Wan and Chen, 2011; Pinto et al., 2013; Ryu and Kim, 2013; Sayyar et al., 2013; Goenka et al., 2014; Luo et al., 2015). Particularly, thanks to the possibility of π–π stacking and hydrophobic interactions, graphene shows a notably elevated drug holding capacity (Liu et al., 2013). This feature can be employed as the basis of development of graphene based drug delivery systems that can target specific sites and deliver anti-cancer drugs and genes in a controlled manner (Liu et al., 2013). It is worthy to note that graphene nanomaterials can offer a drug loading capacity of up to two folds larger than typical drug delivery systems, e.g., nanoparticles (Davis et al., 2008; Heidari et al., 2019). Another advantage of graphene as an additive to polymeric matrices is its reinforcing role, whereby notably improving the elastic modulus, toughness, and tensile strength of polymer composites (Wan and Chen, 2011; Qi et al., 2013). Additionally, graphene related nanomaterials confer polymer matrices antibacterial activity due to their strong destructive effect on the cell (bacteria) membrane. Considering the mentioned pros of graphene, it has been used as an additive to Gel/PCL blend nanofibers to act as a drug (TCH) holding/delivery component and to raise the mechanical properties and electrical conductivity for neural tissue engineering application (Heidari et al., 2019). The as-developed composite PCL nanofibrous material could kill 99% of Gram-positive and Gram-negative bacteria, thanks to the antibacterial activity of graphene as well as the included drug that was steadily released due to the π–π interaction between graphene sheets and the drug molecules. The underlying mechanism for the antibacterial effect of graphene lies in the fact that free electrons within graphene hamper the multiplication process of prokaryotic cells and as a result inhibit the microbial growth. However, this mechanism poses no risk to eukaryotic cells. On the other hand, upon intimate adhesion of bacteria on the graphene surface, the bacteria's membrane is subjected to the stress applied by the sharp edges of graphene, leading to physical damage of the membrane and its disintegration (Lu et al., 2012; Heidari et al., 2019). Seonwoo et al. (2018) incorporated rGO in PCL nanofibers as a platform promoting dental pulp stem cells (DPSC) neurogenic differentiation and thus their neurogenesis. In such a system, the PCL nanofibers *per se* provide the cells with structural cues, while rGO enables electrochemical signalling. As a result, cooperatively the nanocomposite nanofibers provoke DPSC differentiation for neurogenesis. **Figures 7A,B** show the preparation procedure of the rGO/PCL nanofibers and their different alignment modes that could impact cell behavior and morphology. While DPSCs seeded on the randomly aligned fibers (RFs) did not take any particular shape, those located on the aligned fibers (AFs) stretched along the fibers orientation,

Figure 7C. Furthermore, the alignment mode was also dependent on the rGO filling factor. The highest rGO amount (1%) led to lower alignment of the cells. In terms of cell proliferation, it was shown that a proper filling factor of rGO as well as the presence of aligned fibers (AFs) notably rise the cell number. **Figure 7D** demonstrates the interplay of rGO filling factor and fibers orientation with the neurogenic differentiation of the DPSC cells. The morphology of the cells notably alters after 3 and 7 days incubation of the cells with the nanofibers containing 0.1% and 1% rGO. These nanofibers provoke expression of Tuj-1 and NeuN, i.e., the early and late marker of neurogenesis, respectively. Particularly, the NeuN expression was found to be more profound on the nanofibers with the highest rGO concentration or aligned nanofibers.

Table 6 tabulates the main inorganic and carbon nanomaterials that have been investigated as additives to PCL nanofibers for biomedicine.

CONCLUSION AND OUTLOOK

PCL electrospun nanofibers are highly attractive for a plethora of biomedical applications spanning from wound dressing to various tissue engineering scaffolds. Such attractive capacity originates from biodegradability, easy processability, and the relatively low cost of this polymer. However, insufficient interaction with cells, hydrophobicity, and poor mechanical properties of PCL nanofibrous systems that might mismatch with the hosting tissue properties limit their further usability in biomedicine. The main solutions for such shortcomings are either the surface treatment of PCL nanofibers or their hybridization. Thanks to a large specific surface area that can be engineered to encompass many functional groups and to load hydrophilic, bioactive and/or therapeutic agents, PCL nanohybrid nanofibers can turn to a bioactive, hydrophilic nanostructured therapeutic/regenerative platform. On the other hand, inclusion of drugs and therapeutic agents in PCL nanofibers can lead to their controlled release while incorporation of nanofillers can guarantee improved physicochemical properties of the nanofibrous biomedical systems made thereof. Despite the significant progress taken place in the design, engineering, and application of PCL hybrid nanofibers, there are still several gaps that should be targeted in the future by researchers to address and thereby to further develop their potential applications.

A simple glimpse in the literature reflects that applications of PCL hybrid nanofibers have been investigated for wound dressing and engineering of bone, nerve, cornea, vessels, cartilage, and meniscus tissues. Additionally, PCL hybrid nanofibers have been used in relation to cancer research and treatment of periodontal disease (periodontitis). Considering the versatility and high potential of PCL nanofibers, many more applications related to hard and soft tissue engineering can be aimed in the future. One potential area could be electroactive scaffolds that are typically used to restore the performance of destroyed cardiac tissue and in general muscle tissue engineering.

With respect to soft tissue engineering, in addition to surface functionality, PCL nanofibrous systems should support cell anchorage signals mechanically thus enabling the cells to spread largely on the surface. The modulation of surface mechanical properties of PCL nanofibers within the range of soft tissues' has been overlooked and insufficient attention has been paid to mechanotransduction to govern the cellular adhesion on these electrospun nanofibers. Typically, PCL hybrid nanofibers are highly stiff, while soft tissue engineering requires the nanofiber scaffolds much softer than those currently available. Otherwise, biomechanical disharmony will lead to failure of the tissue regeneration strategy based on such nanofiber scaffolds, as the cell adhesion is directly associated with cell signalling and gene expression of the cells depends on the cell interaction with the substrate.

Synthesis approaches for PCL hybrid nanofibers are limited to a few techniques, mainly blend electrospinning. Co-axial and emulsion electrospinning techniques have been rarely employed probably due to their complexity compared to blend electrospinning. On the other hand, surface functionalization and in general post treatment of PCL nanofibers have been insignificantly taken into account. This might originate from poor functionality of the PCL nanofiber surface that mandates the involvement of supplementary techniques such as plasma oxidization. One significant challenge regarding blend electrospinning, particularly in the case of inclusion of nanofillers, is their entrapment within the nanofibers, rather than their surface residence. This issue definitely restricts the interactivity of bioactive nanofillers with the external medium and thus their efficiency. On the other hand, according to the Coffee stain effect, some therapeutic agents that are highly soluble in the electrospinning solvent might be driven towards the surface, while being loosely bound. This will lead to their burst release in a short time window and adverse toxic effects. The incorporation of delicate, sensitive agents into PCL nanofibers via core-shell electrospinning might be also challenging, considering the high shearing forces and high voltages applied where shell and core fluids meet. Taken together, the synthesis strategy should be properly regulated considering all the involved risks and concerns. One further issue is related to the porosity and pore size of PCL hybrid nanofiber mats that should be maintained properly and not sacrificed against inclusion of additives. As some additives are readily ionized, they can potentially reduce the nanofiber diameter during electrospinning. As a result, pore size can decline notably, cell penetration into the mat could be inhibited and permeability to nutrients/waste and air/water exchange could be exacerbated. On the other hand, some additives physicochemically interact with PCL and thus raise the viscosity of the PCL solution that is being electrospun. Consequently, the nanofiber diameter increases and pore size expands, resulting in less topographical cues and mechanical support for the cells. Conclusively, the formulation of the hybrid fibers should be so designed that does not lead to reduction of structural properties.

In terms of formulation, PCL nanofibers hybridized with nature derived compounds that are inherently biocompatible

and offer antibacterial and anti-inflammatory effects seem to be better candidates for biomedical applications compared to those hybridized with synthetic additives. Despite such promising potentials of this class of PCL hybrid nanofibers for biomedicine, certified via many relevant studies, there is no commercially viable product made of them in the healthcare market, to the best of the authors' knowledge. This gap stems from the likely challenges of scalable co-electrospinning of nature-derived therapeutic agents or natural polymers with PCL, that will necessitate involvement of potentially hazardous cross-linkers and other functional impurities to assure their uniform distribution across the nanofiber. On the other hand, PCL is typically electrospun using organic, hazardous solvents whose trace residual amount in the nanofiber could lead to adverse biological and immunological consequences. This fact is generating increasing research efforts on benign solvents for PCL electrospinning.

To provide an antibacterial effect, PCL nanofibers need to incorporate additives such as antimicrobial peptides, Ag ions, drugs (antibiotics), or nature-derived antibacterial compounds. Recalling the fast-paced emergence of antibiotic resistant bacteria, research is directed towards creation of alternative systems for traditional drug delivery PCL nanofibers. One solution could be the development of AMP functionalized PCL nanofibers. This strategy also prevails over metal nanoparticle loaded PCL nanofibers that could excessively release ions beyond the WHO limits. However, *in vitro* and *in vivo* testing of these hybrid nanofibers in long term studies are still necessary to assure their efficiency over the course of the therapeutic process. Similar consideration in terms of lack of long-term *in vivo* studies can be made for the promising technology of ion doped bioactive glass loaded PCL fibers. As a plausible possibility, the *in vivo* trial study might be unsuccessful. Even so, the negative data and the reason behind failure are as important as the positive data and can help the researchers fine tune their approach and material design to raise the potential success of a given therapeutic strategy.

Taking into account the complexity of tissue regeneration and wound healing processes involving various biological steps such as inflammation, angiogenesis, and tissue remodelling, many proposed systems lack efficiency and are not multipurposed. They target only one particular healing goal and are designed to be interactive in that specific respect, e.g., inflammation, or infection. To fulfil realistic medical needs, the nanofiber system should be able to interact with the body from different standpoints and address various therapeutical needs concurrently. This need could be met through development of multifunctional PCL nanofiber systems that can co-release different therapeutic agents, e.g. drugs, bio-derived compounds, etc. over the therapeutic window.

As other nanofiber systems, scalability of PCL nanofibers with a hybrid formulation for purpose of translation into medical technologies is a crucial hurdle. The production process must be scalable and yet cost efficient to justify the utilization of such nanofiber systems in competition with the commercial counterparts currently available in the medical product market.

AUTHOR CONTRIBUTIONS

SH conceived the research idea and wrote the first draft of the manuscript. ARB contributed to conception and to writing the manuscript. Both authors contributed to manuscript revision, read, and approved the submitted version.

FUNDING

SH and ARB would like to acknowledge the financial support received from the European Union's Horizon 2020 - Research and Innovation Program under the Marie Skłodowska-Curie grant agreement No. 839165.

REFERENCES

Adeli-Sardou, M., Yaghoobi, M. M., Torkzadeh-Mahani, M., and Dodel, M. (2019). Controlled Release of Lawsone from Polycaprolactone/gelatin Electrospun Nano Fibers for Skin Tissue Regeneration. *Int. J. Biol. macromolecules* 124, 478–491. doi:10.1016/j.ijbiomac.2018.11.237

Al-Kaabi, W. J., Albukhaty, S., Al-Fartosy, A. J. M., Al-Karagoly, H. K., Al-Musawi, S., Sulaiman, G. M., et al. (2021). Development of Inula Graveolens (L.) Plant Extract Electrospun/polycaprolactone Nanofibers: a Novel Material for Biomedical Application. *Appl. Sci.* 11 (2), 828. doi:10.3390/app11020828

Amri, A., Chaumeil, J. C., Sfar, S., and Charrueau, C. (2012). Administration of Resveratrol: what Formulation Solutions to Bioavailability Limitations. *J. controlled release* 158 (2), 182–193. doi:10.1016/j.jconrel.2011.09.083

Anjum, F., Agabalyan, N. A., Sparks, H. D., Rosin, N. L., Kallos, M. S., and Biernaskie, J. (2017). Biocomposite Nanofiber Matrices to Support ECM Remodeling by Human Dermal Progenitors and Enhanced Wound Closure. *Sci. Rep.* 7 (1), 10291. doi:10.1038/s41598-017-10735-x

Araujo, J. V., Martins, A., Leonor, I. B., Pinho, E. D., Reis, R. L., and Neves, N. M. (2008). Surface Controlled Biomimetic Coating of Polycaprolactone Nanofiber Meshes to Be Used as Bone Extracellular Matrix Analogues. *J. Biomater. Sci. Polym. Edition* 19 (10), 1261–1278. doi:10.1163/156856208786052335

Atkinson, S. J., Ward, R. V., Reynolds, J. J., and Murphy, G. (1992). Cell-mediated Degradation of Type IV Collagen and Gelatin Films Is Dependent on the Activation of Matrix Metalloproteinases. *Biochem. J.* 288 (2), 605–611. doi:10.1042/bj2880605

Bagheri, M., and Mahmoodzadeh, A. (2020). Polycaprolactone/graphene Nanocomposites: Synthesis, Characterization and Mechanical Properties of Electrospun Nanofibers. *J. Inorg. Organomet. Polym.* 30 (5), 1566–1577. doi:10.1007/s10904-019-01340-8

Baker, P. J., Evans, R. T., Coburn, R. A., and Genco, R. J. (1983). Tetracycline and its Derivatives Strongly Bind to and Are Released from the Tooth Surface in Active Form. *J. Periodontol.* 54 (10), 580–585. doi:10.1902/jop.1983.54.10.580

Bala Balakrishnan, P., Gardella, L., Forouharshad, M., Pellegrino, T., and Monticelli, O. (2018). Star Poly(ε-Caprolactone)-Based Electrospun Fibers as Biocompatible Scaffold for Doxorubicin with Prolonged Drug Release Activity. *Colloids Surf. B: Biointerfaces* 161, 488–496. doi:10.1016/j.colsurfb.2017.11.014

Balasubramanian, P., Büttner, T., Miguez Pacheco, V., and Boccaccini, A. R. (2018). Boron-containing Bioactive Glasses in Bone and Soft Tissue Engineering. *J. Eur. Ceram. Soc.* 38 (3), 855–869. doi:10.1016/j.jeurceramsoc.2017.11.001

Basar, A. O., Castro, S., Torres-Giner, S., Lagaron, J. M., and Turkoglu Sasmazel, H. (2017). Novel Poly(ε-Caprolactone)/gelatin Wound Dressings Prepared by

Emulsion Electrospinning with Controlled Release Capacity of Ketoprofen Anti-inflammatory Drug. *Mater. Sci. Eng. C* 81, 459–468. doi:10.1016/j.msec.2017.08.025

Benoit, D. S. W., and Anseth, K. S. (2005). The Effect on Osteoblast Function of Colocalized RGD and PHSRN Epitopes on PEG Surfaces. *Biomaterials* 26 (25), 5209–5220. doi:10.1016/j.biomaterials.2005.01.045

Birt, D. F., Hendrich, S., and Wang, W. (2001). Dietary Agents in Cancer Prevention: Flavonoids and Isoflavonoids. *Pharmacol. Ther.* 90 (2), 157–177. doi:10.1016/s0163-7258(01)00137-1

Bonnelye, E., Chabadel, A., Saltel, F., and Jurdic, P. (2008). Dual Effect of Strontium Ranelate: Stimulation of Osteoblast Differentiation and Inhibition of Osteoclast Formation and Resorption *In Vitro*. *Bone* 42 (1), 129–138. doi:10.1016/j.bone.2007.08.043

Borena, B. M., Martens, A., Broeckx, S. Y., Meyer, E., Chiers, K., Duchateau, L., et al. (2015). Regenerative Skin Wound Healing in Mammals: State-Of-The-Art on Growth Factor and Stem Cell Based Treatments. *Cell Physiol Biochem* 36 (1), 1–23. doi:10.1159/000374049

Burton, C. W., DiFeo Childs, R., McClellan, P., Yu, Q., Bundy, J., Gao, M., et al. (2019). Silica/polycaprolactone Nanofiber Scaffold Variants for Human Periosteal Cell Growth. *J. Biomed. Mater. Res.* 107 (4), 791–801. doi:10.1002/jbm.a.36595

Caccetta, R. A.-A., Croft, K. D., Beilin, L. J., and Puddey, I. B. (2000). Ingestion of Red Wine Significantly Increases Plasma Phenolic Acid Concentrations but Does Not Acutely Affect *Ex Vivo* Lipoprotein Oxidizability. *Am. J. Clin. Nutr.* 71 (1), 67–74. doi:10.1093/ajcn/71.1.67

Cacciotti, I. (2017). Bivalent Cationic Ions Doped Bioactive Glasses: The Influence of Magnesium, Zinc, Strontium and Copper on the Physical and Biological Properties. *J. Mater. Sci.* 52 (15), 8812–8831. doi:10.1007/s10853-017-1010-0

Carlisle, E. M. (1972). Silicon: an Essential Element for the Chick. *Science* 178 (4061), 619–621. doi:10.1126/science.178.4061.619

Carnegie, J. A., and Cabaca, O. (1993). Extracellular Matrix Composition and Resilience: Two Parameters that Influence the *In Vitro* Migration and Morphology of Rat Inner Cell Mass-Derived Cells1. *Biol. Reprod.* 48 (2), 287–299. doi:10.1095/biolreprod48.2.287

Casati, M. Z., Algayer, C., Cardoso da Cruz, G., Ribeiro, F. V., Casarin, R. C. V., Pimentel, S. P., et al. (2013). Resveratrol Decreases Periodontal Breakdown and Modulates Local Levels of Cytokines during Periodontitis in Rats. *J. Periodontol.* 84 (10), e58–e64. doi:10.1902/jop.2013.120746

Castro, A. G. B., Diba, M., Kersten, M., Jansen, J. A., van den Beucken, J. J. J. P., and Yang, F. (2018). Development of a PCL-Silica Nanoparticles Composite Membrane for Guided Bone Regeneration. *Mater. Sci. Eng. C* 85, 154–161. doi:10.1016/j.msec.2017.12.023

Chandra, R., and Rustgi, R. (1998). Biodegradable Polymers. *Prog. Polym. Sci.* 23 (7), 1273–1335. doi:10.1016/s0079-6700(97)00039-7

Chen, C., and Wang, X. (2006). Adsorption of Ni(II) from Aqueous Solution Using Oxidized Multiwall Carbon Nanotubes. *Ind. Eng. Chem. Res.* 45 (26), 9144–9149. doi:10.1021/ie060791z

Chen, J.-P., and Chang, Y.-S. (2011). Preparation and Characterization of Composite Nanofibers of Polycaprolactone and Nanohydroxyapatite for Osteogenic Differentiation of Mesenchymal Stem Cells. *Colloids Surf. B: Biointerfaces* 86 (1), 169–175. doi:10.1016/j.colsurfb.2011.03.038

Chen, J., Altman, G. H., Karageorgiou, V., Horan, R., Collette, A., Volloch, V., et al. (2003). Human Bone Marrow Stromal Cell and Ligament Fibroblast Responses on RGD-Modified Silk Fibers. *J. Biomed. Mater. Res.* 67A (2), 559–570. doi:10.1002/jbm.a.10120

Chiesa, E., Dorati, R., Pisani, S., Bruni, G., Rizzi, L. G., Conti, B., et al. (2020). Graphene Nanoplatelets for the Development of Reinforced PLA-PCL Electrospun Fibers as the Next-Generation of Biomedical Mats. *Polymers* 12 (6), 1390. doi:10.3390/polym12061390

Cho, W.-S., Duffin, R., Bradley, M., Megson, I. L., MacNee, W., Lee, J. K., et al. (2013). Predictive Value of *In Vitro* Assays Depends on the Mechanism of Toxicity of Metal Oxide Nanoparticles. *Part. Fibre Toxicol.* 10 (1), 55. doi:10.1186/1743-8977-10-55

Chong, E., Phan, T., Lim, I., Zhang, Y., Bay, B., Ramakrishna, S., et al. (2007). Evaluation of Electrospun PCL/gelatin Nanofibrous Scaffold for Wound Healing and Layered Dermal Reconstitution☆. *Acta Biomater.* 3 (3), 321–330. doi:10.1016/j.actbio.2007.01.002

Chopra, I., and Roberts, M. (2001). Tetracycline Antibiotics: Mode of Action, Applications, Molecular Biology, and Epidemiology of Bacterial Resistance. *Microbiol. Mol. Biol. Rev.* 65 (2), 232–260. doi:10.1128/mmbr.65.2.232-260.2001

Chou, S.-F., Carson, D., and Woodrow, K. A. (2015). Current Strategies for Sustaining Drug Release from Electrospun Nanofibers. *J. Controlled Release* 220, 584–591. doi:10.1016/j.jconrel.2015.09.008

Chung, M. J., Walker, P. A., and Hogstrand, C. (2006). Dietary Phenolic Antioxidants, Caffeic Acid and Trolox, Protect Rainbow trout Gill Cells from Nitric Oxide-Induced Apoptosis. *Aquat. Toxicol.* 80 (4), 321–328. doi:10.1016/j.aquatox.2006.09.009

Chung, T. W., Moon, S. K., Chang, Y. C., Ko, J. H., Lee, Y. C., Cho, G., et al. (2004). Novel and Therapeutic Effect of Caffeic Acid and Caffeic Acid Phenyl Ester on Hepatocarcinoma Cells: Complete Regression of Hepatoma Growth and Metastasis by Dual Mechanism. *FASEB j.* 18 (14), 1670–1681. doi:10.1096/fj.04-2126com

Clark, R. A. F., Ghosh, K., and Tonnesen, M. G. (2007). Tissue Engineering for Cutaneous Wounds. *J. Invest. Dermatol.* 127 (5), 1018–1029. doi:10.1038/sj.jid.5700715

Cohn, D., and Hotovely Salomon, A. (2005). Designing Biodegradable Multiblock PCL/PLA Thermoplastic Elastomers. *Biomaterials* 26 (15), 2297–2305. doi:10.1016/j.biomaterials.2004.07.052

Collier, J. H., and Segura, T. (2011). Evolving the Use of Peptides as Components of Biomaterials. *Biomaterials* 32 (18), 4198–4204. doi:10.1016/j.biomaterials.2011.02.030

Colnot, C., Zhang, X., and Tate, M. L. K. (2012). Current Insights on the Regenerative Potential of the Periosteum: Molecular, Cellular, and Endogenous Engineering Approaches. *J. Orthop. Res.* 30 (12), 1869–1878. doi:10.1002/jor.22181

Contesini, F. J., Lopes, D. B., Macedo, G. A., da Graça Nascimento, M., and de Oliveira Carvalho, P. (2010). Aspergillus Sp. Lipase: Potential Biocatalyst for Industrial Use. *J. Mol. Catal. B: Enzymatic* 67 (3-4), 163–171. doi:10.1016/j.molcatb.2010.07.021

Cr, R., Ps, S., O, M., Pp, S., and A, S. (2018). Nanochitosan Enriched Poly ε-caprolactone Electrospun Wound Dressing Membranes: A fine Tuning of Physicochemical Properties, Hemocompatibility and Curcumin Release Profile. *Int. J. Biol. Macromol* 108, 1261–1272. doi:10.1016/j.ijbiomac.2017.11.035

Dasgupta, S., Banerjee, S. S., Bandyopadhyay, A., and Bose, S. (2010). Zn- and Mg-Doped Hydroxyapatite Nanoparticles for Controlled Release of Protein. *Langmuir* 26 (7), 4958–4964. doi:10.1021/la903617e

Davis, M. E., Chen, Z., and Shin, D. M. (2008). Nanoparticle Therapeutics: an Emerging Treatment Modality for Cancer. *Nat. Rev. Drug Discov.* 7 (9), 771–782. doi:10.1038/nrd2614

Day, R. M., Boccaccini, A. R., Shurey, S., Roether, J. A., Forbes, A., Hench, L. L., et al. (2004). Assessment of Polyglycolic Acid Mesh and Bioactive Glass for Soft-Tissue Engineering Scaffolds. *Biomaterials* 25 (27), 5857–5866. doi:10.1016/j.biomaterials.2004.01.043

Dias, A. M., da Silva, F. G., Monteiro, A. P. d. F., Pinzón-García, A. D., Sinisterra, R. D., and Cortés, M. E. (2019). Polycaprolactone Nanofibers Loaded Oxytetracycline Hydrochloride and Zinc Oxide for Treatment of Periodontal Disease. *Mater. Sci. Eng. C* 103, 109798. doi:10.1016/j.msec.2019.109798

El-Rashidy, A. A., Roether, J. A., Harhaus, L., Kneser, U., and Boccaccini, A. R. (2017). Regenerating Bone with Bioactive Glass Scaffolds: A Review of *In Vivo* Studies in Bone Defect Models. *Acta Biomater.* 62, 1–28. doi:10.1016/j.actbio.2017.08.030

Engelhardt, S., Hoch, E., Borchers, K., Meyer, W., Krüger, H., Tovar, G. E. M., et al. (2011). Fabrication of 2D Protein Microstructures and 3D Polymer-Protein Hybrid Microstructures by Two-Photon Polymerization. *Biofabrication* 3 (2), 025003. doi:10.1088/1758-5082/3/2/025003

Entcheva, E., Bien, H., Yin, L., Chung, C.-Y., Farrell, M., and Kostov, Y. (2004). Functional Cardiac Cell Constructs on Cellulose-Based Scaffolding. *Biomaterials* 25 (26), 5753–5762. doi:10.1016/j.biomaterials.2004.01.024

Eskitoros-Togay, Ş. M., Bulbul, Y. E., Tort, S., Demirtaş Korkmaz, F., Acartürk, F., and Dilsiz, N. (2019). Fabrication of Doxycycline-Loaded Electrospun PCL/PEO Membranes for a Potential Drug Delivery System. *Int. J. Pharmaceutics* 565, 83–94. doi:10.1016/j.ijpharm.2019.04.073

Ezhilarasu, H., Ramalingam, R., Dhand, C., Lakshminarayanan, R., Sadiq, A., Gandhimathi, C., et al. (2019). Biocompatible Aloe Vera and Tetracycline Hydrochloride Loaded Hybrid Nanofibrous Scaffolds for Skin Tissue Engineering. *Ijms* 20 (20), 5174. doi:10.3390/ijms20205174

Fadaie, M., Mirzaei, E., Geramizadeh, B., and Asvar, Z. (2018). Incorporation of Nanofibrillated Chitosan into Electrospun PCL Nanofibers Makes Scaffolds with Enhanced Mechanical and Biological Properties. *Carbohydr. Polym.* 199, 628–640. doi:10.1016/j.carbpol.2018.07.061

Fahimirad, S., Abtahi, H., Satei, P., Ghaznavi-Rad, E., Moslehi, M., and Ganji, A. (2021). Wound Healing Performance of PCL/chitosan Based Electrospun Nanofiber Electrosprayed with Curcumin Loaded Chitosan Nanoparticles. *Carbohydr. Polym.* 259, 117640. doi:10.1016/j.carbpol.2021.117640

Feng, B., Ji, T., Wang, X., Fu, W., Ye, L., Zhang, H., et al. (2020). Engineering Cartilage Tissue Based on Cartilage-Derived Extracellular Matrix cECM/PCL Hybrid Nanofibrous Scaffold. *Mater. Des.* 193, 108773. doi:10.1016/j.matdes.2020.108773

Feng, B., Tu, H., Yuan, H., Peng, H., and Zhang, Y. (2012). Acetic-acid-mediated Miscibility toward Electrospinning Homogeneous Composite Nanofibers of GT/PCL. *Biomacromolecules* 13 (12), 3917–3925. doi:10.1021/bm3009389

Fiedler, J., Özdemir, B., Bartholomä, J., Plettl, A., Brenner, R. E., and Ziemann, P. (2013). The Effect of Substrate Surface Nanotopography on the Behavior of Multipotnent Mesenchymal Stromal Cells and Osteoblasts. *Biomaterials* 34 (35), 8851–8859. doi:10.1016/j.biomaterials.2013.08.010

Fordham, J. B., Raza Naqvi, A., and Nares, S. (2014). Leukocyte Production of Inflammatory Mediators Is Inhibited by the Antioxidants Phloretin, Silymarin, Hesperetin, and Resveratrol. *Mediators Inflamm.* 2014, 938712. doi:10.1155/2014/938712

Gámez, E., Elizondo-Castillo, H., Tascon, J., García-Salinas, S., Navascues, N., Mendoza, G., et al. (2020). Antibacterial Effect of Thymol Loaded SBA-15 Nanorods Incorporated in PCL Electrospun Fibers. *Nanomaterials* 10 (4), 616. doi:10.3390/nano10040616

Gan, Z., Liang, Q., Zhang, J., and Jing, X. (1997). Enzymatic Degradation of Poly(ε-Caprolactone) Film in Phosphate Buffer Solution Containing Lipases. *Polym. Degrad. Stab.* 56 (2), 209–213. doi:10.1016/s0141-3910(96)00208-x

Gautam, S., Sharma, C., Purohit, S. D., Singh, H., Dinda, A. K., Potdar, P. D., et al. (2021). Gelatin-polycaprolactone-nanohydroxyapatite Electrospun Nanocomposite Scaffold for Bone Tissue Engineering. *Mater. Sci. Eng. C* 119, 111588. doi:10.1016/j.msec.2020.111588

Ghadimi, M., Zangenehtabar, S., and Homaeigohar, S. (2020). An Overview of the Water Remediation Potential of Nanomaterials and Their Ecotoxicological Impacts. *Water* 12 (4), 1150. doi:10.3390/w12041150

Ghasemi-Mobarakeh, L., Prabhakaran, M. P., Morshed, M., Nasr-Esfahani, M.-H., and Ramakrishna, S. (2008). Electrospun Poly(ε-Caprolactone)/gelatin Nanofibrous Scaffolds for Nerve Tissue Engineering. *Biomaterials* 29 (34), 4532–4539. doi:10.1016/j.biomaterials.2008.08.007

Ghosal, K., Manakhov, A., Zajíčková, L., and Thomas, S. (2017). Structural and Surface Compatibility Study of Modified Electrospun Poly(ε-Caprolactone) (PCL) Composites for Skin Tissue Engineering. *Aaps Pharmscitech* 18 (1), 72–81. doi:10.1208/s12249-016-0500-8

Gloria, A., De Santis, R., and Ambrosio, L. (2010). Polymer-based Composite Scaffolds for Tissue Engineering. *J. Appl. Biomater. Biomech.* 8 (2), 57–67. doi:10.1177/228080001000800201

Goenka, S., Sant, V., and Sant, S. (2014). Graphene-based Nanomaterials for Drug Delivery and Tissue Engineering. *J. Controlled Release* 173, 75–88. doi:10.1016/j.jconrel.2013.10.017

Gönen, S. Ö., Erol Taygun, M., and Küçükbayrak, S. (2016). Fabrication of Bioactive Glass Containing Nanocomposite Fiber Mats for Bone Tissue Engineering Applications. *Compos. structures* 138, 96–106. doi:10.1016/j.compstruct.2015.11.033

Gorustovich, A. A., Roether, J. A., and Boccaccini, A. R. (2010). Effect of Bioactive Glasses on Angiogenesis: a Review of *In Vitro* and *In Vivo* Evidences. *Tissue Eng. B: Rev.* 16 (2), 199–207. doi:10.1089/ten.teb.2009.0416

Guarino, V., Altobelli, R., della Sala, F., Borzacchiello, A., and Ambrosio, L. (2018). *Alginate Processing Routes to Fabricate Bioinspired Platforms for Tissue Engineering and Drug Delivery*. Springer: Alginates and Their Biomedical Applications, 101–120.

Guha Ray, P., Pal, P., Srivas, P. K., Basak, P., Roy, S., and Dhara, S. (2018). Surface Modification of Eggshell Membrane with Electrospun Chitosan/Polycaprolactone Nanofibers for Enhanced Dermal Wound Healing. *ACS Appl. Bio Mater.* 1 (4), 985–998. doi:10.1021/acsabm.8b00169

Gunn, J. W., Turner, S. D., and Mann, B. K. (2005). Adhesive and Mechanical Properties of Hydrogels Influence Neurite Extension. *J. Biomed. Mater. Res.* 72A (1), 91–97. doi:10.1002/jbm.a.30203

Havsteen, B. H. (2002). The Biochemistry and Medical Significance of the Flavonoids. *Pharmacol. Ther.* 96 (2), 67–202. doi:10.1016/s0163-7258(02)00298-x

He, X., Huang, Z., Liu, W., Liu, Y., Qian, H., Lei, T., et al. (2021). Electrospun polycaprolactone/hydroxyapatite/ZnO Films as Potential Biomaterials for Application in Bone-Tendon Interface Repair. *Colloids Surf. B: Biointerfaces* 204, 111825. doi:10.1016/j.colsurfb.2021.111825

Heidari, M., Bahrami, S. H., Ranjbar-Mohammadi, M., and Milan, P. B. (2019). Smart Electrospun Nanofibers Containing PCL/gelatin/graphene Oxide for Application in Nerve Tissue Engineering. *Mater. Sci. Eng. C* 103, 109768. doi:10.1016/j.msec.2019.109768

Hench, L. L. (1991). Bioceramics: from Concept to Clinic. *J. Am. Ceram. Soc.* 74 (7), 1487–1510. doi:10.1111/j.1151-2916.1991.tb07132.x

Hermanová, S., Bálková, R., Voběrková, S., Chamradová, I., Omelková, J., Richtera, L., et al. (2013). Biodegradation Study on Poly(ε-Caprolactone) with Bimodal Molecular Weight Distribution. *J. Appl. Polym. Sci.* 127 (6), 4726–4735. doi:10.1002/app.38078

Hermanová, S., Omelková, J., Voběrková, S., Bálková, R., Richtera, L., Mravcová, L., et al. (2012). The Effect of Processing of Polycaprolactone Films on Degradation Process Initiated byAspergillus OryzaeLipase. *Int. J. Polym. Anal. Characterization* 17 (6), 465–475. doi:10.1080/1023666x.2012.696402

Herrero-Herrero, M., Gómez-Tejedor, J. A., and Vallés-Lluch, A. (2018). PLA/PCL Electrospun Membranes of Tailored Fibres Diameter as Drug Delivery Systems. *Eur. Polym. J.* 99, 445–455. doi:10.1016/j.eurpolymj.2017.12.045

Hidalgo Pitaluga, L., Trevelin Souza, M., Dutra Zanotto, E., Santocildes Romero, M., and Hatton, P. (2018). Electrospun F18 Bioactive Glass/PCL-Poly (ε-Caprolactone)-Membrane for Guided Tissue Regeneration. *Materials* 11 (3), 400. doi:10.3390/ma11030400

Hirata, E., Ménard-Moyon, C., Venturelli, E., Takita, H., Watari, F., Bianco, A., et al. (2013). Carbon Nanotubes Functionalized with Fibroblast Growth Factor Accelerate Proliferation of Bone Marrow-Derived Stromal Cells and Bone Formation. *Nanotechnology* 24 (43), 435101. doi:10.1088/0957-4484/24/43/435101

Homaeigohar, S., and Elbahri, M. (2017). Graphene Membranes for Water Desalination. *NPG Asia Mater.* 9 (8), e427. doi:10.1038/am.2017.135

Homaeigohar, S., Monavari, M., Koenen, B., and Boccaccini, A. R. (2021a). Biomimetic Biohybrid Nanofibers Containing Bovine Serum Albumin as a Bioactive Moiety for Wound Dressing. *Mater. Sci. Eng. C* 123, 111965. doi:10.1016/j.msec.2021.111965

Homaeigohar, S., Liu, Q., and Kordbacheh, D. (2021b). Biomedical Applications of Antiviral Nanohybrid Materials Relating to the COVID-19 Pandemic and Other Viral Crises. *Polymers* 13 (16), 2833. doi:10.3390/polym13162833

Homaeigohar, S., Tsai, T.-Y., Young, T.-H., Yang, H. J., and Ji, Y.-R. (2019). An Electroactive Alginate Hydrogel Nanocomposite Reinforced by Functionalized Graphite Nanofilaments for Neural Tissue Engineering. *Carbohydr. Polym.* 224, 115112. doi:10.1016/j.carbpol.2019.115112

Homaeigohar, S., Tsai, T.-Y., Zarie, E. S., Elbahri, M., Young, T.-H., and Boccaccini, A. R. (2020). Bovine Serum Albumin (BSA)/polyacrylonitrile (PAN) Biohybrid Nanofibers Coated with a Biomineralized Calcium Deficient Hydroxyapatite (HA) Shell for Wound Dressing. *Mater. Sci. Eng. C* 116, 111248. doi:10.1016/j.msec.2020.111248

Hu, W.-W., Lin, C.-H., and Hong, Z.-J. (2019). The Enrichment of Cancer Stem Cells Using Composite Alginate/polycaprolactone Nanofibers. *Carbohydr. Polym.* 206, 70–79. doi:10.1016/j.carbpol.2018.10.087

Hu, Y., Feng, B., Zhang, W., Yan, C., Yao, Q., Shao, C., et al. (2019). Electrospun Gelatin/PCL and Collagen/PCL Scaffolds for Modulating Responses of Bone Marrow Endothelial Progenitor Cells. *Exp. Ther. Med.* 17 (5), 3717–3726. doi:10.3892/etm.2019.7387

Huang, H., Oizumi, S., Kojima, N., Niino, T., and Sakai, Y. (2007). Avidin-biotin Binding-Based Cell Seeding and Perfusion Culture of Liver-Derived Cells in a Porous Scaffold with a Three-Dimensional Interconnected Flow-Channel

Network. *Biomaterials* 28 (26), 3815–3823. doi:10.1016/j.biomaterials.2007.05.004

Huang, M., Hill, R. G., and Rawlinson, S. C. F. (2017). Zinc Bioglasses Regulate Mineralization in Human Dental Pulp Stem Cells. *Dental Mater.* 33 (5), 543–552. doi:10.1016/j.dental.2017.03.011

Inoue, S., Tanaka, K., Arisaka, F., Kimura, S., Ohtomo, K., and Mizuno, S. (2000). Silk Fibroin of *Bombyx mori* Is Secreted, Assembling a High Molecular Mass Elementary Unit Consisting of H-Chain, L-Chain, and P25, with a 6:6:1 Molar Ratio. *J. Biol. Chem.* 275 (51), 40517–40528. doi:10.1074/jbc.m006897200

Jabbari, E. (2011). Bioconjugation of Hydrogels for Tissue Engineering. *Curr. Opin. Biotechnol.* 22 (5), 655–660. doi:10.1016/j.copbio.2011.01.003

Jain, N., Jain, G. K., Javed, S., Iqbal, Z., Talegaonkar, S., Ahmad, F. J., et al. (2008). Recent Approaches for the Treatment of Periodontitis. *Drug Discov. Today* 13 (21-22), 932–943. doi:10.1016/j.drudis.2008.07.010

Jayakumar, R., Prabaharan, M., Shalumon, K. T., Chennazhi, K. P., and Nair, S. V. (2011). *Biomedical Applications of Polymeric Nanofibers*. Berlin: Springer-Verlag, 263–282. doi:10.1007/12_2011_123

Jiang, Y.-C., Jiang, L., Huang, A., Wang, X.-F., Li, Q., and Turng, L.-S. (2017). Electrospun Polycaprolactone/gelatin Composites with Enhanced Cell-Matrix Interactions as Blood Vessel Endothelial Layer Scaffolds. *Mater. Sci. Eng. C* 71, 901–908. doi:10.1016/j.msec.2016.10.083

Jiang, Y.-C., Wang, X.-F., Xu, Y.-Y., Qiao, Y.-H., Guo, X., Wang, D.-F., et al. (2018). Polycaprolactone Nanofibers Containing Vascular Endothelial Growth Factor-Encapsulated Gelatin Particles Enhance Mesenchymal Stem Cell Differentiation and Angiogenesis of Endothelial Cells. *Biomacromolecules* 19 (9), 3747–3753. doi:10.1021/acs.biomac.8b00870

Joe, A., Park, S.-H., Shim, K.-D., Kim, D.-J., Jhee, K.-H., Lee, H.-W., et al. (2017). Antibacterial Mechanism of ZnO Nanoparticles under Dark Conditions. *J. Ind. Eng. Chem.* 45, 430–439. doi:10.1016/j.jiec.2016.10.013

Jones, J. R. (2013). Review of Bioactive Glass: from Hench to Hybrids. *Acta Biomater.* 9 (1), 4457–4486. doi:10.1016/j.actbio.2012.08.023

Jugdaohsingh, R. (2007). Silicon and Bone Health. *J. Nutr. Health Aging* 11 (2), 99–110.

Kamath, S. M., Sridhar, K., Jaison, D., Gopinath, V., Ibrahim, B. K. M., Gupta, N., et al. (2020). Fabrication of Tri-layered Electrospun Polycaprolactone Mats with Improved Sustained Drug Release Profile. *Sci. Rep.* 10 (1), 18179. doi:10.1038/s41598-020-74885-1

Karuppuswamy, P., Reddy Venugopal, J., Navaneethan, B., Luwang Laiva, A., and Ramakrishna, S. (2015). Polycaprolactone Nanofibers for the Controlled Release of Tetracycline Hydrochloride. *Mater. Lett.* 141, 180–186. doi:10.1016/j.matlet.2014.11.044

Kenawy, el-R., Bowlin, G. L., Mansfield, K., Layman, J., Simpson, D. G., Sanders, E. H., et al. (2002). Release of Tetracycline Hydrochloride from Electrospun Poly(ethylene-Co-Vinylacetate), Poly(lactic Acid), and a Blend. *J. Control. Release* 81 (1), 57–64. doi:10.1016/s0168-3659(02)00041-x

Keong, L. C., and Halim, A. S. (2009). *In Vitro* models in Biocompatibility Assessment for Biomedical-Grade Chitosan Derivatives in Wound Management. *Ijms* 10 (3), 1300–1313. doi:10.3390/ijms10031300

Khan, G., Yadav, S. K., Patel, R. R., Kumar, N., Bansal, M., and Mishra, B. (2017). Tinidazole Functionalized Homogeneous Electrospun Chitosan/poly (ε-Caprolactone) Hybrid Nanofiber Membrane: Development, Optimization and its Clinical Implications. *Int. J. Biol. Macromolecules* 103, 1311–1326. doi:10.1016/j.ijbiomac.2017.05.161

Kim, M. S., Jun, I., Shin, Y. M., Jang, W., Kim, S. I., and Shin, H. (2010). The Development of Genipin-Crosslinked Poly(caprolactone) (PCL)/Gelatin Nanofibers for Tissue Engineering Applications. *Macromol. Biosci.* 10 (1), 91–100. doi:10.1002/mabi.200900168

Kim, M. S., and Kim, G. (2014). Three-dimensional Electrospun Polycaprolactone (PCL)/alginate Hybrid Composite Scaffolds. *Carbohydr. Polym.* 114, 213–221. doi:10.1016/j.carbpol.2014.08.008

Kim, M. S., Kim, H. J., Jang, J. Y., and Shin, H. S. (2018). Development of Coaxial Alginate-PCL Nanofibrous Dressing for Controlled Release of Spirulina Extract. *J. Biomater. Sci. Polym. edition* 29 (12), 1389–1400. doi:10.1080/09205063.2018.1462931

Kim, Y.-J., Park, M. R., Kim, M. S., and Kwon, O. H. (2012). Polyphenol-loaded Polycaprolactone Nanofibers for Effective Growth Inhibition of Human Cancer Cells. *Mater. Chem. Phys.* 133 (2), 674–680. doi:10.1016/j.matchemphys.2012.01.050

Koh, L.-D., Cheng, Y., Teng, C.-P., Khin, Y.-W., Loh, X.-J., Tee, S.-Y., et al. (2015). Structures, Mechanical Properties and Applications of Silk Fibroin Materials. *Prog. Polym. Sci.* 46, 86–110. doi:10.1016/j.progpolymsci.2015.02.001

Komur, B., Bayrak, F., Ekren, N., Eroglu, M. S., Oktar, F. N., Sinirlioglu, Z. A., et al. (2017). Starch/PCL Composite Nanofibers by Co-axial Electrospinning Technique for Biomedical Applications. *Biomed. Eng. Online* 16 (1), 40–13. doi:10.1186/s12938-017-0334-y

Kubow, K. E., Vukmirovic, R., Zhe, L., Klotzsch, E., Smith, M. L., Gourdon, D., et al. (2015). Mechanical Forces Regulate the Interactions of Fibronectin and Collagen I in Extracellular Matrix. *Nat. Commun.* 6 (1), 8026. doi:10.1038/ncomms9026

Kweon, D.-K., Song, S.-B., and Park, Y.-Y. (2003). Preparation of Water-Soluble Chitosan/heparin Complex and its Application as Wound Healing Accelerator. *Biomaterials* 24 (9), 1595–1601. doi:10.1016/s0142-9612(02)00566-5

Labet, M., and Thielemans, W. (2009). Synthesis of Polycaprolactone: a Review. *Chem. Soc. Rev.* 38 (12), 3484–3504. doi:10.1039/b820162p

Lacoulonche, F., Gamisans, F., Chauvet, A., García, M. L., Espina, M., and Egea, M. A. (1999). Stability and *In Vitro* Drug Release of Flurbiprofen-Loaded Poly-ε-Caprolactone Nanospheres. *Drug Dev. Ind. Pharm.* 25 (9), 983–993. doi:10.1081/ddc-100102261

Lakshmi Prasanna, V., and Vijayaraghavan, R. (2015). Insight into the Mechanism of Antibacterial Activity of ZnO: Surface Defects Mediated Reactive Oxygen Species Even in the Dark. *Langmuir* 31 (33), 9155–9162. doi:10.1021/acs.langmuir.5b02266

Langer, R. (2000). Biomaterials in Drug Delivery and Tissue Engineering: One Laboratory's Experience. *Acc. Chem. Res.* 33 (2), 94–101. doi:10.1021/ar9800993

Lee, E. J., Lee, J. H., Shin, Y. C., Hwang, D.-G., Kim, J. S., Jin, O. S., et al. (2014). Graphene Oxide-Decorated PLGA/collagen Hybrid Fiber Sheets for Application to Tissue Engineering Scaffolds. *Biomater. Res.* 18 (1), 18–24.

Lee, J. H., Khang, G., Lee, J. W., and Lee, H. B. (1998). Interaction of Different Types of Cells on Polymer Surfaces with Wettability Gradient. *J. Colloid Interf. Sci.* 205 (2), 323–330. doi:10.1006/jcis.1998.5688

Lee, J. W., Park, J.-W., and Khang, D. (2015). Analysis of Osteoblast Differentiation on Polymer Thin Films Embedded with Carbon Nanotubes. *Plos one* 10 (6), e0129856. doi:10.1371/journal.pone.0129856

Lee, K. H., Kim, H. Y., Khil, M. S., Ra, Y. M., and Lee, D. R. (2003). Characterization of Nano-Structured Poly(ε-Caprolactone) Nonwoven Mats via Electrospinning. *polymer* 44 (4), 1287–1294. doi:10.1016/s0032-3861(02)00820-0

Lee, S. J., Liu, J., Oh, S. H., Soker, S., Atala, A., and Yoo, J. J. (2008). Development of a Composite Vascular Scaffolding System that Withstands Physiological Vascular Conditions. *Biomaterials* 29 (19), 2891–2898. doi:10.1016/j.biomaterials.2008.03.032

Leonés, A., Mujica-Garcia, A., Arrieta, M. P., Salaris, V., Lopez, D., Kenny, J. M., et al. (2020). Organic and Inorganic PCL-Based Electrospun Fibers. *Polymers* 12 (6), 1325. doi:10.3390/polym12061325

Li, J., He, Y., and Inoue, Y. (2001). Study on Thermal and Mechanical Properties of Biodegradable Blends of Poly(ε-Caprolactone) and Lignin. *Polym. J.* 33 (4), 336–343. doi:10.1295/polymj.33.336

Li, W.-J., Tuli, R., Huang, X., Laquerriere, P., and Tuan, R. S. (2005). Multilineage Differentiation of Human Mesenchymal Stem Cells in a Three-Dimensional Nanofibrous Scaffold. *Biomaterials* 26 (25), 5158–5166. doi:10.1016/j.biomaterials.2005.01.002

Li, C. Y., Li, L., Cai, W., Kodjie, S. L., and Tenneti, K. K. (2005). Nanohybrid Shish-Kebabs: Periodically Functionalized Carbon Nanotubes. *Adv. Mater.* 17 (9), 1198–1202. doi:10.1002/adma.200401977

Li, L., Li, C. Y., and Ni, C. (2006). Polymer Crystallization-Driven, Periodic Patterning on Carbon Nanotubes. *J. Am. Chem. Soc.* 128 (5), 1692–1699. doi:10.1021/ja056923h

Li, P., Ruan, L., Wang, R., Liu, T., Song, G., Gao, X., et al. (2021). Electrospun Scaffold of Collagen and Polycaprolactone Containing ZnO Quantum Dots for Skin Wound Regeneration. *J. Bionic Eng.* 18, 1378–1390. doi:10.1007/s42235-021-00115-7

Li, R., Cheng, Z., Yu, X., Wang, S., Han, Z., and Kang, L. (2019). Preparation of Antibacterial PCL/PVP-AgNP Janus Nanofibers by Uniaxial Electrospinning. *Mater. Lett.* 254, 206–209. doi:10.1016/j.matlet.2019.07.075

Li, S., and Vert, M. (1999). "Biodegradable Polymers: Polyesters," in *Encyclopedia of Controlled Drug Delivery*. Editors E. Mathiowitz (New York: John Wiley & Sons), 71–93.

Li, Y., Chen, M., Zhou, W., Gao, S., Luo, X., Peng, L., et al. (2020). Cell-free 3D Wet-Electrospun PCL/silk fibroin/Sr2+ Scaffold Promotes Successful Total Meniscus Regeneration in a Rabbit Model. *Acta Biomater.* 113, 196–209. doi:10.1016/j.actbio.2020.06.017

Liu, B., Yao, T., Ren, L., Zhao, Y., and Yuan, X. (2018). Antibacterial PCL Electrospun Membranes Containing Synthetic Polypeptides for Biomedical Purposes. *Colloids Surf. B: Biointerfaces* 172, 330–337. doi:10.1016/j.colsurfb.2018.08.055

Liu, J., Cui, L., and Losic, D. (2013). Graphene and Graphene Oxide as New Nanocarriers for Drug Delivery Applications. *Acta Biomater.* 9 (12), 9243–9257. doi:10.1016/j.actbio.2013.08.016

Liverani, L., Lacina, J., Roether, J. A., Boccardi, E., Killian, M. S., Schmuki, P., et al. (2018). Incorporation of Bioactive Glass Nanoparticles in Electrospun PCL/chitosan Fibers by Using Benign Solvents. *Bioactive Mater.* 3 (1), 55–63. doi:10.1016/j.bioactmat.2017.05.003

Longobardi, L., O'Rear, L., Aakula, S., Johnstone, B., Shimer, K., Chytil, A., et al. (2006). Effect of IGF-I in the Chondrogenesis of Bone Marrow Mesenchymal Stem Cells in the Presence or Absence of TGF-Beta Signaling. *J. Bone Miner Res.* 21 (4), 626–636. doi:10.1359/jbmr.051213

Lu, B., Li, T., Zhao, H., Li, X., Gao, C., Zhang, S., et al. (2012). Graphene-based Composite Materials Beneficial to Wound Healing. *Nanoscale* 4 (9), 2978–2982. doi:10.1039/c2nr11958g

Luciani, A., Coccoli, V., Orsi, S., Ambrosio, L., and Netti, P. A. (2008). PCL Microspheres Based Functional Scaffolds by Bottom-Up Approach with Predefined Microstructural Properties and Release Profiles. *Biomaterials* 29 (36), 4800–4807. doi:10.1016/j.biomaterials.2008.09.007

Luginina, M., Schuhladen, K., Orrú, R., Cao, G., Boccaccini, A. R., and Liverani, L. (2020). Electrospun PCL/PGS Composite Fibers Incorporating Bioactive Glass Particles for Soft Tissue Engineering Applications. *Nanomaterials* 10 (5), 978. doi:10.3390/nano10050978

Luo, Y., Shen, H., Fang, Y., Cao, Y., Huang, J., Zhang, M., et al. (2015). Enhanced Proliferation and Osteogenic Differentiation of Mesenchymal Stem Cells on Graphene Oxide-Incorporated Electrospun Poly(lactic-Co-Glycolic Acid) Nanofibrous Mats. *ACS Appl. Mater. Inter.* 7 (11), 6331–6339. doi:10.1021/acsami.5b00862

Mao, L., Xia, L., Chang, J., Liu, J., Jiang, L., Wu, C., et al. (2017). The Synergistic Effects of Sr and Si Bioactive Ions on Osteogenesis, Osteoclastogenesis and Angiogenesis for Osteoporotic Bone Regeneration. *Acta Biomater.* 61, 217–232. doi:10.1016/j.actbio.2017.08.015

Maret, W. (2017). Zinc in Cellular Regulation: the Nature and Significance of "Zinc Signals". *Ijms* 18 (11), 2285. doi:10.3390/ijms18112285

Marrazzo, C., Di Maio, E., and Iannace, S. (2008). Conventional and Nanometric Nucleating Agents in Poly(ε-Caprolactone) Foaming: Crystals vs. Bubbles Nucleation. *Polym. Eng. Sci.* 48 (2), 336–344. doi:10.1002/pen.20937

Marrella, A., Lagazzo, A., Barberis, F., Catelani, T., Quarto, R., and Scaglione, S. (2017). Enhanced Mechanical Performances and Bioactivity of Cell Laden-Graphene Oxide/alginate Hydrogels Open New Scenario for Articular Tissue Engineering Applications. *Carbon* 115, 608–616. doi:10.1016/j.carbon.2017.01.037

Mi, H.-Y., Jing, X., Yu, E., Wang, X., Li, Q., and Turng, L.-S. (2018). Manipulating the Structure and Mechanical Properties of Thermoplastic Polyurethane/polycaprolactone Hybrid Small Diameter Vascular Scaffolds Fabricated via Electrospinning Using an Assembled Rotating Collector. *J. Mech. Behav. Biomed. Mater.* 78, 433–441. doi:10.1016/j.jmbbm.2017.11.046

Miguez-Pacheco, V., Hench, L. L., and Boccaccini, A. R. (2015). Bioactive Glasses beyond Bone and Teeth: Emerging Applications in Contact with Soft Tissues. *Acta Biomater.* 13, 1–15. doi:10.1016/j.actbio.2014.11.004

Miroshnichenko, S., Timofeeva, V., Permyakova, E., Ershov, S., Kiryukhantsev-Korneev, P., Dvořaková, E., et al. (2019). Plasma-coated Polycaprolactone Nanofibers with Covalently Bonded Platelet-Rich Plasma Enhance Adhesion and Growth of Human Fibroblasts. *Nanomaterials* 9 (4), 637. doi:10.3390/nano9040637

Mochane, M. J., Motsoeneng, T. S., Sadiku, E. R., Mokhena, T. C., and Sefadi, J. S. (2019). Morphology and Properties of Electrospun PCL and its Composites for Medical Applications: A Mini Review. *Appl. Sci.* 9 (11), 2205. doi:10.3390/app9112205

Mohamady Hussein, M. A., Guler, E., Rayaman, E., Cam, M. E., Sahin, A., Grinholc, M., et al. (2021). Dual-drug Delivery of Ag-Chitosan Nanoparticles and Phenytoin via Core-Shell PVA/PCL Electrospun Nanofibers. *Carbohydr. Polym.* 270, 118373. doi:10.1016/j.carbpol.2021.118373

Monteiro, A. P. F., Rocha, C. M. S. L., Oliveira, M. F., Gontijo, S. M. L., Agudelo, R. R., Sinisterra, R. D., et al. (2017). Nanofibers Containing Tetracycline/β-Cyclodextrin: Physico-Chemical Characterization and Antimicrobial Evaluation. *Carbohydr. Polym.* 156, 417–426. doi:10.1016/j.carbpol.2016.09.059

Moyers, S. B., and Kumar, N. B. (2004). Green tea Polyphenols and Cancer Chemoprevention: Multiple Mechanisms and Endpoints for Phase II Trials. *Nutr. Rev.* 62 (5), 204–211. doi:10.1111/j.1753-4887.2004.tb00041.x

Nadim, A., Khorasani, S. N., Kharaziha, M., and Davoodi, S. M. (2017). Design and Characterization of Dexamethasone-Loaded Poly (Glycerol Sebacate)-Poly Caprolactone/gelatin Scaffold by Coaxial Electro Spinning for Soft Tissue Engineering. *Mater. Sci. Eng. C* 78, 47–58. doi:10.1016/j.msec.2017.04.047

Nair, L. S., and Laurencin, C. T. (2007). Biodegradable Polymers as Biomaterials. *Prog. Polym. Sci.* 32 (8-9), 762–798. doi:10.1016/j.progpolymsci.2007.05.017

Nam, S., Smith, D. M., and Dou, Q. P. (2001). Ester Bond-Containing Tea Polyphenols Potently Inhibit Proteasome Activity *In Vitro* and *In Vivo*. *J. Biol. Chem.* 276 (16), 13322–13330. doi:10.1074/jbc.m004209200

Naseem, A., Tabasum, S., Zia, K. M., Zuber, M., Ali, M., and Noreen, A. (2016). Lignin-derivatives Based Polymers, Blends and Composites: A Review. *Int. J. Biol. Macromolecules* 93, 296–313. doi:10.1016/j.ijbiomac.2016.08.030

Natta, F. J. v., Hill, J. W., and Carothers, W. H. (1934). Studies of Polymerization and Ring Formation. XXIII.1 ε-Caprolactone and its Polymers. *J. Am. Chem. Soc.* 56 (2), 455–457. doi:10.1021/ja01317a053

Nazeer, M. A., Yilgor, E., and Yilgor, I. (2019). Electrospun Polycaprolactone/silk Fibroin Nanofibrous Bioactive Scaffolds for Tissue Engineering Applications. *Polymer* 168, 86–94. doi:10.1016/j.polymer.2019.02.023

Nichol, J. W., Koshy, S. T., Bae, H., Hwang, C. M., Yamanlar, S., and Khademhosseini, A. (2010). Cell-laden Microengineered Gelatin Methacrylate Hydrogels. *Biomaterials* 31 (21), 5536–5544. doi:10.1016/j.biomaterials.2010.03.064

Norgren, M., and Edlund, H. (2014). Lignin: Recent Advances and Emerging Applications. *Curr. Opin. Colloid Interf. Sci.* 19 (5), 409–416. doi:10.1016/j.cocis.2014.08.004

Núñez, M. J., Novío, S., Balboa, J., Seoane, J., Suárez, J. A., and Freire-Garabal, M. (2010). Effects of Resveratrol on Expression of Vascular Endothelial Growth Factor in Human Gingival Fibroblasts Stimulated by Periodontal Pathogens. *Acta odontologica Scand.* 68 (4), 239–247. doi:10.3109/00016357.2010.494269

Okada, M. (2002). Chemical Syntheses of Biodegradable Polymers. *Prog. Polym. Sci.* 27 (1), 87–133. doi:10.1016/s0079-6700(01)00039-9

Panagiotis, M. (2005). Classification of Non-union. *Injury* 36 (4), S30–S37. doi:10.1016/j.injury.2005.10.008

Pasquet, J., Chevalier, Y., Couval, E., Bouvier, D., Noizet, G., Morlière, C., et al. (2014). Antimicrobial Activity of Zinc Oxide Particles on Five Micro-organisms of the Challenge Tests Related to Their Physicochemical Properties. *Int. J. Pharm.* 460 (1-2), 92–100. doi:10.1016/j.ijpharm.2013.10.031

Patrulea, V., Ostafe, V., Borchard, G., and Jordan, O. (2015). Chitosan as a Starting Material for Wound Healing Applications. *Eur. J. Pharmaceutics Biopharmaceutics* 97, 417–426. doi:10.1016/j.ejpb.2015.08.004

Pedram Rad, Z., Mokhtari, J., and Abbasi, M. (2019). Calendula officinalis extract/PCL/Zein/Gum Arabic Nanofibrous Bio-Composite Scaffolds via Suspension, Two-Nozzle and Multilayer Electrospinning for Skin Tissue Engineering. *Int. J. Biol. Macromolecules* 135, 530–543. doi:10.1016/j.ijbiomac.2019.05.204

Pelipenko, J., Kocbek, P., and Kristl, J. (2015). Critical Attributes of Nanofibers: Preparation, Drug Loading, and Tissue Regeneration. *Int. J. Pharm.* 484 (1-2), 57–74. doi:10.1016/j.ijpharm.2015.02.043

Perumal, G., Sivakumar, P. M., Nandkumar, A. M., and Doble, M. (2020). Synthesis of Magnesium Phosphate Nanoflakes and its PCL Composite Electrospun Nanofiber Scaffolds for Bone Tissue Regeneration. *Mater. Sci. Eng. C* 109, 110527. doi:10.1016/j.msec.2019.110527

Pinto, A. M., Gonçalves, I. C., and Magalhães, F. D. (2013). Graphene-based Materials Biocompatibility: A Review. *Colloids Surf. B: Biointerfaces* 111, 188–202. doi:10.1016/j.colsurfb.2013.05.022

Pitt, C. G. (1990). Poly-ε-caprolactone and its Copolymers. *Drugs Pharm. Sci.* 45, 71–120.

Pok, S., Myers, J. D., Madihally, S. V., and Jacot, J. G. (2013). A Multilayered Scaffold of a Chitosan and Gelatin Hydrogel Supported by a PCL Core for Cardiac Tissue Engineering. *Acta Biomater.* 9 (3), 5630–5642. doi:10.1016/j.actbio.2012.10.032

Puiggalí-Jou, A., Cejudo, A., del Valle, L. J., and Alemán, C. (2018). Smart Drug Delivery from Electrospun Fibers through Electroresponsive Polymeric Nanoparticles. *ACS Appl. Bio Mater.* 1 (5), 1594–1605. doi:10.1021/acsabm.8b00459

Qi, Y. Y., Tai, Z. X., Sun, D. F., Chen, J. T., Ma, H. B., Yan, X. B., et al. (2013). Fabrication and Characterization of Poly(vinyl Alcohol)/graphene Oxide Nanofibrous Biocomposite Scaffolds. *J. Appl. Polym. Sci.* 127 (3), 1885–1894. doi:10.1002/app.37924

Qian, Y., Zhou, X., Zhang, F., Diekwisch, T. G. H., Luan, X., and Yang, J. (2019). Triple PLGA/PCL Scaffold Modification Including Silver Impregnation, Collagen Coating, and Electrospinning Significantly Improve Biocompatibility, Antimicrobial, and Osteogenic Properties for Orofacial Tissue Regeneration. *ACS Appl. Mater. Inter.* 11 (41), 37381–37396. doi:10.1021/acsami.9b07053

Radisavljevic, A., Stojanovic, D. B., Perisic, S., Djokic, V., Radojevic, V., Rajilic-Stojanovic, M., et al. (2018). Cefazolin-loaded Polycaprolactone Fibers Produced via Different Electrospinning Methods: Characterization, Drug Release and Antibacterial Effect. *Eur. J. Pharm. Sci.* 124, 26–36. doi:10.1016/j.ejps.2018.08.023

Rahmani, A., Hashemi-Najafabadi, S., Eslaminejad, M. B., Bagheri, F., and Sayahpour, F. A. (2019). The Effect of Modified Electrospun PCL-nHA-nZnO Scaffolds on Osteogenesis and Angiogenesis. *J. Biomed. Mater. Res.* 107 (9), 2040–2052. doi:10.1002/jbm.a.36717

Reakasame, S., and Boccaccini, A. R. (2017). Oxidized Alginate-Based Hydrogels for Tissue Engineering Applications: A Review. *Biomacromolecules* 19 (1), 3–21. doi:10.1021/acs.biomac.7b01331

Ren, K., Wang, Y., Sun, T., Yue, W., and Zhang, H. (2017). Electrospun PCL/gelatin Composite Nanofiber Structures for Effective Guided Bone Regeneration Membranes. *Mater. Sci. Eng. C* 78, 324–332. doi:10.1016/j.msec.2017.04.084

Rho, K. S., Jeong, L., Lee, G., Seo, B.-M., Park, Y. J., Hong, S.-D., et al. (2006). Electrospinning of Collagen Nanofibers: Effects on the Behavior of normal Human Keratinocytes and Early-Stage Wound Healing. *Biomaterials* 27 (8), 1452–1461. doi:10.1016/j.biomaterials.2005.08.004

Ribeiro, M., Ferraz, M. P., Monteiro, F. J., Fernandes, M. H., Beppu, M. M., Mantione, D., et al. (2017). Antibacterial Silk Fibroin/nanohydroxyapatite Hydrogels with Silver and Gold Nanoparticles for Bone Regeneration. *Nanomedicine: Nanotechnology, Biol. Med.* 13 (1), 231–239. doi:10.1016/j.nano.2016.08.026

Rizzo, A., Bevilacqua, N., Guida, L., Annunziata, M., Romano Carratelli, C., and Paolillo, R. (2012). Effect of Resveratrol and Modulation of Cytokine Production on Human Periodontal Ligament Cells. *Cytokine* 60 (1), 197–204. doi:10.1016/j.cyto.2012.06.004

Ryu, S., and Kim, B.-S. (2013). Culture of Neural Cells and Stem Cells on Graphene. *Tissue Eng. Regen. Med.* 10 (2), 39–46. doi:10.1007/s13770-013-0384-6

Sadi, A. Y., Shokrgozar, M. A., Homaeigohar, S. S., Hosseinalipour, M., Khavandi, A., and Javadpour, J. (2006). The Effect of Partially Stabilized Zirconia on the Biological Properties of HA/HDPE Composites *In Vitro*. *J. Mater. Sci. Mater. Med.* 17 (5), 407–412. doi:10.1007/s10856-006-8467-8

Sakai, T., Johnson, K. J., Murozono, M., Sakai, K., Magnuson, M. A., Wieloch, T., et al. (2001). Plasma Fibronectin Supports Neuronal Survival and Reduces Brain Injury Following Transient Focal Cerebral Ischemia but Is Not Essential for Skin-Wound Healing and Hemostasis. *Nat. Med.* 7 (3), 324–330. doi:10.1038/85471

Salami, M. A., Kaveian, F., Rafienia, M., Saber-Samandari, S., Khandan, A., and Naeimi, M. (2017). Electrospun Polycaprolactone/lignin-Based Nanocomposite as a Novel Tissue Scaffold for Biomedical Applications. *J. Med. Signals Sens* 7 (4), 228–238.

Sang, Y., Li, M., Liu, J., Yao, Y., Ding, Z., Wang, L., et al. (2018). Biomimetic Silk Scaffolds with an Amorphous Structure for Soft Tissue Engineering. *ACS Appl. Mater. Inter.* 10 (11), 9290–9300. doi:10.1021/acsami.7b19204

Santhosh, C., Velmurugan, V., Jacob, G., Jeong, S. K., Grace, A. N., and Bhatnagar, A. (2016). Role of Nanomaterials in Water Treatment Applications: A Review. *Chem. Eng. J.* 306, 1116–1137. doi:10.1016/j.cej.2016.08.053

Sattary, M., Khorasani, M. T., Rafienia, M., and Rozve, H. S. (2018). Incorporation of Nanohydroxyapatite and Vitamin D3 into Electrospun PCL/Gelatin Scaffolds: The Influence on the Physical and Chemical Properties and Cell Behavior for Bone Tissue Engineering. *Polym. Adv. Technol.* 29 (1), 451–462. doi:10.1002/pat.4134

Sayyar, S., Murray, E., Thompson, B. C., Gambhir, S., Officer, D. L., and Wallace, G. G. (2013). Covalently Linked Biocompatible Graphene/polycaprolactone Composites for Tissue Engineering. *Carbon* 52, 296–304. doi:10.1016/j.carbon.2012.09.031

Schwarz, K., and Milne, D. B. (1972). Growth-promoting Effects of Silicon in Rats. *Nature* 239 (5371), 333–334. doi:10.1038/239333a0

Sen, S., Patil, S., and Argyropoulos, D. S. (2015). Thermal Properties of Lignin in Copolymers, Blends, and Composites: a Review. *Green. Chem.* 17 (11), 4862–4887. doi:10.1039/c5gc01066g

Seonwoo, H., Jang, K.-J., Lee, D., Park, S., Lee, M., Park, S., et al. (2018). Neurogenic Differentiation of Human Dental Pulp Stem Cells on Graphene-Polycaprolactone Hybrid Nanofibers. *Nanomaterials* 8 (7), 554. doi:10.3390/nano8070554

Sergi, R., Cannillo, V., Boccaccini, A. R., and Liverani, L. (2020). Incorporation of Bioactive Glasses Containing Mg, Sr, and Zn in Electrospun PCL Fibers by Using Benign Solvents. *Appl. Sci.* 10 (16), 5530. doi:10.3390/app10165530

Shahi, R. G., Albuquerque, M. T. P., Münchow, E. A., Blanchard, S. B., Gregory, R. L., and Bottino, M. C. (2017). Novel Bioactive Tetracycline-Containing Electrospun Polymer Fibers as a Potential Antibacterial Dental Implant Coating. *Odontology* 105 (3), 354–363. doi:10.1007/s10266-016-0268-z

Shakesheff, K. M., Cannizzaro, S. M., and Langer, R. (1998). Creating Biomimetic Micro-environments with Synthetic Polymer-Peptide Hybrid Molecules. *J. Biomater. Sci. Polym. Ed.* 9 (5), 507–518. doi:10.1163/156856298x00596

Shao, S., Zhou, S., Li, L., Li, J., Luo, C., Wang, J., et al. (2011). Osteoblast Function on Electrically Conductive Electrospun PLA/MWCNTs Nanofibers. *Biomaterials* 32 (11), 2821–2833. doi:10.1016/j.biomaterials.2011.01.051

Sharifi, M., Bahrami, S. H., Nejad, N. H., and Milan, P. B. (2020). Electrospun PCL and PLA Hybrid Nanofibrous Scaffolds Containing Nigella Sativa Herbal Extract for Effective Wound Healing. *J. Appl. Polym. Sci.* 137 (46), 49528. doi:10.1002/app.49528

Shi, Z., Gao, X., Ullah, M. W., Li, S., Wang, Q., and Yang, G. (2016). Electroconductive Natural Polymer-Based Hydrogels. *Biomaterials* 111, 40–54. doi:10.1016/j.biomaterials.2016.09.020

Shimizu, M., Kobayashi, Y., Mizoguchi, T., Nakamura, H., Kawahara, I., Narita, N., et al. (2012). Carbon Nanotubes Induce Bone Calcification by Bidirectional Interaction with Osteoblasts. *Adv. Mater.* 24 (16), 2176–2185. doi:10.1002/adma.201103832

Shitole, A. A., Raut, P. W., Sharma, N., Giram, P., Khandwekar, A. P., and Garnaik, B. (2019). Electrospun polycaprolactone/hydroxyapatite/ZnO Nanofibers as Potential Biomaterials for Bone Tissue Regeneration. *J. Mater. Sci. Mater. Med.* 30 (5), 51–17. doi:10.1007/s10856-019-6255-5

Siddiqui, N., Asawa, S., Birru, B., Baadhe, R., and Rao, S. (2018). PCL-based Composite Scaffold Matrices for Tissue Engineering Applications. *Mol. Biotechnol.* 60 (7), 506–532. doi:10.1007/s12033-018-0084-5

Silva, J. C., Udangawa, R. N., Chen, J., Mancinelli, C. D., Garrudo, F. F. F., Mikael, P. E., et al. (2020). Kartogenin-loaded Coaxial PGS/PCL Aligned Nanofibers for Cartilage Tissue Engineering. *Mater. Sci. Eng. C* 107, 110291. doi:10.1016/j.msec.2019.110291

Singh, S., Casper, R., Fritz, P., Sukhu, B., Ganss, B., Girard, B., Jr, et al. (2000). Inhibition of Dioxin Effects on Bone Formation *In Vitro* by a Newly Described Aryl Hydrocarbon Receptor Antagonist, Resveratrol. *J. Endocrinol.* 167 (1), 183–195. doi:10.1677/joe.0.1670183

Sirelkhatim, A., Mahmud, S., Seeni, A., Kaus, N. H. M., Ann, L. C., Bakhori, S. K. M., et al. (2015). Review on Zinc Oxide Nanoparticles: Antibacterial Activity

and Toxicity Mechanism. *Nano-micro Lett.* 7 (3), 219–242. doi:10.1007/s40820-015-0040-x

Sofia, S., McCarthy, M. B., Gronowicz, G., and Kaplan, D. L. (2001). Functionalized Silk-Based Biomaterials for Bone Formation. *J. Biomed. Mater. Res.* 54 (1), 139–148. doi:10.1002/1097-4636(200101)54:1<139::aid-jbm17>3.0.co;2-7

Son, Y. J., Kim, W. J., and Yoo, H. S. (2014). Therapeutic Applications of Electrospun Nanofibers for Drug Delivery Systems. *Arch. Pharm. Res.* 37 (1), 69–78. doi:10.1007/s12272-013-0284-2

Steele, J., Dalton, B. A., Johnson, G., and Underwood, P. A. (1995). Adsorption of Fibronectin and Vitronectin onto Primaria and Tissue Culture Polystyrene and Relationship to the Mechanism of Initial Attachment of Human Vein Endothelial Cells and BHK-21 Fibroblasts. *Biomaterials* 16 (14), 1057–1067. doi:10.1016/0142-9612(95)98901-p

Suryamathi, M., Ruba, C., Viswanathamurthi, P., Balasubramanian, V., and Perumal, P. (2019). Tridax Procumbens Extract Loaded Electrospun PCL Nanofibers: a Novel Wound Dressing Material. *Macromol. Res.* 27 (1), 55–60. doi:10.1007/s13233-019-7022-7

Tampau, A., González-Martinez, C., and Chiralt, A. (2017). Carvacrol Encapsulation in Starch or PCL Based Matrices by Electrospinning. *J. Food Eng.* 214, 245–256. doi:10.1016/j.jfoodeng.2017.07.005

Toledano, M., Yamauti, M., Osorio, E., and Osorio, R. (2012). Zinc-inhibited MMP-Mediated Collagen Degradation after Different Dentine Demineralization Procedures. *Caries Res.* 46 (3), 201–207. doi:10.1159/000337315

Ueno, T., Mizukawa, N., and Sugahara, T. (1999). Experimental Study of Bone Formation from Autogenous Periosteal Graft Following Insulin-like Growth Factor I Administration. *J. Craniomaxillofac. Surg.* 27 (5), 308–313. doi:10.1054/jcms.1999.0077

Unalan, I., Slavik, B., Buettner, A., Goldmann, W. H., Frank, G., and Boccaccini, A. R. (2019). Physical and Antibacterial Properties of Peppermint Essential Oil Loaded Poly (ε-Caprolactone) (PCL) Electrospun Fiber Mats for Wound Healing. *Front. Bioeng. Biotechnol.* 7, 346. doi:10.3389/fbioe.2019.00346

Underwood, P. A., and Bennett, F. A. (1989). A Comparison of the Biological Activities of the Cell-Adhesive Proteins Vitronectin and Fibronectin. *J. Cel Sci.* 93 (4), 641–649. doi:10.1242/jcs.93.4.641

van Wachem, P. B., Mallens, B. W. L., Dekker, A., Beugeling, T., Feijen, J., Bantjes, A., et al. (1987). Adsorption of Fibronectin Derived from Serum and from Human Endothelial Cells onto Tissue Culture Polystyrene. *J. Biomed. Mater. Res.* 21 (11), 1317–1327. doi:10.1002/jbm.820211104

Venugopal, E., Sahanand, K. S., Bhattacharyya, A., and Rajendran, S. (2019). Electrospun PCL Nanofibers Blended with Wattakaka Volubilis Active Phytochemicals for Bone and Cartilage Tissue Engineering. *Nanomedicine: Nanotechnology, Biol. Med.* 21, 102044. doi:10.1016/j.nano.2019.102044

Wan, C., and Chen, B. (2011). Poly(ε-caprolactone)/graphene Oxide Biocomposites: Mechanical Properties and Bioactivity. *Biomed. Mater.* 6 (5), 055010. doi:10.1088/1748-6041/6/5/055010

Wang, H., Li, Y., Zuo, Y., Li, J., Ma, S., and Cheng, L. (2007). Biocompatibility and Osteogenesis of Biomimetic Nano-Hydroxyapatite/polyamide Composite Scaffolds for Bone Tissue Engineering. *Biomaterials* 28 (22), 3338–3348. doi:10.1016/j.biomaterials.2007.04.014

Wang, H., Tong, D., Wang, L., Chen, L., Yu, N., and Li, Z. (2017). A Facile Strategy for Fabricating PCL/PEG Block Copolymer with Excellent Enzymatic Degradation. *Polym. Degrad. Stab.* 140, 64–73. doi:10.1016/j.polymdegradstab.2017.04.015

Wang, S., Li, Y., Zhao, R., Jin, T., Zhang, L., and Li, X. (2017). Chitosan Surface Modified Electrospun Poly(ε-Caprolactone)/carbon Nanotube Composite Fibers with Enhanced Mechanical, Cell Proliferation and Antibacterial Properties. *Int. J. Biol. Macromolecules* 104, 708–715. doi:10.1016/j.ijbiomac.2017.06.044

Wang, Y., Cui, W., Chou, J., Wen, S., Sun, Y., and Zhang, H. (2018). Electrospun Nanosilicates-Based Organic/inorganic Nanofibers for Potential Bone Tissue Engineering. *Colloids Surf. B: Biointerfaces* 172, 90–97. doi:10.1016/j.colsurfb.2018.08.032

Wang, Y., Pan, H., and Chen, X. (2019). The Preparation of Hollow Mesoporous Bioglass Nanoparticles with Excellent Drug Delivery Capacity for Bone Tissue Regeneration. *Front. Chem.* 7 (283), 283. doi:10.3389/fchem.2019.00283

Wang, D., Jang, J., Kim, K., Kim, J., and Park, C. B. (2019). "Tree to Bone": Lignin/polycaprolactone Nanofibers for Hydroxyapatite Biomineralization. *Biomacromolecules* 20 (7), 2684–2693. doi:10.1021/acs.biomac.9b00451

Wang, Z., Liang, R., Jiang, X., Xie, J., Cai, P., Chen, H., et al. (2019). Electrospun PLGA/PCL/OCP Nanofiber Membranes Promote Osteogenic Differentiation of Mesenchymal Stem Cells (MSCs). *Mater. Sci. Eng. C* 104, 109796. doi:10.1016/j.msec.2019.109796

Wedmore, I., McManus, J. G., Pusateri, A. E., and Holcomb, J. B. (2006). A Special Report on the Chitosan-Based Hemostatic Dressing: Experience in Current Combat Operations. *J. Trauma Inj. Infect. Crit. Care* 60 (3), 655–658. doi:10.1097/01.ta.0000199392.91772.44

Weng, L., Boda, S. K., Teusink, M. J., Shuler, F. D., Li, X., and Xie, J. (2017). Binary Doping of Strontium and Copper Enhancing Osteogenesis and Angiogenesis of Bioactive Glass Nanofibers while Suppressing Osteoclast Activity. *ACS Appl. Mater. Inter.* 9 (29), 24484–24496. doi:10.1021/acsami.7b06521

Williams, R. J., Spencer, J. P. E., and Rice-Evans, C. (2004). Flavonoids: Antioxidants or Signalling Molecules. *Free Radic. Biol. Med.* 36 (7), 838–849. doi:10.1016/j.freeradbiomed.2004.01.001

Woodruff, M. A., and Hutmacher, D. W. (2010). The Return of a Forgotten Polymer-Polycaprolactone in the 21st century. *Prog. Polym. Sci.* 35 (10), 1217–1256. doi:10.1016/j.progpolymsci.2010.04.002

Wu, T., Chen, X., Sha, J., Peng, Y.-Y., Ma, Y.-L., Xie, L.-S., et al. (2019). Fabrication of Shish-Kebab-Structured Carbon Nanotube/poly(ε-Caprolactone) Composite Nanofibers for Potential Tissue Engineering Applications. *Rare Met.* 38 (1), 64–72. doi:10.1007/s12598-017-0965-y

Xiang, P., Wang, S.-S., He, M., Han, Y.-H., Zhou, Z.-H., Chen, D.-L., et al. (2018). The *In Vitro* and *In Vivo* Biocompatibility Evaluation of Electrospun Recombinant Spider Silk protein/PCL/gelatin for Small Caliber Vascular Tissue Engineering Scaffolds. *Colloids Surf. B: Biointerfaces* 163, 19–28. doi:10.1016/j.colsurfb.2017.12.020

Xynos, I. D., Edgar, A. J., Buttery, L. D. K., Hench, L. L., and Polak, J. M. (2001). Gene-expression Profiling of Human Osteoblasts Following Treatment with the Ionic Products of Bioglass 45S5 Dissolution. *J. Biomed. Mater. Res.* 55 (2), 151–157. The Japanese Society for Biomaterials, and The Australian Society for Biomaterials and the Korean Society for Biomaterials. doi:10.1002/1097-4636(200105)55:2<151::aid-jbm1001>3.0.co;2-d

Yang, F., Yang, D., Tu, J., Zheng, Q., Cai, L., and Wang, L. (2011). Strontium Enhances Osteogenic Differentiation of Mesenchymal Stem Cells and *In Vivo* Bone Formation by Activating Wnt/catenin Signaling. *Stem cells* 29 (6), 981–991. doi:10.1002/stem.646

Yang, X., Yang, F., Walboomers, X. F., Bian, Z., Fan, M., and Jansen, J. A. (2010). The Performance of Dental Pulp Stem Cells on Nanofibrous PCL/gelatin/nHA Scaffolds. *J. Biomed. Mater. Res. A.* 93 (1), 247–257. doi:10.1002/jbm.a.32535

Yari Sadi, A., Shokrgozar, M. A., Homaeigohar, S. S., and Khavandi, A. (2008). Biological Evaluation of Partially Stabilized Zirconia Added HA/HDPE Composites with Osteoblast and Fibroblast Cell Lines. *J. Mater. Sci. Mater. Med.* 19 (6), 2359–2365. doi:10.1007/s10856-007-3336-7

Yoshimoto, H., Shin, Y. M., Terai, H., and Vacanti, J. P. (2003). A Biodegradable Nanofiber Scaffold by Electrospinning and its Potential for Bone Tissue Engineering. *Biomaterials* 24 (12), 2077–2082. doi:10.1016/s0142-9612(02)00635-x

Yu, H., Peng, J., Xu, Y., Chang, J., and Li, H. (2016). Bioglass Activated Skin Tissue Engineering Constructs for Wound Healing. *ACS Appl. Mater. Inter.* 8 (1), 703–715. doi:10.1021/acsami.5b09853

Yu, J., Xu, L., Li, K., Xie, N., Xi, Y., Wang, Y., et al. (2017). Zinc-modified Calcium Silicate Coatings Promote Osteogenic Differentiation through TGF-β/Smad Pathway and Osseointegration in Osteopenic Rabbits. *Sci. Rep.* 7 (1), 3440. doi:10.1038/s41598-017-03661-5

Zamani, M., Morshed, M., Varshosaz, J., and Jannesari, M. (2010). Controlled Release of Metronidazole Benzoate from Poly ε-caprolactone Electrospun Nanofibers for Periodontal Diseases. *Eur. J. Pharmaceutics Biopharmaceutics* 75 (2), 179–185. doi:10.1016/j.ejpb.2010.02.002

Zanetti, M., Mazon, L. R., de Meneses, A. C., Silva, L. L., de Araújo, P. H. H., Fiori, M. A., et al. (2019). Encapsulation of Geranyl Cinnamate in Polycaprolactone Nanoparticles. *Mater. Sci. Eng. C* 97, 198–207. doi:10.1016/j.msec.2018.12.005

Zeng, J., Xu, X., Chen, X., Liang, Q., Bian, X., Yang, L., et al. (2003). Biodegradable Electrospun Fibers for Drug Delivery. *J. Controlled Release* 92 (3), 227–231. doi:10.1016/s0168-3659(03)00372-9

Zhang, Y., Cui, X., Zhao, S., Wang, H., Rahaman, M. N., Liu, Z., et al. (2015). Evaluation of Injectable Strontium-Containing Borate Bioactive Glass Cement

with Enhanced Osteogenic Capacity in a Critical-Sized Rabbit Femoral Condyle Defect Model. *ACS Appl. Mater. Inter.* 7 (4), 2393–2403. doi:10.1021/am507008z

Zhang, Y., Lim, C. T., Ramakrishna, S., and Huang, Z.-M. (2005). Recent Development of Polymer Nanofibers for Biomedical and Biotechnological Applications. *J. Mater. Sci. Mater. Med.* 16 (10), 933–946. doi:10.1007/s10856-005-4428-x

Zhou, C.-Z., Confalonieri, F., Medina, N., Zivanovic, Y., Esnault, C., Yang, T., et al. (2000). Fine Organization of *Bombyx mori* Fibroin Heavy Chain Gene. *Nucleic Acids Res.* 28 (12), 2413–2419. doi:10.1093/nar/28.12.2413

Zhou, F., Wen, M., Zhou, P., Zhao, Y., Jia, X., Fan, Y., et al. (2018). Electrospun Membranes of PELCL/PCL-REDV Loading with miRNA-126 for Enhancement of Vascular Endothelial Cell Adhesion and Proliferation. *Mater. Sci. Eng. C* 85, 37–46. doi:10.1016/j.msec.2017.12.005

Zupančič, Š., Baumgartner, S., Lavrič, Z., Petelin, M., and Kristl, J. (2015). Local Delivery of Resveratrol Using Polycaprolactone Nanofibers for Treatment of Periodontal Disease. *J. Drug Deliv. Sci. Techn.* 30, 408–416. doi:10.1016/j.jddst.2015.07.009

Conflict of Interest: The authors declare that the research was conducted in the absence of any commercial or financial relationships that could be construed as a potential conflict of interest.

Publisher's Note: All claims expressed in this article are solely those of the authors and do not necessarily represent those of their affiliated organizations, or those of the publisher, the editors and the reviewers. Any product that may be evaluated in this article, or claim that may be made by its manufacturer, is not guaranteed or endorsed by the publisher.

frontiers in Chemistry

ORIGINAL RESEARCH
published: 20 January 2022
doi: 10.3389/fchem.2021.810256

Electrodeposition as an Alternative Approach for Monolithic Integration of InSb on Silicon

Katarzyna E. Hnida-Gut[1]*, *Marilyne Sousa*[1], *Marinus Hopstaken*[2], *Steffen Reidt*[1], *Kirsten Moselund*[1] *and Heinz Schmid*[1]

[1]IBM Research Europe-Zurich, Rüschlikon, Switzerland, [2]IBM T.J. Watson Research Center-Yorktown Heights, New York, NY, United States

High-performance electronics would greatly benefit from a versatile III-V integration process on silicon. Unfortunately, integration using hetero epitaxy is hampered by polarity, lattice, and thermal expansion mismatch. This work proposes an alternative concept of III-V integration combining advantages of pulse electrodeposition, template-assisted selective epitaxy, and recrystallization from a melt. Efficient electrodeposition of nano-crystalline and stochiometric InSb in planar templates on Si (001) is achieved. The InSb deposits are analysed by high resolution scanning transmission electron microscopy (HR-STEM) and energy-dispersive X-ray spectroscopy (EDX) before and after melting and recrystallization. The results show that InSb can crystallise epitaxially on Si with the formation of stacking faults. Furthermore, X-ray photoelectron (XPS) and Auger electron (AE) spectroscopy analysis indicate that the InSb crystal size is limited by the impurity concentration resulting from the electrodeposition process.

Keywords: integration, InSb, electrodeposition, recrystallization, III-Vs, TASE

OPEN ACCESS

Edited by:
Luís D. Carlos,
University of Aveiro, Portugal

Reviewed by:
Edward Gillan,
The University of Iowa, United States
I. M. Dharmadasa,
Sheffield Hallam University, United Kingdom

***Correspondence:**
Katarzyna E. Hnida-Gut
khn@zurich.ibm.com

Specialty section:
This article was submitted to Electrochemistry, a section of the journal Frontiers in Chemistry

Received: *06 November 2021*
Accepted: *03 December 2021*
Published: *20 January 2022*

Citation:
Hnida-Gut KE, Sousa M, Hopstaken M, Reidt S, Moselund K and Schmid H (2022) Electrodeposition as an Alternative Approach for Monolithic Integration of InSb on Silicon. Front. Chem. 9:810256. doi: 10.3389/fchem.2021.810256

INTRODUCTION

Globally, one of the fastest-growing industries is electronic devices manufacturing based on silicon technology. With an increasing demand for faster, smaller, and better-performing devices, growth CAGR (compound annual growth rate) of 4.6% from 2020 to 2027 for this field is expected. Nonetheless, recently both academia and industry have focused efforts on the search for alternative technologies for which performance in the long run could considerably surpass that of Si (Ramirez et al., 2020), especially in more futuristic applications like quantum computing. These include III-V semiconductors for sensing and high-speed electronics where high value is created (Riel, 2017). The best solution would be to combine the advantages of Si and III-Vs (Hopkinson et al., 2013). However both economic and technological difficulties, like crystal lattice and polarity mismatch, have prevented the integration of foreign materials directly on a silicon platform.

One approach to address this problem, the so-called Template-Assisted Selective Epitaxy (TASE), was developed by IBM a few years ago (Schmid et al., 2015). By directing the growth by an oxide template and using metal-organic vapor phase deposition (MOCVD) to fill the designed structures, successful integration of InGaAs, InP, GaSb, etc. for high-performance MOSFETs or lasers on silicon was possible. However, MOCVD growth is limited by its low growth rates, difficulty of filling high aspect ratio structures, and the use of toxic precursors. Furthermore, not every III-V semiconductor is well suited for this technique. Examples for challenging materials include aluminum containing compounds due to the high sticking coefficient of Al on the mask material and antimonides due to

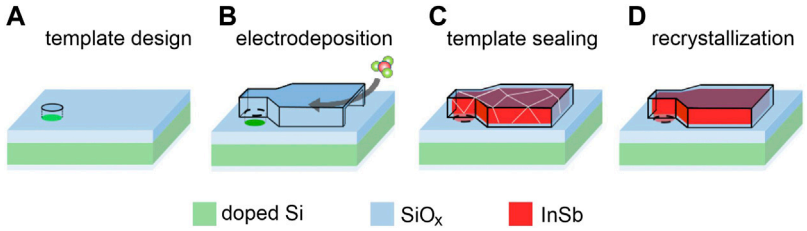

FIGURE 1 | Proposed process flow for InSb integration on Si. Conductive Si substrate with surrounding SiO_x insulation **(A)** Conductive Si substrate with surrounding SiOx insulation and **(B)** 3D template is immersed in the electrochemical cell. **(C)** After electrochemical deposition of polycrystalline InSb, the template is sealed. **(D)** Melting and recrystallization to form a InSb singe crystal on Si.

the small process window to supress droplet formation. InSb is a particularly interesting material with properties such as one of the smallest direct band gap (0.17 eV at 300 K) and highest electron mobility (77,000 $cm^2V^{-1}s^{-1}$) among III-Vs and can ensure applications in a wide range of modern devices, starting from terahertz (Liu et al., 2018a) and gamma rays detectors (Hishiki et al., 2005), through IR (Xie et al., 2016; Shi et al., 2019) and neutron-resistant Hall (Jankowski et al., 2019) sensors, ending on topological quantum devices for Majorana investigation (Chen et al., 2021). As an alternative synthesis path, electrochemical technique is considered since it was demonstrated to fill different shapes and sizes of templates efficiently, with control over composition, and using a simple set-up with water-based electrolytes (Hnida et al., 2015; Hnida et al., 2019). However, due to the characteristics of the InSb electrodeposition, the obtained material is polycrystalline, which significantly limits its practical use. To overcome this, concepts borrowed from micro zone recrystallization (Billings, 1969) and rapid melt growth (Liu et al., 2018b) can be applied. Here, the samples are subjected to a short high temperature step exceeding the melting temperature. During this step the polycrystalline sample melts and recrystallizes from a seed interface, resulting in a single crystalline structure with epitaxial relationship to the substrate.

The goal of this work is to directly integrate InSb on a silicon platform. To reach that we propose combining the three techniques, namely TASE, pulse electrodeposition, and recrystallization. The proposed process is designed to resolve the identified issues and is summarized in **Figure 1**. One of the key aspects is that the low melting point of InSb could allow for a CMOS compatible process.

MATERIALS AND METHODS

One of the requirements for electrodeposition of InSb on silicon is to provide a conductive electrode. In the presented work we used highly doped silicon wafer as global working electrode to simplify the fabrication process, while formation of addressable electrodes would require additional processing steps. Silicon wafers (001) n-type for two sets of templates having larger or smaller structures were prepared. For template fabrication, holes were etched in 100 nm thick SiO_x on Si by reactive ion etching (RIE) to define the electrode/seed area. Then, a 1,350 nm thick bis-benzocyclobutene (BCB, Dow) layer was spin coated and cross-linked at 320°C. Subsequently, the BCB layer was patterned with the layout of template structures, etched using RIE, and coated with a 150 nm thick SiO_x shell by plasma enhanced chemical vapor deposition (PECVD). Finally, openings were patterned on the template structures and etched into the SiO_x shell exposing the BCB layer. The remaining BCB layer was etched using peroxide/sulfuric acid 1:3 solution, resulting in hollow template structures. The as-prepared substrate was dipped for 12–15 s in diluted (2.5%) HF to remove the native oxide on the exposed Si surfaces within the channels before electrodeposition.

All electrochemical syntheses were performed in a water-based electrolyte containing 0.06M $InCl_3$ (Sigma Aldrich, >98%), 0.045M $SbCl_3$ (Sigma Aldrich, ≥99%), 0.2M citric acid (Sigma Aldrich, ≥99%), and 0.17M sodium citrate (Sigma Aldrich, ≥99%) at room temperature. Both citric acid and sodium citrate were used as complexing agents to bring reduction potentials of indium and antimony ions closer to each other. The electrodeposition experiments were carried out using the potentiostat (BioLogic SP300) with a three-electrode setup. An Ag/AgCl (3M NaCl) electrode as a reference electrode (Ref) and Pt wire as a counter electrode (CE) were employed. SiO_x template as a working electrode (WE) was installed at a distance of 1.5 cm from the CE electrode. Unless otherwise stated, all potentials refer to the Ref. The fabrication of InSb nano and microstructures was performed using a cathodic pulse with E_{on} = −2.3 V followed by E_{off} = −0.1 V. The potentials of "on" and "off" pulses were chosen based on Linear Sweep Voltammetry (LSV) and Open Circuit Potential (OCP) measurements on bare n-Si, respectively. The duration of pulse "on" and "off" were 1 and 5 ms, respectively, based on previous research (Hnida et al., 2015). During pulse "on" the reduction of In and Sb citric complexes occur, while during pulse "off" replenishment of electrolyte near the working electrode surface and dissolution of the top surface of deposit happen (Rajska et al., 2021). Section of the typical electrodeposition pulse sequence is presented in **Figure 2A**. Blue dotted frame marks one cycle. Slight variations in potential and current (red and green lines, respectively, slope especially visible for pulse "off") are related to the data accusation. The total deposition times ((t_{on} + t_{off}) × number of cycles) were kept in a range of 12–240 s depending on the size and shape of the

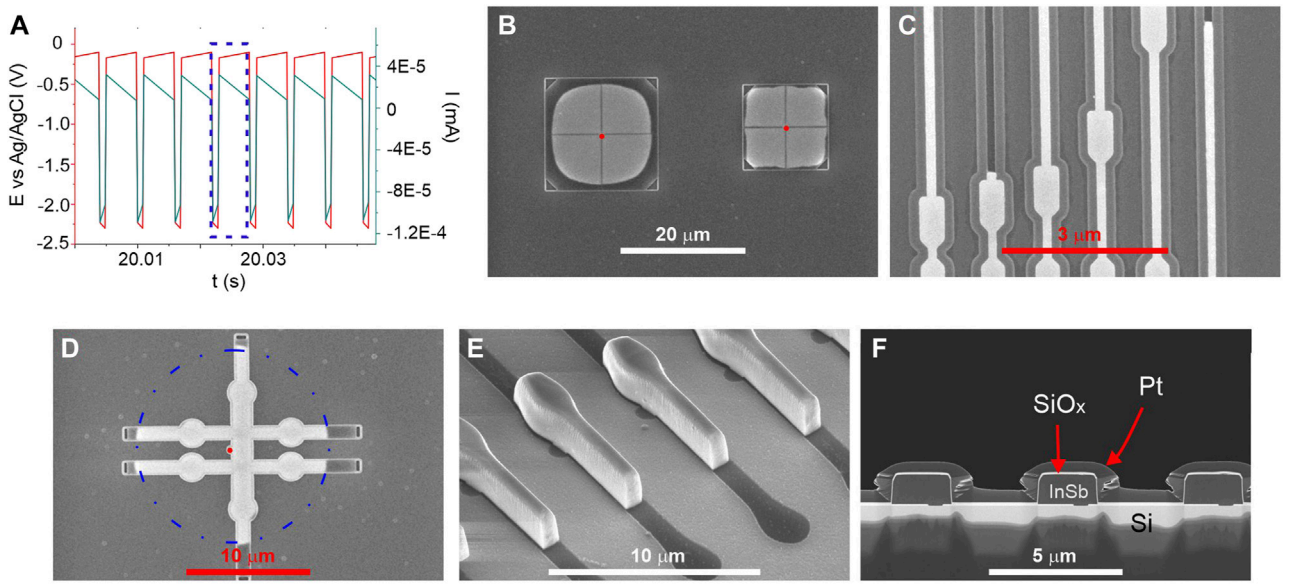

FIGURE 2 | (A) Section of typical potential pulse sequence. Blue dotted frame marks one cycle. **(B–D)** SEM images of filled SiO_x templates with different shapes and sizes. Seed hole marked with the red dot. **(E)** SEM image of InSb deposit after partial removal of the SiO_x template. The dark shade marks the area of the template which was left unfilled. **(F)** A cross-section of filled templates exposing the seed regions. Both SiO_x capping (thin bright part on top of the deposit) and Pt proctective (thick grey part on top of the SiO_x) layers are marked.

oxide template and overall geometrical area of the working electrode.

For a thin intermediate InSb layer synthesis, MOCVD technique was implemented. Selective epitaxy of InSb was carried out using trimethylindium (TMIn), and trimethylantimony (TMSb) at V/III ratio 100 at 430°C for 65 s, followed by 25 s of Sb deposition to further suppress the presence of In droplets.

The melting process was performed on SiO_x-capped samples at 535°C, 50 mbar for 2 s. The system was calibrated prior to the process and offset in the measured temperature was considered. After annealing, the SiO_x capping layer was removed using a combination of RIE and HF etching (either wet or vapor), and the morphology, crystallinity, and chemical composition were characterized using scanning electron microscopy (SEM, Hitachi SU8000) and analytical (scanning) transmission electron microscope ((S)TEM, JEOL ARM200F) equipped with energy-dispersive X-ray spectroscopy detector. Lamellas for (S)TEM-EDX analysis were prepared using the focus ion beam technique (Dual beam FIB/SEM, FEI Helios NanoLab 450S). Priori the lamella preparation samples were covered with 250 nm of SiO_x. The samples have been measured under UHV condition with a Varian Auger system equipped with a TPIS plasma gun.

RESULTS AND DISCUSSION

In preliminary studies, we tested different silicon wafer orientations and doping levels. No change in morphology and composition between deposits was observed as long as ohmic contacts could be established. InSb deposition on BHF passivated Si showed a high nucleation density and dense film formation. However, the film adhesion was low and with the buildup of mechanical strain in the film, leading to delamination with increasing thickness already in the plating solution (Hnida-Gut et al., 2021). **Figure 2** shows representative SEM images of InSb deposited in the template structures. Here, loss of adhesion and strain as encountered with planer films is not a limiting factor anymore. **Figure 2B** shows two squares composed of four quadrants each with the seed located in the center, and the template opening at the corners. The deposition process is very selective, and the InSb is deposited with high uniformity in each quarter. Templates with up to 10 μm large free-standing structures were successfully filled, while larger ones collapsed due to capillary forces during the fabrication process. The smallest structures fabricated and filled (**Figure 2C**) have line width down to 120 nm. **Figure 2D** illustrates uniform filling of the intended Hall bar structure with the seed area indicated as red point and a dashed circle as reference. **Figure 2E** shows a tilted view image of a sample where the SiO_x was partially removed. The smooth top surface is a result of the replication of the inherently low surface roughness of the spin coated BCB film, while the sidewall roughness originates from the BCB etching process. Cross-sections from several structures are shown in **Figure 2F**, confirming the absence of gaps, voids, and cracks in the InSb.

After demonstrating the successful electrodeposition on InSb on Si, and according to **Figure 1**, step D follows with melting and controlled recrystallization of the InSb from the seed area. First, the chemical composition is accessed before and after the melting step, followed by further chemical and structural analysis. **Figure 3** shows (S)TEM cross-section images of two samples

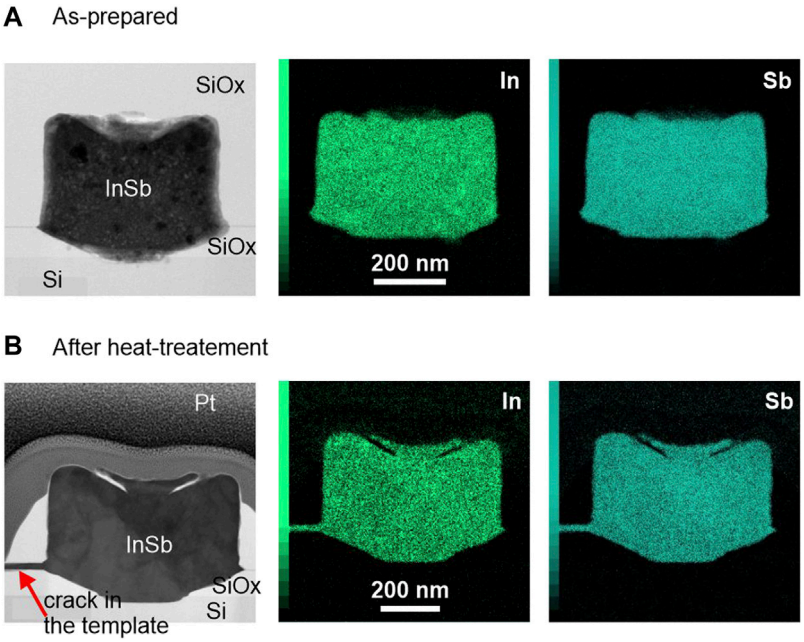

FIGURE 3 | (S)TEM images and EDX maps for **(A)** as-prepared and **(B)** annealed InSb deposits. The scale bar for all images is 200 nm.

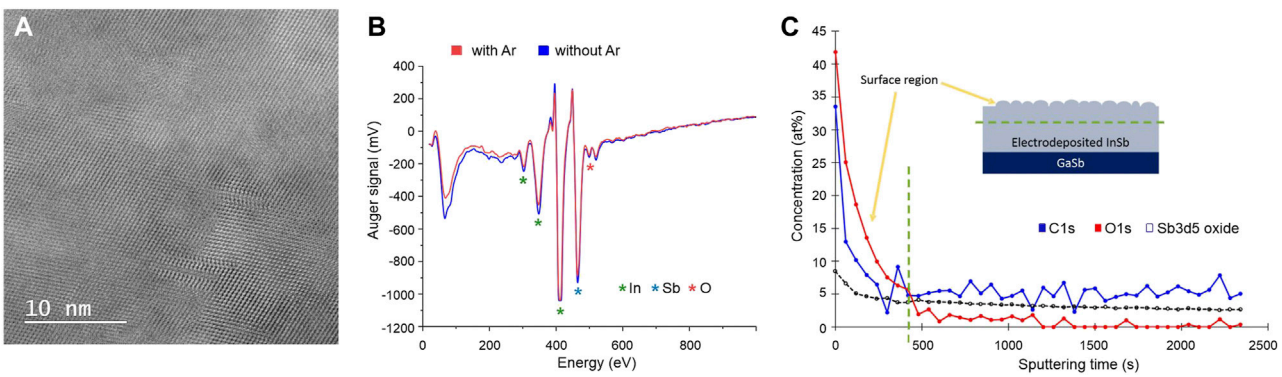

FIGURE 4 | (A) High-resolution (S)TEM image of InSb after annealing process. **(B)** Auger spectra for samples electrodeposited with (blue) and without (red) oxygen dissolved in the electrolyte, respectively. **(C)** XPS depth profile of impurities [O (red), C (blue), and Sb oxide (black)] concentration (at%) distribution in electrodeposited InSb. Sputtering time is directly correlated with the thickness of the deposit. A green dotted line marks the surface region with indicates the presence of electrolyte residues and surface oxides.

(as-prepared and annealed, respectively) which were cut across the samples such as to expose seed areas and including the InSb-Si interface. We note that the unexpected roughness of the top surfaces stems from an artefact during the fabrication process. (S)TEM-EDX mapping was performed to investigate the distribution of In and Sb elements (**Figure 3**, center and right-side panels) in the deposited volume before and after annealing for 2 s at 535°C. In both samples the distribution of In and Sb atoms is uniform with no detectable phase separation. The In/Sb ratio for the as-prepared sample was 45/55 (±10%) and remained constant after annealing. In **Figures 3A,B** a small crack is visible on the left (marked with the red arrow) which was created during the annealing procedure, caused by volume expansion of the melt or thermal stress in the oxide template. Interestingly, the resulting void is completely filled with InSb, thus confirm the melting of the deposit. After the RTA process voids in the InSb structures were frequently detected by SEM inspection, indicating loss of material. This observation was also reported in Menon et al. (2021) and needs further investigation.

Structural analysis using bright field (BF) HR-(S)TEM revealed unexpectedly that both samples remained throughout nanocrystalline with no significant differences in the size of the crystals (**Figure 4A**), despite the fact that the melting was indeed achieved. In addition, the anticipated recrystallization from the Si

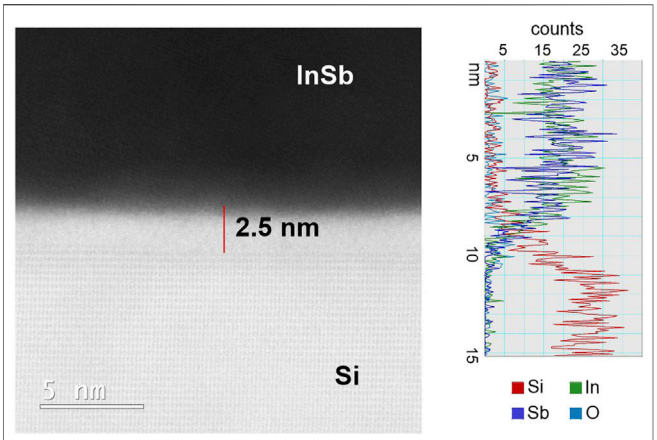

FIGURE 5 | High-resolution (S)TEM image of the Si—InSb interface for recrystallized sample together with EDX spectra.

seed interface did not take place. Regarding the first observation, a possible explanation might be found in the process of diamond crystallization in metal-carbon systems. Palyanov et al. recently reported that oxygen can greatly affect the crystallization (Palyanov et al., 2020). They found that the concentration of O_2 higher than 0.25 wt% can lead to spontaneous nucleation events which hinders crystal growth. As oxygen is present in the water-based electrolyte used for InSb electrodeposition, it is plausible that impurity induced nucleation is limiting the InSb crystallization. The common way of removing oxygen dissolved in the electrolyte is to deoxygenate it with inert gas (such as N_2 or Ar) before and during the synthesis. To explore this hypothesis, two electrodeposition processes were conducted (namely with and without O_2 dissolved in the electrolyte), after which samples were immediately stored in a glove box. Both samples were subjected to Auger electron spectroscopy measurement to determine the influence of O_2 in the electrolyte on its content in the InSb deposits. Both spectra are presented in **Figure 4B** and reveal that regardless of whether the electrolyte used in the synthesis was deoxygenated or not, significant amounts of oxygen are incorporated. To further confirm the intrinsic oxygen and/or carbon contamination in electrodeposited InSb, XPS analysis was performed using a GaSb as substrate for Sb-signal as reference. Due to overlapping spectra for Sb and O, the exact deduction of how much oxygen is dissolved in the InSb deposit is, however, challenging. The XPS depth profile is shown in **Figure 4C** and confirms high concentrations of oxygen, carbon, and antimony oxide on the surface and in the bulk of the electrodeposited InSb. Impurity concentrations are stable around 5.2 at%, 0.8 at%, and 3.1 at% for C, O, and Sb oxide, respectively, which can explain the observed suppression of crystal growth.

As noted, the anticipated recrystallization from the Si interface is not observed, and in addition it is expected that the liquid melt should lead to a dissolution and therefore local etching of the Si surface which is also not observed in **Figure 3B**. A BF HR-(S)TEM of the interface of the annealed sample is presented in **Figure 5** and reveals a 2.5 nm thick amorphous (barrier) layer between Si seed (bottom bright part) and InSb deposit (dark part), whose presence inhibits epitaxial contact between the Si and the InSb melt and correspondingly also etching of the Si surface. The composition of the barrier was further evaluated using EDX, and together with the (S)TEM data indicates the presence of Si- and metal (In, Sb) oxides. The unhindered effectiveness of the electroplating suggests that the amorpous barrier layer acts mainly as material diffusion barrier and barrier for epitaxy, but not as effective electrical insulator. Despite its 2.5 nm thickness, direct tunneling, and more importantly trap assisted tunneling (TAT) can be significant at ~1 Vnm^{-1} in low density oxides. In fact, electron tuneling at high cathodic voltages was previously observed during Cu electrodeposition on thin native silicon oxide (Arrington et al., 2008). Moreover, the barrier may contain intrinsically conductive In or Sb oxides. To overcome the formation of a barrier layer, which might itself be intrinsic to the specific electrodeposition process, a modified strategy is demonstrated in the following section.

To demonstrate the overall validility of the concept illustrated in **Figure 1**, the formation of a barrier layer during electrodeposition must be excluded. This small modification is introduced by selectively depositing a thin intermediate layer of InSb using MOCVD in the Si seed areas. This guarantees an oxide free InSb-Si interface which serves in a later step as interface for the electrodeposition of InSb, and the subsequent steps demonstrated above. Instead of complex templates, arrays of vias in a SiO_x mask were patterned on Si (001) and used as a mask for MOCVD growth of small InSb crystals. The conditions of epitaxial growth were chosen to minimize the presence of In droplets on the InSb crystals, with randomly occurring In droplet still detectable (for detailed description please refer to **section 2** Materials and Methods). The resulting InSb seeds crystals are shown in **Figure 6A**. Each hole contains at least one InSb crystal protecting the InSb-Si interface from reoxidation processes. Directly after MOCVD synthesis, the electrodeposition process was performed in which each 100 nm-sized InSb crystallite was further overgrown by InSb, resulting in >500 nm sized domes (**Figure 6B**). Finally, the samples were capped with SiO_x. The results of (S)TEM-EDX analysis of as-prepared and melted/crystallized samples are presented in **Figures 6C–F**. The arrows in **Figure 6C** point to the crystalline InSb deposited by MOCVD (for better visibility marked with white dotted line) and to the nanocrystalline InSb deposited by ED. The surface roughness of the ED process at is clearly visible around the perimeter of the mushroom. The corresponding EDX map in **Figure 6D** confirms a uniform composition of the ED part, but also a slight In rich area in the InSb seed which might be caused by a In droplet formed during MOCVD growth. The differences of intensities are simply a consequence of the variable lamella thickness, with the stem being thinner compared to the hemisphere. As expected InSb-Si interface is flat.

After melting and crystallization, the morphology changes significantly, as visible in **Figure 6F**. According to the phase diagram, the melted phase gets saturated with Si, leading to a dissolution of Si, confirmed by the presence of the inverted pyramidal structure bound by four Si <111> planes below the seed region. This melt-back etching is a well documented

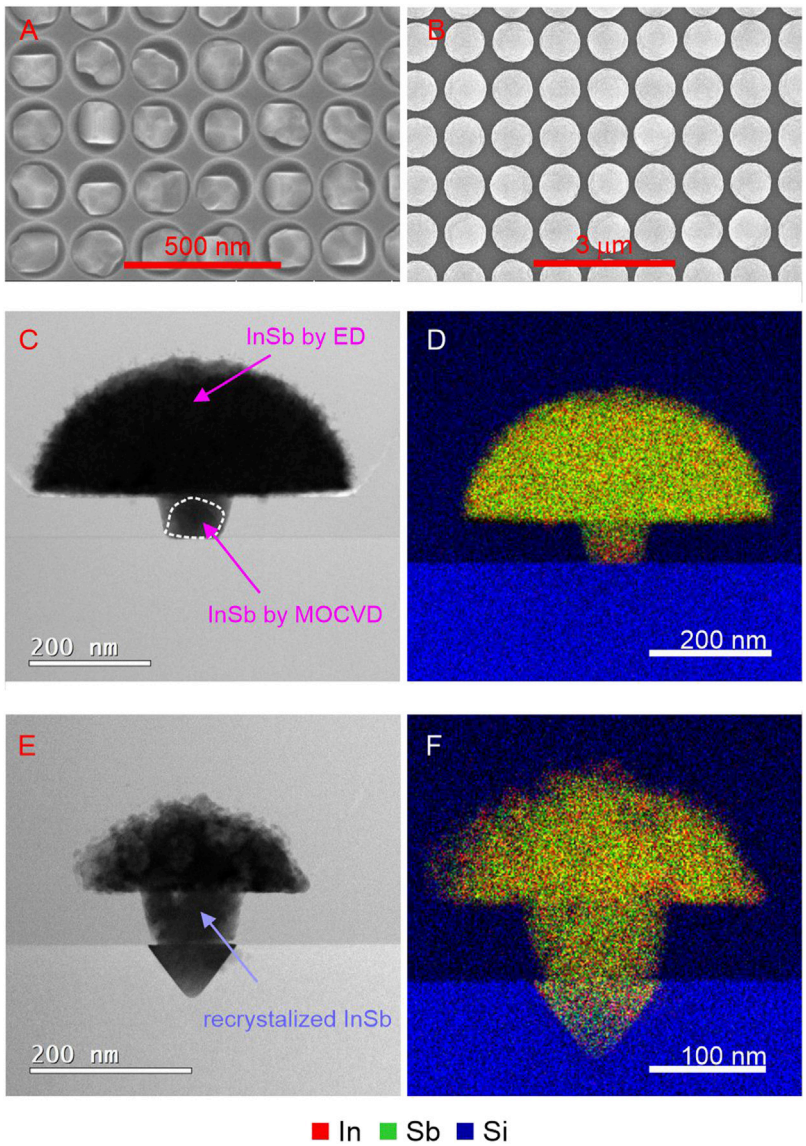

FIGURE 6 | (A) SEM images of dense array of InSb crystallites by MOCVD serving as seeds for later electrodeposition. **(B)** sparser array similar to **(A)** with the small InSb seeds after the electrodeposition step resulting in large InSb mushrooms. **(C)** (S)TEM cross-section image of a representative structure from **(B)** together with **(D)** EDX map of In, Sb, and Si elemental distribution. **(E)** (S)TEM image of **(B)** after melting and crystallization. **(F)** EDX map of **(E)**.

phenomenon and is investigated in detail for gallium (Werner et al., 2014) and gallium nitride (Khoury et al., 2017) epitaxial growth on Si, for example. Upon cooling, the dissolved Si precipitates out again until reaching the equilibrium solubility limit. At first surprising is the large volume of Si that is melt-back etched, corresponding to approximately 15% of the entire InSb volume, by several orders exceeding the solid solubility limit of Si in In (Olesinski et al., 1985) and Sb (Olesinski and Abbaschian, 1985). A closer look at the structure after melting and crystallisation reveals a much increased surface roughness along the perimeter and a correspondingly decreased radius of the hemisphere. This suggests that dissolved Si was diffusing through the InSb melt and precipitating out again on the opposing interface during the melt phase. The etching process slows down when the stable <111> planes are formed, defined by the mask opening, but still continues at reduced speed as is noticeable by the underetching of the mask pattern. EDX measurements (**Figure 6F**) could not confirm the hypothesis by revealing a distinct Si signal at a periphery, due to the overlap of the Si signal stemming from the SiO_x capping layer, and due to the likelihood of the Si forming a SiO_x compound as well considering the high O level in the InSb.

Finally, structural analysis of the crystallized sample is shown in **Figure 7**, where an extended monocrystalline area was found (delineated by a dashed line) with the rest remaining nano crystalline. BF HR-(S)TEM revealed that this single crystalline area has the same epitaxial relationship as the Si (001) substrate,

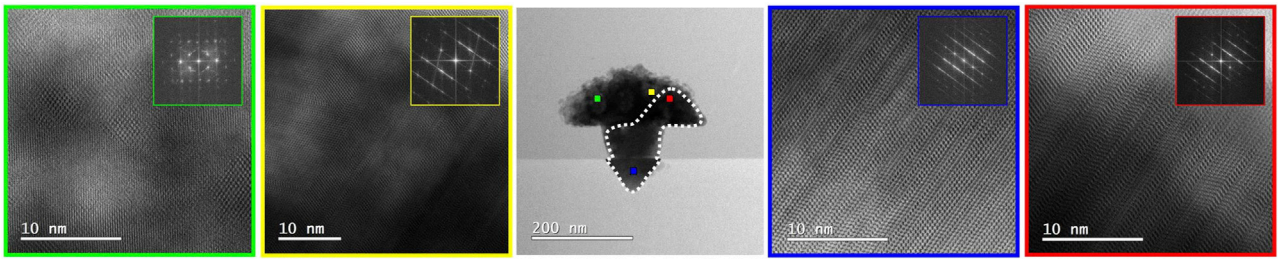

FIGURE 7 | (S)TEM analysis of the melted and crystallized InSb structure. The region with an epitaxial relationship to the substrate is marked with the white dotted line. BF HR-(S)TEM images marked with red and blue show the zinc blend monocrystalline region of the InSb structure. The remaining part of the structure is nano crystalline and marked with yellow and green.

confirming the anticipated process of initial crystallization of the melt from the Si interface. The single crystal has a high density of the stacking faults which run parallel to one of the four possible <111> planes of the substrate. This is the first demonstration that the proposed concept is indeed feasible, although on a limited scale only due to the limit dictated by the impurity concentration of the InSb melt. It is worth noting that using a higher melting point semiconductor such as InAs in place of the InSb crystal deposited by MOCVD in this work, melt-back etching of the Si and therefore unintentional Si doping of the InSb can be avoided.

CONCLUSION

We have proposed and demonstrated the use of electrodeposition as an alternative approach for monolithic integration of a compound semiconductor on silicon. Arbritrary shaped templates were efficiently filled with nanocrystalline InSb from an aqueous solution using pulsed electrodeposition. The melted and crystallized InSb within the templates were found to remain nanocrystalline, which was ascribed to a high impurity concentration in the InSb. Complexing additives to match the reduction potentials of indium and antimony ions closer together are proposed as a source of the impurities and heterogeneous nucleation during melt cooling. Despite the limitation encountered, InSb plating and epitaxial melt crystallization from a Si surface was demonstrated on a sub-micron scale, validating the proposed integration concept. To improve the current results towards large area epitaxial InSb films on Si, a synthesis path including brightener additives to form high purity deposits will be explored.

DATA AVAILABILITY STATEMENT

The raw data supporting the conclusion of this article will be made available by the authors, without undue reservation.

AUTHOR CONTRIBUTIONS

KH-G and HS conceived and carried out the experiments. KH-G, SR, and HS contributed to sample preparation. MS performed (S)TEM analysis, MH performed XPS analysis. KH-G and HS processed the experimental data, performed the analysis, drafted the manuscript, and designed the figures. KM and HS supervised the work. All authors provided critical feedback and helped shape the research, analysis, and manuscript.

FUNDING

The research was carried out thanks to the financial support of the Marie Skłodowska-Curie Action H2020 EU TECNO (894326).

ACKNOWLEDGMENTS

We thank the Cleanroom Operations Team of the Binnig and Rohrer Nanotechnology Center (BRNC) for their help and support and Andreas Bischof for performing AE spectroscopy measurements.

REFERENCES

Arrington, D., Curry, M., Street, S., Pattanaik, G., and Zangari, G. (2008). Copper Electrodeposition onto the Dendrimer-Modified Native Oxide of Silicon Substrates. *Electrochimica Acta* 53, 2644–2649. doi:10.1016/j.electacta.2007.10.054

Billings, A. R. (1969). Microzone Recrystallization of Semiconductor Compound Films. *J. Vacuum Sci. Tech.* 6, 757–765. doi:10.1116/1.1315753

Chen, Y., Huang, S., Pan, D., Xue, J., Zhang, L., Zhao, J., et al. (2021). Strong and Tunable Spin-Orbit Interaction in a Single Crystalline InSb Nanosheet. *Npj 2d Mater. Appl.* 5, 3. doi:10.1038/s41699-020-00184-y

Hishiki, S., Kanno, I., Sugiura, O., Xiang, R., Nakamura, T., and Katagiri, M. (2005). Undoped InSb Schottky Detector for Gamma-ray Measurements. *IEEE Trans. Nucl. Sci.* 52, 3172–3175. doi:10.1109/TNS.2006.869817

Hnida-Gut, K. E., Sousa, M., Moselund, K. E., and Schmid, H. (2021). "Direct Electrodeposition of InSb Devices on Silicon," in Conference Proceedings of 16th IEEE Nanotechnology Materials and Devices Conference (IEEE NMDC 2021), Vancouver, Canada, 12–15.12.2021. in press.

Hnida, K. E., Bäβler, S., Akinsinde, L., Gooth, J., Nielsch, K., Socha, R. P., et al. (2015). Tuning the Polarity of Charge Transport in InSb Nanowires via Heat Treatment. *Nanotechnology* 26, 285701. doi:10.1088/0957-4484/26/28/285701

Hnida, K. E., Marzec, M., Wlaźlak, E., Chlebda, D., Szaciłowski, K., Gilek, D., et al. (2019). Influence of Pulse Frequency on Physicochemical Properties of InSb

Films Obtained via Electrodeposition. *Electrochimica Acta* 304, 396–404. doi:10.1016/j.electacta.2019.02.111

Hopkinson, M., Martin, T., and Smowton, P. (2013). III-V Semiconductor Devices Integrated with Silicon. *Semicond. Sci. Technol.* 28, 090301. doi:10.1088/0268-1242/28/9/090301

Jankowski, J., Prokopowicz, R., Pytel, K., and El-Ahmar, S. (2019). Toward the Development of an InSb-Based Neutron-Resistant Hall Sensor. *IEEE Trans. Nucl. Sci.* 66, 926–931. doi:10.1109/TNS.2019.2912720

Khoury, M., Tottereau, O., Feuillet, G., Vennéguès, P., and Zúñiga-Pérez, J. (2017). Evolution and Prevention of Meltback Etching: Case Study of Semipolar GaN Growth on Patterned Silicon Substrates. *J. Appl. Phys.* 122, 105108. doi:10.1063/1.5001914

Liu, Y., Kanyang, R., Han, G., Fang, C., Zhang, J., Hao, Y., et al. (2018a). "Rainbow Trapping and Releasing in InSb Graded Grating Strip at the Terahert: Range," in 2018 Cross Strait Quad-Regional Radio Science and Wireless Technology Conference (CSQRWC), Xuzhou, China, 21–24.07.2018 (IEEE), 1–3. doi:10.1109/CSQRWC.2018.8455539

Liu, Z., Wen, J., Li, C., Xue, C., and Cheng, B. (2018b). Research Progress of Ge on Insulator Grown by Rapid Melting Growth. *J. Semicond.* 39, 061005. doi:10.1088/1674-4926/39/6/061005

Menon, H., Södergren, L., Athle, R., Johansson, J., Steer, M., Thayne, I., et al. (2021). Improved Quality of InSb-On-Insulator Microstructures by Flash Annealing into Melt. *Nanotechnology* 32, 165602. doi:10.1088/1361-6528/abd656

Olesinski, R. W., and Abbaschian, G. J. (1985). The Sb-Si (Antimony-Silicon) System. *Bull. Alloy Phase Diagrams* 6, 445–448. doi:10.1007/BF02869508

Olesinski, R. W., Kanani, N., and Abbaschian, G. J. (1985). The In–Si (Indium-Silicon) System. *Bull. Alloy Phase Diagrams* 6, 128–130. doi:10.1007/BF02869223

Palyanov, Y. N., Borzdov, Y. M., Kupriyanov, I. N., Bataleva, Y. V., and Nechaev, D. V. (2020). Effect of Oxygen on Diamond Crystallization in Metal-Carbon Systems. *ACS Omega* 5, 18376–18383. doi:10.1021/acsomega.0c02130

Rajska, D., Brzózka, A., Hnida-Gut, K. E., and Sulka, G. D. (2021). Investigation of Electrodeposition Kinetics of in, Sb, and Zn for Advanced Designing of InSb and ZnSb Thin Films. *J. Electroanalytical Chem.* 882, 114967. doi:10.1016/j.jelechem.2020.114967

Ramirez, J. M., Malhouitre, S., Gradkowski, K., Morrissey, P. E., O'Brien, P., Caillaud, C., et al. (2020). III-V-on-Silicon Integration: From Hybrid Devices to Heterogeneous Photonic Integrated Circuits. *IEEE J. Select. Top. Quan. Electron.* 26, 1–13. doi:10.1109/JSTQE.2019.2939503

Riel, H. (2017). "Integrated III-V Nanoelectronic Devices on Si," in 2017 Silicon Nanoelectronics Workshop (SNW), Kyoto, Japan, 4–5.06.2017 (IEEE), 1–2. doi:10.23919/SNW.2017.8242267

Schmid, H., Borg, M., Moselund, K., Gignac, L., Breslin, C. M., Bruley, J., et al. (2015). Template-assisted Selective Epitaxy of III-V Nanoscale Devices for Co-planar Heterogeneous Integration with Si. *Appl. Phys. Lett.* 106, 233101. doi:10.1063/1.4921962

Shi, C., Dong, Y., and Li, Q. (2019). High-Performance Nonequilibrium InSb PIN Infrared Photodetectors. *IEEE Trans. Electron. Devices* 66, 1361–1367. doi:10.1109/TED.2019.2895032

Werner, K., Beyer, A., Oelerich, J. O., Baranovskii, S. D., Stolz, W., and Volz, K. (2014). Structural Characteristics of Gallium Metal Deposited on Si (001) by MOCVD. *J. Cryst. Growth* 405, 102–109. doi:10.1016/j.jcrysgro.2014.07.045

Xie, C., Pusino, V., Khalid, A., Aziz, M., Steer, M. J., and Cumming, D. R. S. (2016). "Monolithic Fabrication of InSb-Based Photo-Pixel for Mid-IR Imaging," in 2016 Compound Semiconductor Week (CSW) [Includes 28th International Conference on Indium Phosphide & Related Materials (IPRM) & 43rd International Symposium on Compound Semiconductors (ISCS), Toyama, Japan, 26–30.06.2016 (IEEE), 1–2. doi:10.1109/ICIPRM.2016.7528581

Conflict of Interest: Authors KH-G, MS, MH, SR, KM, HS were employed by IBM Research.

frontiers in Chemistry

ORIGINAL RESEARCH
published: 07 March 2022
doi: 10.3389/fchem.2022.835733

Phosphorylated and Phosphomimicking Variants May Differ—A Case Study of 14-3-3 Protein

*Aneta Kozeleková[1,2], Alexandra Náplavová[1], Tomáš Brom[2], Norbert Gašparik[1,2], Jan Šimek[1], Josef Houser[1,2] and Jozef Hritz[1,3]**

[1]Central European Institute of Technology, Masaryk University, Brno, Czechia, [2]National Centre for Biomolecular Research, Faculty of Science, Masaryk University, Brno, Czechia, [3]Department of Chemistry, Faculty of Science, Masaryk University, Brno, Czechia

Protein phosphorylation is a critical mechanism that biology uses to govern cellular processes. To study the impact of phosphorylation on protein properties, a fully and specifically phosphorylated sample is required although not always achievable. Commonly, this issue is overcome by installing phosphomimicking mutations at the desired site of phosphorylation. 14-3-3 proteins are regulatory protein hubs that interact with hundreds of phosphorylated proteins and modulate their structure and activity. 14-3-3 protein function relies on its dimeric nature, which is controlled by Ser58 phosphorylation. However, incomplete Ser58 phosphorylation has obstructed the detailed study of its effect so far. In the present study, we describe the full and specific phosphorylation of 14-3-3ζ protein at Ser58 and we compare its characteristics with phosphomimicking mutants that have been used in the past (S58E/D). Our results show that in case of the 14-3-3 proteins, phosphomimicking mutations are not a sufficient replacement for phosphorylation. At physiological concentrations of 14-3-3ζ protein, the dimer-monomer equilibrium of phosphorylated protein is much more shifted towards monomers than that of the phosphomimicking mutants. The oligomeric state also influences protein properties such as thermodynamic stability and hydrophobicity. Moreover, phosphorylation changes the localization of 14-3-3ζ in HeLa and U251 human cancer cells. In summary, our study highlights that phosphomimicking mutations may not faithfully represent the effects of phosphorylation on the protein structure and function and that their use should be justified by comparing to the genuinely phosphorylated counterpart.

Keywords: 14-3-3, phosphorylation, phosphomimicking mutation, oligomeric state, dissociation constant

OPEN ACCESS

Edited by:
Nicole J. Jaffrezic-Renault, UniversitÃ© Claude Bernard Lyon 1, France

Reviewed by:
Adrian Drazic, University of Bergen, Norway
Irene Diaz-Moreno, Sevilla University, Spain

****Correspondence:***
Jozef Hritz
jozef.hritz@ceitec.muni.cz

Specialty section:
This article was submitted to Chemical Biology, a section of the journal Frontiers in Chemistry

Received: *14 December 2021*
Accepted: *14 February 2022*
Published: *07 March 2022*

Citation:
Kozeleková A, Náplavová A, Brom T, Gašparik N, Šimek J, Houser J and Hritz J (2022) Phosphorylated and Phosphomimicking Variants May Differ—A Case Study of 14-3-3 Protein. Front. Chem. 10:835733. doi: 10.3389/fchem.2022.835733

INTRODUCTION

Protein phosphorylation is one of the most common post-translational modifications which has a unique role in regulation of protein function. Up to two thirds of the human proteome have been reported to be phosphorylated (Ardito et al., 2017) and approx. 3.5% of the human genome codes kinases and phosphatases, key players in the dynamic regulation of protein phosphorylation (Pearlman et al., 2011). Phosphorylation is responsible for the modulation of numerous cell processes including DNA

transcription, apoptosis, metabolism, or antigen recognition (Braicu et al., 2019; Bernatik et al., 2020). Phosphorylation is also a focal point of many intricate signaling networks, cycles, feedback loops or cascades, as exemplified by the well-studied MAPK pathway or cell cycle checkpoints (Wei and Liu, 2002; Morrison, 2012).

The introduction of a phosphate group affects protein properties. The chemical properties of the protein surface are modulated by the large hydration shell and negative charge of the phosphate (Hunter, 2012; Laage et al., 2017). New hydrogen bonds may be formed, as well (Mandell et al., 2007). Phosphorylated residues are commonly present in binding motifs, effectively regulating entire protein-protein interactomes.

14-3-3 proteins are regulatory protein hubs expressed in all eukaryotes. The mammalian 14-3-3 protein family consists of seven isoforms (β, γ, ε, ζ, η, θ, and σ) that are involved in a variety of cellular processes, such as regulation of cell cycle, cellular growth and death, modulation of enzymatic activities and transcription factors, interaction with proteins of the cytoskeleton or signaling cascades (Mackintosh, 2004; Sluchanko and Gusev, 2010; Gardino and Yaffe, 2011; Obsilova and Obsil, 2020). 14-3-3 proteins form dimers, which is crucial for their function as protein scaffolds (Shen et al., 2003; Zhou et al., 2003; Messaritou et al., 2010). Interaction with more than 1,200 protein partners has been reported so far (Sluchanko and Bustos, 2019).

Phosphorylation plays a dual role in the 14-3-3 life cycle. First, phosphorylation of its partners significantly increases their binding affinity to a 14-3-3 dimer (Menzel et al., 2020; Munier et al., 2021). Second, the phosphorylation of 14-3-3 alters its own structure and function (Dubois et al., 1997; Tsuruta et al., 2004; Woodcock et al., 2003; Zhou et al., 2009). Phosphorylation of 14-3-3ζ at Ser58 has been proposed to impact the dimer-monomer equilibrium. However, either no effect on the oligomeric state (Powell et al., 2002), only partial dimer dissociation (Powell et al., 2003; Gu et al., 2006; Gerst et al., 2015) or complete monomerization (Woodcock et al., 2003; Kanno and Nishizaki, 2011; Civiero et al., 2017) were observed. Moreover, Ser58 phosphorylation and monomerization were shown to change the 14-3-3 protein properties, for example, monomeric 14-3-3 proteins proved higher chaperone-like activity than their dimeric counterparts (Sluchanko et al., 2012; Sluchanko et al., 2014). However, issues with preparation of the phosphorylated protein, e. g. incomplete phosphorylation or aggregation (Powell et al., 2003; Shen et al., 2003; Sluchanko and Uversky, 2015) obstructed the detailed description of changes in protein structure, properties, and interactions.

14-3-3ζ protein phosphorylated at Ser58 (hereafter pζ) was therefore often replaced by phosphomimicking and monomeric mutants (Sluchanko et al., 2008; Sluchanko et al., 2011b). To mimic the negative charge of the phosphate group, Ser58 was mutated to negatively charged amino acids, namely Asp (S58E) or Glu (S58D) (Powell et al., 2003; Sluchanko et al., 2008; Woodcock et al., 2018). Furthermore, the monomerization effect of Ser58 phosphorylation was substituted by mutations of conserved residues located at the dimeric interface. Several so-called monomeric mutants have been designed, namely septuple mutant E5K_L12Q_A13Q_E14R_Y82Q_K85N_E87Q (Tzivion et al., 1998; Shen et al., 2003), triple mutant L12Q_A13Q_E14R (Zhou et al., 2003; Messaritou et al., 2010; Sluchanko et al., 2011b) or our own double mutants L12E_M78K (hereafter ζm) and L12K_M78E (Jandova et al., 2018).

In general, phosphomimicking mutations have been reported to approximate the impact of phosphorylation with varying success (Thorsness and Koshland, 1987; Paleologou et al., 2008; Dephoure et al., 2013; Pérez-Mejías et al., 2020; Somale et al., 2020). To the best of our knowledge, in case of the 14-3-3 proteins, the properties of such mutants have never been compared to the phosphorylated protein, and thus their use has never been validated properly. Here we report a protocol for the preparation of 14-3-3ζ phosphorylated at Ser58 in high purity and sufficient amounts for biophysical analysis, and compare its characteristics, such as oligomeric state, thermal stability and hydrophobicity, with both phosphomimicking and monomeric mutants. Moreover, we present a novel double phosphomimicking mutant 14-3-3ζ S57D_S58D with its negative charge closer resembling the phosphate group.

MATERIALS AND METHODS

Preparation of 14-3-3ζ Proteins

Six 14-3-3ζ protein constructs, namely 14-3-3ζ WT (abbreviated ζ), 14-3-3ζ phosphorylated at Ser58 (pζ), 14-3-3ζ L12E_M78K (ζm), 14-3-3ζ S58E (ζ_S58E), 14-3-3ζ S58D (ζ_S58D) and 14-3-3ζ S57D_S58D (ζ_S57D_S58D) were used in this study. All 14-3-3ζ protein constructs contained Cys-to-Ala mutations (i. e. C25A C189A) on the protein surface to prevent the formation of intermolecular disulphide bridges in solution (Hritz et al., 2014). cDNA of the 14-3-3ζ proteins, containing an N-terminal 6×His-tag separated by a Tobacco Etch Virus (TEV) protease cleavage site, was expressed from a pET15b plasmid (Novagene). The monomeric mutant ζm and the double mutation L12E_M78K was designed previously (Jandova et al., 2018). The mutations S58E, S58D and double mutation S57D_S58D were incorporated using the PCR mutagenesis protocol of Liu and Naismith (2008). For fluorescence experiments, ζ_S58E_Ntail construct was prepared by adding the SVDACKGSSGG sequence at the ζ_S58E N-terminus. cDNA of all 14-3-3ζ mutants was verified by DNA sequencing (SeqMe, Czech Republic). Except for pζ, all 14-3-3ζ constructs were expressed in the bacterial *E. coli* strain BL21(DE3) CodonPlus RIL (Stratagene) and purified according to a previously optimized protocol (Hritz et al., 2014).

Preparation of 14-3-3ζ Phosphorylated at Ser58

14-3-3ζ phosphorylated at Ser58 was prepared by co-expression of ζ with the catalytic subunit of mouse protein kinase A (hereafter shortly PKA) in *E. coli*. A pACYCduet-1 plasmid, bearing the 6×His-PKA cDNA and chloramphenicol resistance (kindly provided by prof. Nikolai Sluchanko, Russian Academy of

Sciences, Moscow), was transformed into *E. coli* BL21(DE3) (Novagen) using heat shock at 42°C for 30 s. The transformed cells were then made competent using the Inoue method (Inoue et al., 1990) and used for subsequent transformation of the pET15b-14-3-3ζ plasmid (ampicillin resistance).

100 mL Lysogeny broth (LB) overnight culture was pelleted, resuspended in fresh medium, and transferred into 2 L of sterile LB supplemented with ampicillin and chloramphenicol. The culture was incubated at 37°C and 180 RPM until OD_{600} approached ~0.9, when protein expression was induced by 0.5 mM IPTG and expression continued for 4 h under the same conditions. Cells were harvested by centrifugation at 5,000 g, 4°C for 15 min, the bacterial pellet was resuspended in 20 mL of 50 mM Tris-HCl, 150 mM NaCl, 20 mM imidazole, 10% glycerol, pH 8 and stored at −80°C.

Rapidly thawed cell pellet was supplemented with 0.3 mg/mL lysozyme and sonicated for 30 min on ice (50 W, 20 kHz, 1 s pulse duration, 5 s delay) (QSonica Q700 Sonicator). Cell debris was pelleted by centrifugation at 21,000 g, 4°C for 60 min and the cleared supernatant was loaded onto a Ni^{2+} immobilized metal affinity chromatography (IMAC) column (5 mL HisTrap HP, GE Healthcare) equilibrated in 50 mM Tris-HCl, 500 mM NaCl, 3 mM NaN_3, pH 8. His-tagged proteins were eluted with a linear gradient of 20–500 mM imidazole in one column volume (CV). Eluted sample was diluted 2-times with 20 mM Tris-HCl pH 8 to reduce imidazole and salt concentration and 6×-His-TEV protease (in-house prepared recombinant protein) was added in a molar ratio 1 : 20 (TEV: 14-3-3ζ monomer). The mixture was dialyzed against TBS (50 mM Tris-HCl, 150 mM NaCl, 3 mM NaN_3, pH 8) at 4°C overnight. The next day, His-tagged enzymes (TEV and PKA) and cleaved His-tag were removed from 14-3-3ζ by another Ni^{2+} IMAC step. 14-3-3ζ protein was collected in the flow-through and diluted 2-times with 20 mM Tris-HCl pH 8 to decrease the ionic strength of the solution. Subsequently, the protein sample was applied to an anion-exchange chromatography (AEX) column (5 mL HiTrap Q HP, GE Healthcare) equilibrated in 20 mM Tris-HCl, 3 mM NaN_3, pH 8. 14-3-3ζ proteins (ζ and pζ) were separated during elution with a slow linear gradient of NaCl (200–500 mM) in six CVs. The pζ fraction, which eluted at conductivity ~25 mS/cm, was collected and concentrated to 4 mL. Finally, the pζ sample was applied onto a TBS-equilibrated size-exclusion chromatography (SEC) column (HiLoad 16/600 Superdex75 pg, GE Healthcare) to remove any remaining impurities.

Protein purity was evaluated by SDS-PAGE. Accurate protein molecular weight (M_W) was verified by MALDI-TOF mass spectrometry (MS) (ultrafleXtreme, Bruker). The precise position of the phosphorylation site was identified using trypsin proteolysis followed by LC-MS/MS (RSLC nano, Dionex; Orbitrap Fusion Lumos, Thermo Scientific). Protein concentration was determined spectrophotometrically at 280 nm using NanoDrop 2000/2000c Spectrophotometer (ThermoFisher). 14-3-3ζ protein extinction coefficient (27,390 L mol^{-1} cm^{-1}) was determined using the ProtParam tool (Gasteiger et al., 2005).

Circular Dichroism Spectroscopy (CD)

Far-UV CD measurements were performed on a J-815 spectrometer (Jasco) at 20°C in 1-mm Quartz cuvette (Hellma Analytics). CD spectra of 0.2 mg/mL (7.3 μM) 14-3-3ζ proteins in 20 mM sodium phosphate buffer pH 7.4 were acquired as 5 accumulations in the wavelength range 185–260 nm with 1 nm step at scanning speed 50 nm/min. Subsequently, buffer signal was subtracted, and data were converted from circular dichroism units to mean residue molar ellipticity (MRE) to account for precise protein concentration. The presence of secondary structural elements was evaluated using DichroWeb (K2D programme) (Andrade et al., 1993) and K2D3 programme (Louis-Jeune et al., 2012).

Native-PAGE

25 μM 14-3-3ζ protein samples in 50 mM Tris-HCl, 300 mM NaCl, 3 mM NaN_3, pH 8 were equilibrated at 37°C for 20 min. Afterwards, native-PAGE on a 12.5% gel was performed at 90 V for 4.5 h on ice.

Analytical Ultracentrifugation (AUC)

Sedimentation velocity (SV) experiment was performed with 1 mg/mL (36.5 μM) 14-3-3ζ proteins in 50 mM Tris-HCl, 300 mM NaCl, 3 mM NaN_3, pH 8. Measurements were conducted using ProteomeLab XL-I ultracentrifuge (Beckman Coulter) in a 4-hole An-60 Ti rotor at 20°C and 50,000 RPM with continuous absorbance detection at 286 nm. 200 scans in 5-min intervals were acquired with 0.003 cm radial size increment. Partial-specific volume of 14-3-3ζ, solvent density and viscosity were predicted using Sednterp[1] software. The SV data from 100 to 150 scans corresponding to complete sample sedimentation were fitted using Sedfit v15.01c (Schuck, 2000) with a continuous c(s) distribution model. M_W of particles was estimated based on the Svedberg equation. c(s) distributions were normalized and plotted using the GUSSI programme version 1.4.2 (Brautigam, 2015).

Analytical size-exclusion chromatography with right-angle light scattering detection (SEC-RALS).

For comparison of the oligomeric states: Prior to measurement, 1 mg/mL (36.5 μM) 14-3-3ζ proteins in PBS (10 mM Na_2HPO_4, 1.8 mM KH_2PO_4, 137 mM NaCl, 2.7 mM KCl, 1 mM NaN_3, pH 7.4) were centrifuged at 14,000 g, 4°C for 10 min. SEC-RALS measurements were performed on an OmniSEC instrument (Malvern Panalytical). 50 μL of each protein was injected onto a 13-mL Zenix SEC 300 gel filtration column (Sepax Technologies) equilibrated in PBS and analysis was performed in triplicates at 20°C and flow rate 0.7 mL/min. UV detection at 254 nm was used to monitor the separation. Data were evaluated using OMNISEC software 11.21 (Malvern Panalytical). M_W of particles was calculated from the intensity of the scattered light,

[1]https://bitc.sr.unh.edu

measured at right angle for maximal sensitivity, based on the Rayleigh equation.

For estimation of the dimerization dissociation constant (K_D) of pζ, ζm, ζ_S58D and ζ_S57D_S58D: 5 mg/mL (183 μM) pζ and ζm or 4.5 mg/mL (164 μM) ζ_S58D and ζ_S57D_S58D were analyzed using the same setup as above (in triplicates).

Förster Resonance Energy Transfer (FRET) Assay

ζ_S58E_Ntail was fluorescently labelled at position Cys5 with AlexaFluor647-C5-maleimide (AF647) and AlexaFluor488-C2-maleimide (AF488) (Thermo Fisher Scientific), as described in Trošanová et al. (2022). Fluorescence measurements were performed on a FluoroLog-3 Modular Spectrofluorometer (HORIBA Jobin Yvon) in 10.00-mm Quartz glass cuvette (High Precision Cell, Hellma Analytics) with a magnetic stirrer. Prior to measurement, the cuvette was treated with 15 mg/mL BSA for 30 min to prevent adhesion of fluorescently labelled ζ_S58E_Ntail to the cuvette walls. Measurements were conducted in 20 mM sodium phosphate pH 6.8 at 15°C with λ_{ex} = 470 nm (slits 2 mm) and λ_{em} = 666 nm (slits 5 mm). Data were collected each 30 s with 0.5 s integration time.

FRET assay was performed as detailed in Trošanová et al. (2022). In brief, first, fluorescence signal of 200 nM ζ_S58E_Ntail labelled with AF647 was recorded for ~20 min. Afterwards, 200 nM ζ_S58E_Ntail labelled with AF488 was added and FRET was initiated. After stabilization of the fluorescence signal (~60 min), non-labelled ζ_S58E in 100-fold excess was added to disrupt the FRET dimers. Acquired FRET kinetic profiles were fitted, as described in Trošanová et al. (2022) and dissociation constant K_D and dissociation rate constant k_{off} were extracted.

Differential Scanning Calorimetry (DSC)

DSC thermograms of 1 mg/mL (36.5 μM) 14-3-3ζ proteins dialyzed into PBS were acquired using Microcal PEAQ-DSC Automated calorimeter (Malvern Panalytical). Prior to measurement, samples were centrifuged at 18,000 g and 4°C for 10 min. Reference cell was filled with a corresponding buffer after dialysis. DSC measurements were performed in triplicates, and each was composed of three periods: heating (20–90°C, heating rate 1°C/min), cooling (90–20°C, −1°C/min) and final heating (20–90°C, 1°C/min). Buffer measurements were performed prior to each triplicate and these data were then subtracted from the protein scan to eliminate the buffer signal. Second and third heating scans were used for assessment of the denaturation reversibility.

Thermodynamic parameters of 14-3-3ζ proteins were evaluated using MicroCal PEAQ-DSC software (Malvern Panalytical). Thermogram of the buffer was subtracted from the thermogram of the protein and the 'progress' baseline was defined. Data were fitted with a non-two-state model used for determination of enthalpies of denaturation and melting temperatures.

Differential Scanning Fluorimetry (nanoDSF)

Thermal stability of 1 mg/mL (36.5 μM) 14-3-3ζ proteins was measured in PBS or in 20 mM HEPES pH 8.0 with 0/50/200/400/600 mM $NaCl/Na_2SO_4/Na_2HPO_4$ to study the effect of different anions. Measurements were performed in triplicates using a Prometheus NT.48 instrument (NanoTemper Technologies) in the temperature range 20–80°C with a temperature slope of 1°C/min and at excitation power 75%. Protein unfolding was monitored by fluorescence intensity measured at 330 and 350 nm. Subsequently, melting temperature (T_m) was determined from the first derivative of fluorescence ratio (330/350) (Alexander et al., 2014).

BisANS Binding Assay

BisANS (4,4′-Dianilino-1,1′-binaphthyl-5,5′-disulfonic acid dipotassium salt) powder (Sigma-Aldrich) was dissolved in MilliQ water and its concentration was determined spectrophotometrically using NanoDrop 2000/2000c Spectrophotometer (ThermoFisher) based on BisANS absorbance at 385 nm and known extinction coefficient ($\varepsilon_{385nm,water}$ = 16,790 L mol^{-1} cm^{-1}) (Sharma et al., 1998). Fluorescence measurements were performed at 37°C on a FluoroLog-3 Modular Spectrofluorometer (HORIBA Jobin Yvon) in a 10.00-mm Quartz glass cuvette (High Precision Cell, Hellma Analytics) with a magnetic stirrer. 1 μM 14-3-3ζ proteins in 1 mL of PBS were titrated with BisANS to final concentration 1–30 μM. After each addition of BisANS, the system was equilibrated for 6 min and then fluorescence of BisANS was excited at 385 nm and detected in the range 400–700 nm with entrance/intermediate/exit slit widths set to 1.5 mm. BisANS fluorescence intensity at 495 nm was used for assessment of protein hydrophobicity. Between measurements of different proteins, the cuvette was cleaned with 3 M HNO_3 for 30 min while stirring to remove all potential contaminants.

Cell Culture Maintenance

HeLa 1.3 cells and U251 cells were maintained at 37°C with 5% CO_2 in Dulbecco's Modified Eagle Medium (Gibco) supplemented with 10% Fetal Bovine Serum (Capricorn), Non-essential amino acids (Gibco), Penicillin-Streptomycin (Sigma-Aldrich), and L-glutamine (Gibco). For the experiments, cells were grown on #1.5 round coverslips in a 24-well plate with a seeding density of 5×10^4 cells per well.

Immunofluorescence Protocol

The day after seeding, cells were washed three times with PBS and fixed with 4% formaldehyde (Serva) in PBS for 10 min at room temperature followed by a wash with PBS and permeabilization in PBS containing 0.1% Triton X-100 for 10 min at room temperature. Cells were then washed with PBS and blocked in blocking buffer (5% goat serum (Biosera) in PBS) for 1 h at room temperature. After blocking, cells were incubated with a primary antibody (Anti-14-3-3ζ (phospho-S58) antibody (ab51109, Abcam) and 14-3-3ζ Antibody (MA5-37641, Invitrogen)) diluted in blocking buffer at 1:200 for 1 h at room temperature. Then the cells were washed 4 × 5 min with PBS supplemented with 0.05% Tween 20 (PBS-T) and incubated with secondary anti-mouse antibody conjugated with

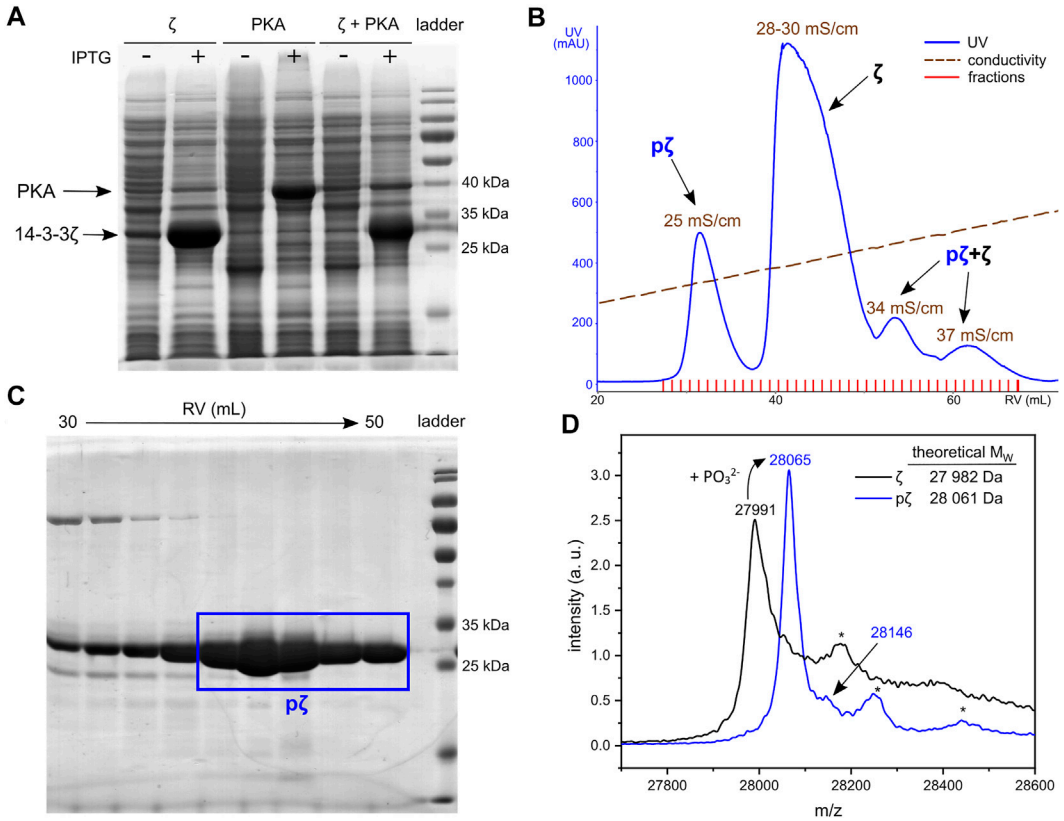

FIGURE 1 | Expression and purification of pζ. **(A)** SDS-PAGE analysis of 14-3-3ζ and PKA co-expression. Cultures without (–) and with (+) induction with IPTG are shown. **(B)** Chromatogram of AEX elution. Average conductivity characterizing the eluted peaks is highlighted. **(C)** SDS-PAGE analysis of the SEC purification step. Fractions corresponding to the final pζ sample are depicted in a blue rectangle. **(D)** MALDI-TOF MS spectrum of purified ζ (in black) and pζ (in blue). Asterisk denotes a protein adduct with the MALDI matrix (ferulic acid, +176).

Alexa Fluor 488 (Goat Anti-Mouse IgG H&L (Alexa Fluor® 488), ab150113) and anti-rabbit antibody conjugated with Alexa Fluor 594 (Goat Anti-Rabbit IgG H&L (Alexa Fluor® 594), ab150080) diluted in blocking buffer at 1:250 for 1 h at room temperature. Finally, the cells were washed 4 × 5 min with PBS-T and mounted on microscope slides using ProLong Omega Glass (Invitrogen) with DAPI staining for nuclear DNA.

Fluorescence Microscopy

Experiments were performed with a wide field epi-fluorescence microscope Zeiss AxioImager Z2 using appropriate filters and dedicated software ZEN studio. The oil-immersion Plan-APO objective 63× was used to capture the desired image. The images were deconvoluted using the ZEN studio imaging module and analyzed using ImageJ.

RESULTS

Preparation of 14-3-3ζ Phosphorylated at Ser58

14-3-3ζ phosphorylated at Ser58 was obtained by co-expression of 14-3-3ζ and protein kinase A (PKA) in *E. coli*. The catalytic subunit of mouse PKA was employed due to its high specificity for the PKA recognition motif 'RRX**S**Y' (Y stands for hydrophobic residue), which corresponds to the sequence surrounding Ser58 (i. e. RRS**S**^{58}W) (Ma et al., 2005; Woodcock et al., 2010; Sluchanko and Uversky, 2015). The bacterial *E. coli* strain BL21(DE3) was transformed consecutively with the cDNA of PKA and 14-3-3ζ, located on compatible plasmids. 14-3-3ζ and PKA were then co-expressed (**Figure 1A**) and Ser58 was phosphorylated *in vivo*. Despite extensive screening of suitable conditions (e. g. temperature, length of expression, culture medium composition), the level of Ser58 phosphorylation reached only approx. 10–20%, and the two forms of protein (ζ, pζ) needed to be separated during the purification process. The optimized protocol is detailed in Methods.

Phosphorylated 14-3-3ζ was separated from the non-phosphorylated ζ by fine-tuning the anion-exchange chromatography (AEX). A linear salt gradient (200–500 mM NaCl in 6 CVs) enabled good separation of pζ from ζ (**Figure 1B**). The pζ fraction was eluted at conductivity ~25 mS/cm, non-phosphorylated ζ at 28–30 mS/cm. Minor fractions which eluted at conductivity 34 and 37 mS/cm contained a mixture of both pζ and ζ and were discarded (**Supplementary Figure S1**). Remaining impurities were

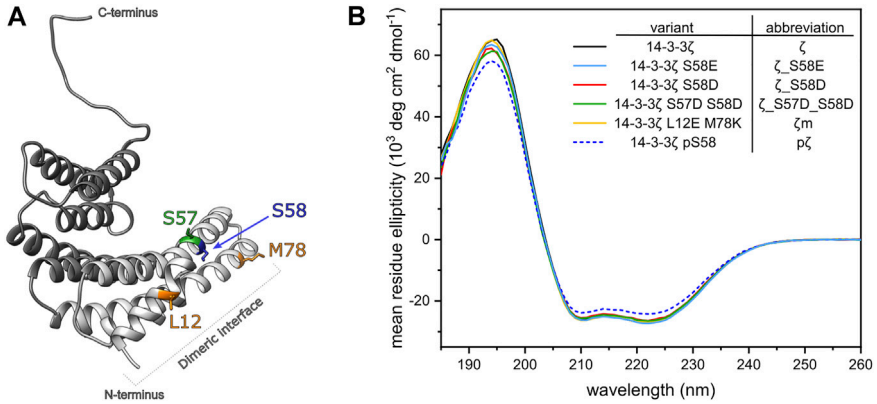

FIGURE 2 | Design and secondary structure analysis of 14-3-3ζ phosphomimicking and monomeric mutants. **(A)** Structural model of the 14-3-3ζ monomeric subunit with the modified residues highlighted in color. Helices forming the dimeric interface are depicted in light grey. Atom coordinates were adopted from Kostelecky et al. (2009) and Nagy et al. (2017). **(B)** Far-UV CD spectrum of 14-3-3ζ variants. For clarity, 14-3-3ζ variants, used in this study, and their abbreviations are listed in the legend.

removed from the pζ fraction by size-exclusion chromatography (SEC) (**Supplementary Figure S2**). Finally, we obtained ~7 mg of pure pζ from 1 L of LB medium.

Protein purity and identity was verified by SDS-PAGE and mass spectrometry. Based on SDS-PAGE (**Figure 1C**), the selected SEC fractions contain protein of high purity that migrates at M_W around 25–30 kDa, which corresponds to calculated M_W of pζ (28,061 Da). Accurate protein M_W was confirmed by MALDI-TOF MS (**Figure 1D**). An additional peak with a higher m/z (+79 for the phosphate group) was also observed and indicated a minor fraction of doubly phosphorylated protein. Trypsin digestion and LC-MS/MS showed that pζ was fully phosphorylated at Ser58 and the residual phosphorylation was located at Ser28 (~4%) (for details see **Supplementary Material**).

Selected 14-3-3ζ Mutants for Comparison With pζ

Phosphomimicking mutants of 14-3-3 proteins have been used extensively to study the impact of Ser58 phosphorylation on protein structure and interactions (Powell et al., 2002, 2003; Gu et al., 2006; Sluchanko et al., 2008; Sluchanko et al., 2011a; Woodcock et al., 2018). In this study, we prepared the previously reported phosphomimicking mutants of 14-3-3ζ protein, namely S58D (ζ_S58D) and S58E (ζ_S58E). Moreover, we wanted to address the problem that Asp and Glu possess a lower negative charge than the phosphate group. At physiological pH ~7.4, the negative charge of phospho-residues is dominantly −2e [pK_{a2} (pSer) = 5.6; pK_{a2} (pThr) = 5.9], whereas Asp and Glu are only singly charged (Xie et al., 2005; Pearlman et al., 2011; Hunter, 2012). Inspired by Strickfaden et al. (2007), we designed a novel double mutant ζ_S57D_S58D with two phosphomimicking mutations at neighboring residues, to mimic the phosphate's negative charge more realistically. Since phosphorylation at Ser58 and the corresponding phosphomimicking mutations have been proposed to induce monomerization (Powell et al., 2003; Woodcock et al., 2003; Sluchanko et al., 2008), we employed our monomeric mutant ζm (Jandova et al., 2018), as a monomer control. Positions of modified residues at the dimeric interface of the constructs used in this study are shown in **Figure 2A** and abbreviations of 14-3-3ζ variants are listed in **Figure 2B**.

To analyze whether the mutations or Ser58 phosphorylation result in any change of 14-3-3ζ secondary structure, we employed far-UV CD spectroscopy. CD spectra (**Figure 2B**) showed that all studied ζ variants retained the α-helical structure characteristic to 14-3-3 proteins. Abundance of the individual secondary structural elements was determined by deconvolution of the acquired CD curves using two programmes, namely K2D (Andrade et al., 1993) and K2D3 (Louis-Jeune et al., 2012). The portion of α-helices was estimated to be 79% and 85%, according to K2D and K2D3, respectively. Deviations in α-helical content between proteins were lower than ±1%. pζ protein displayed the same CD profile, but the MRE magnitude was decreased by approx. 10%, compared to the other 14-3-3ζ variants.

Phosphorylation and Phosphomimicking Mutations Have Different Impact on 14-3-3ζ Oligomeric State

The phosphorylation of Ser58 has been proposed to induce monomerization of 14-3-3ζ protein (Woodcock et al., 2003). Therefore, we inspected the impact of phosphorylation and phosphomimicking mutations on the dimer-monomer equilibrium in detail. We aimed to compare the dimer-monomer distribution of 14-3-3ζ variants at biologically relevant concentrations. We calculated the concentration of the 14-3-3ζ isoform in the human brain based on the equation proposed by Gogl et al. (2021) and data from the PAXdb database[2]. We obtained the value of 25 μM and, as a result, we

[2]https://pax-db.org/

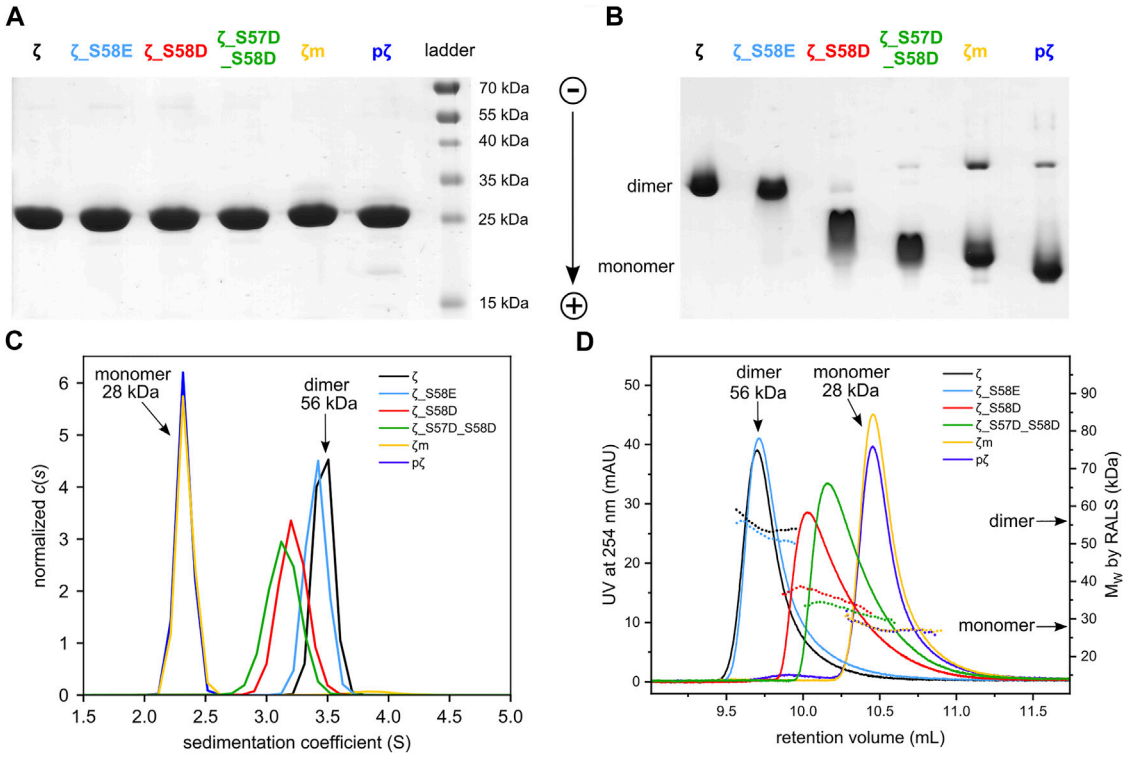

FIGURE 3 | Differences in oligomeric state between 14-3-3ζ variants. **(A)** SDS-PAGE analysis of 25 μM 14-3-3ζ variants comparing their electrophoretic mobility under denaturing conditions, **(B)** native-PAGE of 25 μM 14-3-3ζ proteins, **(C)** AUC of 36.5 μM 14-3-3ζ proteins, **(D)** SEC-RALS of 36.5 μM 14-3-3ζ proteins.

TABLE 1 | AUC and SEC-RALS parameters characterizing the oligomeric state of 14-3-3ζ proteins. The oligomeric state of proteins (36.5 μM) was analyzed at 20°C.

14-3-3	AUC		SEC-RALS	
	$s_{20,w}$ (S)	Apparent M_W (kDa)	RV (mL)	Apparent M_W (kDa)
ζ	3.71	56.4	9.70	54.5
ζ_S58E	3.64	56.3	9.72	50.7
ζ_S58D	3.44	43.7	10.03	34.9
ζ_S57D_S58D	3.35	38.6	10.16	32.0
ζm	2.50	27.0	10.47	27.7
pζ	2.47	28.1	10.46	27.2

examined the 14-3-3ζ oligomeric states at 25 and 36.5 μM (equals to the standard 1 mg/mL) concentrations.

First, to verify the purity and identity of tested 14-3-3ζ variants, we employed SDS-PAGE and mass spectrometry. As expected, all 14-3-3ζ variants exhibit similar electrophoretic mobility in SDS-PAGE. The migration rates correspond to the approx. M_W of 28 kDa, which is in agreement with the calculated M_W of a 14-3-3ζ monomer (**Figure 3A**). Comparable M_W values were also confirmed by MALDI-TOF MS (**Figure 1D**, **Supplementary Figure S3**).

Next, the oligomeric states of 14-3-3ζ variants were analyzed using native-PAGE, AUC and SEC-RALS (**Figures 3B–D**; **Table 1**). In all cases, the phosphomimicking mutants exhibited distinct behavior from pζ. The electrophoretic mobility, sedimentation coefficient (3.6 S) as well as retention volume (9.7 mL) of ζ_S58E was comparable to non-phosphorylated ζ (3.7 S, 9.7 mL) suggesting that ζ_S58E occurs predominantly in the dimeric state at physiological concentration. However, a lower M_W (51 kDa) determined from SEC-RALS data and sedimentation coefficient (**Table 1**) implied that the S58E mutation partially destabilizes the dimer with respect to the ζ variant. The phosphomimicking mutants ζ_S58D and ζ_S57D_S58D formed diffuse bands of intermediate mobility in native-PAGE (**Figure 3B**), indicating a more substantial shift of the dimer-monomer equilibrium towards monomers. Their sedimentation coefficient (~3.4 S), elution position (10.0–10.2 mL) and determined M_W (32–44 kDa) corresponded neither to a dimer (3.7 S, 9.7 mL, 56 kDa) nor a monomer (2.5 S, 10.5 mL, 28 kDa) at these concentrations

TABLE 2 | Dissociation constants of dimerization determined for 14-3-3ζ variants. Populations of monomers and dimers at 25 μM concentrations are included.

14-3-3	K_D	(M) (%)	(D) (%)
ζ_S58E	(0.35 ± 0.25) μM	8.02	91.98
ζ_S58D	(132 ± 7) μM	77.34	22.66
ζ_S57D_S58D	(348 ± 19) μM	88.70	11.30
ζm	(4.6 ± 0.1) mM	98.94	1.06
pζ	(7.6 ± 0.8) mM	99.35	0.65

(**Table 1**). At the same time, the double mutant ζ_S57D_S58D appeared to be more monomeric than ζ_S58D.

On the contrary, phosphorylation was observed to shift the dimer-monomer equilibrium towards monomers more significantly. pζ characteristics were similar to the monomeric mutant ζm (2.5 S, 10.5 mL, 28 kDa). Moreover, pζ migrated faster in native-PAGE than ζm (**Figure 3B**), presumably due to additional negative charge (−2e per monomeric unit) introduced by the phosphate group.

Since the populations of dimeric and monomeric states are dependent on the actual protein concentration, we next aimed to describe the dimer-monomer equilibrium of individual 14-3-3ζ variants quantitatively, using the dimerization dissociation constants (**Table 2**). The dimer-monomer equilibrium can be described as

$$M + M \rightleftarrows D$$

where M corresponds to monomer and D to dimer. The dimerization dissociation constant (K_D) can be then expressed as:

$$K_D = \frac{[M][M]}{[D]} \quad (1)$$

where [M] and [D] stand for molar concentrations of monomer and dimer, respectively.

To determine the dimerization constants of the 14-3-3ζ variants, we employed SEC-RALS and fluorescence assay based on FRET. Since ζm and pζ were observed to adopt both dimeric and monomeric states in native-PAGE and SEC-RALS (**Figure 3B** and **Figure 3D**), the dissociation constants of ζm and pζ were estimated directly from the distribution of proteins in the monomeric and dimeric state. The protein concentration in the dimeric [D] and monomeric [M] peak in SEC-RALS (**Supplementary Figure S4**) was determined based on known total protein concentration and protein percentage in individual peaks (**Figure 4A**).

The dissociation constants of ζ_S58D and ζ_S57D_S58D were calculated from M_W determined by SEC-RALS (**Supplementary Figure S4**). From the measurement at 36.5 μM concentration (**Figure 3D**), we saw that these phosphomimicking mutants exist as a heterogenous mixture of dimer and monomer. Since particles of different size contribute to RALS proportionally to their population, the observed M_W is a weighted average of molecular weights corresponding to dimer and monomer. Considering the following **Equation 2**, we calculated the fractions of proteins in the dimeric (D) and monomeric state (M) (**Figure 4A**).

$$M_{W,obs} = M_{W,\zeta}(D) + M_{W,p\zeta}(M) \quad (2)$$

where $M_{W,obs}$ corresponds to M_W of ζ_S58D and ζ_S57D_S58D determined from RALS, $M_{W,\zeta}$ and $M_{W,p\zeta}$ stand for M_W of ζ (dimer) and pζ (monomer) determined from RALS, respectively. Afterwards, knowing the total protein concentration, we determined [D] and [M] and finally the K_D.

In contrast to other 14-3-3ζ variants, the dissociation constant of ζ_S58E could not be obtained from SEC-RALS due to high preference of ζ_S58E for the dimeric form at selected concentrations (1–5 mg/mL). A more sensitive approach using much lower protein concentrations was required. Therefore, we applied a kinetic assay based on FRET. First, ζ_S58E was specifically labelled with the fluorescent donor as well as the

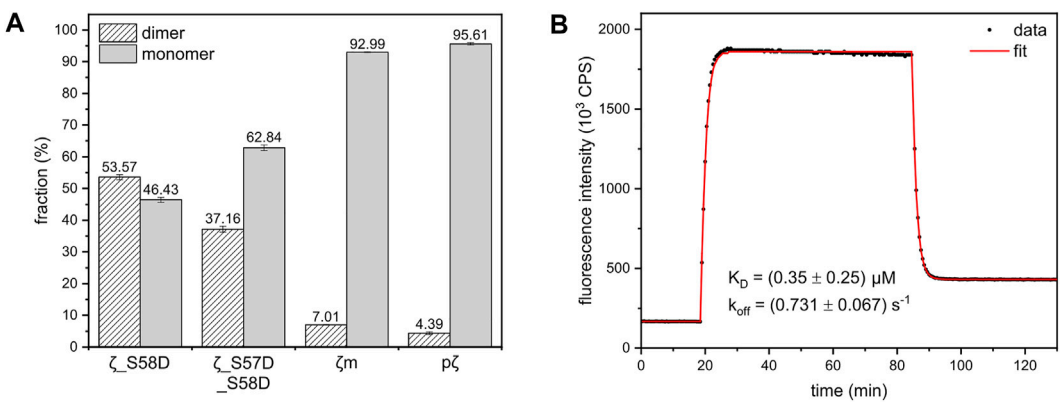

FIGURE 4 | Dimer-monomer distributions and FRET experiment used for calculation of the dimerization K_D of 14-3-3ζ variants. **(A)** The populations of 14-3-3ζ proteins (*x*-axis) in the dimeric and monomeric state determined from SEC-RALS experiments **(Supplementary Figure S4)** as described in the text. The dimer-monomer populations for 164 μM ζ_S58D and ζ_S57D_S58D mutants and 183 μM ζm and pζ variants at 20°C are shown. **(B)** FRET kinetic profile of ζ_S58E dimerization at 15°C. The experimental data (black dots) were fitted (red line), as in Trošanová et al. (2022), to obtain K_D and k_{off} values.

TABLE 3 | Thermodynamic parameters of 14-3-3ζ variants. Melting temperatures and enthalpies were measured in triplicates. ΔH_{vH} is expressed per mole of the cooperative unit corresponding to the most populated oligomeric state of the 14-3-3ζ variant, i. e. dimer for ζ and ζ_S58E or monomer for ζ_S58D, ζ_S57D_S58D, ζm and pζ.

14-3-3	T_m (°C) nanoDSF	T_m (°C) DSC	ΔH_{cal} (kcal/mol)	ΔH_{vH} (kcal/mol)
ζ	60.35 ± 0.15	60.28 ± 0.01	105.33 ± 0.58	195.50 ± 0.87
ζ_S58E	58.19 ± 0.09	57.64 ± 0.01	118.33 ± 0.58	172.17 ± 0.29
ζ_S58D	54.21 ± 0.03	53.89 ± 0.01	106.00 ± 1.00	206.00 ± 1.00
ζ_S57D_S58D	53.58 ± 0.10	53.70 ± 0.01	101.33 ± 0.58	184.33 ± 0.58
ζm	53.04 ± 0.12	53.34 ± 0.02	80.47 ± 3.59	204.00 ± 5.00
pζ	50.70 ± 0.11	50.88 ± 0.02	74.83 ± 0.55	140.67 ± 0.58

acceptor. Afterwards, time dependence of FRET intensity originating from the formation of ζ_S58E dimers was measured and fitted (**Figure 4B**) by a set of differential equations, as described in Trošanová et al. (2022). The best fit values for the dimerization K_D and dissociation rate constant (k_{off}) altogether with their errors were extracted from heatmap analysis (**Supplementary Figure S5**).

From the definition equation of K_D (**Eq. 1**) and mass conservation equation:

$$[M] + 2[D] = c_{tot} \tag{3}$$

where c_{tot} corresponds to total molar concentration of proteins (per 14-3-3ζ monomer), we can calculate the [M] at any protein concentration as follows:

$$[M] = \frac{-K_D + \sqrt{K_D^2 + 8K_D c_{tot}}}{4} \tag{4}$$

In **Table 2**, for illustration, we provide calculated populations of dimers and monomers at physiological concentration of 14-3-3ζ (25 μM).

Phosphorylation and Monomerization Decreases Thermal Stability

To assess the impact of phosphorylation and phosphomimicking mutations on 14-3-3ζ protein thermal stability, we employed nanoDSF and DSC measurements. We have found that individual 14-3-3ζ variants have different thermal stability that depends mostly on their oligomeric state. Phosphorylation of Ser58 destabilized the 14-3-3ζ protein significantly. The melting temperature (T_m) of pζ decreased by approx. 10°C in comparison with ζ (**Table 3**; **Figure 5A**). The stability of monomeric ζm and phosphomimicking mutants ζ_S58D and ζ_S57D_S58D was also affected but the decline in T_m of 6–7°C was less prominent. The phosphomimicking mutation S58E lowered the T_m value of 14-3-3ζ by 2–3°C. Interestingly, the unfolding of pζ and the rather monomeric variants was more gradual and spread over a broader temperature range, compared to the dimeric variants (**Figure 5A**). For all studied variants, the heat denaturation was irreversible.

DSC experiments enabled further determination of the thermodynamic parameters, such as unfolding enthalpies. All studied proteins displayed non-two-state transition behavior during denaturation and thus the calorimetric enthalpy (ΔH_{cal}) and van't Hoff enthalpy (ΔH_{vH}) were obtained (**Table 3**). The calorimetric enthalpies of both pζ and ζm were lower than ΔH_{cal} of ζ and the phosphomimicking mutants. ΔH_{vH} of all proteins was larger than ΔH_{cal} suggesting cooperativity during protein unfolding.

Diverse Effects of Selected Anions on Thermal Stability of 14-3-3ζ Variants

Protein stability may be affected by particular buffer composition. In this study, we investigated the impact of three sodium salts, commonly present in buffer formulations, on 14-3-3ζ protein thermal stabilities. 14-3-3ζ stability was assessed in the presence of chloride (Cl^-), sulphate (SO_4^{2-}) and phosphate (HPO_4^{2-}) anions at four different concentrations. Based on good agreement between T_m values measured by DSC and nanoDSF (**Table 3**), we selected nanoDSF, as a high-throughput method, for this screening.

Sulphate and phosphate ions mostly exhibited a stabilizing effect with increasing concentration (**Figure 5B**). Stabilization as high as ΔT_m = 11.6°C was detected for ζ_S58E in 600 mM phosphate. A similar response was observed for the dimeric ζ (ΔT_m ~ 9°C). On the contrary, for proteins with the dimer-monomer equilibrium shifted towards monomers, the stabilizing effect of certain anions was not that significant. In some cases, destabilization even occurred, i. e. for pζ, mζ and ζ_S57D_S58D (**Figure 5B**). A major difference in behavior was seen with the chloride ions. Whilst dimeric ζ and ζ_S58E were stabilized in all concentrations, a remarkable decrease in T_m was measured for monomerization-inducing constructs. The effect was strongest in case of pζ, which was destabilized by chloride in the whole concentration range, most substantially at the lowest (50 mM) chloride concentration (**Figure 5B**).

Phosphorylation Significantly Increases 14-3-3ζ Hydrophobicity

The protein dimeric interface is composed mostly of residues forming salt bridges and conserved hydrophobic interactions. Based on the assumption that 14-3-3ζ monomerization should result in solvent exposure of hydrophobic residues (Sluchanko et al., 2011b), we investigated the hydrophobicity of all 14-3-3ζ variants. The fluorescent probe BisANS, sensitive to the polarity of its environment, was titrated to the protein and changes in BisANS fluorescence at 495 nm were measured, similarly to studies by Sluchanko and co-authors (Sluchanko et al., 2008; Sluchanko et al., 2011b). BisANS fluorescence intensity increased

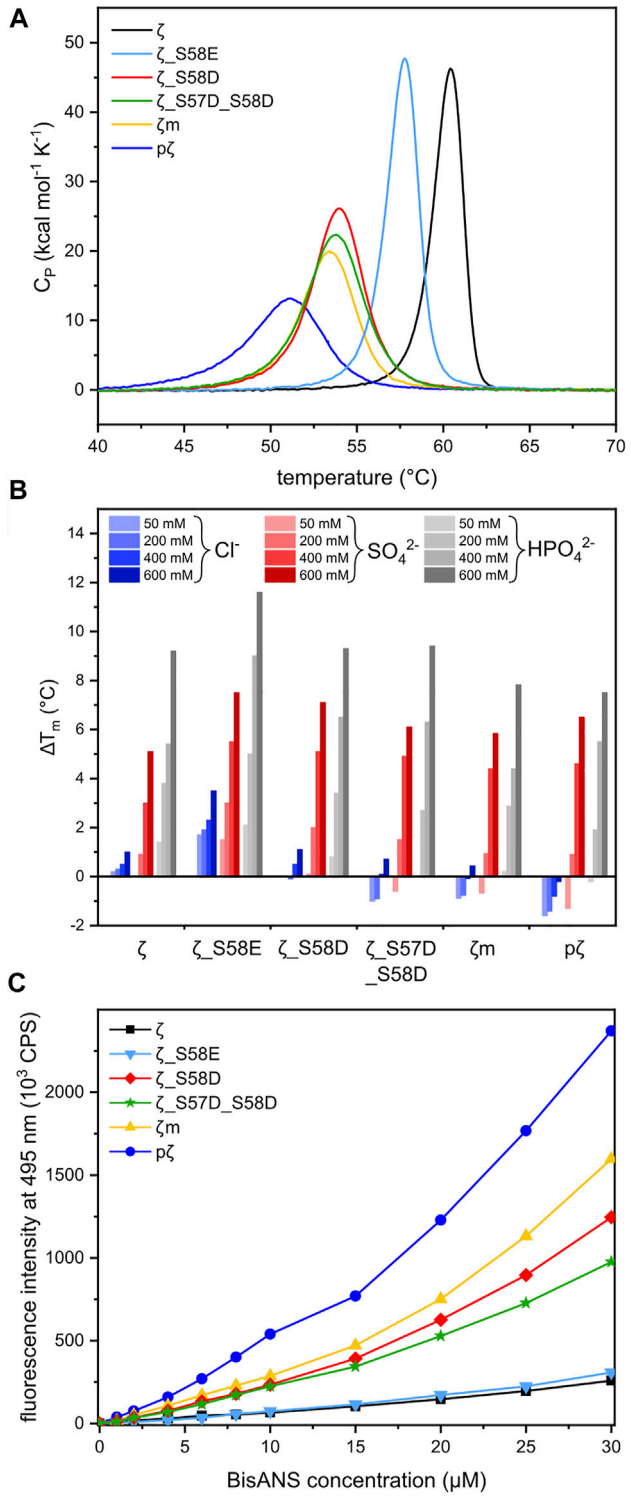

FIGURE 5 | Thermal stability and hydrophobicity of 14-3-3ζ variants. **(A)** DSC thermograms of 14-3-3ζ proteins demonstrating differences in T_m and global unfolding. T_m values were determined from the peak maxima. **(B)** Diverse effects of selected sodium salts on the stability of 14-3-3ζ variants. T_m of each protein variant in 20 mM HEPES pH 8 **(Supplementary Table S1)** was set as a reference (0°C). **(C)** BisANS fluorescence intensity at 495 nm used for comparison of 14-3-3ζ hydrophobicity.

in the order ζ ≤ ζ_S58E << ζ_S57D_S58D < ζ_S58D < ζm << pζ (**Figure 5C**).

Phosphorylation Modulates 14-3-3ζ Cellular Localization in HeLa and U251 Cells

Post-translational modifications have frequently been observed to change the attributes of proteins due to modified intracellular localization or trafficking (Michel et al., 1993; Humphries et al., 2008; Jin et al., 2014). We were interested to see if there is a functional impact of 14-3-3ζ Ser58 phosphorylation on protein expression *in vivo*. Therefore, we performed immunofluorescence colocalization experiments. Endogenous expression levels of ζ and pζ were detected in HeLa 1.3 cells and U251 cells, using specific anti-14-3-3ζ and anti-14-3-3ζ phospho-S58 primary antibodies.

Using our setup, we were able to observe different expression patterns with respect to 14-3-3ζ phosphorylation (**Figure 6**). We noticed a rather diffuse presence of ζ in the cytoplasm with non-specific occurrence of foci in both cell lines. There was no notable expression seen in the cell nucleus. Surprisingly, the expression of pζ was recorded almost exclusively in the nucleus of both cell lines as distinct strong foci, with minimal expression in the cytoplasm (**Figure 6**). We did not detect any significant overlap between the fluorescence signals for ζ and pζ.

DISCUSSION

Preparation of 14-3-3ζ Phosphorylated at Ser58

The phosphorylation of Ser58 and its effects on protein properties and oligomeric state has been an important unresolved issue in the community. The ambiguity of reported observations, especially their impact on the oligomeric state (Powell et al., 2002; Woodcock et al., 2003; Gu et al., 2006), motivated us to find a way to prepare 14-3-3ζ protein phosphorylated at Ser58 in high purity and yield for its biophysical analysis. In past studies, 14-3-3ζ protein could not be completely phosphorylated under the presented experimental conditions (Powell et al., 2003; Shen et al., 2003; Sluchanko and Uversky, 2015; Woodcock et al., 2018). Here, we have established a protocol for the preparation of 14-3-3ζ protein specifically and fully phosphorylated at Ser58.

Phosphorylated 14-3-3ζ protein was prepared by co-expression of 14-3-3ζ and PKA in *E. coli*. This technique has been successfully employed in other studies for *in vivo* phosphorylation of proteins in prokaryotic cells (Sluchanko et al., 2017; Tugaeva et al., 2017). Despite optimization of conditions, phosphorylation of 14-3-3ζ at Ser58 has not reached 100% in our hands, as reported elsewhere (Powell et al., 2003; Shen et al., 2003; Sluchanko and Uversky, 2015; Woodcock et al., 2018), likely due to limited accessibility of Ser58 to PKA and/or the activity of *E. coli* phosphatases

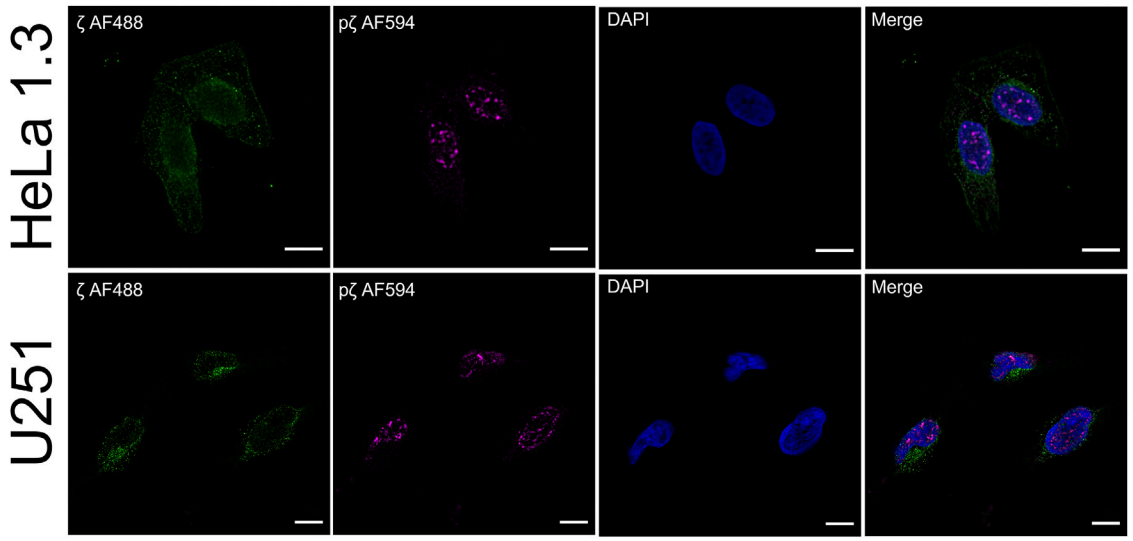

FIGURE 6 | Phosphorylation of 14-3-3ζ shifts its localization from the cytosol to the nucleus. Endogenous expression levels of ζ (green) and pζ (magenta) were analyzed using immunofluorescence in HeLa 1.3 cells and U251 cells. Immunostaining was performed using specific primary anti-14-3-3ζ and anti-14-3-3ζ pS58 antibodies, and corresponding AF-conjugated secondary antibodies. Nuclei were stained with DAPI (blue). Scale bars represent 10 μm. Negative controls were performed to exclude nonspecific binding of primary antibodies **(Supplementary Figure S6)**.

(Kennelly, 2002). 14-3-3ζ phosphorylated at Ser58 was separated from the non-phosphorylated fraction by AEX chromatography. pζ was eluted first (**Figure 1B**), since at these experimental conditions pζ exists as a monomer with approx. overall charge −17e, whereas ζ is a dimer with overall charge −30e (−15e/monomer).

Besides full phosphorylation at Ser58, minor phosphorylation (~4%) was detected at position Ser28, although the sequence 'AMKpS^{28}V' does not correspond to an ideal PKA recognition motif. It should also be mentioned that our 14-3-3ζ constructs contain an artificial C25A mutation in this short region, to avoid the formation of intermolecular disulphide bridges. This mutation could possibly influence PKA specificity.

The co-expression approach enabled the preparation of pure pζ in milligram quantities. To obtain similar yields *in vitro* (Gu et al., 2006; Powell et al., 2003; Woodcock et al., 2003, 2010), this would require a prior purification of the 14-3-3ζ protein in high amounts and the purification or purchase of protein kinase at substantial cost. Moreover, the protein must be subjected to the phosphorylation reaction and additional purification steps must be performed to recover pζ. Besides, problems with aggregation of the *in vitro* prepared pζ have been reported (Sluchanko and Uversky, 2015).

The presented *in vivo* phosphorylation assay is a more convenient alternative to *in vitro* assays since it increases time efficiency and yield. Protein expression and phosphorylation proceed in the cell simultaneously, and the phosphorylated protein can be isolated directly from the soluble fraction of the cell lysate. In addition, an analogous protocol may be used to phosphorylate other 14-3-3 isoforms (β, γ, ε, η), while only minor optimization of expression conditions should be necessary.

Phosphorylation Has a Different Impact on 14-3-3ζ Oligomeric State Than Phosphomimicking Mutations

We have demonstrated that the studied 14-3-3ζ variants prefer distinct oligomeric states at physiologically relevant concentrations (**Figure 3**). In addition, we have determined their dimerization dissociation constants (**Table 2**). The mutually consistent qualitative and quantitative results were obtained by multiple biophysical methods such as AUC, SEC-RALS, native-PAGE and FRET (**Figure 3**, **Figure 4**). The provided K_D values allow one to calculate the monomeric (M) and dimeric (D) fractions of 14-3-3ζ variants at any concentration using the derived **Equation 4**. For illustration, the dimer-monomer populations of 14-3-3ζ proteins at the estimated physiological concentration (25 μM) are listed in the last two columns of **Table 2**.

We would like to note that for those 14-3-3ζ variants, whose determined K_D values were out of the concentration range used in SEC-RALS experiments (7.3–183 μM), i. e. for pζ and ζm (K_D in mM range), we observed an artificial "concentration dependence of extracted K_D values" (data not shown). Therefore, we calculated these K_D values from the dimer-monomer populations at the highest measured concentration (183 μM), where the expected errors are the lowest. Still, the listed values in **Table 2** should be considered as estimates rather than accurate values.

Despite the mentioned shortcoming, the dimerization K_D values for individual 14-3-3ζ variants differ by several orders of

magnitude (**Table 2**). We have shown that the K_D for pζ is ~8 mM in contrast to the phosphomimicking mutants used in the past, i. e. ζ_S58E (Gu et al., 2006; Sluchanko et al., 2008; Sluchanko et al., 2011a) and ζ_S58D (Powell et al., 2003; Haladová et al., 2012; Civiero et al., 2017; Woodcock et al., 2018), whose K_D values we determined to be ~0.35 and 130 μM, respectively. The monomerization of ζ_S58E at very low micromolar concentration has been reported by Sluchanko and co-workers (Sluchanko et al., 2008; Sluchanko et al., 2011b). On the contrary, Gu et al. (2006) did not observe the formation of any ζ_S58E dimers. To compare the commonly used mutants from past works, the lower monomerization potency of S58E mutation in comparison to S58D is likely caused by the longer and more flexible side chain of Glu, which allows for an easier formation of 14-3-3 dimers.

The significant difference in the dimerization K_D values between pζ and the phosphomimicking mutants calls into question the outcomes of studies where such phosphomimicking mutations were used. Particularly, results obtained with the ζ_S58E mutant should be taken with a dose of caution (Gu et al., 2006; Sluchanko et al., 2008; Sluchanko et al., 2011a).

Although we have described an approach for preparation of pζ in high purity and yields, we can imagine experimental setups when the mutated variants may be preferred. In such cases, we recommend using the double phosphomimicking mutant ζ_S57D_S58D with a K_D ~350 μM, which possesses the closest dimerization K_D value of any listed phosphomimicking mutant to the truly phosphorylated variant. In other cases, when the negative charge at the dimeric interface is not essential and a pζ-like monomeric preference is rather desired, we recommend employing the monomeric mutant ζm, with the K_D of ζm being ~5 mM comparable to pζ.

Despite the varying oligomeric preferences among the studied 14-3-3ζ variants, their secondary structure as inspected by CD spectroscopy is very similar. Overall predicted α-helical content (79–85%) was in accordance with helicity determined from known crystal structures of 14-3-3ζ protein (Gardino et al., 2006). MRE at 222 nm for all proteins ranged between −23,000 and −27,000 deg $cm^2\,dmol^{-1}$ (**Figure 2B**), which agrees with previously published data for 14-3-3ζ protein (Sluchanko et al., 2008; Sluchanko and Uversky, 2015; Woodcock et al., 2018).

A decrease in MRE by ~10% observed for pζ may indicate minor changes in the pζ structure. Sluchanko and Uversky (2015) and Woodcock et al. (2018) proposed the unfolding of ~40 residues in the N-terminal helices. On the contrary, we did not observe any changes in MRE magnitude for ζ_S58E and ζ_S58D, as previously reported to be decreased by ~12–16 and ~12%, respectively (Sluchanko and Uversky, 2015; Woodcock et al., 2018). We hypothesize that discrepancies in these data may be caused by problems with measurement of accurate protein concentration due to different modifications at Ser58 (phosphorylation or mutations). Ser58 is in juxtaposition to Trp59, one of two tryptophanes that are the main contributors to the overall absorbance at 280 nm, which is used for the protein concentration determination.

Distinct Dimer-Monomer Equilibria Affect the Thermostability and Hydrophobicity of 14-3-3ζ Variants

Differences in the oligomeric state of 14-3-3ζ variants also impacted their thermal stability. Measured melting temperatures demonstrated that monomerization on its own significantly contributes to protein destabilization, but phosphorylation decreases the thermal stability to an even greater extent (**Table 3**). This was also observed after phosphorylation of the monomeric mutant ζm, whose T_m decreased to comparable level as for pζ (data not shown). This suggests that phosphorylation might, in addition to monomerization, cause additional changes in the protein structure and stability.

The melting temperature of ζ (~60°C) and the phosphomimicking mutants ζ_S58E (~58°C) and ζ_S58D (~54°C) agreed well with published studies (Sluchanko et al., 2008, 2012; Woodcock et al., 2018). A mild thermal destabilization observed for ζ_S58E correlates with the preferred dimeric arrangement. Interestingly, melting temperatures of monomeric mutants examined here or reported in the literature were always fluctuating around 53 °C (Sluchanko et al., 2011b; Sluchanko and Uversky, 2015), but none of the mutations destabilized 14-3-3ζ to the same extent as phosphorylation (**Table 3**).

From the DSC measurements, we also obtained enthalpies accompanying the protein unfolding (**Table 3**). Van't Hoff enthalpy higher than calorimetric enthalpy indicates that unfolding of 14-3-3ζ proteins is a non-two-state process, which is accompanied by cooperation. We note, however, that all studied variants exhibited irreversible denaturation, and therefore one cannot confidently use the analysis that is valid for reversible thermodynamics.

Next, we inspected the effect of common salts on thermal stability of 14-3-3ζ variants. In general, sulphate and phosphate were shown to stabilize 14-3-3ζ proteins, while the impact of chloride was much smaller or even destabilizing (**Figure 5B**). This is in good agreement with the Hofmeister series (Hofmeister, 1888; Kunz et al., 2004) and observations for 14-3-3γ (Bustad et al., 2012).

In case of the preferentially monomeric proteins, and especially pζ, we observed destabilization of the protein in the presence of sodium chloride (**Figure 5B**). We hypothesize that chloride may interact unfavorably with the exposed hydrophobic patches, as its interaction with water is substantially weaker than both phosphate and sulphate. Even though the sulphate anion is considered more stabilizing than phosphate according to the Hofmeister series (Hofmeister, 1888), 14-3-3ζ proteins exhibited greater stabilization by the latter (**Figure 5B**). We speculate, that possible binding of the phosphate ion into the phospho-peptide binding groove of 14-3-3 would increase its stability, which is in agreement with the overall phospho-target binding nature of the 14-3-3 family (Yaffe et al., 1997; Obsil and Obsilova, 2011).

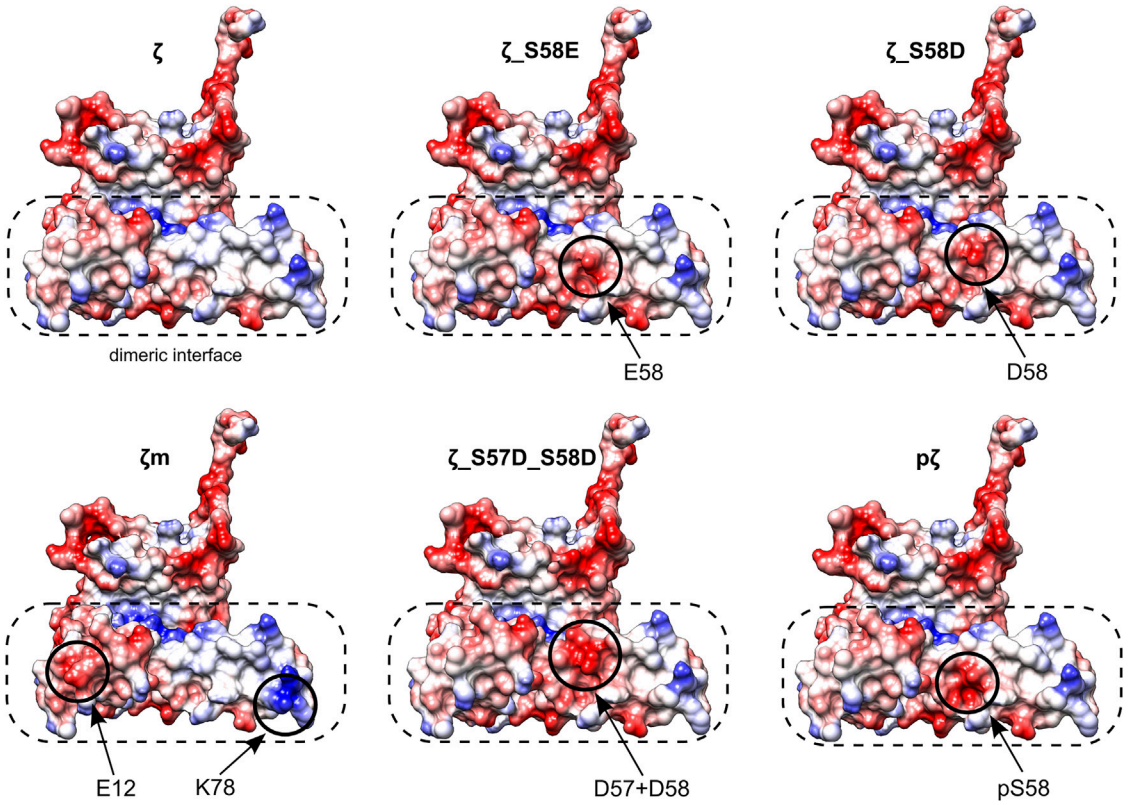

FIGURE 7 | Electrostatic potential maps of all 14-3-3ζ variants. Only monomeric subunits are shown. Modifications and corresponding changes in charge distributions at the dimeric interface (in a dashed rectangle) are highlighted (in solid circles). Negative electrostatic potential is depicted in red, positive in blue. Atom coordinates of the 14-3-3ζ were adopted from Kostelecky et al. (2009) and Nagy et al. (2017). The desired residues were mutated *in silico* and their conformations were selected from a library of possible conformers. Mutagenesis and generation of the electrostatic potential maps with Coulombic surface coloring were performed in UCSF Chimera (Pettersen et al., 2004).

Different monomerization tendencies among 14-3-3ζ variants were reflected in protein hydrophobicity, as well. In general, the preferentially monomeric 14-3-3ζ variants exhibited higher affinity to the fluorescent probe BisANS than dimers. We attribute the distinct affinity towards BisANS to two main factors. First, monomerization results in the exposure of hydrophobic patches that were originally hidden at the dimeric interface. Therefore, monomeric variants appear to be more hydrophobic, similarly to previous studies (Sluchanko et al., 2008, 2014; Sluchanko et al., 2011b; Woodcock et al., 2018). Second, the affinity to BisANS is influenced by differences in the charge distribution at the dimeric interface between variants, as demonstrated on the electrostatic potential maps (**Figure 7**).

Considering those two factors, the overall trends seen in **Figure 5C** appear to be in line with the dimerization K_D values, with two outstanding distinctions. First, the affinity towards BisANS is higher for ζ_S58D compared to ζ_S57D_S58D, although the double phosphomimicking mutant is slightly more monomeric (**Table 2**). This behavior may be explained by the higher negative charge of ζ_S57D_S58D (**Figure 7**) and thus larger repulsion of the BisANS probe that is also partially negatively charged. Second, the hydrophobicity of pζ seems much higher than of ζm, despite similar dimerization K_D values (**Table 2**). During the design of the monomeric mutant ζm, we replaced two hydrophobic residues by charged amino acids (namely L12E_M78K) (Jandova et al., 2018), which reduced the size of hydrophobic patches (**Figure 7**). On the contrary, these hydrophobic patches are preserved within pζ, making pζ more hydrophobic.

Phosphorylation of 14-3-3ζ Alters its Subcellular Localization in HeLa 1.3 and U251 Cells

Immunofluorescence experiments revealed a clear difference in expression levels of ζ and pζ with respect to subcellular compartments in the tested cell lines. ζ was mostly found dispersed throughout the cytoplasm, while pζ was seen in the nucleus in the form of strong foci (**Figure 6**). Our results suggest that upon phosphorylation, pζ is transported and concentrated in the nucleus by an unknown mechanism. Hence, we deduce that pζ has a differing role to ζ in the cell, perhaps in regulation of the cell cycle or genome transcription, as reported elsewhere (Hermeking and Benzinger, 2006; Hou et al., 2010; Tzivion et al., 2011). A connection to changes in the oligomeric state of the protein may not be excluded. Note that the cell lines used in

this study are derived from cervical carcinoma (HeLa 1.3) (Takai et al., 2010) and glioblastoma tumor cells (U251) (Westermark et al., 1973), thus the described localization pattern might be specific to cancer cells. The presented results will be corroborated in future work by testing additional cell lines, and by pull-down experiments coupled with mass spectrometry analysis, to address the varying functional roles of ζ and pζ by looking at binding partners. Immunofluorescence experiments with cells transiently transfected with ζ_S57D_S58D and ζm will likely shed light on the question whether the nuclear translocation is driven primarily by the additional negative charge or monomerization.

We did not notice double labelling of the same spots during immunofluorescence, which could be expected depending on the specificity of the used antibodies. To this end, we tested their specificity by Western blotting (**Supplementary Figure S7**). When purified proteins were blotted, both ζ and pζ were detected by the anti-14-3-3ζ antibody, but only pζ was detected by the anti-14-3-3ζ pS58 antibody, confirming its specificity (**Supplementary Figure S7A**). When we blotted cell lysates with the same antibodies, we did not record any corresponding signal with the anti-14-3-3ζ pS58 antibody, but clear bands were seen when using the anti-14-3-3ζ antibody (**Supplementary Figure S7B**). Even though pζ could not be detected in the whole cell lysates by Western blotting it could be visualized by immunofluorescence as distinct strong foci using the anti-14-3-3ζ pS58 antibody. However, using the anti-14-3-3ζ antibody which could visualize both variants (**Supplementary Figure S7A**), we could detect only a diffuse signal that prevailed in the cytoplasm and no distinct foci in the nucleus (**Figure 6**). The absence of pζ foci when using the anti-14-3-3ζ antibody can be explained by high levels of ζ with respect to pζ which could compromise detection of the pζ variant.

CONCLUSION

Our case study, focused on 14-3-3ζ protein, demonstrates that phosphomimicking mutants are quite poor substitutes for the phosphorylated variant. Two phosphomimicking mutants used in previous studies, namely ζ_S58E and ζ_S58D, and a novel double mutant ζ_S57D_S58D were compared with 14-3-3 pζ. Significant differences were revealed in the dimerization dissociation constants between the phosphomimicking mutants ζ_S58E, ζ_S58D, and ζ_S57D_S58D (~0.35, 132, 348 μM) and the phosphorylated variant (~7.6 mM). The dissimilarity in the oligomeric states was also reflected in the melting temperatures of the phosphomimicking mutants (T_m ~ 57.6, 53.9, 53.7°C) with respect to the phosphorylated variant (T_m ~ 50.9°C). Ser58 phosphorylation also increased the hydrophobicity more than two times compared to the phosphomimicking mutants. Moreover, phosphorylation changed the cellular localization of 14-3-3ζ from the cytoplasm towards the nucleus. For future studies of 14-3-3 phosphorylation, when the use of phosphorylated protein is not applicable, e. g. *in vivo* experiments, we recommend utilizing the double mutant ζ_S57D_S58D, as its behavior was most similar to pζ. When the adequate oligomeric state is more important than the negative charge at the dimeric interface, we would opt for the monomeric mutant ζm. In conclusion, our findings highlight the importance of careful mutant design and encourage the verification of their properties with the original modification.

DATA AVAILABILITY STATEMENT

The datasets presented in this study can be found in the Figshare repository (https://doi.org/10.6084/m9.figshare.c.5813213.v1).

AUTHOR CONTRIBUTIONS

AK optimized the preparation of pζ and prepared the protein; AN prepared the phosphomimicking mutants; AK and AN designed and performed the experiments and wrote the manuscript; TB prepared the monomeric mutant and performed immunofluorescence experiments; NG performed molecular cloning and mutagenesis work; JŠ performed and evaluated the FRET assay; JHo performed SEC-RALS and DSC measurements and helped with data interpretation; TB, NG, and JHo contributed to the writing of the manuscript; JH supervised the work, secured funding, designed the experiments and wrote the manuscript.

FUNDING

This study was financed by the Czech Science Foundation (no. GF20-05789L). AK acknowledges the Grant Agency of Masaryk University (MU) for the support of an excellent diploma thesis within the rector's program (no. MUNI/C/1562/2019). We acknowledge CEITEC (Central European Institute of Technology) Proteomics Core Facility and Biomolecular Interactions and Crystallization Core Facility of CIISB, Instruct-CZ Centre, supported by MEYS CR (LM2018127) and European Regional Development Fund-Project 'UP CIISB' (CZ.02.1.01/0.0/0.0/18_046/0015974). We acknowledge the CEITEC Core Facility Cellular Imaging supported by MEYS CR (LM2018129 Czech-BioImaging).

ACKNOWLEDGMENTS

We gratefully acknowledge Dr. Monika Kubíčková from the Core Facility Biomolecular Interactions and Crystallization of CEITEC MU for AUC measurements and data evaluation. We acknowledge Mgr. Petr Louša for help with analysis of the FRET data. We acknowledge CEITEC Proteomics Core Facility, especially Dr. Ondrej Šedo, for MALDI-TOF MS and LC-MS/MS analysis. The pACYCduet-1 plasmid with cDNA of PKA was kindly provided by prof. Nikolai Sluchanko (Russian Academy of Sciences, Moscow).

SUPPLEMENTARY MATERIAL

The Supplementary Material for this article can be found online at: https://www.frontiersin.org/articles/10.3389/fchem.2022.835733/full#supplementary-material

REFERENCES

Alexander, C. G., Wanner, R., Johnson, C. M., Breitsprecher, D., Winter, G., Duhr, S., et al. (2014). Novel Microscale Approaches for Easy, Rapid Determination of Protein Stability in Academic and Commercial Settings. *Biochim. Biophys. Acta (Bba) - Proteins Proteomics* 1844, 2241–2250. doi:10.1016/j.bbapap.2014.09.016

Andrade, M. A., Chacón, P., Merelo, J. J., and Morán, F. (1993). Evaluation of Secondary Structure of Proteins from Uv Circular Dichroism Spectra Using an Unsupervised Learning Neural Network. *Protein Eng. Des. Sel* 6, 383–390. doi:10.1093/protein/6.4.383

Ardito, F., Giuliani, M., Perrone, D., Troiano, G., and Muzio, L. L. (2017). The Crucial Role of Protein Phosphorylation in Cell Signaling and its Use as Targeted Therapy (Review). *J. Mol. Med.* 40, 271–280. doi:10.3892/ijmm.2017.3036

Bernatik, O., Pejskova, P., Vyslouzil, D., Hanakova, K., Zdrahal, Z., and Cajanek, L. (2020). Phosphorylation of Multiple Proteins Involved in Ciliogenesis by Tau Tubulin Kinase 2. *MBoC* 31, 1032–1046. doi:10.1091/MBC.E19-06-0334

Braicu, C., Buse, M., Busuioc, C., Drula, R., Gulei, D., Raduly, L., et al. (2019). A Comprehensive Review on MAPK: A Promising Therapeutic Target in Cancer. *Cancers (Basel)* 11, 1–25. doi:10.3390/cancers11101618

Brautigam, C. A. (2015). Calculations and Publication-Quality Illustrations for Analytical Ultracentrifugation Data. *Methods Enzymol.* Vol 562, 109–133. doi:10.1016/bs.mie.2015.05.001

Bustad, H. J., Skjaerven, L., Ying, M., Halskau, Ø., Baumann, A., Rodriguez-Larrea, D., et al. (2012). The Peripheral Binding of 14-3-3γ to Membranes Involves Isoform-specific Histidine Residues. *PLoS One* 7, e49671–11. doi:10.1371/journal.pone.0049671

Civiero, L., Cogo, S., Kiekens, A., Morganti, C., Tessari, I., Lobbestael, E., et al. (2017). PAK6 Phosphorylates 14-3-3γ to Regulate Steady State Phosphorylation of LRRK2. *Front. Mol. Neurosci.* 10, 417–17. doi:10.3389/fnmol.2017.00417

Dephoure, N., Gould, K. L., Gygi, S. P., and Kellogg, D. R. (2013). Mapping and Analysis of Phosphorylation Sites: A Quick Guide for Cell Biologists. *MBoC* 24, 535–542. doi:10.1091/mbc.E12-09-0677

Dubois, T., Rommel, C., Howell, S., Steinhussen, U., Soneji, Y., Morrice, N., et al. (1997). 14-3-3 Is Phosphorylated by Casein Kinase I on Residue 233. *J. Biol. Chem.* 272, 28882–28888. doi:10.1074/jbc.272.46.28882

Gardino, A. K., Smerdon, S. J., and Yaffe, M. B. (2006). Structural Determinants of 14-3-3 Binding Specificities and Regulation of Subcellular Localization of 14-3-3-ligand Complexes: A Comparison of the X-ray crystal Structures of All Human 14-3-3 Isoforms. *Semin. Cancer Biol.* 16, 173–182. doi:10.1016/j.semcancer.2006.03.007

Gardino, A. K., and Yaffe, M. B. (2011). 14-3-3 Proteins as Signaling Integration Points for Cell Cycle Control and Apoptosis. *Semin. Cel Dev. Biol.* 22, 688–695. doi:10.1016/j.semcdb.2011.09.008

Gasteiger, E., Hoogland, C., Gattiker, A., Duvaud, S., Wilkins, M. R., Appel, R. D., et al. (2005). Protein Identification and Analysis Tools on the ExPASy Server. *The Proteomics Protoc. Handbook* 112, 531–552. doi:10.1385/1592598900

Gerst, F., Kaiser, G., Panse, M., Sartorius, T., Pujol, A., Hennige, A. M., et al. (2015). Protein Kinase Cδ Regulates Nuclear export of FOXO1 through Phosphorylation of the Chaperone 14-3-3ζ. *Diabetologia* 58, 2819–2831. doi:10.1007/s00125-015-3744-z

Gogl, G., Tugaeva, K. V., Eberling, P., Kostmann, C., Trave, G., and Sluchanko, N. N. (2021). Hierarchized Phosphotarget Binding by the Seven Human 14-3-3 Isoforms. *Nat. Commun.* 12, 2–13. doi:10.1038/s41467-021-21908-8

Gu, Y.-M., Jin, Y.-H., Choi, J.-K., Baek, K.-H., Yeo, C.-Y., and Lee, K.-Y. (2006). Protein Kinase A Phosphorylates and Regulates Dimerization of 14-3-3ζ. *FEBS Lett.* 580, 305–310. doi:10.1016/j.febslet.2005.12.024

Haladová, K., Mrázek, H., Ječmen, T., Halada, P., Man, P., Novák, P., et al. (2012). The Combination of Hydrogen/deuterium Exchange or Chemical Cross-Linking Techniques with Mass Spectrometry: Mapping of Human 14-3-3ζ Homodimer Interface. *J. Struct. Biol.* 179, 10–17. doi:10.1016/j.jsb.2012.04.016

Hermeking, H., and Benzinger, A. (2006). 14-3-3 Proteins in Cell Cycle Regulation. *Semin. Cancer Biol.* 16, 183–192. doi:10.1016/j.semcancer.2006.03.002

Hofmeister, F. (1888). Zur Lehre von der Wirkung der Salze. *Archiv F. Experiment. Pathol. U. Pharmakol* 24, 247–260. doi:10.1007/BF01918191

Hou, Z., Peng, H., White, D. E., Wang, P., Lieberman, P. M., Halazonetis, T., et al. (2010). 14-3-3 Binding Sites in the Snail Protein Are Essential for Snail-Mediated Transcriptional Repression and Epithelial-Mesenchymal Differentiation. *Cancer Res.* 70, 4385–4393. doi:10.1158/0008-5472.CAN-10-0070

Hritz, J., Byeon, I.-J. L., Krzysiak, T., Martinez, A., Sklenar, V., and Gronenborn, A. M. (2014). Dissection of Binding between a Phosphorylated Tyrosine Hydroxylase Peptide and 14-3-3ζ: A Complex Story Elucidated by NMR. *Biophysical J.* 107, 2185–2194. doi:10.1016/j.bpj.2014.08.039

Humphries, M. J., Ohm, A. M., Schaack, J., Adwan, T. S., and Reyland, M. E. (2008). Tyrosine Phosphorylation Regulates Nuclear Translocation of PKCδ. *Oncogene* 27, 3045–3053. doi:10.1038/sj.onc.1210967

Hunter, T. (2012). Why Nature Chose Phosphate to Modify Proteins. *Phil. Trans. R. Soc. B* 367, 2513–2516. doi:10.1098/rstb.2012.0013

Inoue, H., Nojima, H., and Okayama, H. (1990). High Efficiency Transformation of *Escherichia coli* with Plasmids. *Gene* 96, 23–28. doi:10.1016/0378-1119(90)90336-P

Jandova, Z., Trosanova, Z., Weisova, V., Oostenbrink, C., and Hritz, J. (2018). Free Energy Calculations on the Stability of the 14-3-3ζ Protein. *Biochim. Biophys. Acta (Bba) - Proteins Proteomics* 1866, 442–450. doi:10.1016/j.bbapap.2017.11.012

Jin, C., Strich, R., and Cooper, K. F. (2014). Slt2p Phosphorylation Induces Cyclin C Nuclear-To-Cytoplasmic Translocation in Response to Oxidative Stress. *MBoC* 25, 1396–1407. doi:10.1091/mbc.E13-09-0550

Kanno, T., and Nishizaki, T. (2011). Sphingosine Induces Apoptosis in Hippocampal Neurons and Astrocytes by Activating Caspase-3/-9 via a Mitochondrial Pathway Linked to SDK/14-3-3 protein/Bax/cytochrome C. *J. Cel. Physiol.* 226, 2329–2337. doi:10.1002/jcp.22571

Kennelly, P. J. (2002). Protein Kinases and Protein Phosphatases in Prokaryotes: A Genomic Perspective. *FEMS Microbiol. Lett.* 206, 1–8. doi:10.1016/S0378-1097(01)00479-710.1111/j.1574-6968.2002.tb10978.x

Kostelecky, B., Saurin, A. T., Purkiss, A., Parker, P. J., and Mcdonald, N. Q. (2009). Recognition of an Intra-chain Tandem 14-3-3 Binding Site within PKCε. *EMBO Rep.* 10, 983–989. doi:10.1038/embor.2009.150

Kunz, W., Henle, J., and Ninham, B. W. (2004). 'Zur Lehre von der Wirkung der Salze' (about the science of the effect of salts): Franz Hofmeister's historical papers. *Curr. Opin. Colloid Interf. Sci.* 9, 19–37. doi:10.1016/j.cocis.2004.05.005

Laage, D., Elsaesser, T., and Hynes, J. T. (2017). Water Dynamics in the Hydration Shells of Biomolecules. *Chem. Rev.* 117, 10694–10725. doi:10.1021/acs.chemrev.6b00765

Liu, H., and Naismith, J. H. (2008). An Efficient One-step Site-Directed Deletion, Insertion, Single and Multiple-Site Plasmid Mutagenesis Protocol. BMC Biotechnol. 8., doi:10.1186/1472-6750-8-91

Louis-Jeune, C., Andrade-Navarro, M. A., and Perez-Iratxeta, C. (2012). Prediction of Protein Secondary Structure from Circular Dichroism Using Theoretically Derived Spectra. *Proteins* 80, 374–381. doi:10.1002/prot.23188

Ma, Y., Pitson, S., Hercus, T., Murphy, J., Lopez, A., and Woodcock, J. (2005). Sphingosine Activates Protein Kinase A Type II by a Novel cAMP-independent Mechanism. *J. Biol. Chem.* 280, 26011–26017. doi:10.1074/jbc.M409081200

Mackintosh, C. (2004). Dynamic Interactions between 14-3-3 Proteins and Phosphoproteins Regulate Diverse Cellular Processes. *Biochem. J.* 381, 329–342. doi:10.1042/BJ20031332

Mandell, D. J., Chorny, I., Groban, E. S., Wong, S. E., Levine, E., Rapp, C. S., et al. (2007). Strengths of Hydrogen Bonds Involving Phosphorylated Amino Acid Side Chains. *J. Am. Chem. Soc.* 129, 820–827. doi:10.1021/ja063019w

Menzel, J., Kownatzki-Danger, D., Tokar, S., Ballone, A., Unthan-Fechner, K., Kilisch, M., et al. (2020). 14-3-3 Binding Creates a Memory of Kinase Action by Stabilizing the Modified State of Phospholamban. *Sci. Signal.* 13, 1–16. doi:10.1126/SCISIGNAL.AAZ1436

Messaritou, G., Grammenoudi, S., and Skoulakis, E. M. C. (2010). Dimerization Is Essential for 14-3-3ζ Stability and Function *In Vivo*. *J. Biol. Chem.* 285, 1692–1700. doi:10.1074/jbc.M109.045989

Michel, T., Li, G. K., and Busconi, L. (1993). Phosphorylation and Subcellular Translocation of Endothelial Nitric Oxide Synthase. *Proc. Natl. Acad. Sci.* 90, 6252–6256. doi:10.1073/pnas.90.13.6252

Morrison, D. K. (2012). MAP Kinase Pathways. *Cold Spring Harb Perspect. Biol.* 4, 1–5. doi:10.1101/cshperspect.a011254

Munier, C. C., De Maria, L., Edman, K., Gunnarsson, A., Longo, M., MacKintosh, C., et al. (2021). Glucocorticoid Receptor Thr524 Phosphorylation by MINK1 Induces Interactions with 14-3-3 Protein Regulators. *J. Biol. Chem.* 296, 100551–100615. doi:10.1016/j.jbc.2021.100551

Nagy, G., Oostenbrink, C., and Hritz, J. (2017). Exploring the Binding Pathways of the 14-3-3ζ Protein: Structural and Free-Energy Profiles Revealed by Hamiltonian Replica Exchange Molecular Dynamics with Distancefield Distance Restraints. PLoS One 1–30. doi:10.1371/journal.pone.0180633

Obsil, T., and Obsilova, V. (2011). Structural Basis of 14-3-3 Protein Functions. *Semin. Cel Dev. Biol.* 22, 663–672. doi:10.1016/j.semcdb.2011.09.001

Obsilova, V., and Obsil, T. (2020). The 14-3-3 Proteins as Important Allosteric Regulators of Protein Kinases. *Int. J. Mol. Sci.* 21, 1–16. doi:10.3390/ijms21228824

Paleologou, K. E., Schmid, A. W., Rospigliosi, C. C., Kim, H.-Y., Lamberto, G. R., Fredenburg, R. A., et al. (2008). Phosphorylation at Ser-129 but Not the Phosphomimics S129E/D Inhibits the Fibrillation of α-Synuclein. *J. Biol. Chem.* 283, 16895–16905. doi:10.1074/jbc.M800747200

Pearlman, S. M., Serber, Z., and Ferrell, J. E., Jr. (2011). A Mechanism for the Evolution of Phosphorylation Sites. *Cell* 147, 934–946. doi:10.1016/j.cell.2011.08.052.A

Pérez-Mejías, G., Velázquez-Cruz, A., Guerra-Castellano, A., Baños-Jaime, B., Díaz-Quintana, A., González-Arzola, K., et al. (2020). Exploring Protein Phosphorylation by Combining Computational Approaches and Biochemical methodsExploring Protein Phosphorylation by Combining Computational Approaches and Biochemical Methods. Comput. Struct. Biotechnol. *Comput. Struct. Biotechnol. J.* 18, 1852–1863. doi:10.1016/j.csbj.2020.06.043

Pettersen, E. F., Goddard, T. D., Huang, C. C., Couch, G. S., Greenblatt, D. M., Meng, E. C., et al. (2004). UCSF Chimera?A Visualization System for Exploratory Research and Analysis. *J. Comput. Chem.* 25, 1605–1612. doi:10.1002/jcc.20084

Powell, D. W., Rane, M. J., Chen, Q., Singh, S., and McLeish, K. R. (2002). Identification of 14-3-3ζ as a Protein Kinase B/Akt Substrate. *J. Biol. Chem.* 277, 21639–21642. doi:10.1074/jbc.M203167200

Powell, D. W., Rane, M. J., Joughin, B. A., Kalmukova, R., Hong, J.-H., Tidor, B., et al. (2003). Proteomic Identification of 14-3-3ζ as a Mitogen-Activated Protein Kinase-Activated Protein Kinase 2 Substrate: Role in Dimer Formation and Ligand Binding. *Mol. Cel. Biol.* 23, 5376–5387. doi:10.1128/MCB.23.15.5376-5387.2003

Schuck, P. (2000). Size-distribution Analysis of Macromolecules by Sedimentation Velocity Ultracentrifugation and Lamm Equation Modeling. *Biophysical J.* 78, 1606–1619. doi:10.1016/S0006-3495(00)76713-0

Sharma, K. K., Kaur, H., Kumar, G. S., and Kester, K. (1998). Interaction of 1,1′-Bi(4-Anilino)naphthalene-5,5′-Disulfonic Acid with α-Crystallin. *J. Biol. Chem.* 273, 8965–8970. doi:10.1074/jbc.273.15.8965

Shen, Y. H., Godlewski, J., Bronisz, A., Zhu, J., Comb, M. J., Avruch, J., et al. (2003). Significance of 14-3-3 Self-Dimerization for Phosphorylation-dependent Target Binding. *MBoC* 14, 4721–4733. doi:10.1091/mbc.e02-12-0821

Sluchanko, N. N., Artemova, N. V., Sudnitsyna, M. V., Safenkova, I. V., Antson, A. A., Levitsky, D. I., et al. (2012). Monomeric 14-3-3ζ Has a Chaperone-like Activity and Is Stabilized by Phosphorylated HspB6. *Biochemistry* 51, 6127–6138. doi:10.1021/bi300674e

Sluchanko, N. N., Beelen, S., Kulikova, A. A., Weeks, S. D., Antson, A. A., Gusev, N. B., et al. (2017). Structural Basis for the Interaction of a Human Small Heat Shock Protein with the 14-3-3 Universal Signaling Regulator. *Structure* 25, 305–316. doi:10.1016/j.str.2016.12.005

Sluchanko, N. N., and Bustos, D. M. (2019). Intrinsic Disorder Associated with 14-3-3 Proteins and Their Partners. *Prog. Mol. Biol. Transl. Sci.* 166, 19–61. doi:10.1016/bs.pmbts.2019.03.007

Sluchanko, N. N., Chernik, I. S., Seit-nebi, A. S., Pivovarova, A. V., Levitsky, D. I., and Gusev, N. B. (2008). Effect of Mutations Mimicking Phosphorylation on the Structure and Properties of Human 14-3-3ζ. *Arch. Biochem. Biophys.* 477, 305–312. doi:10.1016/j.abb.2008.05.020

Sluchanko, N. N., and Gusev, N. B. (2010). 14-3-3 Proteins and Regulation of Cytoskeleton. *Biochem. Mosc.* 75, 1528–1546. doi:10.1134/S0006297910130031

Sluchanko, N. N., Roman, S. G., Chebotareva, N. A., and Gusev, N. B. (2014). Chaperone-like Activity of Monomeric Human 14-3-3ζ on Different Protein Substrates. *Arch. Biochem. Biophys.* 549, 32–39. doi:10.1016/j.abb.2014.03.008

Sluchanko, N. N., Sudnitsyna, M. V., Chernik, I. S., Seit-Nebi, A. S., and Gusev, N. B. (2011a). Phosphomimicking Mutations of Human 14-3-3ζ Affect its Interaction with Tau Protein and Small Heat Shock Protein HspB6. *Arch. Biochem. Biophys.* 506, 24–34. doi:10.1016/j.abb.2010.11.003

Sluchanko, N. N., Sudnitsyna, M. V., Seit-nebi, A. S., Antson, A. A., and Gusev, N. B. (2011b). Properties of the Monomeric Form of Human 14-3-3ζ Protein and its Interaction with Tau and HspB6. *Biochemistry* 50, 9797–9808. doi:10.1021/bi201374s

Sluchanko, N. N., and Uversky, V. N. (2015). Hidden Disorder Propensity of the N-Terminal Segment of Universal Adapter Protein 14-3-3 Is Manifested in its Monomeric Form: Novel Insights into Protein Dimerization and Multifunctionality. *Biochim. Biophys. Acta (Bba) - Proteins Proteomics* 1854, 492–504. doi:10.1016/j.bbapap.2015.02.017

Somale, D., Di Nardo, G., di Blasio, L., Puliafito, A., Vara-Messler, M., Chiaverina, G., et al. (2020). Activation of RSK by Phosphomimetic Substitution in the Activation Loop Is Prevented by Structural Constraints. *Sci. Rep.* 10, 591–614. doi:10.1038/s41598-019-56937-3

Strickfaden, S. C., Winters, M. J., Ben-ari, G., Lamson, R. E., Tyers, M., and Pryciak, P. M. (2007). A Mechanism for Cell-Cycle Regulation of MAP Kinase Signaling in a Yeast Differentiation Pathway. *Cell* 128, 519–531. doi:10.1016/j.cell.2006.12.032

Takai, K. K., Hooper, S., Blackwood, S., Gandhi, R., and de Lange, T. (2010). *In Vivo* stoichiometry of Shelterin Components. *J. Biol. Chem.* 285, 1457–1467. doi:10.1074/jbc.M109.038026

Thorsness, P. E., and Koshland, D. E. (1987). Inactivation of Isocitrate Dehydrogenase by Phosphorylation Is Mediated by the Negative Charge of the Phosphate. *J. Biol. Chem.* 262, 10422–10425. doi:10.1016/s0021-9258(18)60975-5

Trošanová, Z., Louša, P., Kozeleková, A., Brom, T., Gašparik, N., Tungli, J., et al. (2022). Quantitation of Human 14-3-3ζ Dimerization and the Effect of Phosphorylation on Dimer-Monomer Equilibria. *J. Mol. Biol.* 167479. doi:10.1016/j.jmb.2022.167479

Tsuruta, F., Sunayama, J., Mori, Y., Hattori, S., Shimizu, S., Tsujimoto, Y., et al. (2004). JNK Promotes Bax Translocation to Mitochondria through Phosphorylation of 14-3-3 Proteins. *EMBO J.* 23, 1889–1899. doi:10.1038/sj.emboj.7600194

Tugaeva, K. V., Tsvetkov, P. O., and Sluchanko, N. N. (2017). Bacterial Co-expression of Human Tau Protein with Protein Kinase A and 14-3-3 for Studies of 14-3-3/phospho-Tau Interaction. *PLoS One* 12, e0178933–18. doi:10.1371/journal.pone.0178933

Tzivion, G., Dobson, M., and Ramakrishnan, G. (2011). FoxO Transcription Factors; Regulation by AKT and 14-3-3 Proteins. *Biochim. Biophys. Acta (Bba) - Mol. Cel Res.* 1813, 1938–1945. doi:10.1016/j.bbamcr.2011.06.002

Tzivion, G., Luo, Z., and Avruch, J. (1998). A Dimeric 14-3-3 Protein Is an Essential Cofactor for Raf Kinase Activity. *Nature* 394, 88–92. doi:10.1038/27938

Wei, Z., and Liu, H. T. (2002). MAPK Signal Pathways in the Regulation of Cell Proliferation in Mammalian Cells. *Cell Res.* 12, 9–18. doi:10.1038/sj.cr.7290105

Westermark, B., Pontén, J., and Hugosson, R. (1973). Determinants for the Establishment of Permanent Tissue Culture Lines from Human Gliomas. *Acta Pathol. Microbiol. Scand. A.* 81, 791–805. doi:10.1111/j.1699-0463.1973.tb03573.x

Woodcock, J. M., Goodwin, K. L., Sandow, J. J., Coolen, C., Perugini, M. A., Webb, A. I., et al. (2018). Role of Salt Bridges in the Dimer Interface of 14-3-3ζ in Dimer Dynamics, N-Terminal α-helical Order, and Molecular Chaperone Activity. *J. Biol. Chem.* 293, 89–99. doi:10.1074/jbc.M117.801019

Woodcock, J. M., Ma, Y., Coolen, C., Pham, D., Jones, C., Lopez, A. F., et al. (2010). Sphingosine and FTY720 Directly Bind Pro-survival 14-3-3 Proteins to Regulate Their Function. *Cell Signal.* 22, 1291–1299. doi:10.1016/j.cellsig.2010.04.004

Woodcock, J. M., Murphy, J., Stomski, F. C., Berndt, M. C., and Lopez, A. F. (2003). The Dimeric versus Monomeric Status of 14-3-3ζ Is Controlled by Phosphorylation of Ser58 at the Dimer Interface. *J. Biol. Chem.* 278, 36323–36327. doi:10.1074/jbc.M304689200

Xie, Y., Jiang, Y., and Ben-Amotz, D. (2005). Detection of Amino Acid and Peptide Phosphate Protonation Using Raman Spectroscopy. *Anal. Biochem.* 343, 223–230. doi:10.1016/j.ab.2005.05.038

Yaffe, M. B., Rittinger, K., Volinia, S., Caron, P. R., Aitken, A., Leffers, H., et al. (1997). The Structural Basis for 14-3-3:Phosphopeptide Binding Specificity. *Cell* 91, 961–971. doi:10.1016/S0092-8674(00)80487-0

Zhou, J., Shao, Z., Kerkela, R., Ichijo, H., Muslin, A. J., Pombo, C., et al. (2009). Serine 58 of 14-3-3ζ Is a Molecular Switch Regulating ASK1 and Oxidant Stress-Induced Cell Death. *Mol. Cel. Biol.* 29, 4167–4176. doi:10.1128/MCB.01067-08

Zhou, Y., Reddy, S., Murrey, H., Fei, H., and Levitan, I. B. (2003). Monomeric 14-3-3 Protein Is Sufficient to Modulate the Activity of the Drosophila Slowpoke Calcium-dependent Potassium Channel. *J. Biol. Chem.* 278, 10073–10080. doi:10.1074/jbc.M211907200

Conflict of Interest: The authors declare that the research was conducted in the absence of any commercial or financial relationships that could be construed as a potential conflict of interest.

Publisher's Note: All claims expressed in this article are solely those of the authors and do not necessarily represent those of their affiliated organizations, or those of the publisher, the editors and the reviewers. Any product that may be evaluated in this article, or claim that may be made by its manufacturer, is not guaranteed or endorsed by the publisher.

frontiers in Chemistry

ORIGINAL RESEARCH
published: 15 March 2022
doi: 10.3389/fchem.2022.833784

Photocatalytic Anaerobic Oxidation of Aromatic Alcohols Coupled With H_2 Production Over $CsPbBr_3$/GO-Pt Catalysts

Taoran Chen[1], Mengqing Li[1], Lijuan Shen[1], Maarten B. J. Roeffaers[2], Bo Weng[2], Haixia Zhu[3], Zhihui Chen[3], Dan Yu[4], Xiaoyang Pan[5], Min-Quan Yang[1]* and Qingrong Qian[1]*

[1]College of Environmental Science and Engineering, Fujian Key Laboratory of Pollution Control & Resource Reuse, Fujian Normal University, Fuzhou, China, [2]CMACS, Department of Microbial and Molecular Systems, Leuven, Belgium, [3]Hunan Key Laboratory of Nanophononics and Devices, School of Physics and Electronics, Central South University, Changsha, China, [4]State Key Lab of Photocatalysis on Energy and Environment, College of Chemistry, Fuzhou University, Fuzhou, China, [5]College of Chemical Engineering and Materials, Quanzhou Normal University, Quanzhou, China

Metal halide perovskites (MHPs) have been widely investigated for various photocatalytic applications. However, the dual-functional reaction system integrated selective organic oxidation with H_2 production over MHPs is rarely reported. Here, we demonstrate for the first time the selective oxidation of aromatic alcohols to aldehydes integrated with hydrogen (H_2) evolution over Pt-decorated $CsPbBr_3$. Especially, the functionalization of $CsPbBr_3$ with graphene oxide (GO) further improves the photoactivity of the perovskite catalyst. The optimal amount of $CsPbBr_3$/GO-Pt exhibits an H_2 evolution rate of 1,060 μmol g^{-1} h^{-1} along with high selectivity (>99%) for benzyl aldehyde generation (1,050 μmol g^{-1} h^{-1}) under visible light ($\lambda > 400$ nm), which is about five times higher than the $CsPbBr_3$-Pt sample. The enhanced activity has been ascribed to two effects induced by the introduction of GO: 1) GO displays a structure-directing role, decreasing the particle size of $CsPbBr_3$ and 2) GO and Pt act as electron reservoirs, extracting the photogenerated electrons and prohibiting the recombination of the electron–hole pairs. This study opens new avenues to utilize metal halide perovskites as dual-functional photocatalysts to perform selective organic transformations and solar fuel production.

Keywords: perovskite, CsPbBr3, graphene oxide, anaerobic oxidation of aromatic alcohols, H2 production, photocatalysis

OPEN ACCESS

Edited by:
Wee-Jun Ong,
Xiamen University, Malaysia

Reviewed by:
Hexing Li,
Shanghai Normal University, China
Nan Zhang,
Hunan University, China

****Correspondence:***
Bo Weng
bo.weng@kuleuven.be
Min-Quan Yang
yangmq@fjnu.edu.cn

Specialty section:
This article was submitted to Catalysis and Photocatalysis, a section of the journal Frontiers in Chemistry

Received: *12 December 2021*
Accepted: *11 February 2022*
Published: *15 March 2022*

Citation:
Chen T, Li M, Shen L, Roeffaers MBJ, Weng B, Zhu H, Chen Z, Yu D, Pan X, Yang M-Q and Qian Q (2022) Photocatalytic Anaerobic Oxidation of Aromatic Alcohols Coupled With H_2 Production Over $CsPbBr_3$/GO-Pt Catalysts. Front. Chem. 10:833784. doi: 10.3389/fchem.2022.833784

INTRODUCTION

The selective oxidation of alcohols to carbonyls represents one of the most important reactions in both the fine chemical industry and laboratory research (Shibuya et al., 2011; Yang and Xu, 2013; Sharma et al., 2016; Xue Yang et al., 2017; Liu et al., 2018a; Huang et al., 2018; Li et al., 2020; Shang et al., 2021); the carbonyl products are widely used intermediates and precursors for the manufacture of perfumes, pharmaceuticals, and dyes (Liu et al., 2015; Agosti et al., 2020; Xia et al., 2020; Shang et al., 2021). Generally, the oxidative dehydrogenation of alcohols is carried out in the presence of chemical oxidants such as iodine, manganese, chromium oxide, or molecular oxygen. The utilization of costly and toxic chemical agents not only results in the production of stoichiometric amounts of waste but also often generates overoxidized products (Mallat and Baiker, 2004; Lang et al., 2014;

Meng et al., 2018a; Meng et al., 2018b; Kampouri and Stylianou, 2019; Crombie et al., 2021; Shang et al., 2021). Particularly, the removed protons are consumed by the oxidant in these strategies resulting in the loss of a potentially interesting source of hydrogen gas (Han et al., 2020; Wang et al., 2021). In this respect, if the hydrogen atoms released from the alcohols during oxidation can be converted into H_2, that is, combining the dehydrogenation reaction with H_2 evolution, it would not only improve the atom economy of the reaction and the added value of the products but also provide a revolutionary technology for H_2 production. However, coupling the oxidative dehydrogenation of alcohols with reductive hydrogen production is challenging.

Within this context, the advancement of photocatalytic anaerobic oxidation technology in recent years provides a promising strategy. This approach utilizes photogenerated holes to oxidize organics while employing photoelectrons to reduce the removed protons to produce H_2, thus completing the oxidative–reductive coupled reaction (Weng et al., 2016; Han et al., 2017; Zhou et al., 2020; Peixian Li et al., 2021). Different from traditional photocatalytic aerobic oxidation, the oxygen-free condition effectively inhibits the consumption of the removed protons to produce water and avoids the formation of strong oxidation radicals (like superoxide radicals), which is favorable for improving the product selectivity. Theoretically, the anaerobic dehydrogenation coupled to H_2 evolution is initiated by the oxidation half-reaction to remove protons, which is considered to be a rate-limiting step (Liu et al., 2018b; Wang et al., 2021). As such, to obtain high catalytic efficiency, the efficient separation and migration of holes, that is, the exploration of advanced photocatalytic materials with high hole mobility and long carrier lifetime, to oxidize the organic substrates, is essential.

In recent years, the halide perovskite (ABX_3) material has been deemed as a promising new-generation photocatalyst alternative due to its remarkable optoelectronic properties such as a large extinction coefficient and an excellent visible light-harvesting ability (Zhao and Zhu, 2016; Xu et al., 2017; Akkerman et al., 2018; Huang et al., 2019; Huang et al., 2020; Wang et al., 2022). Importantly, the halide perovskite with a delocalized energy level exhibits a small hole effective mass (Yuan et al., 2015) and high hole mobility ($100\ cm^2\ V^{-1}\ s^{-1}$), which is hundreds of times higher than traditional semiconductor materials such as TiO_2 (Wehrenfennig et al., 2014; Bin Yang et al., 2017). Moreover, the perovskite also shows a long carrier lifetime of tens to hundreds of μs and diffusion length of μm levels, providing more opportunities for the diffusion and utilization of photoinduced holes and electrons (Dong et al., 2015; Bi et al., 2016). In this context, these unique features enable the metal halogen perovskite to be an appealing candidate for the organic conversion-coupled hydrogen production reaction, but the research is still rarely reported so far.

Inspired by the foregoing considerations, we herein fabricate $CsPbBr_3$/GO-Pt composites for photocatalytic coupling redox reaction. In the composite, the $CsPbBr_3$ acts as a photoactive component, while the GO plays an important role in decreasing the particle size of $CsPbBr_3$, together with Pt as electron reservoirs to extract photogenerated electrons and prohibit the recombination of electron–hole pairs. By taking selective anaerobic oxidation of aromatic alcohols as model reactions, the as-prepared $CsPbBr_3$/GO-Pt shows obvious photoactivity for the simultaneous production of aromatic aldehydes and H_2. An optimal H_2 evolution rate of 1,060 μmol g^{-1} h^{-1} along with a benzyl aldehyde production rate of 1,050 μmol g^{-1} h^{-1} is realized over the $CsPbBr_3$/1.0% GO-1%Pt composite under visible light irradiation ($\lambda > 400$ nm). Mechanism study reveals that the carbon-centered radical serves as a pivotal radical intermediate during the photoredox process.

EXPERIMENTAL SECTION

Materials

Cesium bromide (CsBr, 99.999%) and lead bromide ($PbBr_2$, 99.0%) were purchased from Macklin. N, N-dimethylformamide (DMF), toluene, graphite powder, potassium persulfate ($K_2S_2O_8$), phosphorus pentoxide (P_2O_5), concentrated sulfuric acid (H_2SO_4, 98%), concentrated nitric acid (HNO_3, 65%), hydrogen peroxide solution (H_2O_2, 30%), potassium permanganate ($KMnO_4$, 99.5%), tetrabutylammonium hexafluorophosphate ($TBAPF_6$, 98%), hydrochloric acid (HCl, 36%), ethanol, acetonitrile, ethyl acetate, acetone, isopropanol, and benzyl alcohol all were obtained from Sinopharm Chemical Reagent Co., Ltd. (Shanghai, China). All the chemicals were used as received without further purification.

Catalyst Preparation

Preparation of Graphene Oxide

GO was synthesized from natural graphite powder using a modified Hummers' method (Hummers and Offeman, 1958; Yang and Xu, 2013). The details are described in the supporting information.

Synthesis of $CsPbBr_3$/Graphene Oxide and $CsPbBr_3$

$CsPbBr_3$/GO was synthesized *via* a well-established anti-solvent precipitation method at room temperature (Huang et al., 2018). In brief, a certain amount of GO (2.5, 5, 7.5, 10 mg) was first dispersed in 10 ml of N, N-dimethylformamide (DMF) by ultrasonication. Then, 1 mmol CsBr and 1 mmol $PbBr_2$ were added to the solution. After completely dissolving CsBr and $PbBr_2$, the mixture was added dropwise into 80 ml toluene under vigorous stirring, which generated orange precipitation immediately. After that, the precipitation was centrifuged, washed with toluene three times, and then dried in a vacuum oven at 60 °C for 12 h. The blank $CsPbBr_3$ was prepared by following the same procedure without the addition of GO.

Characterizations

Scanning electron microscopy (SEM) images of the samples were characterized by using Hitachi 8100. Transmission electron microscopy (TEM) images were recorded using a 200 kV JEOL-2100f transmission electron microscope. The X-ray diffraction (XRD) patterns of the catalysts were characterized on a Bruker D8 advance X-ray diffractometer operated at 40 kV and 40 mA with Cu Kα radiation in the 2θ ranging from 10° to 80°.

UV–vis diffuse reflectance spectra (DRS) were obtained on an Agilent CARY-100 spectrophotometer using 100% $BaSO_4$ as an internal standard. X-ray photoelectron spectroscopy (XPS) was recorded on Thermo Fisher (Thermo Scientific K-Alpha+) equipped with a monochromatic Al Kα as the X-ray source. All binding energies were referenced to the C 1s peak at 284.8 eV of surface adventitious carbon. Raman spectra were recorded by using a Thermo Fisher-DXR 2xi with a laser at a wavelength of 532 nm. Photoluminescence (PL) measurements were performed on a spectrophotometer (MS3504i) with an excitation wavelength of 405 nm, and time-resolved PL (TRPL) was recorded by using a photon-counting photomultiplier (PMT) (Pico Quant, PMC-100–1).

Electron paramagnetic resonance (EPR) measurements were performed at room temperature using a Magnettech ESR5000 spectrometer. For EPR measurements, 10 mg sample powders were dispersed in a mixed solution of 0.5 ml CH_3CN containing 10 μL benzyl alcohol (BA) and 2 μL 5,5-dimethyl-1-pyrroline-N-oxide (DMPO). Then, the suspension was injected into a glass capillary, which was further placed in a sealed glass tube under argon (Ar) atmosphere. The sealed glass tube was placed in the microwave cavity of the EPR spectrometer and was irradiated with a 300-W Xe lamp (PLS-SXE 300D, Beijing Perfectlight Technology Co., Ltd.) equipped with a 400-nm cutoff filter during the EPR measurement at room temperature.

Electrochemical Measurements

All the electrochemical measurements were recorded in a conventional three electrodes cell using a CHI 760E instrument. A platinum wire was used as the counter electrode (CE), and an Ag/AgCl electrode was used as the reference electrode (RE). The electrolyte was ethyl acetate solution containing 0.1 M tetrabutylammonium hexafluorophosphate ($TBAPF_6$). The working electrodes were prepared using $CsPbBr_3$ and CPB/1.0% GO samples. Typically, the fluorine-doped tin oxide (FTO) substrate was first cleaned by ultrasonication in ethanol and then rinsed with deionized water and acetone for half an hour. Then, 10 mg of the catalyst was dispersed in 1 ml of isopropanol to get slurry. After that, 50 μL of the slurry was spread on the conductive surface of the FTO glass and then dried at 60°C for 2 h to improve adhesion. The exposed area of the working electrode was 1 cm^2. A 300-W Xe lamp system (PLS-SXE 300D, Beijing Perfectlight Technology Co., Ltd.) equipped with a 400-nm cutoff filter was used as the irradiation source. The electrochemical impedance spectroscopy (EIS) measurements were carried out in a frequency range from 1 Hz to 1 MHz. The photocurrent measurement was performed under visible light irradiation ($\lambda >$ 400 nm) using a 300-W Xenon lamp source (PLS-SXE 300D, Beijing Perfectlight Technology Co., Ltd.).

Photocatalytic Activity

The photocatalytic H_2 evolution integrated with aromatic alcohol oxidation was tested in a quartz reactor. Typically, 10 mg of photocatalyst, 0.2 mmol aromatic alcohol, and 1.0% Pt (H_2PtCl_6 as a precursor) were added into a quartz reactor containing 3 ml CH_3CN (purge with Ar gas for 15 min). Then, the reactor was irradiated by visible light ($\lambda >$ 400 nm) using a 300 W Xe lamp (PLS-SXE 300D, Beijing Perfect light Technology Co., Ltd.) under continuous stirring. After the reaction, the gas product was analyzed by a gas chromatograph (GC 9790pLus, Fu Li, China, TCD detector, Ar as the carrier gas). Liquid products were analyzed by gas chromatography (Shimadzu GC-2030, FID detector) after centrifuging the suspension at 10,000 rpm to remove the catalyst. The test conditions for the long-time experiment were similar to the aforementioned description, except that the reaction time was extended to 20 h.

The conversion efficiency of aromatic alcohols (A) and selectivity of aldehydes (AD) production were calculated using the following equations:

$$\text{Conversion}\,(\%) = 100 \times [\,(C_0 - C_A)/C_0\,]\,\%,$$
$$\text{Selectivity}\,(\%) = 100 \times [C_{AD}/\,(C_0 - C_A)]\%$$

where C_0 is the initial concentration of aromatic alcohols, and C_A and C_{AD} are the concentrations of aromatic alcohols and aldehydes measured after the photocatalytic reaction for a specific time, respectively.

RESULTS AND DISCUSSION

The fabrication of the $CsPbBr_3$/GO (denoted as CPB/GO) composite is realized *via* a simple anti-solvent method by adding GO into the precursor solution of $CsPbBr_3$ (for more details, please refer to the experimental section), as illustrated in **Scheme 1**. The crystal structures of the $CsPbBr_3$ and CPB/GO composites were analyzed by X-ray diffraction (XRD). As displayed in **Supplementary Figure S1A** (Supporting Information), for all the as-obtained samples, the main XRD peaks are indexed to the monoclinic $CsPbBr_3$ (JCPDS card NO. 00–018–0,364) (Chen et al., 2021). No GO diffraction peaks were observed in the XRD patterns of the CPB/GO samples because of the low weight content (≤1.5%). Raman analysis in **Supplementary Figure S1B** shows that the as-prepared GO and CPB/GO composite both display two peaks at 1,599 and 1,360 cm^{-1}, which belong to the typical D and G bands of GO, respectively (Huang et al., 2021). Moreover, an obvious peak at 308 cm^{-1} assigned to the $CsPbBr_3$ was detected in $CsPbBr_3$ and CPB/GO (Wang et al., 2020), which verifies the formation of the hybrid composite. **Supplementary Figure S1C** shows the UV–vis diffuse reflectance spectra (DRS) of blank $CsPbBr_3$ and CPB/GO composites. Owing to the addition of GO, the light absorption of CPB/GO composites in the region of visible light (550–800 nm) gradually enhances with the increase in the weight ratios of GO, and the colors of the samples change from yellow to brown (**Supplementary Figure S2**), which can be attributed to the significant background absorption of GO (Xu et al., 2011). The absorption edges for $CsPbBr_3$ and CPB/GO are around 548 nm, which correlates with the intrinsic absorption of the material (**Supplementary Figure S3**).

Noble metal Pt nanoparticles are further introduced into the CPB/GO composite for enhancing the catalytic performance. The valence states of different elements have been investigated by

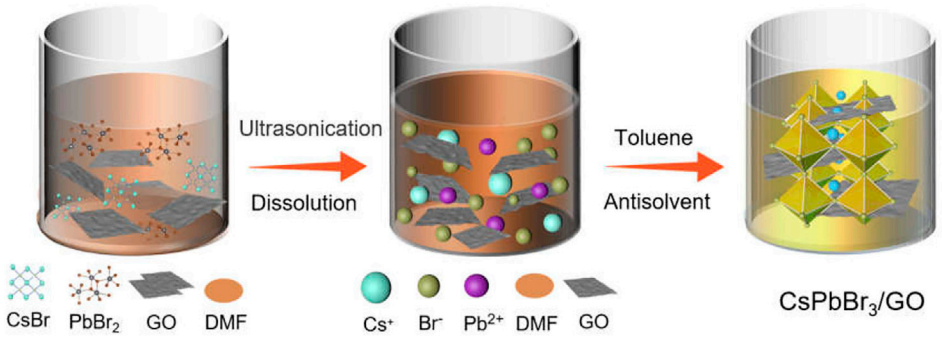

SCHEME 1 | Schematic diagram for the fabrication of $CsPbBr_3$/GO composites.

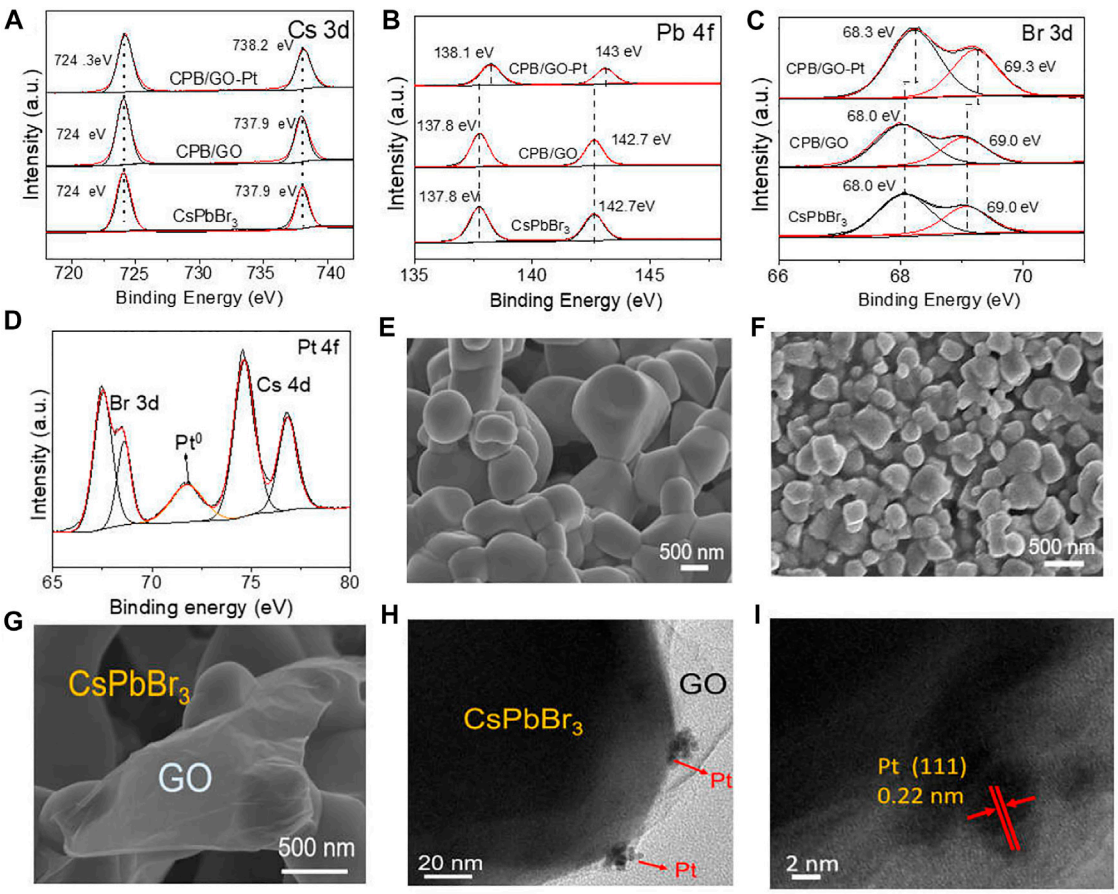

FIGURE 1 | (A) Cs 3d, **(B)** Pb 4f, **(C)** Br 3d, and **(D)** Pt 4f XPS spectra of $CsPbBr_3$, CPB/GO, and CPB/GO-Pt composites; SEM images of **(E)** blank $CsPbBr_3$ and **(F,G)** the CPB/GO composite; **(H)** TEM and **(I)** HRTEM images of the CPB/GO-Pt composite.

X-ray photoelectron spectroscopy (XPS). High-resolution C 1s peaks of CPB/GO and CPB/GO-Pt samples in **Supplementary Figure S4** show a C–O bond at 286.6 eV and C=O bond at 287.7 eV, which can be ascribed to the introduction of GO. **Figure 1A** shows the Cs 3d spectra of blank $CsPbBr_3$, CPB/GO, and CPB/GO-Pt samples. The double peaks of Cs 3d at 724.1 and 738.1 eV are ascribed to Cs^+ in $CsPbBr_3$ (Jiang et al., 2020; Liang Li et al., 2021), and no obvious change was observed for blank $CsPbBr_3$ and CPB/GO, while a positive shift was detected for the CPB/GO-Pt sample. This is attributed to the electron transfer from $CsPbBr_3$ to Pt, thus reducing the electron density and altering the coordination environment of Cs. A similar observation can

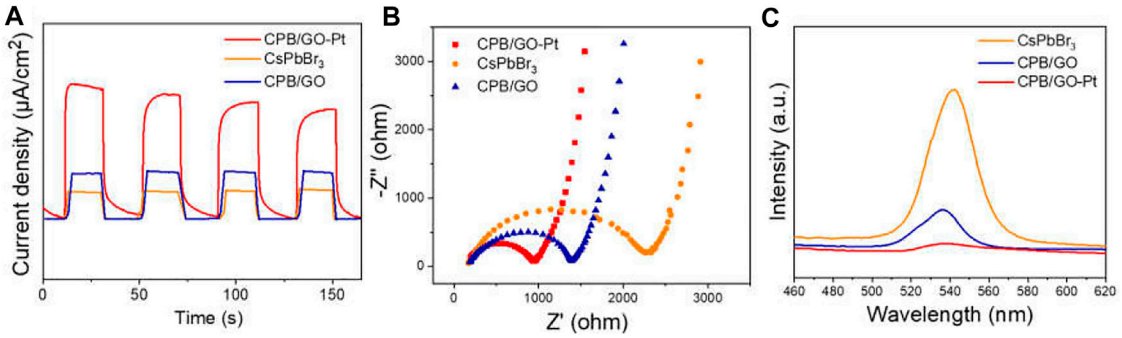

FIGURE 2 | (A) Chopped photocurrent responses, **(B)** Nyquist plots, **(C)** PL spectra of $CsPbBr_3$, CPB/GO, and CPB/GO-Pt composites.

also be made for both the Pb 4f and Br 3d spectra over these samples (**Figures 1B, C**). The Pt 4f spectrum in **Figure 1D** exhibited a peak located at 71.6 eV assigned to the Pt^0 (Qadir et al., 2012), while another peak is the superposition with the Cs 4d peaks, which suggests that Pt is present in metallic state (Wang et al., 2017). The $CsPbBr_3$/1.0% GO-1%Pt was characterized by inductively coupled plasma mass spectrometry (ICP-MS), and the detected mass content of Pt is ca. 0.95% (**Supplementary Table S1**), closely matching the targeted amount (i.e., 1%).

Scanning electron microscopy (SEM) is used to study the morphologic details of blank $CsPbBr_3$, CPB/GO, and CPB/GO-Pt samples (**Figures 1E–G** and **Supplementary Figure S5**). The average particle size of the CPB/GO composite is much smaller (0.3–0.5 μm) than that of the blank $CsPbBr_3$ sample (0.8–1.2 μm) (**Supplementary Figure S6A**). This can be attributed to the fact that GO with abundant functional groups promotes the nucleation process of $CsPbBr_3$, thus producing more seeds and hence leading to the smaller size of final perovskite. The structure-directing role of GO to decrease the size of a semiconductor has been widely reported over graphene-based semiconductor composites (Yang et al., 2014). The enlarged SEM image of the CPB/GO composite in **Figure 1G** shows an intimate interfacial contact between the GO sheets and the $CsPbBr_3$ particles. The CPB/GO-Pt sample features the same morphology as CPB/GO (**Supplementary Figure S5**), proving the maintenance of the structure during the Pt modification. This has been further verified by TEM analysis. As shown in **Supplementary Figures S6B, C**, the TEM image of the CPB/GO composite discloses the fact that the $CsPbBr_3$ particles have been well linked with or wrapped by GO nanosheets, and Cs, Pb, and Br are homogeneously distributed on the C element (**Supplementary Figure S6D**). Moreover, **Figures 1H, I** clearly show that the Pt nanoparticles are loaded onto the surface of $CsPbBr_3$ with a lattice fringe of 0.22 nm corresponding to Pt (111), and the size of Pt was calculated to be ca. 3.1 nm (**Supplementary Figure S7**).

To further study the influence of the introduction of GO and Pt on charge separation and migration, a series of photoelectrochemical characterizations over blank $CsPbBr_3$, CPB/GO, and CPB/GO-Pt composites have been carried out. As shown in **Figure 2A**, the photocurrent response tests of these samples reveal that the CPB/GO-Pt hybrid composite (taking CPB/1.0% GO-1%Pt with optimal photoactivity as an example) displays higher current density than blank $CsPbBr_3$ and CPB/GO samples, indicating a more efficient separation of the photogenerated carrier (Liao et al., 2021). **Figure 2B** presents the electrochemical impedance spectroscopy (EIS) study of these samples, which is employed to study the charge transfer resistance of the samples. The hybrid CPB/GO-Pt shows the smallest arc diameter among these samples, demonstrating a more efficient charge transfer between the electrode and electrolyte solution over CPB/GO-Pt as compared with $CsPbBr_3$ and CPB/GO samples (Lu et al., 2021). This result is consistent with the observation in photocurrent responses tests.

Moreover, photoluminescence (PL) has been performed to investigate electron–hole recombination. As shown in **Figure 2C**, blank $CsPbBr_3$ shows a strong emission peak at 546 nm in the PL spectrum upon excitation with 364-nm electromagnetic waves. For CPB/GO and CPB/GO-Pt composites, the PL intensity is significantly quenched since the radiative recombination of photogenerated electron–hole pairs is diminished due to the electron-accepting nature of GO and Pt (Min-Quan Yang et al., 2017; Chen et al., 2021). This is also supported by the time-resolved photoluminescence (TRPL) decay analysis, as displayed in **Supplementary Figure S8** and **Supplementary Table S2**. The TRPL curve of CPB/GO exhibits a faster decay than that of blank $CsPbBr_3$, which can be attributed to the efficient transfer of photogenerated electrons from $CsPbBr_3$ to GO sheets at a suitable energy level (Xu et al., 2017; Su et al., 2020). The collective photoelectrochemical analyses consolidate that the integration of GO and Pt with $CsPbBr_3$ leads to a more efficient electron–hole separation and rapid charge transfer in the composite, which is critical for boosting the photoactivity (Yang et al., 2019).

Next, the photocatalytic performances of the samples have been evaluated for the anaerobic photocatalytic oxidation of aromatic alcohols coupled with H_2 production under visible light irradiation ($\lambda > 400$ nm). Both H_2 and BAD are not detected in the dark or without the catalyst, indicating that the reaction is driven by a photocatalytic process (**Supplementary Figure S9**). The samples of GO and GO-Pt mainly serve as cocatalysts since no products are detected

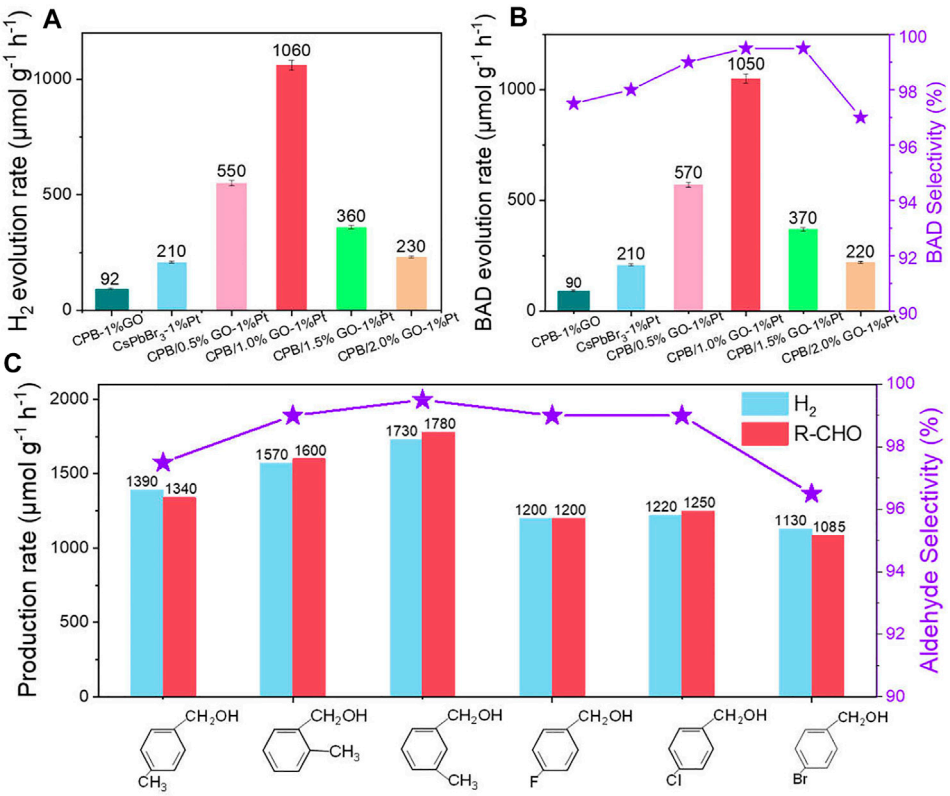

FIGURE 3 | (A) Photocatalytic activity of H_2 evolution, **(B)** BAD evolution and selectivity of $CsPbBr_3$-1%Pt and CPB/x% GO-1%Pt with different weight ratios of GO. **(C)** The photocatalytic activities for H_2 and aldehyde generation of different aromatic alcohols using CPB/1.0% GO-1%Pt as a photocatalyst. Reaction conditions: 10 mg catalyst, 1.0% Pt, 0.2 mmol BA, 3 ml of CH_3CN, Ar atmosphere, and visible light (λ > 400 nm).

during the photocatalytic reaction process. Moreover, the blank $CsPbBr_3$ cannot produce any products due to the limited reaction kinetics, while the construction of the CPB/1%GO composite leads to low photoactivity toward H_2 (90 μmol g^{-1} h^{-1}) and BAD (94 μmol g^{-1} h^{-1}) generation. The introduction of Pt into $CsPbBr_3$ improves the catalytic performance, and the production of BAD and H_2 are obtained in almost stoichiometric amounts over $CsPbBr_3$-1%Pt, indicating a high selectivity (>99%) of the reaction.

After integration with both GO and Pt, the BAD and H_2 evolution efficiencies are further enhanced compared with those of $CsPbBr_3$-1%Pt and CPB/1%GO. In detail, the optimal photoactivity is obtained on the sample of the CPB/1% GO-1%Pt composite (H_2 and BAD evolution rates of 1,060 and 1,050 μmol g^{-1} h^{-1} respectively), which is about fivefold as high as that of the $CsPbBr_3$-1%Pt sample (**Figures 3A,B**). This is well in accordance with previous reports stating that loading a suitable amount of GO, which acts as an electron acceptor, with semiconductor photocatalysts can notably improve photoactivity (Chen et al., 2021). Increasing the GO content further to 1.5% resulted in decreased photoactivity. This may be ascribed to the shielding effect of the GO (Yang et al., 2013). On the one hand, the active sites on the surface of $CsPbBr_3$ may be blocked due to the addition of high amounts of GO. On the other hand, GO with black color could also absorb the light, which is competed with $CsPbBr_3$ and inhibits light passing through the depth of the reaction solution.

Based on the high photocatalytic performance of the CPB/1.0% GO-1%Pt, the photocatalytic anaerobic dehydrogenation of a series of aromatic alcohols with different substituents has been tested. As shown in **Figure 3C**, moderate H_2 generation and aldehyde production are obtained for 4-chlorobenzyl alcohol, 4-bromobenzyl alcohol, 4-fluorobenzyl alcohol, 4-methylbenzyl alcohol, 3-methylbenzyl alcohol, and 2-methylbenzyl alcohol. Particularly, for all the substrates bearing electron-donating or electron-withdrawing functional groups, the reactions show high selectivity for aldehyde production (>98%). There is no other byproduct generated during the photocatalytic period, verifying good applicability of the CPB/GO-Pt as a photocatalyst toward solar light–driven integrated organic synthesis and H_2 evolution.

To assess the stability of the CPB/GO-Pt composite, a long-term photoactivity test has been carried out. As depicted in **Supplementary Figure S10**, under continuous irradiation for 20 h, the CPB/1.0% GO-1%Pt photocatalyst shows no obvious deactivation with consistent H_2 and BAD production. The composite material manifests excellent stability of the binary composite. In addition, the morphology and crystal structure of the used CPB/1.0% GO-1% Pt have been investigated by SEM (**Supplementary Figures S11 and S12**) and XRD (**Supplementary Figure S13**), and no obvious changes

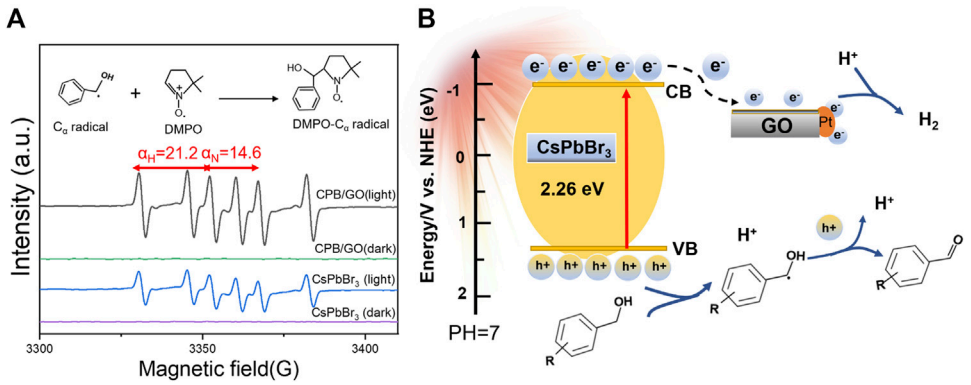

FIGURE 4 | (A) *In situ* EPR spectra of $CsPbBr_3$ and CPB/GO composites tested in Ar-saturated CH_3CN solution in the presence of DMPO. **(B)** Schematic illustration of photocatalytic H_2 production integrated with aromatic aldehyde synthesis.

between the used and fresh composites were detected. All these aforementioned results are strong evidence for the good stability of the CPB/GO-Pt composite under the used experimental conditions, which is attributed to the mild polarity of acetonitrile and $CsPbBr_3$ substrates that are demonstrated to be stable in this solution (Ou et al., 2018; Zhang et al., 2021).

To further study the radical intermediates involved in the catalytic system, electron paramagnetic resonance (EPR) analysis is performed under visible light using 5,5-dimethyl-1-pyrroline N-oxide (DMPO) as a trapping agent. As presented in **Figure 4A**, there were no free radical signals in the dark. Under light illumination, six characteristic signal peaks were observed for both $CsPbBr_3$ and the CPB/1.0% GO composite, which belongs to the carbon-centered radical adduct (α_H = 21.2 and α_N = 14.6, corresponding to the hydrogen and nitrogen hyperfine splitting for the nitroxide nitrogen) (Qi et al., 2020). The signal intensity of DMPO-CH(OH)Ph over the CPB/GO composite is stronger than that of blank $CsPbBr_3$, indicating that a larger amount of such carbon-centered radicals was generated in the CPB/GO-catalytic system. This should be ascribed to the enhanced photogenerated charge–transferring ability of CPB/GO in contrast to blank $CsPbBr_3$, which increases their likelihood of interaction with the alcohol substrates. The chemical reaction equations for photocatalytic BA oxidation coupled with H_2 generation over $CsPbBr_3$/GO-Pt are presented in **Supplementary Figure S14**.

On the basis of the aforementioned analyses, a tentative photocatalytic mechanism is proposed for the coupled reaction system toward H_2 evolution integrated with the conversion of aromatic alcohols to aromatic aldehydes over the CPB/GO-Pt composite. As displayed in **Figure 4B**, under the illumination of visible light, $CsPbBr_3$ in the CPB/GO-Pt composite is excited to generate electrons and holes. Owing to the matched energy level and intimate interfacial contact between $CsPbBr_3$ and GO, the electrons tend to migrate from $CsPbBr_3$ to GO and Pt, leaving photoinduced holes in the valence band (VB) of $CsPbBr_3$. Meanwhile, the holes will attack the C–H bond of absorbed BA to generate CH(OH)Ph radicals and protons (Wu et al., 2018). Then, the CH(OH)Ph radicals can be further oxidized to generate BAD and protons. The abstracted protons from BA are reduced to produce H_2 by the electrons collected on the surfaces of GO and Pt in the CPB/GO-Pt composite, thus completing the coupled redox reaction.

CONCLUSION

In summary, we have realized efficient photocatalytic dehydrogenation of aromatic alcohols for simultaneous aldehyde production and H_2 evolution over $CsPbBr_3$/GO-Pt composite under visible light (λ > 400 nm). The results show that optimal amounts of $CsPbBr_3$/GO-Pt composite can obtain nearly five times the yield of products (BAD and H_2) as high as that of $CsPbBr_3$-Pt. The enhanced photoactivity of CPB/GO-Pt composite is ascribed to the critical roles of GO in tuning the size of $CsPbBr_3$ and together with Pt to extract the photogenerated electrons to boost the migration of photogenerated charge carriers. Furthermore, the carbon-centered radicals have been proven as the pivotal radical intermediate during the photoredox reaction by *in situ* electron paramagnetic resonance (EPR). This work is anticipated to open an avenue for the utilization of halide perovskites as promising candidates in cooperative organic transformation coupling with solar fuel production by the full utilization of photogenerated electrons and holes.

DATA AVAILABILITY STATEMENT

The raw data supporting the conclusions of this article will be made available by the authors, without undue reservation.

AUTHOR CONTRIBUTIONS

TC proposed and performed the experiments. ML and LS performed the TEM measurement. ZC and HZ measured the PL and TRPL images. MR, DY, XP, and QQ assisted in designing

experiments and manuscript revision. BW and M-QY proposed the research direction and supervised the project. All authors participated in the discussion and reviewed the manuscript before submission.

FUNDING

This work is financially supported by the National Natural Science Foundation of China (21905049, 21902132, 22178057), the Award Program for the Minjiang Scholar Professorship and the Natural Science Foundation of the Fujian Province (2020J01201), the Research Foundation–Flanders (FWO Grant Nos. G.0B39.15, G.0B49.15, G098319N, 1280021N, 12Y7221N, 12Y6418N, VS052320N, and ZW15_09-GOH6316N), the KU Leuven Research Fund (C14/19/079, iBOF-21–085 PERSIST, and C3/19/046), the Flemish government through long term structural funding Methusalem (CASAS2, Meth/15/04), and the European Union's Horizon 2020 research and innovation program under the Marie Skłodowska-Curie grant agreement No. 891276.

SUPPLEMENTARY MATERIAL

The Supplementary Material for this article can be found online at: https://www.frontiersin.org/articles/10.3389/fchem.2022.833784/full#supplementary-material

REFERENCES

Agosti, A., Nakibli, Y., Amirav, L., and Bergamini, G. (2020). Photosynthetic H_2 Generation and Organic Transformations with CdSe@CdS-Pt Nanorods for Highly Efficient Solar-To-Chemical Energy Conversion. *Nano Energy* 70, 104510. doi:10.1016/j.nanoen.2020.104510

Akkerman, Q. A., Rainò, G., Kovalenko, M. V., and Manna, L. (2018). Genesis, Challenges and Opportunities for Colloidal lead Halide Perovskite Nanocrystals. *Nat. Mater* 17 (5), 394–405. doi:10.1038/s41563-018-0018-4

Bi, Y., Hutter, E. M., Fang, Y., Dong, Q., Huang, J., and Savenije, T. J. (2016). Charge Carrier Lifetimes Exceeding 15 μs in Methylammonium Lead Iodide Single Crystals. *J. Phys. Chem. Lett.* 7 (5), 923–928. doi:10.1021/acs.jpclett.6b00269

Chen, Y.-H., Ye, J.-K., Chang, Y.-J., Liu, T.-W., Chuang, Y.-H., Liu, W.-R., et al. (2021). Mechanisms behind Photocatalytic CO_2 Reduction by $CsPbBr_3$ Perovskite-Graphene-Based Nanoheterostructures. *Appl. Catal. B: Environ.* 284, 119751. doi:10.1016/j.apcatb.2020.119751

Crombie, C. M., Lewis, R. J., Taylor, R. L., Morgan, D. J., Davies, T. E., Folli, A., et al. (2021). Enhanced Selective Oxidation of Benzyl Alcohol via *In Situ* H_2O_2 Production over Supported Pd-Based Catalysts. *ACS Catal.* 11 (5), 2701–2714. doi:10.1021/acscatal.0c04586

Dong, Q., Fang, Y., Shao, Y., Mulligan, P., Qiu, J., Cao, L., et al. (2015). Electron-hole Diffusion Lengths > 175 μm in Solution-Grown $CH_3NH_3PbI_3$ Single Crystals. *Science* 347 (6225), 967–970. doi:10.1126/science.aaa5760

Han, G., Jin, Y.-H., Burgess, R. A., Dickenson, N. E., Cao, X.-M., and Sun, Y. (2017). Visible-Light-Driven Valorization of Biomass Intermediates Integrated with H_2 Production Catalyzed by Ultrathin Ni/CdS Nanosheets. *J. Am. Chem. Soc.* 139 (44), 15584–15587. doi:10.1021/jacs.7b08657

Han, G., Liu, X., Cao, Z., and Sun, Y. (2020). Photocatalytic Pinacol C-C Coupling and Jet Fuel Precursor Production on $ZnIn_2S_4$ Nanosheets. *ACS Catal.* 10 (16), 9346–9355. doi:10.1021/acscatal.0c01715

Huang, H., Yuan, H., Janssen, K. P. F., Solís-Fernández, G., Wang, Y., Tan, C. Y. X., et al. (2018). Efficient and Selective Photocatalytic Oxidation of Benzylic Alcohols with Hybrid Organic-Inorganic Perovskite Materials. *ACS Energ. Lett.* 3 (4), 755–759. doi:10.1021/acsenergylett.8b00131

Huang, H., Yuan, H., Zhao, J., Solís-Fernández, G., Zhou, C., Seo, J. W., et al. (2019). C(sp^3)-H Bond Activation by Perovskite Solar Photocatalyst Cell. *ACS Energ. Lett.* 4 (1), 203–208. doi:10.1021/acsenergylett.8b01698

Huang, H., Pradhan, B., Hofkens, J., Roeffaers, M. B. J., and Steele, J. A. (2020). Solar-Driven Metal Halide Perovskite Photocatalysis: Design, Stability, and Performance. *ACS Energ. Lett.* 5 (4), 1107–1123. doi:10.1021/acsenergylett.0c00058

Huang, Z., Wang, J., Lu, S., Xue, H., Chen, Q., Yang, M.-Q., et al. (2021). Insight into the Real Efficacy of Graphene for Enhancing Photocatalytic Efficiency: A Case Study on CVD Graphene-TiO_2 Composites. *ACS Appl. Energ. Mater.* 4 (9), 8755–8764. doi:10.1021/acsaem.1c00731

Hummers, W. S., and Offeman, R. E. (1958). Preparation of Graphitic Oxide. *J. Am. Chem. Soc.* 80 (6), 1339. doi:10.1021/ja01539a017

Jiang, Y., Chen, H. Y., Li, J. Y., Liao, J. F., Zhang, H. H., Wang, X. D., et al. (2020). Z-Scheme 2D/2D Heterojunction of $CsPbBr_3/Bi_2WO_6$ for Improved Photocatalytic CO_2 Reduction. *Adv. Funct. Mater.* 30 (50), 2004293. doi:10.1002/adfm.202004293

Kampouri, S., and Stylianou, K. C. (2019). Dual-Functional Photocatalysis for Simultaneous Hydrogen Production and Oxidation of Organic Substances. *ACS Catal.* 9 (5), 4247–4270. doi:10.1021/acscatal.9b00332

Lang, X., Ma, W., Chen, C., Ji, H., and Zhao, J. (2014). Selective Aerobic Oxidation Mediated by TiO_2 Photocatalysis. *Acc. Chem. Res.* 47 (2), 355–363. doi:10.1021/ar4001108

Li, J., Li, M., Sun, H., Ao, Z., Wang, S., and Liu, S. (2020). Understanding of the Oxidation Behavior of Benzyl Alcohol by Peroxymonosulfate via Carbon Nanotubes Activation. *ACS Catal.* 10 (6), 3516–3525. doi:10.1021/acscatal.9b05273

Li, L., Zhang, Z., Ding, C., and Xu, J. (2021). Boosting Charge Separation and Photocatalytic CO_2 Reduction of $CsPbBr_3$ Perovskite Quantum Dots by Hybridizing with P3HT. *Chem. Eng. J.* 419, 129543. doi:10.1016/j.cej.2021.129543

Li, P., Yan, X., Gao, S., and Cao, R. (2021). Boosting Photocatalytic Hydrogen Production Coupled with Benzyl Alcohol Oxidation over CdS/metal-Organic Framework Composites. *Chem. Eng. J.* 421, 129870. doi:10.1016/j.cej.2021.129870

Liao, W., Chen, W., Lu, S., Zhu, S., Xia, Y., Qi, L., et al. (2021). Alkaline $Co(OH)_2$-Decorated 2D Monolayer Titanic Acid Nanosheets for Enhanced Photocatalytic Syngas Production from CO_2. *ACS Appl. Mater. Inter.* 13 (32), 38239–38247. doi:10.1021/acsami.1c08251

Liu, Y., Zhang, P., Tian, B., and Zhang, J. (2015). Core-Shell Structural CdS@SnO_2 Nanorods with Excellent Visible-Light Photocatalytic Activity for the Selective Oxidation of Benzyl Alcohol to Benzaldehyde. *ACS Appl. Mater. Inter.* 7 (25), 13849–13858. doi:10.1021/acsami.5b04128

Liu, H., Xu, C., Li, D., and Jiang, H.-L. (2018). Photocatalytic Hydrogen Production Coupled with Selective Benzylamine Oxidation over MOF Composites. *Angew. Chem. Int. Ed.* 57 (19), 5379–5383. doi:10.1002/anie.201800320

Liu, H., Xu, C., Li, D., and Jiang, H.-L. (2018). Photocatalytic Hydrogen Production Coupled with Selective Benzylamine Oxidation over MOF Composites. *Angew. Chem.* 130 (19), 5477–5481. doi:10.1002/ange.201800320

Lu, S., Weng, B., Chen, A., Li, X., Huang, H., Sun, X., et al. (2021). Facet Engineering of Pd Nanocrystals for Enhancing Photocatalytic Hydrogenation: Modulation of the Schottky Barrier Height and Enrichment of Surface Reactants. *ACS Appl. Mater. Inter.* 13 (11), 13044–13054. doi:10.1021/acsami.0c19260

Mallat, T., and Baiker, A. (2004). Oxidation of Alcohols with Molecular Oxygen on Solid Catalysts. *Chem. Rev.* 104 (6), 3037–3058. doi:10.1021/cr0200116

Meng, S., Ye, X., Zhang, J., Fu, X., and Chen, S. (2018). Effective Use of Photogenerated Electrons and Holes in a System: Photocatalytic Selective Oxidation of Aromatic Alcohols to Aldehydes and Hydrogen Production. *J. Catal.* 367, 159–170. doi:10.1016/j.jcat.2018.09.003

Meng, S., Ning, X., Chang, S., Fu, X., Ye, X., and Chen, S. (2018). Simultaneous Dehydrogenation and Hydrogenolysis of Aromatic Alcohols in One Reaction

System via Visible-Light-Driven Heterogeneous Photocatalysis. *J. Catal.* 357, 247–256. doi:10.1016/j.jcat.2017.11.015

Ou, M., Tu, W., Yin, S., Xing, W., Wu, S., Wang, H., et al. (2018). Amino-Assisted Anchoring of $CsPbBr_3$ Perovskite Quantum Dots on Porous g-C_3N_4 for Enhanced Photocatalytic CO_2 Reduction. *Angew. Chem. Int. Ed.* 57 (41), 13570–13574. doi:10.1002/anie.201808930

Qadir, K., Kim, S. H., Kim, S. M., Ha, H., and Park, J. Y. (2012). Support Effect of Arc Plasma Deposited Pt Nanoparticles/TiO_2 Substrate on Catalytic Activity of CO Oxidation. *J. Phys. Chem. C* 116 (45), 24054–24059. doi:10.1021/jp306461v

Qi, M.-Y., Li, Y.-H., Anpo, M., Tang, Z.-R., and Xu, Y.-J. (2020). Efficient Photoredox-Mediated C-C Coupling Organic Synthesis and Hydrogen Production over Engineered Semiconductor Quantum Dots. *ACS Catal.* 10 (23), 14327–14335. doi:10.1021/acscatal.0c04237

Shang, W., Li, Y., Huang, H., Lai, F., Roeffaers, M. B. J., and Weng, B. (2021). Synergistic Redox Reaction for Value-Added Organic Transformation via Dual-Functional Photocatalytic Systems. *ACS Catal.* 11 (8), 4613–4632. doi:10.1021/acscatal.0c04815

Sharma, R. K., Yadav, M., Monga, Y., Gaur, R., Adholeya, A., Zboril, R., et al. (2016). Silica-Based Magnetic Manganese Nanocatalyst - Applications in the Oxidation of Organic Halides and Alcohols. *ACS Sustain. Chem. Eng.* 4 (3), 1123–1130. doi:10.1021/acssuschemeng.5b01183

Shibuya, M., Osada, Y., Sasano, Y., Tomizawa, M., and Iwabuchi, Y. (2011). Highly Efficient, Organocatalytic Aerobic Alcohol Oxidation. *J. Am. Chem. Soc.* 133 (17), 6497–6500. doi:10.1021/ja110940c

Su, K., Dong, G.-X., Zhang, W., Liu, Z.-L., Zhang, M., and Lu, T.-B. (2020). *In Situ* Coating $CsPbBr_3$ Nanocrystals with Graphdiyne to Boost the Activity and Stability of Photocatalytic CO_2 Reduction. *ACS Appl. Mater. Inter.* 12 (45), 50464–50471. doi:10.1021/acsami.0c14826

Wang, W., Wang, Z., Wang, J., Zhong, C.-J., and Liu, C.-J. (2017). Highly Active and Stable Pt-Pd Alloy Catalysts Synthesized by Room-Temperature Electron Reduction for Oxygen Reduction Reaction. *Adv. Sci.* 4 (4), 1600486. doi:10.1002/advs.201600486

Wang, X., He, J., Li, J., Lu, G., Dong, F., Majima, T., et al. (2020). Immobilizing Perovskite $CsPbBr_3$ Nanocrystals on Black Phosphorus Nanosheets for Boosting Charge Separation and Photocatalytic CO_2 Reduction. *Appl. Catal. B: Environ.* 277, 119230. doi:10.1016/j.apcatb.2020.119230

Wang, H., Hu, P., Zhou, J., Roeffaers, M. B. J., Weng, B., Wang, Y., et al. (2021). Ultrathin 2D/2D Ti_3C_2Tx/semiconductor Dual-Functional Photocatalysts for Simultaneous Imine Production and H_2 Evolution. *J. Mater. Chem. A.* 9 (35), 19984–19993. doi:10.1039/d1ta03573h

Wang, C., Huang, H., Weng, B., Verhaeghe, D., Keshavarz, M., Jin, H., et al. (2022). Planar Heterojunction Boosts Solar-Driven Photocatalytic Performance and Stability of Halide Perovskite Solar Photocatalyst Cell. *Appl. Catal. B: Environ.* 301, 120760. doi:10.1016/j.apcatb.2021.120760

Wehrenfennig, C., Eperon, G. E., Johnston, M. B., Snaith, H. J., and Herz, L. M. (2014). High Charge Carrier Mobilities and Lifetimes in Organolead Trihalide Perovskites. *Adv. Mater.* 26 (10), 1584–1589. doi:10.1002/adma.201305172

Weng, B., Quan, Q., and Xu, Y.-J. (2016). Decorating Geometry- and Size-Controlled Sub-20 Nm Pd Nanocubes onto 2D TiO_2 Nanosheets for Simultaneous H_2 Evolution and 1,1-diethoxyethane Production. *J. Mater. Chem. A.* 4 (47), 18366–18377. doi:10.1039/c6ta07853b

Wu, Y., Ye, X., Zhang, S., Meng, S., Fu, X., Wang, X., et al. (2018). Photocatalytic Synthesis of Schiff Base Compounds in the Coupled System of Aromatic Alcohols and Nitrobenzene Using $Cd_XZn_{1-X}S$ Photocatalysts. *J. Catal.* 359, 151–160. doi:10.1016/j.jcat.2017.12.025

Xia, B., Zhang, Y., Shi, B., Ran, J., Davey, K., and Qiao, S. Z. (2020). Photocatalysts for Hydrogen Evolution Coupled with Production of Value-Added Chemicals. *Small Methods* 4 (7), 2000063. doi:10.1002/smtd.202000063

Xu, T., Zhang, L., Cheng, H., and Zhu, Y. (2011). Significantly Enhanced Photocatalytic Performance of ZnO via Graphene Hybridization and the Mechanism Study. *Appl. Catal. B* 101 (3), 382–387. doi:10.1016/j.apcatb.2010.10.007

Xu, Y.-F., Yang, M.-Z., Chen, B.-X., Wang, X.-D., Chen, H.-Y., Kuang, D.-B., et al. (2017). A $CsPbBr_3$ Perovskite Quantum Dot/Graphene Oxide Composite for Photocatalytic CO_2 Reduction. *J. Am. Chem. Soc.* 139 (16), 5660–5663. doi:10.1021/jacs.7b00489

Yang, M.-Q., Dan, J., Pennycook, S. J., Lu, X., Zhu, H., Xu, Q.-H., et al. (2017). Ultrathin Nickel boron Oxide Nanosheets Assembled Vertically on Graphene: a New Hybrid 2D Material for Enhanced Photo/electro-Catalysis. *Mater. Horiz.* 4 (5), 885–894. doi:10.1039/c7mh00314e

Yang, B., Zhang, F., Chen, J., Yang, S., Xia, X., Pullerits, T., et al. (2017). Ultrasensitive and Fast All-Inorganic Perovskite-Based Photodetector via Fast Carrier Diffusion. *Adv. Mater.* 29 (40), 1703758. doi:10.1002/adma.201703758

Yang, X., Zhao, H., Feng, J., Chen, Y., Gao, S., and Cao, R. (2017). Visible-light-driven Selective Oxidation of Alcohols Using a Dye-Sensitized TiO_2-Polyoxometalate Catalyst. *J. Catal.* 351, 59–66. doi:10.1016/j.jcat.2017.03.017

Yang, M.-Q., and Xu, Y.-J. (2013). Selective Photoredox Using Graphene-Based Composite Photocatalysts. *Phys. Chem. Chem. Phys.* 15 (44), 19102–19118. doi:10.1039/c3cp53325e

Yang, M.-Q., Zhang, Y., Zhang, N., Tang, Z.-R., and Xu, Y.-J. (2013). Visible-Light-Driven Oxidation of Primary C-H Bonds over CdS with Dual Co-catalysts Graphene and TiO_2. *Sci. Rep.* 3 (1), 3314. doi:10.1038/srep03314

Yang, M.-Q., Zhang, N., Pagliaro, M., and Xu, Y.-J. (2014). Artificial Photosynthesis over Graphene-Semiconductor Composites. Are We Getting Better? *Chem. Soc. Rev.* 43 (24), 8240–8254. doi:10.1039/c4cs00213j

Yang, M. Q., Shen, L., Lu, Y., Chee, S. W., Lu, X., Chi, X., et al. (2019). Disorder Engineering in Monolayer Nanosheets Enabling Photothermic Catalysis for Full Solar Spectrum (250-2500 Nm) Harvesting. *Angew. Chem. Int. Ed.* 58 (10), 3077–3081. doi:10.1002/anie.201810694

Yuan, Y., Xu, R., Xu, H.-T., Hong, F., Xu, F., and Wang, L.-J. (2015). Nature of the Band gap of Halide Perovskites ABX_3 (A=CH_3 NH_3, Cs; B=Sn, Pb; X=Cl, Br, I): First-Principles Calculations. *Chin. Phys. B* 24 (11), 116302. doi:10.1088/1674-1056/24/11/116302

Zhang, Z., Shu, M., Jiang, Y., and Xu, J. (2021). Fullerene Modified $CsPbBr_3$ Perovskite Nanocrystals for Efficient Charge Separation and Photocatalytic CO_2 Reduction. *Chem. Eng. J.* 414, 128889. doi:10.1016/j.cej.2021.128889

Zhao, Y., and Zhu, K. (2016). Organic-inorganic Hybrid lead Halide Perovskites for Optoelectronic and Electronic Applications. *Chem. Soc. Rev.* 45 (3), 655–689. doi:10.1039/c4cs00458b

Zhou, P., Chao, Y., Lv, F., Wang, K., Zhang, W., Zhou, J., et al. (2020). Metal Single Atom Strategy Greatly Boosts Photocatalytic Methyl Activation and C-C Coupling for the Coproduction of High-Value-Added Multicarbon Compounds and Hydrogen. *ACS Catal.* 10 (16), 9109–9114. doi:10.1021/acscatal.0c01192

Conflict of Interest: The authors declare that the research was conducted in the absence of any commercial or financial relationships that could be construed as a potential conflict of interest.

Publisher's Note: All claims expressed in this article are solely those of the authors and do not necessarily represent those of their affiliated organizations, or those of the publisher, the editors, and the reviewers. Any product that may be evaluated in this article, or claim that may be made by its manufacturer, is not guaranteed or endorsed by the publisher.

frontiers | Frontiers in Chemistry

MINI REVIEW
published: 08 April 2022
doi: 10.3389/fchem.2022.866959

Designing Nanoconfined $LiBH_4$ for Solid-State Electrolytes

Suwarno Suwarno[1], Angeloclaudio Nale[2], Putu Suwarta[1], Ika Dewi Wijayanti[1] and Mohammad Ismail[3]*

[1]Department of Mechanical Engineering, Institut Teknologi Sepuluh Nopember (ITS), Surabaya, Indonesia, [2]"Section of Chemistry for Technologies", Department of Industrial Engineering, University of Padova, Padova, Italy, [3]Energy Storage Research Group, Faculty of Ocean Engineering Technology and Informatics, Universiti Malaysia Terengganu, Kuala Terengganu, Malaysia

Solid-state electrolytes are necessary for high-density and safe lithium-ion batteries. Lithium borohydride ($LiBH_4$) is one of the hydride compounds that shows promising candidates for solid-state electrolytes and enables all-solid-state batteries. $LiBH_4$ has good wetting properties and preferable mechanical properties when used in battery cells. The Li-ion conduction in $LiBH_4$ can be modified with nanoconfinement as a result of distinct properties on the interfaces. The ion conductivities can be modified further by choosing property support materials, i.e., composition, textural properties, and surface chemistry. The present work briefly reviews the Li-ion conduction in nanoconfined $LiBH_4$. A future perspective on the development of $LiBH_4$ as a solid-state electrolyte is further elaborated in the last section.

Keywords: hydrides, lithium borohydrides, battery, electrolyte, solid-state, batteries and energy storage

OPEN ACCESS

Edited by:
Hai-Wen Li,
Hefei General Machinery Research Institute, China

Reviewed by:
Martin Wilkening,
Graz University of Technology, Austria

****Correspondence:***
Suwarno Suwarno
warno@me.its.ac.id

Specialty section:
This article was submitted to Inorganic Chemistry, a section of the journal Frontiers in Chemistry

Received: *31 January 2022*
Accepted: *07 March 2022*
Published: *08 April 2022*

Citation:
Suwarno S, Nale A, Suwarta P, Wijayanti ID and Ismail M (2022) Designing Nanoconfined $LiBH_4$ for Solid-State Electrolytes. Front. Chem. 10:866959. doi: 10.3389/fchem.2022.866959

INTRODUCTION

The availability and widespread use of clean and sustainable energy are a global challenge in the present century. Clean energy can be obtained from converting renewable energy sources such as solar, waves, and wind. However, most renewable energy sources are intermittent, and thus, storage technology is required to maximize widespread usage. Energy storage uses various technologies from mechanical, chemical, and electrochemical storage. Batteries and fuel cells are the two electrochemical storage technologies currently employed for mobile and stationary energy storage and have shown the potential to be developed further. For batteries, specific energy density, in terms of both weight and volume, is an essential parameter besides the costs and abundance of the element. Currently, the battery used in electric cars uses lithium-ion technology, which has a capacity ranging from 100 to 300 Wh/kg based on the intercalation electrode concepts (Schmuch et al., 2018). Increasing the energy density up to 10 times the current technology is expected based on the initial investigation and theoretical calculation using Li as an anode instead of carbon or silicon materials (Adelhelm et al., 2015). The advanced lithium cell battery has an energy density of around 260 Wh/kg using state-of-the-art intercalation electrodes, for example, in the NCA/Si–C cell (Schmuch et al., 2018). Nevertheless, there is enormous room for improvement in increasing the energy density, such as using the lithium anode and sulfur or lithium–air chemistry (Bruce et al., 2012).

Advanced development is enabled by a solid-state electrolyte that has the potential to overcome the well-known battery challenge, i.e., the formation of lithium dendrite. In addition to this safety issue, a high-energy density battery can be realized. Enabling a high-density battery and stable cell operation requires high ionic conductivity, a large potential window, and excellent wetting properties to achieve intimate contact with the electrode. To date, several classes of inorganic materials can be used for ionic conducting materials, such as oxide base LISICON-like, NASICON-like, perovskite,

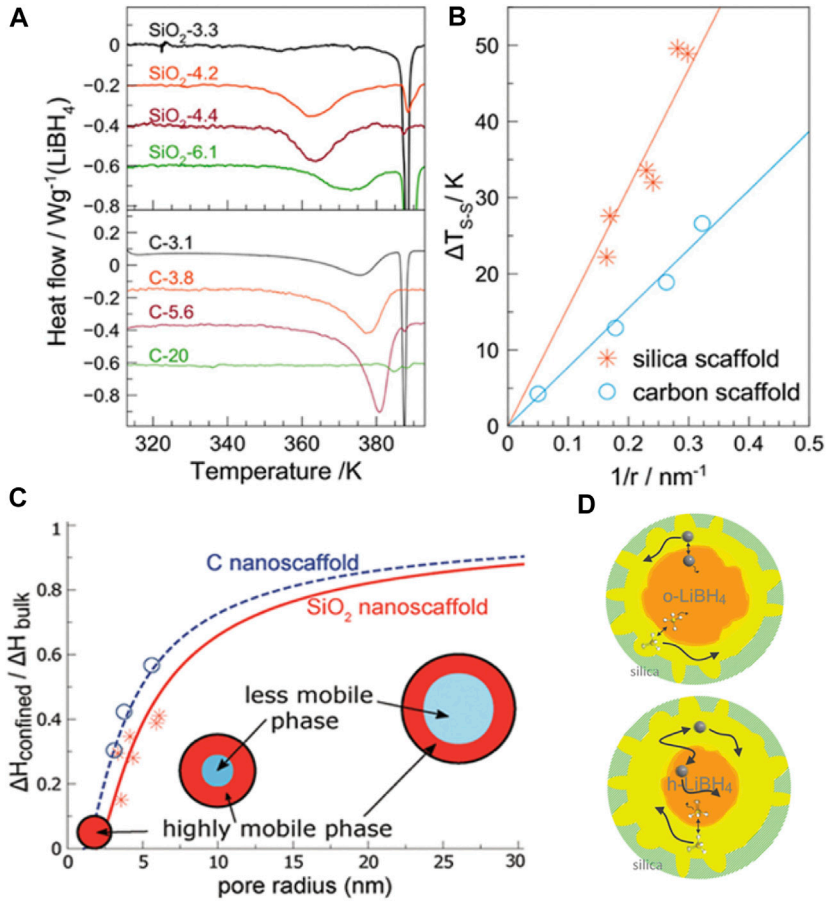

FIGURE 1 | Effect of nanoconfinement on $LiBH_4$: **(A)** differential scanning calorimetry profile showing the other bottom of the profile that originated from confined $LiBH_4$ at a lower temperature than that of the bulk; **(B)** transformation temperature depression (ΔT) as a function of the pore size for two different support materials; **(C)** ratio of enthalpy from confined and bulk $LiBH_4$ in the composite for fitting the layer thickness of the mobile phase; **(D)** schematic of mobile phase dynamics from analyzing the NMR data (Suwarno et al., 2017; Lambregts et al., 2019).

and hydride compound materials, with their advantages and disadvantages when implemented in the battery system.

A considerable effort to increase ionic conduction has been explored; this includes designing an alloying element that provides a tunable lattice volume, energy landscape, and phonon vibration (Krauskopf et al., 2018; Muy et al., 2018). Another approach is materials confinement to benefit from the support materials' interfacial properties. The journey for finding a new class of electrolytes is ongoing; recently, a boron hydride class has been found to have high ionic conductivity and stability to be used in the Li–S system (Kim et al., 2019). In addition to the properties within the crystal, the interface properties such as grain boundaries play a role in the bulk ionic mobility due to space charge developing at the interface (Yu and Siegel, 2017).

NANOCONFINED HYDRIDE

$LiBH_4$ is thermodynamically stable with an enthalpy of formation of 78 kJ/mol H_2. The compound desorbs up to 18.5 wt% H and thus is well known as a promising material for hydrogen storage (Schlapbach and Züttel, 2001). However, hydrogen can only be released at above 673 K *via* various desorption steps hindering further practical application. $LiBH_4$ experiences polymorph transformation from the orthorhombic phase into the hexagonal type structure. At room temperature, the crystalline phase $LiBH_4$ has an orthorhombic structure. It transforms to the hexagonal phase at 383 K. Interestingly, for the hexagonal phase, Li^+ in $LiBH_4$ is highly mobile, resulting in high ionic conductivity, up to 10^{-3} S/cm, which is several orders of magnitude compared to that of the low-temperature phase (Matsuo et al., 2007) and has approximately 6 V stability. Further study using temperature- and frequency-dependent nuclear magnetic resonance (NMR) spectroscopy showed low dimensionality of Li^+ in $LiBH_4$ (Epp and Wilkening, 2010). Therefore, this material is promising for the solid-state ionic conductor in Li-ion batteries. These lead to further research on the application of $LiBH_4$ as superionic conductors. Several light hydride materials based on boron have ionic conductivity (Callini et al., 2016; Mohtadi and Orimo, 2017; Guzik et al., 2019; Mohtadi, 2020). Lithium borohydride ($LiBH_4$) consists of Li^+ cation and $[BH_4]^-$ anion complexes.

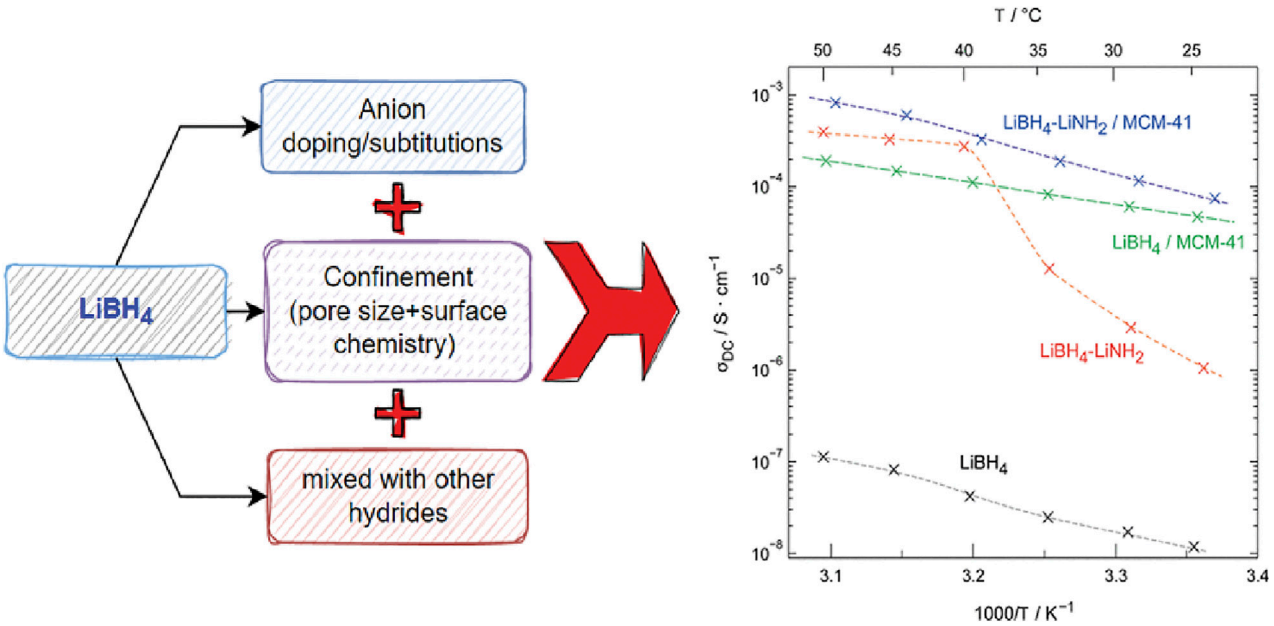

FIGURE 2 | Summary of various strategies for designing enhanced Li^+ conductivity in $LiBH_4$ and the Li^+ conductivity plot from the previously reported study. The conductivity plot is taken from the study of Zettl et al. (2020).

Various routes/methods have been explored in search of improvement of the properties of $LiBH_4$, and several research groups have been reviewed on this topic (Ley et al., 2014; Bannenberg et al., 2020). Since it has low surface tension, $LiBH_4$ infiltrates porous support such as SBA 15, in which the key was adding hydrogen pressure during the process (Ngene et al., 2010). The wetting properties lead to an excellent capillary infiltration on any porous material such as carbon materials and porous oxides (de Jongh and Eggenhuisen, 2013). This led to nanoconfined materials for hydrogen storage with enhanced properties (de Jongh and Adelhelm, 2010). Another strategy is to confine the metal hydrides in porous matrices, which can be achieved *via* melt infiltration (Ngene et al., 2010; de Jongh and Eggenhuisen, 2013).

Recently, fast ionic conductivity in silica-confined $LiBH_4$ has been identified (Blanchard et al., 2014). The reason for that is an increased mobility of the $[BH_4]^-$ units and possibly Li^+ in the confined phase (Verkuijlen et al., 2012). Earlier neutron scattering experiments and NMR suggested that the confined materials comprise a highly mobile phase, which was argued to be a consequence of the confinement's stress. It has also been recommended that the confined $LiBH_4$ is composed of two distinct fractions of $LiBH_4$: fast mobility in the interface and slow mobility at the core (Liu et al., 2013; Verdal et al., 2013; Breuer et al., 2018).

The Li^+ conductivity is structurally dependent and reaches up to 1×10^{-3} S/cm, at high temperature and when $LiBH_4$ is in its hexagonal phase. This value is close to that of liquid electrolytes primarily used in Li-ion batteries (Blanchard et al., 2015). The high conductivity has been explained because of the formation of highly mobile liquid-like $LiBH_4$ close to the surface of the pores (Suwarno et al., 2017). **Figures 1A,B** show the pore size dependence of the transition temperature of the confined $LiBH_4$. The interfacial thickness layer has been estimated to be 1.94 and 1.41 nm for silicon and carbon support materials (**Figure 1C**). Later studies using NMR confirmed the existence of two phases for the high mobility of lithium, as shown in **Figure 1D** (Lambregts et al., 2019).

DISCUSSION

The beneficial effect of $LiBH_4$ as a potential solid-state electrolyte that can be realized is the low melting of $LiBH_4$ and low surface tension in a liquid phase. Lower melting temperature and surface tension can be easier for fabrication and integration in ASSL batteries (Xiao et al., 2021). In addition, the softness increases the interfacial properties of the battery cell compared to the ceramic-based electrolyte. Another essential feature of the solid-state electrolyte used in the cell is the thermodynamic stability. A preliminary experiment showed that the voltage window was at 5–6 V, even though a recent investigation revealed that $LiBH_4$ works well at 2–3 V in the Li–S system. The most important requirement of solid electrolytes is fast ionic conduction at room temperature (10^{-3} S/cm) to compete with the current liquid electrolyte.

The Li^+ mobility in $LiBH_4$ can be modified by using various methods. **Figure 2** (left side) summarizes the different methods to increase the Li conductivity, and the initial attempt was by using anion doping. This can be achieved, for example, by doping with LiCl. The most successful was the addition of LiI (Maekawa et al., 2013). This earlier experiment showed that doping the anion dynamics enhanced the Li-ion conduction (Maekawa et al., 2013; Sveinbjörnsson et al., 2013). The second approach is

nanoconfinement using support materials such as nanoporous silica or alumina. Since the hexagonal high-temperature phase $LiBH_4$ has high conductivity, it is rational to stabilize the high-temperature phase by confinement. This comes from the Gibbs–Thomson relation of the transformation temperature dependent on the particle size. The third approach is a composite of two Li-based hydrides such as $LiNH_2$.

The initial experiment on the nanoconfined $LiBH_4$ mobility used NMR, which showed that the highly mobile phase is suggested from within a thin layer of high-temperature phase that is stable because of the stress by the confinement in SiO_2 porous materials (Verkuijlen et al., 2010; Blanchard et al., 2015). The role of an interface has also been shown in the $LiBH_4/Al_2O$ composite (Epp and Wilkening, 2013). Thus, the thickness of the interfacial layer could play a significant role in the conductivity. The possibility to tune a well-defined geometry and pore radius of ordered porous silica allowed further research to access the thickness interfacial layer. Furthermore, the surface effect is indicated by comparing silica and carbon to elucidate the interface effect. This was an initial attempt to study the surface effect in addition to the pore size dependency on controlling properties of $LiBH_4$. A later study showed a significant impact on the surface of silica, in which the silanol group played/had a prominent role in Li^+ conduction (Ngene et al., 2019). Experiments using various oxides to study the effects of support on the Li-ion conduction show that MgO has a better role in increasing the Li^+ conductivity (Gulino et al., 2020, 2021). **Figure 2** shows several results from an approach or combination of the Li^+ conductivities to highlight a summary of results. As shown in **Figure 2** (right), combining two approaches has also been tried, which showed a promising result. Experiments on the nanoconfined $LiBH_4$–LiI in SiO_2 support further improvement of ionic conductivity and decreased activation energy for Li^+ diffusion (Zettl et al., 2020). The Li^+ conductivity enhancement was also observed in $LiBH_4$–$LiNH_2$ confined in mesoporous silica (MCM-41). Surprisingly, in the confined $LiBH_4$–$LiNH_2$ composites, the surface effect is less dominant than that in $LiBH_4$ alone (Kort et al., 2020). The recent study of the composites containing $LiBH_4$–LiI/Al_2O_3 and $LiBH_4/Al_2O_3$ highlighted the crucial effect of the insulator–conductor interface in creating the path for fast ion conduction (Zettl et al., 2021). Thus, further exploration of combining various approaches seems promising to enhance the Li^+ conductivity in $LiBH_4$.

CONCLUSION

Lithium borohydride has been widely studied in the last decade and is a promising candidate for solid-state electrolytes used in all-solid-state batteries. The hexagonal phase can be stabilized by nanoconfinement, and the interfacial properties between $LiBH_4$ and the support materials determine the Li^+ conductivity. Various approaches combining nanoconfinement with other approaches such as anion substitutions and surface modification yield an increase in ionic conductivities. However, the effect seems different between single-phase $LiBH_4$ and when it is mixed with $LiNH_2$. The effect of the pore volume is dominant rather than the surface effects in the confined $LiBH_4$+$LiNH_2$. Further studies on the impact of $LiBH_4$ doping and textural properties of the support materials on the Li^+ conductivity can be the direction of future explorations.

AUTHOR CONTRIBUTIONS

SS and AN conceptualized the research idea. SS acquired the funds. SS, IW, and PS wrote the original draft. SS, AN, IW, and PS reviewed the paper. All authors contributed to the article and approved the submitted version.

FUNDING

This work received support from the EU Horizon 2020 program by the European Commission in the H2020-MSCARISE-2017 action, under the HYDRIDE4MOBILITY project, Grant Agreement No. 778307. This work was partially funded by the Indonesian Ministry of Research and Technology/National Agency for Research and Innovation and the Indonesian Ministry of Education and Culture under the World Class University Program managed by Institut Teknologi Bandung.

ACKNOWLEDGMENTS

SS acknowledges Petra de Jongh and Peter Ngene at Utrecht University, The Netherlands.

REFERENCES

Adelhelm, P., Hartmann, P., Bender, C. L., Busche, M., Eufinger, C., and Janek, J. (2015). From Lithium to Sodium: Cell Chemistry of Room Temperature Sodium-Air and Sodium-Sulfur Batteries. *Beilstein J. Nanotechnol.* 6, 1016–1055. doi:10.3762/bjnano.6.105

Bannenberg, L. J., Heere, M., Benzidi, H., Montero, J., Dematteis, E. M., Suwarno, S., et al. (2020). Metal (Boro-) Hydrides for High Energy Density Storage and Relevant Emerging Technologies. *Int. J. Hydrogen Energ.* 45, 33687–33730. doi:10.1016/j.ijhydene.2020.08.119

Blanchard, D., Nale, A., Sveinbjörnsson, D., Eggenhuisen, T. M., Verkuijlen, M. H. W., Suwarno, et al. (2014). *Nanoconfined $LiBH_4$ as a Fast Lithium Ion Conductor*. Wiley Online Library. submitted.

Blanchard, D., Nale, A., Sveinbjörnsson, D., Eggenhuisen, T. M., Verkuijlen, M. H. W., Suwarno, T., et al. (2015). Nanoconfined LiBH4as a Fast Lithium Ion Conductor. *Adv. Funct. Mater.* 25, 184–192. doi:10.1002/adfm.201402538

Breuer, S., Uitz, M., and Wilkening, H. M. R. (2018). Rapid Li Ion Dynamics in the Interfacial Regions of Nanocrystalline Solids. *J. Phys. Chem. Lett.* 9, 2093–2097. doi:10.1021/acs.jpclett.8b00418

Bruce, P. G., Freunberger, S. A., Hardwick, L. J., and Tarascon, J.-M. (2012). Li-O2 and Li-S Batteries with High Energy Storage. *Nat. Mater* 11, 19–29. doi:10.1038/nmat3191

Callini, E., Atakli, Z. Ö. K., Hauback, B. C., Orimo, S.-i., Jensen, C., Dornheim, M., et al. (2016). Complex and Liquid Hydrides for Energy Storage. *Appl. Phys. A.* 122, 353. doi:10.1007/s00339-016-9881-5

de Jongh, P. E., and Adelhelm, P. (2010). Nanosizing and Nanoconfinement: New Strategies Towards Meeting Hydrogen Storage Goals. *ChemSusChem* 3, 1332–1348.

de jongh, P. E., and Eggenhuisen, T. M. (2013). Melt Infiltration: An Emerging Technique for the Preparation of Novel Functional Nanostructured Materials. *Adv. Mater.* 25, 6672–6690. doi:10.1007/s00339-016-9881-5

de Kort, L. M., Harmel, J., de Jongh, P. E., and Ngene, P. (2020). The Effect of Nanoscaffold Porosity and Surface Chemistry on the Li-Ion Conductivity of LiBH4-LiNH2/metal Oxide Nanocomposites. *J. Mater. Chem. A.* 8, 20687–20697. doi:10.1039/D0TA07600G

Epp, V., and Wilkening, M. (2010). Fast Li Diffusion in crystallineLiBH4due to Reduced Dimensionality: Frequency-dependent NMR Spectroscopy. *Phys. Rev. B* 82, 020301. doi:10.1103/PhysRevB.82.020301

Epp, V., and Wilkening, M. (2013). Motion of Li+in Nanoengineered LiBH4and LiBH4:Al2O3Comparison with the Microcrystalline Form. *ChemPhysChem* 14, 3706–3713. doi:10.1002/cphc.201300743

Gulino, V., Barberis, L., Ngene, P., Baricco, M., and de Jongh, P. E. (2020). Enhancing Li-Ion Conductivity in LiBH4-Based Solid Electrolytes by Adding Various Nanosized Oxides. *ACS Appl. Energ. Mater.* 3, 4941–4948. doi:10.1021/acsaem.9b02268

Gulino, V., Brighi, M., Murgia, F., Ngene, P., de Jongh, P., Černý, R., et al. (2021). Room-Temperature Solid-State Lithium-Ion Battery Using a LiBH4-MgO Composite Electrolyte. *ACS Appl. Energ. Mater.* 4, 1228–1236. doi:10.1021/acsaem.0c02525

Guzik, M. N., Mohtadi, R., and Sartori, S. (2019). Lightweight Complex Metal Hydrides for Li-, Na-, and Mg-Based Batteries. *J. Mater. Res.* 34, 877–904. doi:10.1557/jmr.2019.82

Kim, S., Oguchi, H., Toyama, N., Sato, T., Takagi, S., Otomo, T., et al. (2019). A Complex Hydride Lithium Superionic Conductor for High-Energy-Density All-Solid-State Lithium Metal Batteries. *Nat. Commun.* 10, 1081. doi:10.1038/s41467-019-09061-9

Krauskopf, T., Muy, S., Culver, S. P., Ohno, S., Delaire, O., Shao-Horn, Y., et al. (2018). Comparing the Descriptors for Investigating the Influence of Lattice Dynamics on Ionic Transport Using the Superionic Conductor Na3PS4-xSex. *J. Am. Chem. Soc.* 140, 14464–14473. doi:10.1021/jacs.8b09340

Lambregts, S. F. H., van Eck, E. R. H., SuwarnoNgene, P., Ngene, P., de Jongh, P. E., and Kentgens, A. P. M. (2019). Phase Behavior and Ion Dynamics of Nanoconfined LiBH4 in Silica. *J. Phys. Chem. C* 123, 25559–25569. doi:10.1021/acs.jpcc.9b06477

Ley, M. B., Jepsen, L. H., Lee, Y.-S., Cho, Y. W., Bellosta von Colbe, J. M., Dornheim, M., et al. (2014). Complex Hydrides for Hydrogen Storage - New Perspectives. *Mater. Today* 17, 122–128. doi:10.1016/j.mattod.2014.02.013

Liu, X., Majzoub, E. H., Stavila, V., Bhakta, R. K., Allendorf, M. D., Shane, D. T., et al. (2013). Probing the Unusual Anion Mobility of LiBH4 Confined in Highly Ordered Nanoporous Carbon Frameworks via Solid State NMR and Quasielastic Neutron Scattering. *J. Mater. Chem. A.* 1, 9935–9941. doi:10.1039/c3ta12051a

Maekawa, H., Matsuo, M., Takamura, H., Ando, M., Noda, Y., Karahashi, T., et al. (2009). Halide-Stabilized LiBH4, a Room-Temperature Lithium Fast-Ion Conductor. *J. Am. Chem. Soc.* 131, 894–895. doi:10.1021/ja807392k

Matsuo, M., Nakamori, Y., Orimo, S.-i., Maekawa, H., and Takamura, H. (2007). Lithium Superionic Conduction in Lithium Borohydride Accompanied by Structural Transition. *Appl. Phys. Lett.* 91, 224103. doi:10.1063/1.2817934

Mohtadi, R. (2020). Beyond Typical Electrolytes for Energy Dense Batteries. *Molecules* 25, 1791. doi:10.3390/molecules25081791

Mohtadi, R., and Orimo, S.-i. (2017). The Renaissance of Hydrides as Energy Materials. *Nat. Rev. Mater.* 2, 16091. doi:10.1038/natrevmats.2016.91

Muy, S., Bachman, J. C., Chang, H.-H., Abernathy, D. L., Bansal, D., Delaire, O., et al. (2018). Tuning Mobility and Stability of Lithium Ion Conductors Based on Lattice Dynamics. *Energy Environ. Sci.* 11, 850–859. doi:10.1039/C7EE03364H

Ngene, P., Adelhelm, P., Beale, A. M., de Jong, K. P., and de Jongh, P. E. (2010). LiBH4/SBA-15 Nanocomposites Prepared by Melt Infiltration Under Hydrogen Pressure: Synthesis and Hydrogen Sorption Properties. *J. Phys. Chem. C* 114, 6163–6168. doi:10.1021/jp9065949

Ngene, P., Lambregts, S. F. H., Vegge, T., Sharma, M., Hagemann, H., de Jongh, P. E., et al. (2019). The Influence of Silica Surface Groups on the Li-Ion Conductivity of LiBH4/SiO2 Nanocomposites. *Phys. Chem. Chem. Phys.* 21, 22456–22466. doi:10.1039/C9CP04235K

Schlapbach, L., and Züttel, A. (2001). Hydrogen-storage Materials for mobile Applications. *Nature* 414, 353–358. doi:10.1038/35104634

Schmuch, R., Wagner, R., Hörpel, G., Placke, T., and Winter, M. (2018). Performance and Cost of Materials for Lithium-Based Rechargeable Automotive Batteries. *Nat. Energ.* 3, 267–278. doi:10.1038/s41560-018-0107-2

Suwarno, S., Ngene, P., Nale, A., Eggenhuisen, T. M., Oschatz, M., Embs, J. P., et al. (2017). Confinement Effects for Lithium Borohydride: Comparing Silica and Carbon Scaffolds. *J. Phys. Chem. C* 121, 4197–4205. doi:10.1021/acs.jpcc.6b13094

Sveinbjörnsson, D., Myrdal, J. S. G., Blanchard, D., Bentzen, J. J., Hirata, T., Mogensen, M. B., et al. (2013). Effect of Heat Treatment on the Lithium Ion Conduction of the LiBH4-LiI Solid Solution. *J. Phys. Chem. C* 117, 3249–3257. doi:10.1021/jp310050g

Verdal, N., Udovic, T. J., Rush, J. J., Liu, X., Majzoub, E. H., Vajo, J. J., et al. (2013). Dynamical Perturbations of Tetrahydroborate Anions in LiBH4 Due to Nanoconfinement in Controlled-Pore Carbon Scaffolds. *J. Phys. Chem. C* 117, 17983–17995. doi:10.1021/jp4063737

Verkuijlen, M. H. W., Gao, J., Adelhelm, P., van Bentum, P. J. M., de Jongh, P. E., and Kentgens, A. P. M. (2010). Solid-State NMR Studies of the Local Structure of NaAlH4/C Nanocomposites at Different Stages of Hydrogen Desorption and Rehydrogenation. *J. Phys. Chem. C* 114, 4683–4692. doi:10.1021/jp911228x

Verkuijlen, M. H. W., Ngene, P., de Kort, D. W., Barré, C., Nale, A., van Eck, E. R. H., et al. (2012). Nanoconfined LiBH4 and Enhanced Mobility of Li+ and BH4- Studied by Solid-State NMR. *J. Phys. Chem. C* 116, 22169–22178. doi:10.1021/jp306175b

Xiao, Y., Turcheniuk, K., Narla, A., Song, A.-Y., Ren, X., Magasinski, A., et al. (2021). Electrolyte Melt Infiltration for Scalable Manufacturing of Inorganic All-Solid-State Lithium-Ion Batteries. *Nat. Mater.* 20, 984–990. doi:10.1038/s41563-021-00943-2

Yu, S., and Siegel, D. J. (2017). Grain Boundary Contributions to Li-Ion Transport in the Solid Electrolyte Li7La3Zr2O12 (LLZO). *Chem. Mater.* 29, 9639–9647. doi:10.1021/acs.chemmater.7b02805

Zettl, R., de Kort, L., Gombotz, M., Wilkening, H. M. R., de Jongh, P. E., and Ngene, P. (2020). Combined Effects of Anion Substitution and Nanoconfinement on the Ionic Conductivity of Li-Based Complex Hydrides. *J. Phys. Chem. C* 124, 2806–2816. doi:10.1021/acs.jpcc.9b10607

Zettl, R., Hogrefe, K., Gadermaier, B., Hanzu, I., Ngene, P., de Jongh, P. E., et al. (2021). Conductor-Insulator Interfaces in Solid Electrolytes: A Design Strategy to Enhance Li-Ion Dynamics in Nanoconfined LiBH4/Al2O3. *J. Phys. Chem. C* 125, 15052–15060. doi:10.1021/acs.jpcc.1c03789

Conflict of Interest: The authors declare that the research was conducted in the absence of any commercial or financial relationships that could be construed as a potential conflict of interest.

Publisher's Note: All claims expressed in this article are solely those of the authors and do not necessarily represent those of their affiliated organizations, or those of the publisher, the editors, and the reviewers. Any product that may be evaluated in this article, or claim that may be made by its manufacturer, is not guaranteed or endorsed by the publisher.

frontiers | Frontiers in Chemistry

MINI REVIEW
published: 11 April 2022
doi: 10.3389/fchem.2022.878799

Green Solvents for the Liquid Phase Exfoliation Production of Graphene: The Promising Case of Cyrene

João Fernandes[1], *Siva Sankar Nemala*[1], *Giovanni De Bellis*[2,3] *and Andrea Capasso*[1]*

[1]International Iberian Nanotechnology Laboratory, Braga, Portugal, [2]Department of Astronautical, Electrical and Energy Engineering, Sapienza University of Rome, Rome, Italy, [3]Research Center on Nanotechnology Applied to Engineering of Sapienza (CNIS), Sapienza University of Rome, Rome, Italy

The liquid phase exfoliation (LPE) of graphite has allowed to produce graphene materials on a large scale and at a reasonable cost. By this method, stable dispersions, inks and liquid suspensions containing atomic-thick graphene flakes with tailored concentrations can be produced, opening up applications in a wide range of cutting-edge technologies such as functional coatings, printed and flexible electronics, and composites. However, currently established LPE techniques raise several health and environmental risks, since unsafe and toxic solvents (such as NMP, DMF, and DMSO) are often regarded as the most effective liquid media for the process. Therefore, it appears necessary to unlock eco-friendly and sustainable methods for the production of graphene at an industrial scale. This review focuses on the latest developments in terms of green solvents for LPE production of graphene. We highlight the use of a new green solvent, Cyrene, and its performance when compared to conventional solvents.

Keywords: 2D materials, solution processing method, sonication, high-shear mixing, inkjet printing, environmental risks, sustainability

OPEN ACCESS

Edited by:
Diego Cazorla-Amoros, University of Alicante, Spain

Reviewed by:
Horacio Javier Salavagione, Institute of Polymer Science and Technology (CSIC), Spain

***Correspondence:**
Andrea Capasso
andrea.capasso@inl.int

Specialty section:
This article was submitted to Nanoscience, a section of the journal Frontiers in Chemistry

Received: *18 February 2022*
Accepted: *11 March 2022*
Published: *11 April 2022*

Citation:
Fernandes J, Nemala SS, De Bellis G and Capasso A (2022) Green Solvents for the Liquid Phase Exfoliation Production of Graphene: The Promising Case of Cyrene. Front. Chem. 10:878799. doi: 10.3389/fchem.2022.878799

INTRODUCTION

As the archetypal two-dimensional material, graphene has been the proposed material in the last decade for several technologies such as wearable/flexible electronics (Tan et al., 2017), structural and multifunctional nanocomposites (Wang et al., 2021), energy storage (Li and Zhi, 2018), strain sensors (Mehmood et al., 2020), water treatment (Bhol et al., 2021) and biomedical devices (Yang et al., 2013). A scalable mass production of highly pure graphene at low cost is the prerequisite for the commercialization phase. Among the many production methods, liquid phase exfoliation (LPE) allows to obtain liquid dispersions of graphene flakes with high yield. LPE technique was initially reported in 1989 for MoS_2 and WSe_2 (Gutiérrez and Henglein, 1989) and translated to graphene in 2008, demonstrating an affordable production of 2D materials in large quantities (Hernandez et al., 2008). LPE graphene flake dispersions are suitable for several applications, such as flexible, transparent, and printable electronics (Secor et al., 2013; Secor et al., 2015; Li et al., 2018; Shin et al., 2018). Usually, LPE identifies a group of approaches where natural and synthetic bulk materials are directly exfoliated into their corresponding isolated layers in a liquid medium, using the energy provided by different techniques: ultrasonication (Turner et al., 2019), wet ball-milling (Zhao et al., 2010), electrochemical, micro-fluidization (Xu et al., 2018), and high-shear mixing force (Paton et al., 2014), wet-jet milling (Del Rio Castillo et al., 2018) and high-pressure system (using an airless paint sprayer) (Nemala et al., 2018). These approaches can be executed in a variety of liquid solvents, including water (frequently mixed with surfactants), organic solvents, ionic liquids, oils, and salts

(Xu et al., 2018). The general LPE process consists of three steps: intercalation, exfoliation and separation (Li et al., 2020). The solvent is a crucial factor in the exfoliation process, and to be effective it should fulfil three main requirements: 1) transmit the exfoliating power efficiently, 2) minimize the energy needed to disrupt the van der Waals forces among layers and 3) stabilize the exfoliated layers by providing steric hindrance to prevent re-agglomeration (Banavath et al., 2021). We will start this mini review by giving an overview of the most effective solvents for LPE of graphite. Although commonly used, these solvents entail severe health and environmental risks and should be replaced to reach a sustainable commercialization phase. The search for "green" solvents thus appears pivotal. By analyzing recent literature, we will describe the most representative green options to make stable graphene-based dispersions at high yield. As a case study, we will focus on dihydrolevoglucosenone (trademarked as Cyrene), which can be currently regarded as the most promising green solvent for LPE graphene.

TOWARDS GREEN SOLVENTS FOR THE LPE OF GRAPHITE

An ideal solvent for the exfoliation of graphite into graphene should meet several key requirements. In general, an ideal solvent would allow the complete exfoliation of graphite, leaving no un-exfoliated flakes in the sediment. The Hansen solubility parameters offer a framework to predict if and how a material will disperse in a particular solvent and form a solution (Charles, 2007). The surface tension of the solvent and graphite should ideally match to stabilize the graphene flakes in the dispersion after the exfoliation, preventing their re-agglomeration (Shen et al., 2015). For these reasons, researchers have originally selected solvents that matched as much as possible the Hansen solubility parameters and surface tension value of graphite (Hernandez et al., 2008; Capasso et al., 2015; Shen et al., 2016; Xu et al., 2018). The dynamic viscosity of the solvent is another important parameter in terms of exfoliation efficiency and stability. In principle, a high viscosity would be beneficial for the LPE process, increasing the exfoliation yield and decreasing the defect density and sedimentation rate (Manna et al., 2016; Salavagione et al., 2017; Simfukwe et al., 2017). However, a threshold must be set for practical applications, since an excessive viscosity favors the stable suspension of large agglomerates/particles during the centrifugation step, thus preventing the separation from thinner and lighter flakes (Backes, 2020). As a last consideration, a LPE solvent should feature a low boiling point to allow an easy removal of any solvent residue, which might degrade the properties of graphene (especially in terms of electrical conductivity) (Neill, 2009).

Conventional solvents for the LPE of graphite (surface tension ~55 mN m^{-1} (Bonaccorso et al., 2012)) exhibit a surface tension ranging within 40–50 mN m^{-1} and Hansen solubility parameters close to those of graphite (δ_D = 18.0 $MPa^{0.5}$, δ_P = 9.3 $MPa^{0.5}$, δ_H = 7.7 $MPa^{0.5}$) (Hernandez et al., 2010). Within this range, several highly polar solvents were selected, including N-methylpyrrolidone (NMP), N,N-dimethylformamide (DMF), dimethylsulfoxide (DMSO), N,N-dimethylacetamide (DMAC), and γ-butyrolactone (GBL) (Güler et al., 2021). Non-polar solvents such as ortho-dichlorobenzene (DCB) were also reported to produce homogeneous graphene dispersions (Güler et al., 2021). In general, amine-based solvents such as NMP and DMF are the most effective in producing crystalline, oxygen-free graphene flakes (Güler and Sönmez, 2020). Hernandez et al. originally reported the production of stable dispersions of few-layer graphene in NMP (Hernandez et al., 2008; Xu et al., 2018). The initially reported concentration of 0.01 mg mL^{-1} has been gradually increased above 1 mg ml^{-1} by several groups with longer sonication times (Khan et al., 2010; Wang et al., 2012; Wu et al., 2014). Successful exfoliation and stable dispersions were also reported in DMF and DMSO, with concentrations similar to those obtained in NMP (Coleman, 2013; Xu et al., 2018; Trusova et al., 2021; Vacacela Gomez et al., 2021). Although the exfoliation is effective, NMP, DMF, and DMSO have high boiling points which cause issues in the removal of solvent residues. More importantly, these solvents present severe health risks. In 2008, NMP and DMF were classified as Substances of Very High Concern. According to the European REACH (Registration, Evaluation, Authorisation and Restriction of Chemicals) regulation (Regulation No 1907/2, 2022), several restrictions were applied regarding their use or import to Europe. Same warnings were raised in the USA. DMSO has also recently raised serious safety concerns, after several studies have demonstrated both the toxicity on retinal neuronal cells (Galvao et al., 2014) and the "extreme changes in micro RNAs and alterations in the epigenetic landscape", in both cardiac and hepatic micro-tissues, even for concentrations as low as 0.1% (Verheijen et al., 2019).

In this context, current solvents for LPE graphene appear as a limiting factor in the long-term development and sustainability of the production. Safety concerns also demand the need for impractical and expensive equipment (*e.g.*, safety equipment, fume-hoods, exhausts, etc.), with a direct impact on the production cost. In order to scale-up the process and approach an industrial production, the identification of environmentally safe solvents that do not raise health risks is thus imperative. These solvents should be efficient for the exfoliation process, while having a moderate cost. A low boiling point is also a desired feature. Such characteristics would at once minimize the ecological impact and lower the production complexity and cost of the production of graphene. Capello et al. proposed a framework for a comprehensive assessment of how "green" a solvent is (Capello et al., 2007). The authors used a complementary, multi-criteria evaluation: They combined EHS (environment, health and safety) considerations on the inherent hazards of a solvent, and a LCA (life-cycle-assessment) that quantifies the energy use connected to solvent production and disposal/treatment as waste (Capello et al., 2007). According to this definition, low-boiling-point solvents such as acetone and isopropyl alcohol (61°C and 56°C, respectively) can be considered green alternatives (Capello et al., 2007). They have been previously used to disperse graphene at low concentration (few μg mL^{-1})

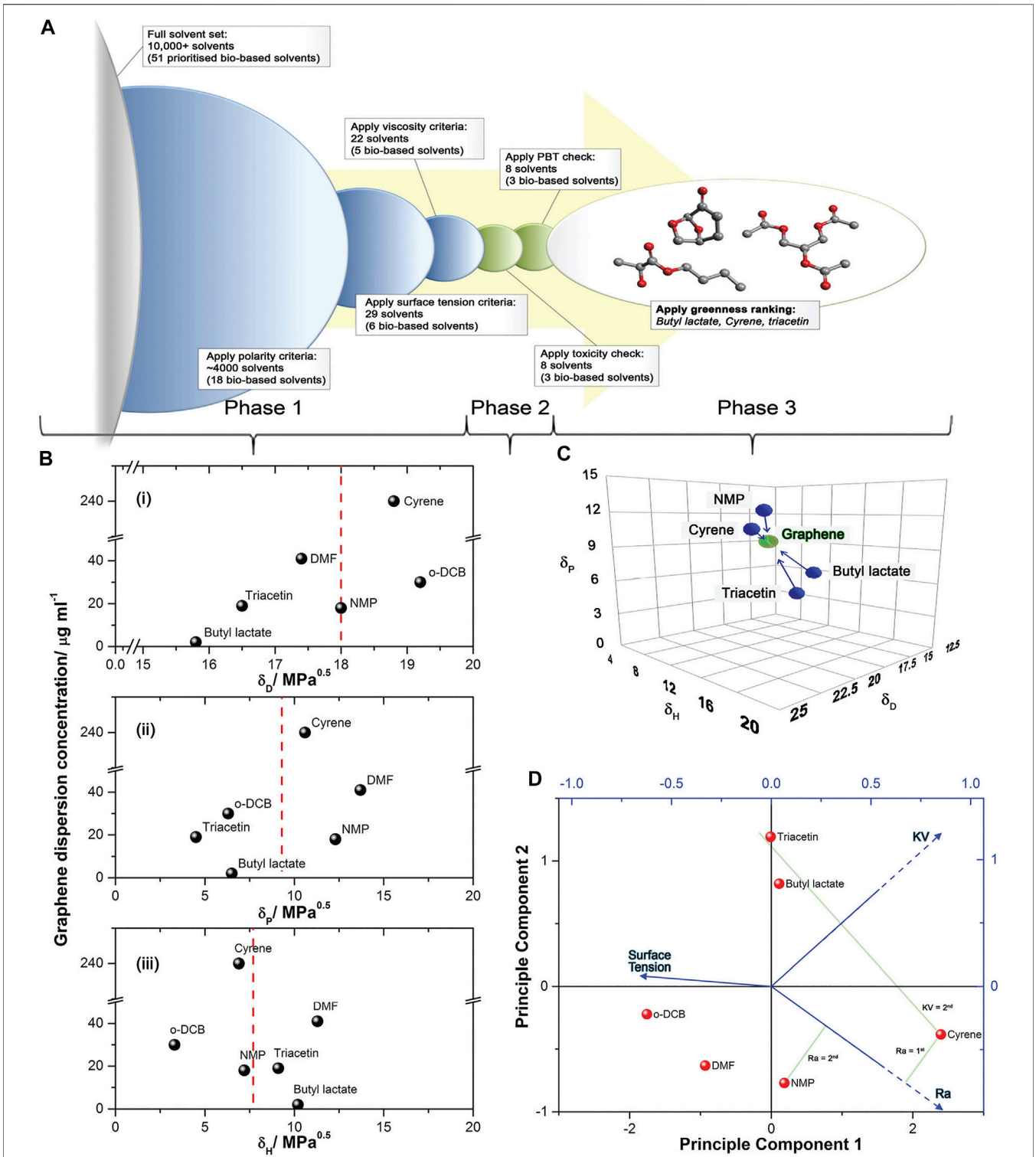

FIGURE 1 | The application of solvent selection criteria for optimizing graphene dispersions. **(A)** Illustration of the solvent selection steps applied for the computational screening of suitable solvents. **(B)** Graphene dispersion concentration as a function of (i) dispersive, δD (ii) polar, δP and (iii), hydrogen-bonding, δH Hansen solubility parameters, with the dashed red line being indicative of ideal graphene properties. NMP, DMF and DCB are shown as reference. **(C)** Hansen solubility map showing the similarity of the final bio-based solvent candidates (and NMP) to graphene in terms of their polarity. The Hansen radius (Ra) is the radius of the sphere in the Hansen space, where each axis corresponds to one solubility parameter. **(D)** Principle Component Analysis (PCA) bi-plot for candidate solvents (including NMP, DCB and DMF for reference) with vectors indicating surface tension, kinematic viscosity (KV) are and Hansen radius (Ra). Reproduced with permission from Ref (Salavagione et al., 2017). Copyright © The Royal Society of Chemistry 2017.

(Hernandez et al., 2010). However, these solvents have low flash points (12–13°C), which raise safety concerns for industrial use. Cyclohexanone and cyclopentanone have also been previously proposed as green and bio-based LPE solvents, but they present similar issues (flash point of 44°C and 31°C, respectively) (Hernandez et al., 2010).

Other green alternatives are represented by aqueous media with surfactants (*e.g.*, sodium dodecylbenzenesulfonate (Lotya et al., 2009), sodium cholate, (Green and Hersam, 2009), and sodium deoxycholate (Hasan et al., 2010)), and/or polymers (e.g., Pluronic® (Seo et al., 2011)) useful to overcome surface tension mismatch (water has a surface tension of 72 mN m^{-1}). Surfactant-assisted exfoliation in aqueous media is one of the most suitable alternatives to achieve high-quality graphene at high concentrations (Zhang et al., 2018). Green et al. prepared stable dispersions of graphene using sodium cholate (SC) as a surfactant in aqueous medium, yet achieving a low concentration (10 μg ml^{-1}) (Green and Hersam, 2009). In an analogous study, dispersions in water and SC were prepared by tip-sonication up to 7 mg/ml concentration using longer exfoliation times (96 h) and high SC concentration (5 mg/ml) (Nawaz et al., 2016). Coleman et al. made graphene dispersions in a range of aqueous solutions (containing ionic or non-ionic surfactants) at similar concentrations (10–30 μg ml^{-1}) (Smith et al., 2010). Dispersions of graphene flakes (average lateral size of ~1 μm and layer number of ~4.5) in water and Triton X-100 (a non-ionic surfactant) were also obtained by tip-sonication at a concentration of 0.54 mg/ml (Arao and Kubouchi, 2015). Nevertheless, residuals arising from the surfactants are known to reduce the quality and the electrical conductivity of the exfoliated flakes, thus limiting their use in electronic applications. To overcome this issue, mixtures of solvents were also considered (Zhou et al., 2011), such as water/isopropyl alcohol (Halim et al., 2013) and water/ethanol (Capasso et al., 2015). However, these mixtures also do not allow to obtain dispersions at high concentration.

Therefore, there is a need for new green solvents which fulfill the aforementioned requirements. Salavagione et al. identified efficient solvents by computational methods. The authors applied criteria including polarity, surface tension, viscosity, toxicity and "greenness" to evaluate and shortlist a solvent set of more than 10,000 (**Figure 1A**). Three bio-based solvents fulfilling the criteria were selected and tested experimentally: cyrene, triacetin, and butyl lactate (Salavagione et al., 2017). **Figure 1B** shows the Hansen solubility parameters δ_D, δ_P and δ_H (measuring the energies from dispersion forces, dipolar intermolecular forces and hydrogen bonds between molecules, respectively). These three parameters can be set as coordinates for a point in a three dimensional graph known as the Hansen space. The Hansen solubility space in **Figure 1C** shows how bio-based candidates (and NMP) and graphene compare. Triacetin and butyl lactate have appropriate parameters, with the exception of δ_P. Nonetheless, they have high boiling points and led to dispersions with low concentration.

Other green alternatives [triethanolamine (Chen et al., 2017)—TEA–and urea aqueous solutions (He et al., 2015)] have been tested for the LPE of graphite. In **Table 1**, we summarize the features of these green solvents, comparing them to conventional ones. In the single report currently available on the use of TEA, the authors obtained dispersions of crystalline graphene flakes with high stability (over 9 months) (Chen et al., 2017). However, TEA can induce detrimental chemical modifications in the flakes, possibly due to functionalization (Song et al., 2015; Ryu et al., 2017; Paolucci et al., 2020). Furthermore, its very high viscosity precludes the deposition of the dispersion by versatile techniques, such as inkjet printing (usually requiring 1–10 cP) (Paolucci et al., 2020). As a next alternative, urea aqueous solution has also been tested and led to crystalline flakes and 15-days stability (He et al., 2015; Hou et al., 2019). However, this solvent is theoretically not ideal for graphite exfoliation, since both the surface tension and Hansen solubility parameters are higher than desired (especially the δ_H and δ_P components). As a proof of that, a very low yield (2.4%) was reported (Paolucci et al., 2020). Methyl-5-(dimethylamino)-2-methyl-5-oxopentanoate (Rhodiasolv Polarclean) is a polar solvent that was also tested in sonication-assisted LPE of graphite, MoS_2 and WS_2. It showed good performance, with a ~350% higher amount of few-layer nanosheets (<5 nm thickness) and 10 times lower defect density with respect to NMP (Paolucci et al., 2020). However, its high boiling point represents a pivotal drawback. As for TEA, we note that there is just a single report available on the use of Polarclean, making it difficult to draw a conclusive comparison to the other solvents. Overall, these results point out that TEA, urea and Polarclean are not suited to a scalable production of graphene.

As shown in **Figure 1**, Cyrene has the smallest Hansen radius (2.2 $MPa^{0.5}$), demonstrating the greatest affinity to graphite (as shown in **Figures 1C,D**). It has the second highest kinematic viscosity (**Figure 1D**), high enough to guarantee a high exfoliation yield, while preventing severe sedimentation over time. This value is also suitable to allow the deposition by techniques such as inkjet printing. Cyrene has a higher surface tension than other conventional solvents, which should be evaluated in terms of dispersion stabilization. Recent reports indicate Cyrene as a promising green solvent for LPE of graphite, so we analyze it in detail in the following section.

CASE STUDY: CYRENE AS THE MOST ADVANCED GREEN SOLVENT FOR LPE OF GRAPHITE

Cyrene (dihydrolevoglucosenone, $C_6H_8O_3$) is a bio-based solvent derived (Pecka et al., 1974) in two steps from cellulose via levoglucosenone (biomass) (De bruyn, 2016), a process that guarantees at once low environmental impact and economic feasibility. In 2014, dihydrolevoglucosenone was marketed by Australian biotechnology company Circa Group in conjunction with Professor James Clark (University of York's - Green Chemistry Centre of Excellence) as Cyrene. Nowadays, Cyrene is commercialized by Merck. Composed of two fused rings, Cyrene does not present the amide functionality (typical of NMP and DMF) that is linked to reproductive toxicity effects (Salavagione et al., 2017). It neither contains any chlorine groups,

TABLE 1 | Summary of the features of conventional (NMP, DMF and DMSO) and green solvents used for LPE of graphite.

Solvent	Surface tension (σ_S [mN m^{-1}])~55[a]	Dynamic viscosity@ 25°C (cP)	Boiling Point (°C)	Hansen solubility parameters			Cost[b] (for 1 L) €	Dispersion Concentration (mg ml^{-1})
				δ_d [MPa$^{1/2}$] 18.0[a]	δ_P [MPa$^{1/2}$] 9.3[a]	δ_H [MPa$^{1/2}$] 7.7[a]		
NMP	**40.1** (Paolucci et al., 2020)	**1.65** (Pourabadeh et al., 2020)	**202** (Sherwood et al., 2014)	**18.0** (Hernandez et al., 2010)	**12.3** (Hernandez et al., 2010)	**7.2** (Hernandez et al., 2010)	**147.00**	**1.50** (Wu et al., 2014)
DMF	**37.1** (Paolucci et al., 2020)	**0.9** (Alam et al., 2019)	**153** (Sherwood et al., 2014)	**17.4** (Hernandez et al., 2010)	**13.7** (Hernandez et al., 2010)	**11.3** (Hernandez et al., 2010)	**161.00**	**1.30** (Trusova et al., 2021)
DMSO	**42.9** (Yaws, 2014)	**1.99** (Zhang et al., 2017)	**189** (Sherwood et al., 2014)	**18.4** (Charles, 2007)	**16.4** (Charles, 2007)	**10.2** (Charles, 2007)	**88.10**	**0.03–0.2** (Chouhan et al., 2020)
Triacetin	**32.6** (Yaws, 2014)	**16.31** (Rodríguez et al., 1994)	**258**	**16.5** (Salavagione et al., 2017)	**4.4** (Salavagione et al., 2017)	**9.0** (Salavagione et al., 2017)	**57.40**	**0.02** (Salavagione et al., 2017)
Butyl lactate	**29.2**	**3.9**	**188**	**15.7** (Salavagione et al., 2017)	**6.4** (Salavagione et al., 2017)	**10.2** (Salavagione et al., 2017)	**190.80**	**0.002** (Salavagione et al., 2017)
TEA	**45.9** (Paolucci et al., 2020)	**607** (Maham et al., 2002)	**89.28**	**17.3** (Paolucci et al., 2020)	**7.6** (Paolucci et al., 2020)	**21.0** (Paolucci et al., 2020)	**95.70**	NA
Urea aqueous solutions (30%)	**74.0** (Paolucci et al., 2020)	**1.36** (Kawahara and Tanford, 1966)	NA	**17.0** (Paolucci et al., 2020)	**16.7** (Paolucci et al., 2020)	**38.0** (Paolucci et al., 2020)	NA	**0.15** (He et al., 2015)
Polarclean	**38.0** (Paolucci et al., 2020)	**9.78**	**273.7**	**15.8** (Paolucci et al., 2020)	**10.7** (Paolucci et al., 2020)	**9.2** (Paolucci et al., 2020)	NA	**0.3** (Paolucci et al., 2020)
Cyrene	**72.5** (Salavagione et al., 2017)	**14.5** (Paolucci et al., 2020)	**227** (Sherwood et al., 2014)	**18.7** (Salavagione et al., 2017)	**10.8** (Salavagione et al., 2017)	**6.9** (Salavagione et al., 2017)	196.00	**0.7** (Salavagione et al., 2017)

[a]*Reference values of graphite.*
[b]*From Sigma Aldrich.*

which are usually responsible for end-of-life pollution issues. When incinerated, Cyrene yields only carbon dioxide and water as byproducts: This is a major difference over NMP, which liberates NO_x when decomposed. Also, Cyrene has very low acute and aquatic toxicity with LD_{50} (lethal dose, 50%) and EC50 (effective concentration, 50%) values of >2000 mg kg^{-1} and >100 mg L^{-1}, respectively. Overall, Cyrene is biodegradable and not mutagenic. Although it has a rather high boiling point (227°C), its low flash point (108°C, lower than several oxygenated solvents, such as alcohols and ketones) makes it safe to handle.

Salavagione et al. first demonstrate the preparation of LPE graphene in Cyrene. After 2 h of bath sonication, the dispersion showed a final concentration ~0.7 mg ml^{-1}, with a very high yield (~48%). These values are larger than those obtained by most conventional organic solvents, also requiring more complex LPE procedures (Lavin-Lopez et al., 2016). In their analysis, 92.5% of the dispersed flakes were few-layer (more than 10), 75% within five layers, and 7.5% monolayer (final average of 4.5 layers). In similar bath sonication experiments, Gharib et al. obtained a 6 times higher concentration with respect to NMP and DMF (Gharib et al., 2017). Tkachev et al. proposed the preparation of a graphene-based inks in Cyrene by a combination of two LPE methods (*i.e.*, tip-sonication and high-shear mixing). The authors produced highly concentrated dispersions (up to 3.70 g L^{-1}) of few-layer graphene flakes (three to five layers) with mean lateral size of ~200 nm (Tkachev, 2021). Pan et al. developed an environmentally friendly, sustainable, low-cost graphene-based ink in Cyrene with concentration up to 10 mg ml^{-1}, by using sonication assisted exfoliation. The authors added cellulose acetate butyrate (CAB) as a stabilizing agent to achieve even a higher concentrated ink (70 mg ml^{-1}) (Pan et al., 2018) of multilayer graphene flakes (thickness ~5 nm) with lateral size of a few μm.

In terms of applications, Pan et al. screen-printed electrodes from graphene inks in Cyrene and NMP. They obtained analogous sheet resistance values (~1 Ω □$^{-1}$) using inks produced with significantly different sonication times (8 h for Cyrene *vs.* 48 h for NMP). The electrical conductivity of dried and compressed graphene laminates from Cyrene ink (8 h sonication) was 7.13 × 10^4 S m^{-1}. These results pave the way to low-cost, screen-printable graphene-based wearables for Internet of Things applications, such as healthcare and wellbeing monitoring (Pan et al., 2018). Tkachev et al. prepared graphene-based inks in Cyrene to spray-coat flexible semi-transparent electrodes with high optical transmittance (78%) and low sheet resistance (290 Ω □$^{-1}$). They embedded such electrodes in a working prototype of a multi-touch screen with a high signal-to-noise ratio (14 dB). These results illustrate a potential pathway toward the integration of LPE-graphene in commercial flexible electronics (Tkachev, 2021). Hassan et al. proposed a green ink combining Cyrene and ethyl cellulose (polymeric binder that helps lowering sheet resistance by enhancing connectivity and filling the gaps). They used it to fabricate (by 3D extrusion printing) low-cost

patterned electrodes for volatile organic compounds detection fabricated. The devices showed a resistivity as low as 70 Ω cm and high sensitivity to organic compounds (*i.e.*, acetone, ethanol, and methanol). In particular, the device showed a high sensitivity towards ethanol (Hassan et al., 2021). These case study results suggest that Cyrene based graphene inks are more stable and suitable than the currently employed solvents for commercial applications, without any toxicity issues.

CONCLUSION

In summary, there is an urgent need of replacing conventional solvents like NMP and DMF for the liquid phase production of graphene, in order to reduce health and environmental issues and enable a sustainable industrial production. We have presented the most viable "green" solvents in the field, comparing their different properties and their effectiveness (in terms of concentration and yield) as exfoliation media. Among the possible options, Cyrene appears as the most promising green solvent for LPE techniques. The performance of Cyrene for the exfoliation of graphite was analyzed, also focusing on research literature reporting graphene-based devices prepared using this solvent. This mini-review sheds light on a sustainable solution processing methods for graphene, but the findings could be translated to other layered 2D materials, such as hBN, transition metal dichalcogenides and MXenes.

AUTHOR CONTRIBUTIONS

All authors listed have made a substantial, direct and intellectual contribution to the work, and approved it for publication.

FUNDING

AC acknowledges the support of the European Union's Horizon 2020 Research and Innovation Program under the Marie Skłodowska-Curie grant agreement no. 713640. We acknowledge the financial support of the project "GEMIS–Graphene-enhanced Electro Magnetic Interference Shielding," with the reference POCI-01-0247-FEDER-045939, co-funded by COMPETE 2020—Operational Programme for Competitiveness and Internationalization and FCT–Science and Technology Foundation, under the Portugal 2020 Partnership Agreement, through the European Regional Development Fund (ERDF).

REFERENCES

Alam, M. S., Ashokkumar, B., and Siddiq, A. M. (2019). The Density, Dynamic Viscosity and Kinematic Viscosity of Protic and Aprotic Polar Solvent (Pure and Mixed) Systems: An Experimental and Theoretical Insight of Thermophysical Properties. *J. Mol. Liquids* 281, 584–597. doi:10.1016/j.molliq.2019.02.097

Arao, Y., and Kubouchi, M. (2015). High-rate Production of Few-Layer Graphene by High-Power Probe Sonication. *Carbon* 95, 802–808. doi:10.1016/j.carbon.2015.08.108

Backes, C. (2020). Production and Processing of Graphene and Related Materials. *2d Mater.* 7.

Banavath, R., Nemala, S. S., Srivastava, R., and Bhargava, P. (2021). Non-Enzymatic H2O2 Sensor Using Liquid Phase High-Pressure Exfoliated Graphene. *J. Electrochem. Soc.* 168, 086508. doi:10.1149/1945-7111/ac1eb6

Bhol, P., Yadav, S., Altaee, A., Saxena, M., Misra, P. K., and Samal, A. K. (2021). Graphene-Based Membranes for Water and Wastewater Treatment: A Review. *ACS Appl. Nano Mater.* 4, 3274–3293. doi:10.1021/acsanm.0c03439

Bonaccorso, F., Lombardo, A., Hasan, T., Sun, Z., Colombo, L., and Ferrari, A. C. (2012). Production and Processing of Graphene and 2d Crystals. *Mater. Today* 15, 564–589. doi:10.1016/s1369-7021(13)70014-2

Capasso, A., Del Rio Castillo, A. E., Sun, H., Ansaldo, A., Pellegrini, V., and Bonaccorso, F. (2015). Ink-jet Printing of Graphene for Flexible Electronics: An Environmentally-Friendly Approach. *Solid State. Commun.* 224, 53–63. doi:10.1016/j.ssc.2015.08.011

Capello, C., Fischer, U., and Hungerbühler, K. (2007). What Is a green Solvent? A Comprehensive Framework for the Environmental Assessment of Solvents. *Green. Chem.* 9, 927–993. doi:10.1039/b617536h

Charles, M. (2007). *Hansen.* Hansen Solubility Parameters*A User's Handbook*. Second edition. Boca Raton, Florida: Psikologi Perkembangan.

Chen, H., Liu, B., Yang, Q., Wang, S., Liu, W., Zheng, X., et al. (2017). Facile One-step Exfoliation of Large-Size 2D Materials via Simply Shearing in Triethanolamine. *Mater. Lett.* 199, 124–127. doi:10.1016/j.matlet.2017.04.066

Chouhan, A., Mungse, H. P., and Khatri, O. P. (2020). Surface Chemistry of Graphene and Graphene Oxide: A Versatile Route for Their Dispersion and Tribological Applications. *Adv. Colloid Interf. Sci.* 283, 102215. doi:10.1016/j.cis.2020.102215

Coleman, J. N. (2013). Liquid Exfoliation of Defect-free Graphene. *Acc. Chem. Res.* 46, 14–22. doi:10.1021/ar300009f

De bruyn, M. (2016). A New Perspective in Bio-Refining: Levoglucosenone and Cleaner Lignin from Waste Biorefinery Hydrolysis Lignin by Selective Conversion of Residual Saccharides. *Energy Environ. Sci.* 9, 2571–2574. doi:10.1039/C6EE01352J

Del Rio Castillo, A. E., Pellegrini, V., Ansaldo, A., Ricciardella, F., Sun, H., Marasco, L., et al. (2018). High-yield Production of 2D Crystals by Wet-Jet Milling. *Mater. Horiz.* 5, 890–904. doi:10.1039/c8mh00487k

Galvao, J., Davis, B., Tilley, M., Normando, E., Duchen, M. R., and Cordeiro, M. F. (2014). Unexpected Low-dose Toxicity of the Universal Solvent DMSO. *FASEB j.* 28, 1317–1330. doi:10.1096/fj.13-235440

Gharib, D. H., Gietman, S., Malherbe, F., and Moulton, S. E. (2017). High Yield, Solid Exfoliation and Liquid Dispersion of Graphite Driven by a Donor-Acceptor Interaction. *Carbon* 123, 695–707. doi:10.1016/j.carbon.2017.08.025

Green, A. A., and Hersam, M. C. (2009). Solution Phase Production of Graphene with Controlled Thickness via Density Differentiation. *Nano Lett.* 9, 4031–4036. doi:10.1021/nl902200b

Güler, Ö., and Sönmez, A. (2020). The Effect of Liquid Media on the Efficiency of Graphene Production by Liquid-phase Exfoliation from Micromechanically Pre-exfoliated Graphite. *J. Electron. Mater.* 49, 5335–5345. doi:10.1007/s11664-020-08257-w

Güler, Ö., Tekeli, M., Taşkın, M., Güler, S. H., and Yahia, I. S. (2021). The Production of Graphene by Direct Liquid Phase Exfoliation of Graphite at Moderate Sonication Power by Using Low Boiling Liquid media: The Effect of Liquid media on Yield and Optimization. *Ceram. Int.* 47, 521–533. doi:10.1016/j.ceramint.2020.08.159

Gutiérrez, M., and Henglein, A. (1989). Preparation of Colloidal Semiconductor Solutions of MoS2 and WSe2 via Sonication. *Ultrasonics* 27, 259–261. doi:10.1016/0041-624X(89)90066-8

Halim, U., Zheng, C. R., Chen, Y., Lin, Z., Jiang, S., Cheng, R., et al. (2013). A Rational Design of Cosolvent Exfoliation of Layered Materials by Directly Probing Liquid-Solid Interaction. *Nat. Commun.* 4, 2213–2217. doi:10.1038/ncomms3213

Hasan, T., Torrisi, F., Sun, Z., Popa, D., Nicolosi, V., Privitera, G., et al. (2010). Solution-phase Exfoliation of Graphite for Ultrafast Photonics. *Phys. Stat. Sol. (B)* 247, 2953–2957. doi:10.1002/pssb.201000339

Hassan, K., Tung, T. T., Stanley, N., Yap, P. L., Farivar, F., Rastin, H., et al. (2021). Graphene Ink for 3D Extrusion Micro Printing of Chemo-Resistive Sensing Devices for Volatile Organic Compound Detection. *Nanoscale* 13, 5356–5368. doi:10.1039/d1nr00150g

He, P., Zhou, C., Tian, S., Sun, J., Yang, S., Ding, G., et al. (2015). Urea-assisted Aqueous Exfoliation of Graphite for Obtaining High-Quality Graphene. *Chem. Commun.* 51, 4651–4654. doi:10.1039/c5cc00059a

Hernandez, Y., Lotya, M., Rickard, D., Bergin, S. D., and Coleman, J. N. (2010). Measurement of Multicomponent Solubility Parameters for Graphene Facilitates Solvent Discovery. *Langmuir* 26, 3208–3213. doi:10.1021/la903188a

Hernandez, Y., Nicolosi, V., Lotya, M., Blighe, F. M., Sun, Z., De, S., et al. (2008). High-yield Production of Graphene by Liquid-phase Exfoliation of Graphite. *Nat. Nanotech* 3, 563–568. doi:10.1038/nnano.2008.215

Kawahara, K., and Tanford, C. (1966). Viscosity and Density of Aqueous Solutions of Urea and Guanidine Hydrochloride. *J. Biol. Chem.* 241, 3228–3232. doi:10.1016/s0021-9258(18)96519-1

Khan, U., O'Neill, A., Lotya, M., De, S., and Coleman, J. N. (2010). High-Concentration Solvent Exfoliation of Graphene. *Small* 6, 864–871. doi:10.1002/smll.200902066

Lavin-Lopez, M. P., Valverde, J. L., Sanchez-Silva, L., and Romero, A. (2016). Solvent-Based Exfoliation via Sonication of Graphitic Materials for Graphene Manufacture. *Ind. Eng. Chem. Res.* 55, 845–855. doi:10.1021/acs.iecr.5b03502

Li, D., Lai, W. Y., Zhang, Y. Z., and Huang, W. (2018). Printable Transparent Conductive Films for Flexible Electronics. *Adv. Mater.* 30, 1–24. doi:10.1002/adma.201704738

Li, X., and Zhi, L. (2018). Graphene Hybridization for Energy Storage Applications. *Chem. Soc. Rev.* 47, 3189–3216. doi:10.1039/c7cs00871f

Li, Z., Young, R. J., Backes, C., Zhao, W., and Zhang, X. (2020). *Mechanisms of Liquid Phase Exfoliation for the Production of Graphene*. Washington: American Chemical Society, 1–35.

Lotya, M., Hernandez, Y., King, P. J., Smith, R. J., Nicolosi, V., Karlsson, L. S., et al. (2009). Liquid Phase Production of Graphene by Exfoliation of Graphite in Surfactant/Water Solutions. *J. Am. Chem. Soc.* 131, 3611–3620. doi:10.1021/ja807449u

Maham, Y., Liew, C.-N., and Mather, A. E. (2002). Viscosities and Excess Properties of Aqueous Solutions of Ethanolamines from 25 to 80°C. *J. Solution Chem.* 31, 743–756. doi:10.1023/a:1021133008053

Manna, K., Huang, H.-N., Li, W.-T., Ho, Y.-H., and Chiang, W.-H. (2016). Toward Understanding the Efficient Exfoliation of Layered Materials by Water-Assisted Cosolvent Liquid-phase Exfoliation. *Chem. Mater.* 28, 7586–7593. doi:10.1021/acs.chemmater.6b01203

Mehmood, A., Mubarak, N. M., Khalid, M., Walvekar, R., Abdullah, E. C., Siddiqui, M. T. H., et al. (2020). Graphene Based Nanomaterials for Strain Sensor Application-A Review. *J. Environ. Chem. Eng.* 8, 103743. doi:10.1016/j.jece.2020.103743

Nawaz, K., Ayub, M., Khan, M. B., Hussain, A., Malik, A. Q., Niazi, M. B. K., et al. (2016). Effect of Concentration of Surfactant on the Exfoliation of Graphite to Graphene in Aqueous media. *Nanomater. Nanotechnol.* 6, 1–7. doi:10.5772/62290

Neill, A. O. (2009). Graphene Dispersion and Exfoliation in Low Boiling Point Solvents Graphene Dispersion and Exfoliation in Low Boiling Point Solvents. *J. Am. Chem. Soc.* 131, 3611–3620. doi:10.1021/jp110942e

Nemala, S. S., Aneja, K. S., Bhargava, P., Bohm, H. L. M., Mallick, S., and Bohm, S. (2018). Novel High-Pressure Airless spray Exfoliation Method for Graphene Nanoplatelets as a Stable Counter Electrode in DSSC. *Electrochimica Acta* 285, 86–93. doi:10.1016/j.electacta.2018.07.229

Pan, K., Fan, Y., Leng, T., Li, J., Xin, Z., Zhang, J., et al. (2018). Sustainable Production of Highly Conductive Multilayer Graphene Ink for Wireless Connectivity and IoT Applications. *Nat. Commun.* 9, 5197. doi:10.1038/s41467-018-07632-w

Paolucci, V., D'Olimpio, G., Lozzi, L., Mio, A. M., Ottaviano, L., Nardone, M., et al. (2020). Sustainable Liquid-phase Exfoliation of Layered Materials with Nontoxic Polarclean Solvent. *ACS Sust. Chem. Eng.* 8, 18830–18840. doi:10.1021/acssuschemeng.0c04191

Paton, K. R., Varrla, E., Backes, C., Smith, R. J., Khan, U., O'Neill, A., et al. (2014). Scalable Production of Large Quantities of Defect-free Few-Layer Graphene by Shear Exfoliation in Liquids. *Nat. Mater* 13, 624–630. doi:10.1038/nmat3944

Pourabadeh, A., Sanjari Fard, A., and Jalaei Salmani, H. (2020). VLE and Viscosity Modeling of N-Methyl-2-Pyrrolidone (NMP) + Water (Or 2-propanol or 2-butanol) Mixtures by Cubic-Plus-Association Equation of State. *J. Mol. Liquids* 307, 112980. doi:10.1016/j.molliq.2020.112980

Regulation (EC) No 1907/2006 (2022). *Registration, Evaluation, Authorisation and Restriction of Chemicals (REACH) | Safety and Health at Work EU-OSHA*.

Rodríguez, M., Galán, M., Muñoz, M. J., and Martín, R. (1994). Viscosity of Triglycerides + Alcohols from 278 to 313 K. *J. Chem. Eng. Data* 39, 102–105. doi:10.1021/je00013a027

Ryu, M.-Y., Jang, H.-K., Lee, K. J., Piao, M., Ko, S.-P., Shin, M., et al. (2017). Triethanolamine Doped Multilayer MoS2 Field Effect Transistors. *Phys. Chem. Chem. Phys.* 19, 13133–13139. doi:10.1039/c7cp00589j

Salavagione, H. J., Sherwood, J., De bruyn, M., Budarin, V. L., Ellis, G. J., Clark, J. H., et al. (2017). Identification of High Performance Solvents for the Sustainable Processing of Graphene. *Green. Chem.* 19, 2550–2560. doi:10.1039/c7gc00112f

Secor, E. B., Ahn, B. Y., Gao, T. Z., Lewis, J. A., and Hersam, M. C. (2015). Rapid and Versatile Photonic Annealing of Graphene Inks for Flexible Printed Electronics. *Adv. Mater.* 27, 6683–6688. doi:10.1002/adma.201502866

Secor, E. B., Prabhumirashi, P. L., Puntambekar, K., Geier, M. L., and Hersam, M. C. (2013). Inkjet Printing of High Conductivity, Flexible Graphene Patterns. *J. Phys. Chem. Lett.* 4, 1347–1351. doi:10.1021/jz400644c

Seo, J.-W. T., Green, A. A., Antaris, A. L., and Hersam, M. C. (2011). High-concentration Aqueous Dispersions of Graphene Using Nonionic, Biocompatible Block Copolymers. *J. Phys. Chem. Lett.* 2, 1004–1008. doi:10.1021/jz2003556

Shen, J., He, Y., Wu, J., Gao, C., Keyshar, K., Zhang, X., et al. (2015). Liquid Phase Exfoliation of Two-Dimensional Materials by Directly Probing and Matching Surface Tension Components. *Nano Lett.* 15, 5449–5454. doi:10.1021/acs.nanolett.5b01842

Shen, J., Wu, J., Wang, M., Dong, P., Xu, J., Li, X., et al. (2016). Surface Tension Components Based Selection of Cosolvents for Efficient Liquid Phase Exfoliation of 2D Materials. *Small* 12, 2741–2749. doi:10.1002/smll.201503834

Sherwood, J., De bruyn, M., Constantinou, A., Moity, L., McElroy, C. R., Farmer, T. J., et al. (2014). Dihydrolevoglucosenone (Cyrene) as a Bio-Based Alternative for Dipolar Aprotic Solvents. *Chem. Commun.* 50, 9650–9652. doi:10.1039/c4cc04133j

Shin, D. W., Barnes, M. D., Walsh, K., Dimov, D., Tian, P., Neves, A. I. S., et al. (2018). A New Facile Route to Flexible and Semi-transparent Electrodes Based on Water Exfoliated Graphene and Their Single-Electrode Triboelectric Nanogenerator. *Adv. Mater.* 30, e1802953–7. doi:10.1002/adma.201802953

Simfukwe, J., Mapasha, R. E., Braun, A., and Diale, M. (2017). The Effect of Solvent Viscosity on Production of Few-Layer Graphene from Liquid-phase Exfoliation of Graphite. *MRS Adv.* 357, 1–8. doi:10.1557/adv.2019.13

Hou, D., Liu, Q., Wang, X., Qiao, Z., Wu, Z., Wu, Y., et al. (2019). Urea-Assisted Liquid-Phase Exfoliation of Natural Graphite into Few-Layer Graphene. *Chem. Phys. Lett.* 700, 108–113. doi:10.1016/j.cplett.2018.04.019

Smith, R. J., Lotya, M., and Coleman, J. N. (2010). The Importance of Repulsive Potential Barriers for the Dispersion of Graphene Using Surfactants. *New J. Phys.* 12, 125. doi:10.1088/1367-2630/12/12/125008

Song, B., Sizemore, C., Li, L., Huang, X., Lin, Z., Moon, K.-s., et al. (2015). Triethanolamine Functionalized Graphene-Based Composites for High Performance Supercapacitors. *J. Mater. Chem. A.* 3, 21789–21796. doi:10.1039/c5ta05674h

Tan, R. K. L., Reeves, S. P., Hashemi, N., Thomas, D. G., Kavak, E., Montazami, R., et al. (2017). Graphene as a Flexible Electrode: Review of Fabrication Approaches. *J. Mater. Chem. A.* 5, 17777–17803. doi:10.1039/c7ta05759h

Tkachev, S. (2021). Environmentally Friendly Graphene Inks for Touch Screen Sensors. *Adv. Funct. Mater.* 31,3287. doi:10.1002/adfm.202103287

Trusova, E. A., Klimenko, I. V., Afzal, A. M., Shchegolikhin, A. N., and Jurina, L. V. (2021). Comparison of Oxygen-free Graphene Sheets Obtained in DMF and DMF-Aqua media. *New J. Chem.* 45, 10448–10458. doi:10.1039/d1nj01015h

Turner, P., Hodnett, M., Dorey, R., and Carey, J. D. (2019). Controlled Sonication as a Route to *In-Situ* Graphene Flake Size Control. *Sci. Rep.* 9, 8710–8718. doi:10.1038/s41598-019-45059-5

Vacacela Gomez, C., Guevara, M., Tene, T., Villamagua, L., Usca, G. T., Maldonado, F., et al. (2021). The Liquid Exfoliation of Graphene in Polar Solvents. *Appl. Surf. Sci.* 546, 149046. doi:10.1016/j.apsusc.2021.149046

Verheijen, M., Lienhard, M., Schrooders, Y., Clayton, O., Nudischer, R., Boerno, S., et al. (2019). DMSO Induces Drastic Changes in Human Cellular Processes and Epigenetic Landscape *In Vitro*. *Sci. Rep.* 9, 4641–4652. doi:10.1038/s41598-019-40660-0

Wang, J., Shi, Z., Ge, Y., Wang, Y., Fan, J., and Yin, J. (2012). Solvent Exfoliated Graphene for Reinforcement of PMMA Composites Prepared by *In Situ* Polymerization. *Mater. Chem. Phys.* 136, 43–50. doi:10.1016/j.matchemphys.2012.06.017

Wang, Y., Zhou, W., Cao, K., Hu, X., Gao, L., and Lu, Y. (2021). Architectured Graphene and its Composites: Manufacturing and Structural Applications. *Composites A: Appl. Sci. Manufacturing* 140, 106177. doi:10.1016/j.compositesa.2020.106177

Wu, C., Cheng, Q., Wu, K., Wu, G., and Li, Q. (2014). Graphene Prepared by One-Pot Solvent Exfoliation as a Highly Sensitive Platform for Electrochemical Sensing. *Analytica Chim. Acta* 825, 26–33. doi:10.1016/j.aca.2014.03.036

Xu, Y., Cao, H., Xue, Y., Li, B., and Cai, W. (2018). Liquid-phase Exfoliation of Graphene: An Overview on Exfoliation media, Techniques, and Challenges. *Nanomaterials (Basel)* 8, 942. doi:10.3390/nano8110942

Yang, Y., Asiri, A. M., Tang, Z., Du, D., and Lin, Y. (2013). Graphene Based Materials for Biomedical Applications. *Mater. Today* 16, 365–373. doi:10.1016/j.mattod.2013.09.004

Yaws, C. L. (2014). *Surface Tension – Organic CompoundsThermophysical Properties of Chemicals and Hydrocarbons*, 700. Elsevier.

Zhang, K., Zhang, X., Li, H., Xing, X., Jin, L. e., Cao, Q., et al. (2018). Direct Exfoliation of Graphite into Graphene in Aqueous Solution Using a Novel Surfactant Obtained from Used Engine Oil. *J. Mater. Sci.* 53, 2484–2496. doi:10.1007/s10853-017-1729-7

Zhang, Q., Cai, S., Zhang, W., Lan, Y., and Zhang, X. (2017). Density, Viscosity, Conductivity, Refractive index and Interaction Study of Binary Mixtures of the Ionic Liquid 1–Ethyl–3–Methylimidazolium Acetate with Methyldiethanolamine. *J. Mol. Liquids* 233, 36. doi:10.1016/j.molliq.2017.03.036

Zhao, W., Fang, M., Wu, F., Wu, H., Wang, L., and Chen, G. (2010). Preparation of Graphene by Exfoliation of Graphite Using Wet ball Milling. *J. Mater. Chem.* 20, 5817–5819. doi:10.1039/c0jm01354d

Zhou, K.-G., Mao, N.-N., Wang, H.-X., Peng, Y., and Zhang, H.-L. (2011). A Mixed-Solvent Strategy for Efficient Exfoliation of Inorganic Graphene Analogues. *Angew. Chem. Int. Ed.* 50, 10839–10842. doi:10.1002/anie.201105364

Conflict of Interest: The authors declare that the research was conducted in the absence of any commercial or financial relationships that could be construed as a potential conflict of interest.

Publisher's Note: All claims expressed in this article are solely those of the authors and do not necessarily represent those of their affiliated organizations, or those of the publisher, the editors, and the reviewers. Any product that may be evaluated in this article, or claim that may be made by its manufacturer, is not guaranteed or endorsed by the publisher.

Frontiers in Chemistry

Explores all fields of chemical science across the periodic table

Advances our understanding of how atoms, ions, and molecules come together and come apart. It explores the role of chemistry in our everyday lives - from electronic devices to health and wellbeing.

Discover the latest Research Topics

See more →

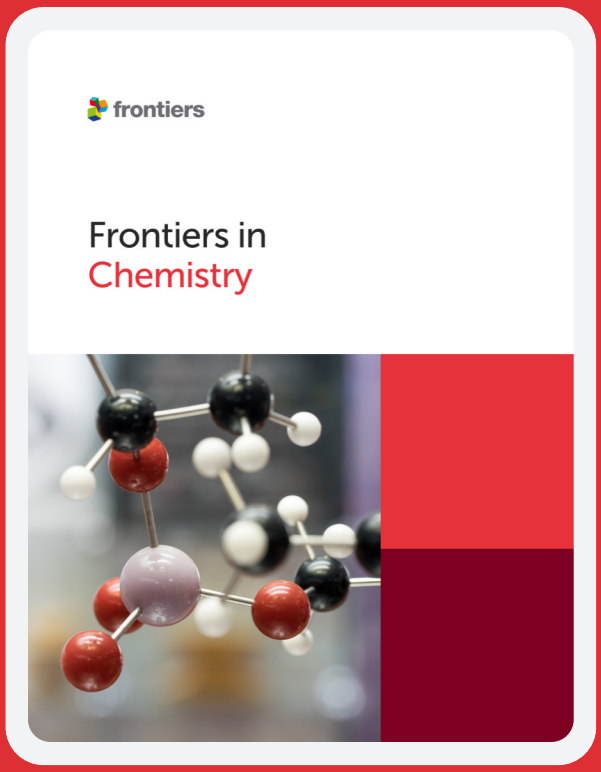

Frontiers

Avenue du Tribunal-Fédéral 34
1005 Lausanne, Switzerland
frontiersin.org

Contact us

+41 (0)21 510 17 00
frontiersin.org/about/contact